

# Important Notice

This copy may be used only for the purposes of research and private study, and any use of the copy for a purpose other than research or private study may require the authorization of the copyright owner of the work in question. Responsibility regarding questions of copyright that may arise in the use of this copy is assumed by the recipient.

THE UNIVERSITY OF CALGARY

**Processing of P-SV Surface-Seismic Data:  
Anisotropy Analysis, Dip Moveout, and Migration**

by

Mark Paul Harrison

A DISSERTATION

SUBMITTED TO THE FACULTY OF GRADUATE STUDIES  
IN PARTIAL FULFILLMENT OF THE REQUIREMENTS FOR THE  
DEGREE OF DOCTOR OF PHILOSOPHY

DEPARTMENT OF GEOLOGY AND GEOPHYSICS

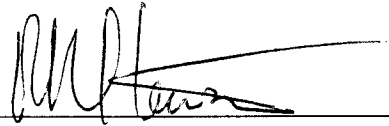
CALGARY, ALBERTA  
SEPTEMBER, 1992

© Mark Paul Harrison 1992

THE UNIVERSITY OF CALGARY

FACULTY OF GRADUATE STUDIES

The undersigned certify that they have read, and recommend to the Faculty of Graduate Studies for acceptance, a dissertation entitled "Processing of P-SV Surface-Seismic Data: Anisotropy Analysis, Dip Moveout, and Migration" submitted by Mark Paul Harrison in partial fulfillment of the requirements of the degree of Doctor of Philosophy.



---

Supervisor, Dr. R. R. Stewart,  
Department of Geology and Geophysics



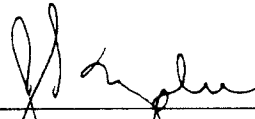
---

Dr. D. C. Lawton,  
Department of Geology and Geophysics



---

Dr. E. S. Krebs,  
Department of Geology and Geophysics



---

Dr. J. S. Murphree,  
Department of Physics and Astronomy



---

External Examiner, Dr. E. R. Kanasevich,  
The University of Alberta

September 14, 1992

## Abstract

In this dissertation, the current state of multicomponent converted-wave ( $P$ - $SV$ ) processing for surface seismic data is summarized and a number of new algorithms are developed and tested. These include:  $P$ - $SV$  geometric spreading compensation;  $P$ - $SV$  poststack velocity inversion;  $S$ -wave anisotropy analysis;  $P$ - $SV$  dip moveout (DMO); and  $P$ - $SV$  poststack migration.

The problem of  $S$ -wave birefringence for the case of a singly-polarized shear source is examined, and an algorithm for the determination of the amount of  $S$ -wave splitting and the orientation of the natural coordinate system is developed. This algorithm is based upon the modeling of the crosscorrelation function between rotated radial and transverse field components. Synthetic examples indicate that it can resolve time delays of about 1 ms or greater for noise-free data with an 8-35 Hz bandwidth; the receiver azimuth relative to the natural coordinate system is accurately determined for time delays of about 2 ms or greater. A study of the method's performance versus signal-to-noise power ratio suggests that a signal-to-noise ratio of about 36 db is needed to obtain both the time-delay and rotation angle from a single receiver data set. For data with a signal-to-noise power ratio of 0 db, an analysis fold of about 60 is needed to determine the correct time delay and rotation angle. Application of the method to converted-wave data from Carrot Creek, Alberta, produces results that are in agreement with the difference in orientation between the two lines in the survey.

An expression for common-conversion-point (CCP) dispersal for  $P$ - $SV$  data is derived, and is found to give greater dispersal for data converted in the down-dip direction than in the up-dip direction. The apparent stacking velocity for the single-layer case is shown to also be asymmetric about reflector zero-dip, and for large positive (down-dip) values the apparent velocity can become imaginary. A dip moveout (DMO) equation for converted-wave data is derived, and is proven to properly account for  $P$ - $SV$  CCP dispersal.

A new cubic equation for determining the location to the zero-dip conversion point is also developed. The  $P$ - $SV$  DMO equation is implemented using an integral-summation technique and applied to both synthetic and real data examples. In synthetic data,  $P$ - $SV$  DMO gives better amplitude preservation of  $P$ - $SV$  diffractions and dipping reflections.

The application of poststack migration to converted-wave stack data is studied. It is shown that the exploding reflector model does not strictly hold for converted-wave stack data, but is a reasonable approximation if there are no large depth variations in  $V_p/V_s$  ratio. A  $P$ - $SV$  migration velocity equation is developed, and gives velocities that are less than  $P$ - $SV$  stacking velocities by 6-11%. Migration of synthetic  $P$ - $SV$  diffractions demonstrate that stacking velocities produce substantial overmigration, whereas the  $P$ - $SV$  migration velocities do not. A physical model data set simulating a buried reef is also migrated, and the  $P$ - $SV$  data are found to give a good structural image.

The processing techniques developed and discussed in this dissertation are applied to a three-component vibroseis survey from Carrot Creek, Alberta. The radial-component ( $P$ - $SV$ ) stack section is of good quality, with amplitude anomalies that correspond to the known location of oil pools. These anomalies are largely absent on the vertical-component ( $P$ - $P$ ) sections.

The processing results for a two-component data set from Springbank, Alberta, are presented. The radial-component data are found to be of very poor quality; the stack section, however, has many coherent reflections that correlate well to those of the vertical-component stacked data.

The results of processing a three-component dynamite survey from Casper Creek South, Wyoming, are also presented. Two-component geophone rotation produces some improvement in the rotated radial-component data signal strength. Reflections with substantial dips are imaged on both the  $P$ - $P$  and  $P$ - $SV$  stack sections. The converted-wave section, however, has a higher noise level and much lower bandwidth than the vertical-component ( $P$ - $P$ ) section.

## Acknowledgments

Rob Stewart has contributed many useful suggestions to this dissertation, and has created an interesting and enjoyable working environment within the CREWES group. Tina Howell gave technical assistance with the data processing, and Eric Gallant helped with the physical model data. Skip Walden and Jack Cameron of UNOCAL generously donated the Casper Creek South data set.

I thank all these people, and, most of all, Megan, who has often nearly forgotten what her dad looks like, and Sarah for their patience and support over the last three years.

# Table of Contents

Abstract .....	iii
Acknowledgments .....	v
Table of Contents .....	vi
List of Tables .....	ix
List of Figures .....	x
Chapter 1 - Introduction .....	1
1.1 Background .....	1
1.2 Dissertation objectives .....	3
1.3 Data sets used in the dissertation .....	3
1.3.1 Synthetic <i>P-SV</i> data sets .....	3
1.3.2 Physical model data .....	4
1.3.3 Carrot Creek, Alberta .....	4
1.3.4 Springbank, Alberta .....	4
1.3.5 Casper Creek South, Wyoming .....	5
1.4 Hardware and software used .....	5
Chapter 2 - General processing of <i>P-SV</i> seismic data .....	6
2.1 Introduction .....	6
2.2 Polarity reversal of trailing spread .....	6
2.3 Rotation of horizontal components .....	8
2.4 Geometric spreading compensation .....	9
2.5 <i>P-SV</i> stacking velocity estimation and NMO correction .....	13
2.6 <i>P-SV</i> static solution .....	15
2.7 CCP binning .....	17
2.8 CCP trim statics .....	19
2.9 <i>P-SV</i> dip moveout .....	20
2.10 <i>P-SV</i> zero-offset migration .....	20
2.11 <i>P-SV</i> poststack inversion .....	21
Chapter 3 - Birefringence analysis for <i>P-SV</i> data .....	24
3.1 Introduction .....	24
3.2 Mathematical background .....	25
3.3 Birefringence analysis algorithms .....	32
3.3.1 Modeling the odd part of the crosscorrelation function .....	33
3.3.2 Modeling the total crosscorrelation function .....	34

3.4 Application of birefringence analysis .....	36
3.4.1 Analysis of synthetic data .....	38
3.4.2 Analysis of data from Carrot Creek, Alberta .....	44
3.5 Discussion .....	48
Chapter 4 - Dip moveout for <i>P-SV</i> data .....	51
4.1 Introduction .....	51
4.2 Conversion-point dispersal for <i>P-SV</i> data .....	53
4.3 Apparent slowness for <i>P-SV</i> data .....	58
4.4 <i>P-SV</i> zero-offset mapping .....	60
4.4.1 Derivation using geometric optics .....	62
4.4.2 Derivation using Snell's Law .....	68
4.4.3 Discussion of <i>P-SV</i> DMO equation .....	71
4.5 Envelope of the <i>P-SV</i> DMO operator .....	74
4.6 Location of the zero-dip conversion point .....	78
4.7 <i>P-SV</i> DMO and conversion-point dispersal .....	79
4.8 Implementation of <i>P-SV</i> dip moveout .....	81
4.8.1 <i>P-SV</i> operator amplitude and phase correction .....	81
4.8.2 Modification for depth-varying velocities .....	88
4.8.3 Application of <i>P-SV</i> DMO to synthetic data .....	96
4.9 Discussion .....	102
Chapter 5 - Poststack migration for <i>P-SV</i> data .....	104
5.1 Introduction .....	104
5.2 Migration velocity derivation .....	105
5.3 Migration examples .....	111
5.3.1 Synthetic data .....	111
5.3.2 Physical model data .....	118
5.4 Discussion .....	130
Chapter 6 - Multicomponent processing: Carrot Creek, Alberta .....	132
6.1 Introduction .....	132
6.2 Data acquisition .....	132
6.3 Data processing .....	138
6.4 Discussion .....	166
Chapter 7 - Multicomponent processing: Springbank, Alberta .....	170
7.1 Introduction .....	170
7.2 Data acquisition .....	170
7.3 Data processing .....	172

7.4 Discussion .....	191
Chapter 8 - Multicomponent processing: Casper Creek South, Wyoming .....	193
8.1 Introduction .....	193
8.2 Data acquisition .....	194
8.3 Data processing .....	195
8.4 Discussion .....	211
Chapter 9 - Conclusions .....	218
9.1 Dissertation summary .....	218
9.2 Future work .....	220
References .....	222

## List of Tables

Table 4.1.	Velocities used to generate the ray-traced migration and DMO responses. ....	93
Table 4.2.	Parameters used in generating the synthetic DMO test data. ....	97
Table 5.1.	Parameters used in generating the synthetic migration test data. ....	112
Table 6.1.	Field acquisition and recording parameters for the Carrot Creek survey. ....	133
Table 7.1.	Field acquisition and recording parameters for line FS90-1 of the Springbank survey. ....	172
Table 8.1.	Field acquisition and recording parameters for the Casper Creek South survey. ....	195

## List of Figures

FIG. 2.1.	Processing flow for $P$ - $SV$ mode-converted data. Steps not always performed are indicated in dashed boxes. ....	7
FIG. 2.2.	Geometric energy spreading for $P$ - $SV$ data. The energy flowing through the area swept out by rotating $dl$ about the source is the same for all offsets. ....	10
FIG. 2.3.	Near-surface raypaths for reflected and converted rays. MP indicates the $P$ - $P$ reflection point, and CP indicates the $P$ - $SV$ conversion point. ....	16
FIG. 2.4.	Flowchart for the $P$ - $SV$ poststack velocity inversion algorithm. ....	23
FIG. 3.1.	Plan view of a multicomponent line in an area of vertical $S$ -wave birefringence. ....	26
FIG. 3.2.	Flowchart for the birefringence analysis algorithm of Section 3.3.2. ....	36
FIG. 3.3.	Synthetic data created for differing natural-coordinate-system angle $\theta$ and varying amounts of time lag $\delta$ : (a) radial component; (b) transverse component. ....	37
FIG. 3.4.	Synthetic data created for natural-coordinate-system-angle $\theta=-30^\circ$ and time lag $\delta=4$ ms: (a) radial (R) and transverse (T) data; (b) total autocorrelation $A$ ; (c) crosscorrelation $X$ between rotated radial and transverse components for various rotation angles $\phi$ ; (d) even part of (c); (e) odd part of (c). ....	39
FIG. 3.5.	Time-delay analysis described in Section 3.3.1 applied to synthetic data in Figure 3.4: (a) energy-normalized crosscorrelation sum $\sigma$ vs. time lag; (b) signal-to-noise variance ratio $S/N$ [equation (3.26)] vs. time lag. ....	40
FIG. 3.6.	$\theta$ - $\delta$ analysis described in Section 3.3.2 applied to noise-free synthetic data: (a) $\theta=-30^\circ$ , $\delta=0$ ms; (b) $\theta=-30^\circ$ , $\delta=1$ ms; (c) $\theta=-30^\circ$ , $\delta=2$ ms; (d) $\theta=-30^\circ$ , $\delta=4$ ms; (e) $\theta=-30^\circ$ , $\delta=8$ ms; (f) $\theta=10^\circ$ , $\delta=4$ ms. ....	41
FIG. 3.7.	Values of (a) the angle $\theta$ and (b) the delay time $\delta$ obtained by $\theta$ - $\delta$ analysis vs. signal-to-noise power ratio ( $SNR$ ) for $\theta=-30^\circ$ and $\delta=4$ ms. ....	45

FIG. 3.8.	Values of (a) the angle $\theta$ and (b) the delay time $\delta$ obtained by $\theta$ - $\delta$ analysis vs. correlation fold for $\theta=-30^\circ$ , $\delta=4$ ms, and $SNR=0$ db. ....	46
FIG. 3.9.	Horizontal-component records for VP 107 of line CC-SW-02: (a) radial; (b) transverse. A 50/60 Hz highcut filter and 800 ms AGC have been applied. ....	47
FIG. 3.10.	$\theta$ - $\delta$ analysis applied to Carrot Creek data: (a) CC-SW-01; (b) CC-SW-02. ....	49
FIG. 4.1.	Raypath geometry for conversion from a dipping reflector. ....	54
FIG. 4.2.	$P$ - $P$ and $P$ - $SV$ dispersal curves for a reflector zero-offset depth of 1 km and source-to-receiver offsets of (a) 0.5 km and (b) 1.0 km. ....	57
FIG. 4.3.	Apparent $P$ - $SV$ slowness curves for a reflector zero-offset depth of 1 km and source-to-receiver offsets of (a) 0.5 km and (b) 1.0 km. ....	61
FIG. 4.4.	Raypath geometry for computing the locus of points from which a datum sample could have originated. ....	62
FIG. 4.5.	$P$ - $P$ migration ellipses for a source-to-receiver offset of 1 km and various two-way times. The curves were generated by placing a spike of constant amplitude at the appropriate time-offset position, then filtering with a bandpass operator. ....	65
FIG. 4.6.	$P$ - $SV$ migration curves for a source-to-receiver offset of 1 km and various two-way times. The curves were generated as in Figure 4.5. ....	65
FIG. 4.7.	Generation of the zero-offset response to a migration curve. ....	66
FIG. 4.8.	Raypath geometry for conversion from a dipping reflector. The origin has been shifted to the source-to-receiver midpoint. ....	68
FIG. 4.9.	DMO curves corresponding to the migration curves of (a) Figure 4.5 ( $P$ - $P$ ) and (b) Figure 4.6 ( $P$ - $SV$ ). The curves were generated as in Figure 4.5. The offset and time axes correspond to the variables $\chi$ and $\tau$ in equation (4.34). ....	72
FIG. 4.10.	$f$ - $k$ migration applied to the $P$ - $SV$ DMO curves of Figure 4.9b. ....	73
FIG. 4.11.	Relationship between changes in zero-offset distance $r$ and operator offset $\chi$ . ....	75
FIG. 4.12.	$P$ - $SV$ DMO responses with dip apertures restricted to (a) $\pm 60^\circ$ and (b) $\pm 30^\circ$ . ....	77

FIG. 4.13. Time difference along the DMO curve. ....	82
FIG. 4.14. (a) Phase function of equation (4.79) and (b) amplitude function of equation (4.81) vs. the integration length, $u_1$ . ....	85
FIG. 4.15. DMO model for depth-varying velocities, consisting of a dipping reflector situated beneath a number of horizontal layers. ....	89
FIG. 4.16. Zero-offset mode-conversion from a dipping reflector situated beneath a number of horizontal layers. ....	91
FIG. 4.17. Ray-traced $P$ - $SV$ migration response for the velocity field given in Table 4.1. The heavy line indicates the ray-traced location of the zero-dip conversion point. ....	93
FIG. 4.18. Ray-traced $P$ - $SV$ DMO response corresponding to the migration response of Figure 4.17. The heavy line indicates the ray-traced location of the zero-dip conversion point. ....	94
FIG. 4.19. $P$ - $SV$ DMO response computed using equation (4.49) and average $P$ - and $S$ -wave velocities. The heavy line indicates the ray-traced location of the zero-dip conversion point. ....	95
FIG. 4.20. Several NMO-corrected source gathers from the synthetic data set. All AVO effects have been removed. ....	97
FIG. 4.21. Synthetic data stacked using the asymptotic gathering method. ....	98
FIG. 4.22. Synthetic data stacked using true conversion-point gathering. ....	98
FIG. 4.23. Synthetic data stacked using $P$ - $SV$ dip moveout. ....	99
FIG. 4.24. NMO-corrected gathers after (a) asymptotic gathering and (b) $P$ - $SV$ DMO. ....	100
FIG. 4.25. AVO synthetic data stacked using asymptotic gathering. ....	101
FIG. 4.26. AVO synthetic data stacked using $P$ - $SV$ dip moveout. ....	101
FIG. 5.1. Zero-offset raypaths traveled through a layered Earth from a point diffractor ....	106
FIG. 5.2. Ratio of RMS velocity to migration velocity as a function of $V_p/V_s$ value for the constant- $V_p/V_s$ case. ....	112
FIG. 5.3. Sample raypaths for diffracted energy received by two geophones. Diffractors are positioned at 250 m depth intervals, ranging from 250 m to 2000 m. ....	113
FIG. 5.4. Sample synthetic $P$ - $SV$ records for the constant-velocity case. The data have been NMO corrected and scaled for spherical divergence. Every second trace is plotted. ....	114

FIG. 5.5.	Constant-velocity data stacked using depth-variant binning (DVB). Every second trace is plotted.....	115
FIG. 5.6.	Constant-velocity data stacked using <i>P-SV</i> DMO. Every second trace is plotted. ....	116
FIG. 5.7.	DMO-stacked constant-velocity data migrated using: (a) the RMS velocity function; (b) the <i>P-SV</i> migration velocity function. Every second trace is plotted. ....	117
FIG. 5.8.	Velocity model used to generate the second synthetic data set, plotted as a function of total two-way <i>P-SV</i> travelttime. The <i>P</i> -wave velocity function is labeled as $\alpha$ , and the <i>S</i> -wave function is labeled as $\beta$ . Also shown is the ratio of RMS and migration velocity functions for this model. ....	119
FIG. 5.9.	Sample synthetic <i>P-SV</i> records for the variable-velocity case. The data have been NMO corrected and scaled for spherical divergence. Every second trace is plotted.....	120
FIG. 5.10.	Variable-velocity data stacked using DVB. Every second trace is plotted.....	121
FIG. 5.11.	Variable-velocity data stacked using depth-variant <i>P-SV</i> DMO. Every second trace is plotted. ....	122
FIG. 5.12.	DMO-stacked variable-velocity data migrated using: (a) the RMS velocity function; (b) the <i>P-SV</i> migration velocity function. Every second trace is plotted. ....	123
FIG. 5.13.	Schematic diagram of the scaled physical model (after Stewart and Marchisio, 1991). All dimensions given are 10000 times actual size. ....	124
FIG. 5.14.	Vertical component of physical-model data. ....	125
FIG. 5.15.	Radial component of physical-model data.....	126
FIG. 5.16.	Radial-component data migrated using the RMS velocity function. ....	127
FIG. 5.17.	Radial-component data migrated using the <i>P-SV</i> migration velocity function. ....	128
FIG. 5.18.	Enlargements of the migrated radial-component data: (a) migrated with RMS velocities; (b) migrated with <i>P-SV</i> migration velocities. Arrows indicate the location of reef-top edges.....	129
FIG. 5.19.	Enlargement of the migrated vertical-component data. Arrows indicate the location of reef-top edges. ....	130

FIG. 6.1.	Location map for the Carrot Creek survey. Cardium pool locations have been outlined by Joiner (1989).....	133
FIG. 6.2.	Vertical-component records for line CC-SW-01: (a) VP 211; (b) VP 115. ....	135
FIG. 6.3.	Radial-component records for line CC-SW-01: (a) VP 211; (b) VP 115. ....	136
FIG. 6.4.	Transverse-component records for line CC-SW-01: (a) VP 211; (b) VP 115. ....	137
FIG. 6.5.	Processing flowchart for the vertical-component ( $P$ - $P$ ) data set. ....	139
FIG. 6.6.	Stack section of vertical-component data. ....	140
FIG. 6.7.	Averaged time-variant cross-power spectra for the $P$ -wave stacked data. The spectrum for a given time was computed from the average crosscorrelation of 20 adjacent stack traces. A 400 ms correlation window was used, and spectra were computed at 100 ms increments. Contours are in percentage of maximum. ....	141
FIG. 6.8.	Stack section of vertical-component data with poststack $f$ - $k$ filter applied. ....	142
FIG. 6.9.	Vertical-component section with poststack migration applied. ....	143
FIG. 6.10.	Enlargement of vertical-component sections: (a) poststack $f$ - $k$ filter; (b) poststack migration. ....	144
FIG. 6.11.	Processing flowchart for the radial-component ( $P$ - $SV$ ) data set. ....	145
FIG. 6.12.	Stack section of radial-component data with final vertical-component statics applied. ....	146
FIG. 6.13.	Surface stacks of radial-component data with final $P$ - $P$ statics applied: (a) common source; (b) common receiver. ....	148
FIG. 6.14.	Final receiver-static solutions: (a) vertical component ( $P$ - $P$ ); (b) radial component ( $P$ - $SV$ ).....	149
FIG. 6.15.	Sample velocity analysis semblance displays: (a) vertical component ( $P$ - $P$ ); (b) radial component ( $P$ - $SV$ ). The solid line is the vertical-component NMO velocity function, and the dashed line is the radial-component NMO function. ....	150
FIG. 6.16.	Sample common-offset gather records: (a) vertical component ( $P$ - $P$ ); (b) radial component ( $P$ - $SV$ ).....	151
FIG. 6.17.	Reflection correlation between (a) the vertical-component section and (b) the radial-component section. ....	152

FIG. 6.18. $V_p/V_s$ values from correlation of vertical- and radial-component reflections. ....	154
FIG. 6.19. Stack section of radial-component data with asymptotic binning. ....	155
FIG. 6.20. Averaged time-variant cross-power spectra for the $S$ -wave stacked data. Spectra were computed as in Figure 6.7. Contours are in percentage of maximum. ....	156
FIG. 6.21. Stack section of radial-component data with asymptotic binning and poststack $f-k$ filter applied. ....	157
FIG. 6.22. Stack section of radial-component data with depth-variant binning. ....	158
FIG. 6.23. Stack section of radial-component data with depth-variant binning and poststack $f-k$ filter applied. ....	159
FIG. 6.24. Stack section of radial-component data with $P$ - $SV$ DMO. ....	160
FIG. 6.25. Stack section of radial-component data with $P$ - $SV$ DMO and poststack $f-k$ filter applied. ....	161
FIG. 6.26. Migrated stack section of radial-component data with $P$ - $SV$ DMO and poststack $f-k$ filter applied. ....	162
FIG. 6.27. Enlargement of radial-component section with asymptotic binning and poststack $f-k$ filter applied. ....	163
FIG. 6.28. Enlargement of radial-component section with depth-variant binning and poststack $f-k$ filter applied. ....	163
FIG. 6.29. Enlargement of radial-component section with $P$ - $SV$ DMO and poststack $f-k$ filter applied. ....	164
FIG. 6.30. Enlargement of migrated radial-component section with $P$ - $SV$ DMO and poststack $f-k$ filter applied. ....	164
FIG. 6.31. $P$ - $SV$ velocity inversion applied to a window of the radial-component section with $P$ - $SV$ DMO and poststack $f-k$ filter applied. ....	165
FIG. 6.32. Major reflections as interpreted by Nazar (1991): (a) $f-k$ filtered vertical-component stack section; (b) $f-k$ filtered radial-component stack section. ....	167
FIG. 7.1. Location map for the Springbank area showing line FS90-1. Contours are elevations in feet ASL. ....	171
FIG. 7.2. Shot records from SP 161 of line FS90-1: (a) conventional; (b) vertical component; (c) radial component. ....	173
FIG. 7.3. Processing flowchart for the vertical-component ( $P$ - $P$ ) data. ....	174
FIG. 7.4. Stack section of single-geophone vertical-component data. ....	175

FIG. 7.5.	Stack section of single-geophone vertical-component data with poststack $f-x$ and $f-k$ filters applied. ....	177
FIG. 7.6.	Stack section of conventional vertical-component data. ....	178
FIG. 7.7.	Stack section of conventional vertical-component data with poststack $f-x$ and $f-k$ filters applied. ....	179
FIG. 7.8.	Processing flowchart for the radial-component ( $P-SV$ ) data. ....	180
FIG. 7.9.	Final receiver static solutions: (a) vertical component ( $P-P$ ); (b) radial component ( $P-SV$ ). ....	181
FIG. 7.10.	Reflector correlation between stack sections for (a) radial component; (b) single-geophone vertical component. ....	182
FIG. 7.11.	Stack section of radial-component data with asymptotic binning. ....	183
FIG. 7.12.	Stack section of radial-component data with depth-variant binning. ....	184
FIG. 7.13.	Stack section of radial-component data with $P-SV$ dip moveout. ....	185
FIG. 7.14.	Stack section of radial-component data with asymptotic binning and poststack $f-x$ and $f-k$ filters applied. ....	186
FIG. 7.15.	Stack section of radial-component data with depth-variant binning and poststack $f-x$ and $f-k$ filters applied. ....	187
FIG. 7.16.	Stack section of radial-component data with $P-SV$ dip moveout and poststack $f-x$ and $f-k$ filters applied. ....	188
FIG. 7.17.	Common-offset stacks from FS90-1: (a) conventional; (b) vertical component; (c) radial component. ....	189
FIG. 7.18.	Spliced sections showing correlation between the main events: (a) radial; (b) vertical. Synthetic seismograms are based on $P$ -wave velocity model at well 6-27-25-4W5 and a $V_p/V_s$ of 2.08. Abbreviations are: Upper det. = upper detachment zone; Lower det. = lower detachment zone; BLRV = Belly River; WPBI = Wapiabi; CRDM = Cardium; TRVL = Turner Valley; WBMN = Wabamum. (From Lawton and Harrison, 1992). ....	190
FIG. 8.1.	Location map for the Casper Creek South survey. Contours indicate structure on the Tensleep Sandstone Formation in feet ASL (after Ruddiman, 1989). ....	194
FIG. 8.2.	Data from SP 131: (a) vertical component; (b) radial component; (c) transverse component. ....	196
FIG. 8.3.	Processing flowchart for the vertical-component ( $P-P$ ) data. ....	197
FIG. 8.4.	Final stack section for the vertical-component data. ....	198

FIG. 8.5.	Migrated stack section for the vertical-component data. ....	199
FIG. 8.6.	Processing flowchart for the radial and transverse component data sets. ....	200
FIG. 8.7.	Radial-component common-receiver stack created using the final static and velocity solutions. ....	201
FIG. 8.8.	Radial-component common-receiver stack after correction for differences in CCP structure time. ....	203
FIG. 8.9.	Radial-component data stacked using the asymptotic method. ....	204
FIG. 8.10.	Transverse-component data stacked using the asymptotic method. ....	205
FIG. 8.11.	Geophone rotation analysis for radial-component data. ....	206
FIG. 8.12.	Geophone rotation analysis for transverse-component data. ....	207
FIG. 8.13.	Rotated radial-component data stacked using the asymptotic method. ....	208
FIG. 8.14.	Rotated transverse-component data stacked using the asymptotic method. ....	209
FIG. 8.15.	Rotated radial-component data stacked using the depth-variant binning method. ....	210
FIG. 8.16.	Rotated radial-component data stacked using <i>P-SV</i> DMO. ....	212
FIG. 8.17.	<i>f-k</i> filter applied to the rotated radial-component data stacked using <i>P-SV</i> DMO. ....	213
FIG. 8.18.	Migration applied to the rotated radial-component data stacked with <i>P-SV</i> DMO and <i>f-k</i> filter. ....	214
FIG. 8.19.	Side-by-side comparison of (a) the <i>f-k</i> filtered DMO section for the rotated radial-component, and (b) the vertical-component stack section. ....	215
FIG. 8.20.	NMO-corrected common-offset stack records: (a) vertical component; (b) radial component. ....	216

## Chapter 1 - Introduction

### 1.1 Background

It is well known (e.g., Aki and Richards, 1980) that in an elastic Earth compressional energy becomes mode-converted into shear energy upon reflection from a boundary at non-zero angles of incidence. This mode conversion has largely been neglected in seismic exploration until roughly the early 1980's (e.g., Ostrander, 1984); most exploration techniques were developed using the assumption of an acoustic Earth. Since then, there has been a growing emphasis placed upon the importance of elastic effects and shear energy in helping to better resolve and interpret exploration seismic data.

As far back as 1940, Muskat and Meres published an article illustrating the variation in reflection amplitude with incidence angle for plane waves. Pickett (1963), and more recently others (Gregory, 1976; Tatham and Stoffa, 1976; Domenico, 1984) have suggested that comparison of shear-wave (*S*-wave) and compressional-wave (*P*-wave) velocities can be instrumental in discriminating between different lithologies. Ostrander (1984) showed how the amplitudes of compressional-wave reflection seismic data vary as a function of incident angle and changes in Poisson's ratio for porous sands, and related these amplitude-versus-offset (AVO) effects to pore content through Poisson's ratio. Shuey (1985) was later able to derive a simple approximation to the Zoeppritz equations (Zoeppritz, 1919) relating changes in reflection amplitude with incident angle to changes in Poisson's ratio across the interface. From this equation, estimates of changes in Poisson's ratio could be obtained by performing AVO analysis of reflections within midpoint gathers. This method makes use of *P*-wave data only, and relies on variations in reflection amplitude, rather than amplitude itself. This is, in general, a small effect, complicated by many factors [Ostrander (1984)]. To supplement information obtained by AVO analysis, there has been increased interest in looking at recording both *S*-wave energy from shear

sources (e.g., Justice et al., 1987; Fix et al., 1987), as well as converted-wave shear data (e.g., Garotta, 1987). This dissertation is concerned with the processing of the latter.

Mode-converted shear waves are polarized in a plane falling along the propagation direction and normal to the reflecting surface, and are commonly known as *SV* or *P-SV* waves. In the absence of out-of-plane scattering and velocity anisotropy, these *P-SV* data emerge at the surface as nearly-horizontal oscillations, oriented in the radial (inline) direction (e.g., Douma and Helbig, 1987). Because geophones used in conventional acquisition record only the vertical (*P-P*) component of ground movement, the mode-converted *S*-waves are largely lost.

Some seismic surveys are presently being conducted using geophones that can sense motion in the horizontal directions as well as the vertical direction, producing multi-component data sets for each sourcepoint. This allows the recording and processing of both *P*-wave and mode-converted *S*-wave data. These data could potentially be used to determine *P*-to-*S* velocity ratios ( $V_p/V_s$ ), from which Poisson's ratio can be calculated. This allows a more direct means of obtaining Poisson's ratio, which can augment the information obtained from AVO analysis of conventional *P*-wave data alone.

*P-SV* recording has several advantages over pure shear (*SV-SV* or *SH-SH*) acquisition, among which are:

- 1) it does not require a special source, which reduces acquisition costs;
- 2) attenuation of the shear waves in the near-surface is only present for the upgoing-raypath, rather than both downgoing and upgoing paths;
- 3) the near-surface static delay problems reduce to having to estimate only a residual receiver component.

The major complexity of *P-SV* data is the asymmetry of the source-to-receiver raypath. This asymmetry makes common-midpoint (CMP) processing techniques inappropriate. Also, *S*-wave first-arrivals are generally not available for *P-SV* data, as they would be for shear-source data; this prevents the estimation of *S*-wave statics by refraction analysis.

## 1.2 Dissertation objectives

This dissertation is concerned with the processing of *P-SV* converted-wave data. A general processing flow is described, and algorithms for the application of geometric spreading gain correction, two-component birefringence analysis, dip moveout (DMO), poststack migration, and poststack inversion are developed and implemented on synthetic and field data. It is hoped that this work will extend the usefulness of *P-SV* recording as an exploration tool, and provide some insight into the capabilities and limitations of the method.

## 1.3 Data sets used in this dissertation

The processing flow and algorithms presented in the following chapters were tested and evaluated on the data sets described below.

### 1.3.1 Synthetic *P-SV* data sets

(1) The synthetic data used in Chapter 3 were created using zero-phase wavelets having a frequency spectrum of 6/10-35/45 Hz; this is approximately the bandwidth seen on the Carrot Creek radial-component stack data (Chapter 6). Anisotropic effects were simulated in order to construct radial and transverse data sets for several orientations of the receiver relative to the natural coordinate system and differing amounts of time lag between fast and slow *S*-wave components. Random noise of various levels were added to these data to test the robustness of the birefringence analysis algorithms.

(2) The synthetic data set shown in Chapter 4 was created using the Uniseis raytracing program on the Landmark workstation donated to the CREWES Project at the University of Calgary. The parameters used to generate the radial-component data are listed in Table

4.2. A description of the model can be found in Section 4.8.2.

(3) The synthetic data sets used in Chapter 5 were created by ray-tracing through both a single-layered medium and a multilayered medium in order to compute the response to a number of point-diffractors located at various depths. The parameters used in data generation are listed in Table 5.1.

### **1.3.2 Physical model data**

The migration velocity equation developed in Chapter 5 was tested on a physical model data set created at the University of Calgary as part of the side-scanning seismic experiments of Stewart and Marchisio (1991). The model consisted of an aluminum dome embedded within plexiglass to simulate a reef overlain by shale. Vertical- and radial-component data from a vertical source were recorded along the top of the model over the simulated reef. A constant source-to-receiver offset was used, giving a single-fold section for each of the two components. These data are further described in Chapter 5.

### **1.3.3 Carrot Creek, Alberta**

A three-component data set was recorded using a conventional *P*-wave vibrator source in the fall of 1984 by Polyseis Research Inc. using the acquisition parameters summarized in Table 6.1. This data set has since been donated to the CREWES Project at the University of Calgary for analysis. The processing of the vertical and radial components of line CC-SW-01 of the survey is discussed in Chapter 6.

### **1.3.4 Springbank, Alberta**

A two-component data set, using a buried dynamite source, was acquired in the fall of 1990 by the Geophysics Field School at the University of Calgary near Springbank, Alberta using the parameters summarized in Table 7.1. In addition, conventional (*P-P*)

recording was done simultaneously, giving three data components for each sourcepoint: conventional ( $P$ - $P$ ); vertical component ( $P$ - $P$ ); and radial component ( $P$ - $SV$ ). The processing of these three components is presented in Chapter 7.

### 1.3.5 Casper Creek South, Wyoming

A three-component line was recorded using a  $P$ -wave dynamite source in the fall of 1988 by Unocal Inc. across the Casper Creek South field in Wyoming using the parameters shown in Table 8.1. This field is formed by a pair of anticlines, giving a dome-like structure with sides that dip at angles as high as  $30^\circ$ . This data set was given to the CREWES Project at the University of Calgary for analysis. The processing of the vertical, radial, and transverse components of the survey is discussed in Chapter 8.

## 1.4 Hardware and software used

Most basic processing of the data used in this dissertation was performed using the seismic software package donated to the CREWES Project by Western Geophysical Company of Canada Ltd. This processing package was operating on an IBM 4381 mainframe computer. The seismic displays shown in Chapters 6, 7, and 8 were generated using a Versatec electrostatic plotter attached to this system. Some additional processing was done using the Inverse Theory and Applications (ITA) processing package, running on a Sun Microsystems Inc. 470 workstation. The two-component birefringence analysis,  $P$ - $SV$  DMO and  $P$ - $SV$  inversion algorithms developed in Chapters 2, 3 and 4 were written in FORTRAN 77 on a Sun Microsystems Inc. 3/160 workstation. Many of the data plots in Chapters 3, 4, and 5 were created on an Epson dot-matrix printer, attached to the Sun 3/160 workstation. All other figures were made using the Canvas® software package on an Apple computer. All text processing was done with Microsoft Word® and Expressionist®, also on an Apple computer.

## Chapter 2 - General processing of *P-SV* seismic data

### 2.1 Introduction

The purpose of this chapter is to outline the flow (Figure 2.1) used to process the *P-SV* data presented in this dissertation. Steps that are substantially different from conventional processing are discussed in the following sections. The first major step, which does not appear in Figure 2.1, is to process the vertical-channel (*P-P*) data. This supplies the source component of the *P-SV* statics solution; it also estimates the receiver-component solution. Also, *P-SV* stacking velocities can be approximated from the final *P-P* stacking function (section 2.5). This is often useful, as the residual receiver statics found in *P-SV* data are typically large, making initial stacking velocity determination difficult. Because the vertical-channel data does not differ substantially from conventional *P-P* data, a standard processing sequence can be applied to it. This sequence is not discussed here.

### 2.2 Polarity reversal of trailing spread

In an isotropic Earth with flat, homogeneous layers *P-SV* mode conversion has radial symmetry about the source location. Consider multicomponent geophones positioned at the surface in a line passing through the source location. The geophones on one side of the source will record motion radially away from the source as one polarity (say a positive voltage). If the radial component of these geophones point at the source, then the radial component of geophones on the other side of the spread point away from the source. As a result, *S*-wave data recorded by the two sides of the spread will have opposite polarity. To compensate for this, the polarity of data recorded by one side of the spread, usually the trailing direction, must consistently be reversed for each source record.

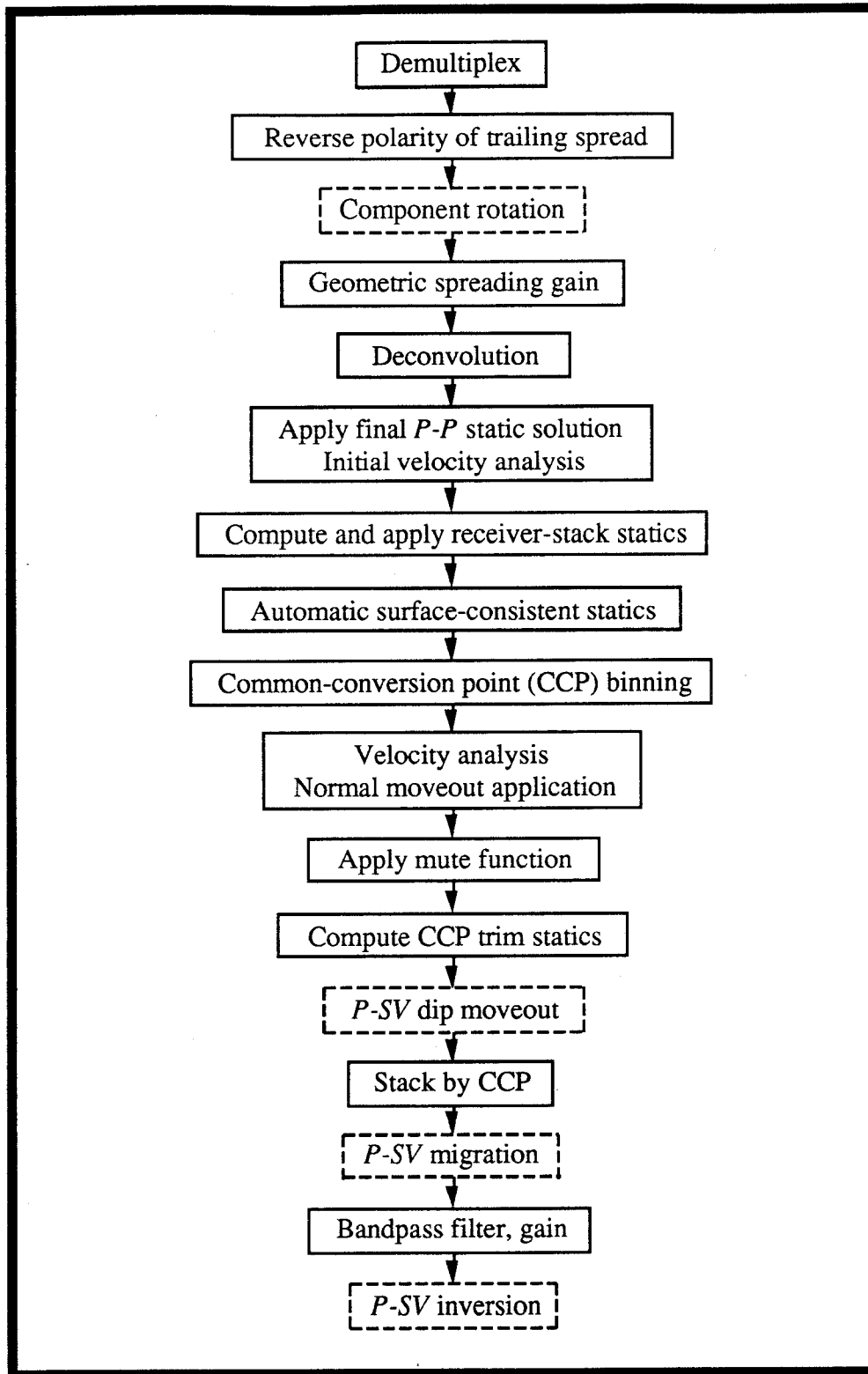


FIG. 2.1. Processing flow for  $P$ - $SV$  mode-converted data. Steps not always performed are indicated in dashed boxes.

### 2.3 Rotation of horizontal components

In an isotropic Earth with flat, homogeneous layers, all of the mode-converted  $S$ -wave energy would be recorded on the radial and vertical components (see Douma and Helbig, 1987), making three-component recording in the absence of out-of-plane reflector dip and inhomogeneities unnecessary. In recent years authors such as Justice et al. (1987), Martin et al. (1986), Lewis et al. (1989), Squires et al. (1989), Winterstein and Meadows (1990), Kramer and Davis (1991), and many others have presented examples of the presence of varying amounts and types of velocity anisotropy in the subsurface. This velocity anisotropy can lead to shear-wave birefringence, in which a shear pulse is split into fast and slow components (Neville, 1986; Crampin et al., 1984; Justice et al., 1987; Winterstein, 1990) in passing through the anisotropic layer. For converted-wave data, the presence of vertical birefringence can cause shear energy to be recorded on both horizontal components (e.g., McBeth and Crampin, 1991), giving a decrease in the signal-to-noise ratio of the radial channel. Also, the fast and slow components can each contribute energy to a recorded radial or transverse channel, potentially leading to destructive interference and greater difficulty in interpretation.

These problems can be overcome if the orientation of the natural coordinate axes [see Winterstein (1990) for definition] are known or can be determined by analysis of the data. For four-component data in which multicomponent data from both  $SH$  and  $SV$  sources are recorded, Alford (1986) has devised an analysis method to find the orientation of the natural coordinate system. As shown by Thomsen (1988), this method is not appropriate for data generated with a single source polarization, such as converted-wave data, and some other approach must be used. To date a number of methods have been proposed (e.g., Neville, 1986; Garotta and Granger, 1988; Thomsen, 1988; McBeth and Crampin, 1991; Peron, 1990), but many are somewhat subjective and/or lack robustness. A different method for determining the orientation of the natural coordinate system and the

time lag between fast and slow shear polarizations, based on forward modeling of the crosscorrelation function between radial and transverse channels, is developed and discussed in Chapter 3.

## 2.4 Geometric spreading compensation

One of the first steps in processing any surface data is to attempt to compensate for amplitude loss due to geometric spreading. Newman (1973) has derived a spreading compensation formula for  $P$ - $P$  surface data that requires only RMS-stacking velocity information. The purpose of this section is to extend Newman's equation for  $P$ - $SV$  data. The final  $P$ - $SV$  gain formula, equation (2.17), has been published by Harrison (1989). Since then, the same equation has been published by Ursin (1990), using a derivation similar to the one presented here.

Figure 2.2 shows a source at  $S$  generating  $P$ -waves at a vertical angle  $\theta$ , some of which are mode-converted within the Earth at depth  $z$  and travel back to the surface at  $R$ . An area  $A_r$  is swept out by rotation about the source of the segment  $dl_1$  at radius  $r$  and angle  $\theta$ , and an area  $A_x$  is swept out by the segment  $dl_2$  at horizontal offset  $x$ . These areas are given by

$$A_r = 2\pi r^2 \sin \theta d\theta, \quad (2.1)$$

$$A_x = 2\pi x \cos \phi dx. \quad (2.2)$$

The energy flux through the two areas must be the same if no other effects are present. The ratio  $E$  of the energy densities at  $r$  and  $x$  is equal to the ratio of the two areas, i.e.,

$$E = \frac{A_r}{A_x} = \frac{r^2 \sin \theta d\theta}{x \cos \phi dx}. \quad (2.3)$$

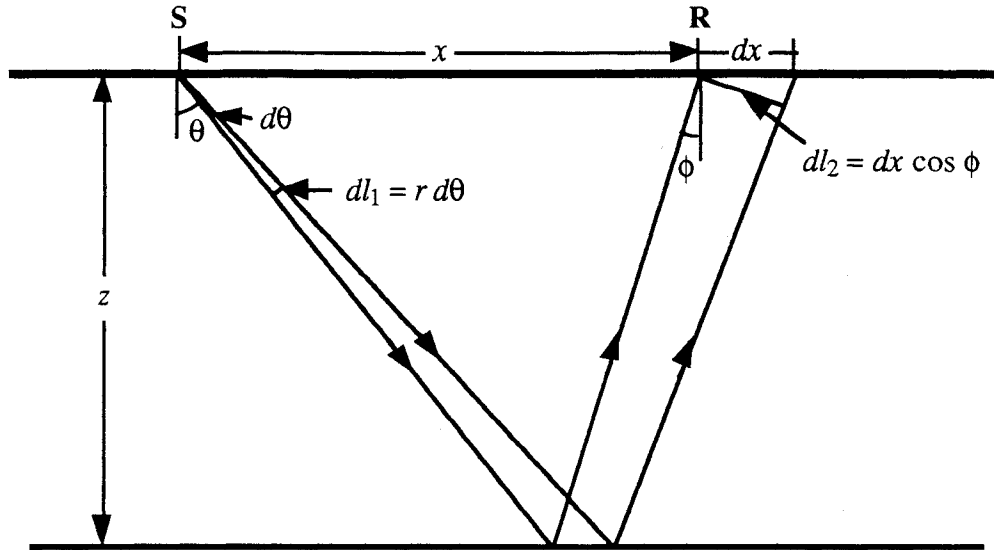


FIG. 2.2. Geometric energy spreading for  $P$ - $SV$  data. The energy flowing through the area swept out by rotating  $dl$  about the source is the same for all offsets.

The radius  $r$  is arbitrary, and can be set to 1. From Snell's Law the ray parameter  $p$  is constant along the raypath;

$$p = \frac{\sin \theta}{\alpha_0} = \frac{\sin \phi}{\beta_0}, \quad (2.4)$$

where  $\alpha_0$  is the  $P$ -wave velocity at  $S$ , and  $\beta_0$  is the  $S$ -wave velocity at  $R$ . Equation (2.3) can be rewritten using the ray parameter as

$$E = \frac{\alpha_0 p}{x \sqrt{1 - p^2 \beta_0^2}} \frac{d\theta}{dx}. \quad (2.5)$$

The amplitude compensation factor  $G$  will be the reciprocal of the square root of  $E$ ;

$$G_{\theta,x} = \sqrt{\frac{\sqrt{1 - p^2 \beta_0^2}}{\alpha_0} \frac{x}{p} \frac{dx}{d\theta}}. \quad (2.6)$$

The total source-to-receiver offset  $x$  is the sum of offset  $x_p$  from the down-going  $P$ -waves and the offset  $x_s$  from the upgoing  $S$ -waves;

$$\begin{aligned}
 x &= x_p + x_s \\
 &= p \int_0^z \left[ \frac{\alpha(z)}{\sqrt{1-p^2\alpha^2(z)}} + \frac{\beta(z)}{\sqrt{1-p^2\beta^2(z)}} \right] dz . \quad (2.7)
 \end{aligned}$$

Differentiating  $x$  w.r.t. the ray parameter  $p$  gives

$$\frac{dx}{dp} = \int_0^z \left\{ \frac{\alpha(z)}{[1-p^2\alpha^2(z)]^{3/2}} + \frac{\beta(z)}{[1-p^2\beta^2(z)]^{3/2}} \right\} dz . \quad (2.8)$$

The derivative of  $p$  w.r.t.  $\theta$  is

$$\frac{dp}{d\theta} = \frac{\cos \theta}{\alpha_0} = \frac{\sqrt{1-p^2\alpha_0^2}}{\alpha_0} . \quad (2.9)$$

Equations (2.8) and (2.9) give

$$\begin{aligned}
 \frac{dx}{d\theta} &= \frac{dp}{d\theta} \frac{dx}{dp} \\
 &= \frac{\sqrt{1-p^2\alpha_0^2}}{\alpha_0} \int_0^z \left\{ \frac{\alpha(z)}{[1-p^2\alpha^2(z)]^{3/2}} + \frac{\beta(z)}{[1-p^2\beta^2(z)]^{3/2}} \right\} dz . \quad (2.10)
 \end{aligned}$$

Equation (2.6) can be rewritten using equation (2.10) to give the gain  $G$  as a function of the ray parameter;

$$G_{px} = \sqrt{\frac{x}{p} \frac{\sqrt{(1-p^2\alpha_0^2)(1-p^2\beta_0^2)}}{\alpha_0^2} \int_0^z \left\{ \frac{\alpha(z)}{[1-p^2\alpha^2(z)]^{3/2}} + \frac{\beta(z)}{[1-p^2\beta^2(z)]^{3/2}} \right\} dz} . \quad (2.11)$$

In general, the computation of the gain  $G$  requires that  $p$  be known. The ray parameter can be computed by solving equation (2.7) for a given geometry using ray tracing. This allows the gain function to be accurately computed, but involves considerable calculation. An

approximate solution can be obtained for short offsets, where  $p \cong 0$ . For this case, equation (2.7) gives

$$\begin{aligned} \frac{x}{p} &= \int_0^z \left[ \frac{\alpha(z)}{\sqrt{1-p^2\alpha^2(z)}} + \frac{\beta(z)}{\sqrt{1-p^2\beta^2(z)}} \right] dz \\ &\cong \int_0^z [\alpha(z) + \beta(z)] dz \quad \text{for small } p, \end{aligned} \quad (2.12)$$

and equation (2.11) reduces to

$$G_{p \cong 0} = \frac{1}{\alpha_0} \int_0^z [\alpha(z) + \beta(z)] dz . \quad (2.13)$$

It is desirable to have the gain as a function of time, rather than depth. The instantaneous two-way vertical transit time is given by

$$d\tau = \left[ \frac{1}{\alpha(z)} + \frac{1}{\beta(z)} \right] dz ,$$

or

$$[\alpha(z) + \beta(z)] dz = \alpha(z) \beta(z) d\tau . \quad (2.14)$$

Equation (2.13) can be rewritten using equation (2.14) as

$$G_{p \cong 0} = \frac{1}{\alpha_0} \int_0^{t_0} \alpha(\tau) \beta(\tau) d\tau , \quad (2.15)$$

where  $t_0$  is the total vertical two-way traveltime for the  $P$ - $SV$  event. Defining the  $P$ - $SV$  RMS velocity  $\tilde{v}$  as

$$\tilde{v}^2 = \frac{1}{t_0} \int_0^{t_0} \alpha(\tau) \beta(\tau) d\tau , \quad (2.16)$$

then

$$G_{p \approx 0} = \frac{t_0 \tilde{v}^2}{\alpha_0}. \quad (2.17)$$

Tessmer and Behle (1988) show that the stacking velocities obtained by conventional velocity analysis are, to first order, equal to the function defined by equation (2.16). Using this result, equation (2.17) states that  $P$ - $SV$  geometric spreading can be approximately compensated for by using only the  $P$ - $SV$  stacking velocity function and total two-way time, and the  $P$ -wave velocity of the near-surface. This is similar to the result obtained by Newman (1973) for the  $P$ - $P$  data case.

## 2.5 $P$ - $SV$ stacking velocity estimation and NMO correction

Tessmer and Behle (1988) show that, to first order,  $P$ - $SV$  moveout curves are hyperbolas given by

$$t^2 = t_0^2 + \frac{4h^2}{\tilde{v}_n^2}, \quad (2.18)$$

where  $h$  is the source-receiver half-offset, and  $t_0$  is the two-way vertical travelttime. The stacking velocity  $\tilde{v}_n$  is the discretized form of equation (2.16);

$$\tilde{v}_n^2 = \frac{\sum_{i=1}^n \alpha_i \beta_i \tau_i}{\sum_{i=1}^n \tau_i}, \quad (2.19)$$

where

$$\begin{aligned} \tau_i &= \left( \frac{1}{\alpha_i} + \frac{1}{\beta_i} \right) z_i \\ &= (1 + \gamma_i) \frac{z_i}{\alpha_i}, \quad \gamma_i = \frac{\alpha_i}{\beta_i}. \end{aligned} \quad (2.20)$$

Because  $P$ - $SV$  NMO curves are hyperbolic to first order, conventional velocity analysis (Taner and Koehler, 1969) can be used to obtain a stacking function. It should be noted

that equation 2.18 is accurate for a smaller offset range than is the  $P$ - $P$  NMO equation (Tessmer and Behle, 1988). Slotboom (1990) has derived a shifted-hyperbola NMO equation for  $P$ - $SV$  data that is claimed to be more accurate at large offsets. His equation has not been used in this dissertation.

It is often difficult to obtain a reasonable velocity estimate from  $P$ - $SV$  data until any residual statics problems have been largely resolved. Finding a residual static solution itself requires using a  $P$ - $SV$  stacking function, which can be approximated as follows. Given a final  $P$ - $P$  RMS velocity function, the  $P$ -wave interval velocities can be determined using the Dix equation (Dix, 1955). Defining the  $P$ - $P$  two-way interval time as

$$t_i = \frac{2z_i}{\alpha_i},$$

then equation (2.19) can be rewritten as

$$\tilde{v}_n^2 = \frac{\sum_{i=1}^n \alpha_i^2 t_i \left( \frac{1+\gamma_i}{\gamma_i} \right)}{\sum_{i=1}^n t_i (1+\gamma_i)}. \quad (2.21)$$

The  $V_p/V_s$  values in equation (2.21) are usually not known until the converted-wave data has been processed to some extent. Assuming some constant, average  $V_p/V_s$  value  $\gamma$ , equation (2.21) becomes (Tessmer and Behle, 1988)

$$\tilde{v}_n \cong \frac{\tilde{\alpha}_n}{\sqrt{\gamma}}, \quad (2.22)$$

where  $\tilde{\alpha}_n$  is the  $P$ - $P$  RMS velocity, given by

$$\tilde{\alpha}_n^2 = \frac{\sum_{i=1}^n \alpha_i^2 t_i}{\sum_{i=1}^n t_i}. \quad (2.23)$$

If the  $P$ -wave data have been processed, then  $P$ - $P$  RMS velocities are known. The  $P$ - $SV$  vertical traveltimes becomes

$$\begin{aligned}
 t_0 &= \sum_{i=1}^n \tau_i \\
 &= \sum_{i=1}^n \frac{t_i}{2} (1+\gamma_i) \\
 &\cong \frac{(1+\gamma)}{2} t_{p-p} ,
 \end{aligned} \tag{2.24}$$

where  $t_{p-p}$  is the  $P$ - $P$  vertical traveltimes. Equations (2.22) and (2.24) allow initial estimation of  $P$ - $SV$  stacking velocities, which can be used for static analysis.

## 2.6 $P$ - $SV$ static solution

Two rays are shown in Figure 2.3 from a  $P$ -wave source that travel through a simple-layered-Earth model to be recorded by a multicomponent geophone at the surface. From the figure, the near-surface raypaths for the down-going reflected and mode-converted rays are seen to be nearly identical. Along this segment, both rays represent  $P$ -wave energy, and both encounter the same surface conditions and delays. Because of this, application of the final  $P$ - $P$  static solution to the  $P$ - $SV$  data can be expected to properly account for source delays; the residual statics problem then reduces to one of having to determine residual receiver statics only.

After conversion occurs at the reflecting interfaces, the signal recorded on the horizontal receiver component is mainly  $SV$  shear. The near-surface delay time of the  $SV$  data might be thought to be greater than that for the  $P$ - $P$  data by a factor roughly equal to the average  $V_p/V_s$  value for the near-surface, assuming that both  $P$  and  $SV$  signals see the same thicknesses of near-surface material. It will be seen in Chapters 6 and 7 that, in general, this is not the case, and the final  $P$ - $P$  receiver static solution does not provide much

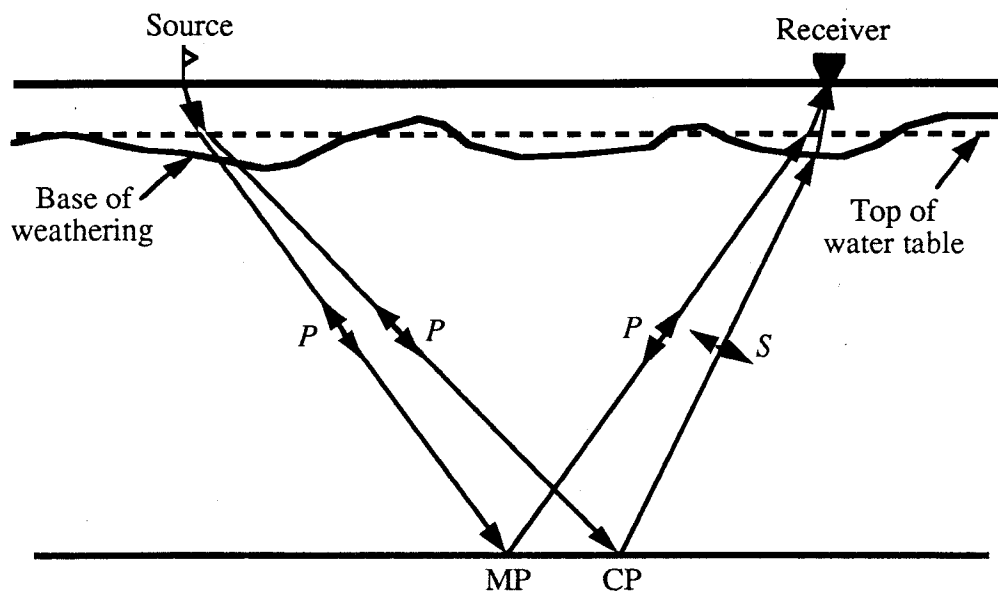


FIG. 2.3. Near-surface raypaths for reflected and converted rays. MP indicates the  $P$ - $P$  reflection point, and CP indicates the  $P$ - $SV$  conversion point.

insight into  $P$ - $SV$  static problems. It has been shown (Wiest and Edelman, 1984; Fromm et al., 1985; Anno, 1987; Lawton, 1991) that this is often due to the difference in effective thickness of the near-surface low-velocity layer (LVL) that the  $P$ - and  $S$ -wave signals see. Fluid-saturated sediments have a greater bulk compressibility, and correspondingly higher  $P$ -wave velocity, than dry sediments. The shear modulus is largely unaffected by water saturation, which gives little change in  $S$ -wave velocity. It is therefore possible that the  $P$ -waves encounter an LVL thickness that terminates at the top of the water table, whereas the  $S$ -waves are affected by the entire low-velocity layer.

Residual receiver static delays as large as 100 ms are commonly found in processing  $P$ - $SV$  data (Figure 6.9). Because of the size of these delays, traditional statics programs (e.g. Wiggins et al., 1976) do not perform well. Also, most statics algorithms attempt to solve for both source and receiver delays. In the  $P$ - $SV$  case, a solution is needed for only the receiver component. This requires that the source component solution be disabled; something that is not always possible.

To overcome these problems, common-receiver stack displays have been used in the  $P$ - $SV$  processing sequence. Because the residual source statics are negligible after applying the final  $P$ - $P$  static solution, the common-receiver stacks can give a very clear indication of residual receiver delays. In creating a common-receiver stack, all of the data traces that have been recorded by a given receiver are summed, after NMO correction, to produce a single stacked trace. Any time delay encountered by the  $S$ -wave energy on its way back through the near surface will be common to all traces collected by a receiver. This creates a time shift on all events in the stacked trace, which can be compared to the event times of neighboring traces. A receiver delay can be obtained by applying that time shift which best aligns the summed receiver trace with its neighboring traces. This method is only able to handle high-frequency residual static problems, and cannot resolve long-wavelength delays. Also, if any structure is present, then the horizontal summing that occurs in forming the stacked receiver traces can obliterate events that have sufficient structure. This confines the method to areas that have small lateral changes in reflector structure time.

Once the very large receiver delays have been approximately removed by use of common-receiver stacks, conventional surface-consistent static methods can usually remove any remaining source and receiver static values.

## 2.7 CCP binning

It is well known (e.g. Chung and Corrigan, 1985; Behle and Dohr, 1985; Fromm et al., 1985; Tessmer and Behle, 1988; Eaton et al., 1990; Stewart, 1991) that for a given offset the conversion point location varies with depth. In order to image events properly, it is necessary to account for this conversion point movement when gathering and stacking the data. The simplest method of CCP gathering is the asymptotic approximation (Fromm et al., 1985), in which the conversion point offset  $x_c$  is approximated by

$$x_c \equiv \left( \frac{\gamma}{1 + \gamma} \right) x, \quad (2.25)$$

where  $x$  is the total offset, and  $\gamma$  is the average  $Vp/Vs$  value down to the reflector of interest. This approximation is most accurate for small offset-to-depth ratios, and has been shown by Eaton et al. (1990) to potentially introduce artifacts into the  $P$ - $SV$  stacked section.

A more accurate binning method is the depth-variant binning algorithm described by Tessmer and Behle (1988) and implemented by Eaton et al. (1990);

$$x_c \equiv \chi + \frac{x}{2}, \quad (2.26a)$$

where  $\chi$  is the solution to the quartic equation

$$\chi^4 + \left( z^2 - \frac{x^2}{2} \right) \chi^2 - z^2 x \left( \frac{\gamma^2 + 1}{\gamma^2 - 1} \right) \chi + \frac{x^2}{16} (x^2 + 4z^2) = 0. \quad (2.26b)$$

In equation (2.26b)  $z$  is the total reflector depth, and  $\gamma$  is the ratio of the average  $P$ - and  $S$ -wave velocities down to the reflector, i.e.,

$$\gamma = \frac{\bar{\alpha}}{\bar{\beta}} = \frac{\sum_{i=1}^n \frac{z_i}{\beta_i}}{\sum_{i=1}^n \frac{z_i}{\alpha_i}}, \quad (2.26c)$$

where  $z_i$  is the thickness of the  $i$ 'th layer, having  $P$ - and  $S$ -wave velocities of  $\alpha_i$  and  $\beta_i$  respectively. Both the asymptotic approximation [equation (2.25)] and the depth-variant binning method [equations (2.26)] were used to stack the data sets of Chapters 6, 7, and 8, and comparisons of the results, as well as CCP stacking using  $P$ - $SV$  dip moveout, are presented later in this dissertation.

All stacking methods require estimates of either  $S$ -wave interval velocities or  $Vp/Vs$  values. These can be obtained from either the  $P$ - $SV$  stacking velocities (Tessmer and

Behle, 1988; Iverson et al., 1989), or from event correlation and interval time comparison between the  $P$ - $P$  and  $P$ - $SV$  stacked sections (Garotta, 1987). The  $P$ - $P$  two-way interval transit time through the  $i$ 'th layer having thickness  $z_i$ ,  $P$ -wave velocity  $\alpha_i$  and  $S$ -wave velocity  $\beta_i$ , is given by

$$\tau_{p-p} = \frac{2z_i}{\alpha_i}, \quad (2.27)$$

and the  $P$ - $SV$  two-way interval transit time is given by

$$\tau_{p-sv} = \left( \frac{\alpha_i + \beta_i}{\alpha_i \beta_i} \right) z_i. \quad (2.28)$$

Eliminating  $z_i$  from equations (2.27) and (2.28) and rearranging gives (Garotta, 1987)

$$\gamma_i = \frac{\alpha_i}{\beta_i} = \frac{2\tau_{p-sv}}{\tau_{p-p}} - 1. \quad (2.29)$$

Once a reasonably good  $P$ - $SV$  section is obtained, events can be correlated between the  $P$ - $P$  and  $P$ - $SV$  sections, giving the interval transit times  $\tau_{p-p}$  and  $\tau_{p-sv}$ . Equation (2.29) can then be used to compute  $V_p/V_s$  values, from which  $S$ -wave velocities can be calculated using the known  $P$ -wave velocities. The results can be used to regather and stack the  $P$ - $SV$  data. It was found in processing the  $P$ - $SV$  data sets that the  $S$ -wave interval velocities obtained from stacking velocity analysis were generally unreliable, and the best velocity estimates were obtained using equation (2.29).

## 2.8 CCP trim statics

Trim static application involves computing the time shift that best aligns a gather trace to some CCP model trace. The model is usually constructed by stacking the traces within the gather, together with traces in neighboring CCP gathers. These time shifts correct for any delays that were not accounted for by surface-consistent static analysis, and

improve the overall coherency of the stacked section.

If the  $P$ - $SV$  data have been binned using the asymptotic approximation (equation 2.25), then trim shifts can be easily computed. If depth-variant binning (equation 2.26) or  $P$ - $SV$  DMO is applied, however, then the data are initially binned by CMP, rather than CCP. After these operations have been performed, each input trace has been distributed laterally over a range of CCP locations, and correlation is very difficult. As a partial solution to this problem, the data of Chapters 6, 7, and 8 were initially binned using the asymptotic approximation, and CCP alignment shifts were computed for each gather trace. These trim-corrected data were then resorted by CMP and used as input to the depth-variant binning and DMO procedures.

## **2.9 $P$ - $SV$ dip moveout**

In areas of substantial structure, it is desirable to perform dip moveout (DMO) on prestack data to reduce the attenuation of dipping events (Judson et al., 1978; Deregowski and Rocca, 1981; Hale, 1983). The DMO concept is extended in Chapter 4 of this dissertation to handle  $P$ - $SV$  data. Examples of  $P$ - $SV$  DMO application to synthetic and real data examples are presented in Chapters 4, 5, 6, 7, and 8.

## **2.10 $P$ - $SV$ zero-offset migration**

The preceding steps can be used to construct a stacked section that is zero-offset in the kinematic sense. The amplitudes of a  $P$ - $SV$  stacked section represent the average of a range of amplitudes, generated by conversion at various angles of incidence. A useful extension to the  $P$ - $SV$  processing flow is to apply some sort of poststack migration to stacked sections in order to properly position dipping reflectors and collapse diffractions. A ray-theoretical expression for the shape of  $P$ - $SV$  diffraction curves on a zero-offset

section is obtained in Chapter 5. The curves are shown to be approximately hyperbolic; this allows the migration of  $P$ - $SV$  stacked sections using standard migration algorithms and an appropriately-constructed velocity function.

## 2.11 $P$ - $SV$ poststack inversion

Consider a layered medium with  $P$ -wave velocities  $\alpha_j$ ,  $S$ -wave velocities  $\beta_j$ , and densities  $\rho_j$ . Stewart (1991) derives the following expression for the  $P$ - $SV$  reflectivity at the  $j$ 'th interface;

$$R_j = -k_j \left[ (1 + \delta_j) \ln \left( \frac{\rho_{j+1}}{\rho_j} \right) + 2\delta_j \ln \left( \frac{\beta_{j+1}}{\beta_j} \right) \right], \quad (2.30)$$

where

$$k_j = \frac{\gamma \tan \phi}{2}, \quad (2.31)$$

$$\delta_j = \frac{2}{\gamma} \left( \cos \theta \cos \phi - \frac{\sin^2 \theta}{\gamma} \right), \quad (2.32)$$

$\theta$  is the average incident angle across the interface,  $\phi$  is the average reflected angle, and  $\gamma$  is the ratio of the average  $P$ -wave and  $S$ -wave velocities. A stacked trace is formed by summing over the traces within the CCP gather. The reflectivity of equation (2.30) can be written for the  $i$ 'th trace in the gather as

$$R_{ij} = -k_{ij} (1 + \delta_{ij}) \ln \left( \frac{\rho_{j+1}}{\rho_j} \right) - 2k_{ij} \delta_{ij} \ln \left( \frac{\beta_{j+1}}{\beta_j} \right). \quad (2.33)$$

The stacked reflectivity at the  $j$ 'th interface is given by

$$\begin{aligned} \bar{R}_j &= \frac{1}{n} \sum_{i=1}^n R_{ij} \\ &= -(\bar{k}_j + \bar{k} \delta_j) \ln \left( \frac{\rho_{j+1}}{\rho_j} \right) - 2\bar{k} \delta_j \ln \left( \frac{\beta_{j+1}}{\beta_j} \right). \end{aligned} \quad (2.34)$$

where

$$\bar{k}_j = \frac{1}{n} \sum_{i=1}^n k_{ij}, \text{ and } \bar{k}\delta_j = \frac{1}{n} \sum_{i=1}^n k_{ij}\delta_{ij}. \quad (2.35)$$

Equation (2.34) can be rearranged to give the  $S$ -wave velocity as

$$\beta_{j+1} = \beta_j \exp \left[ \left( \frac{\bar{k}_j + \bar{k}\delta_j}{2\bar{k}\delta_j} \right) \ln \left( \frac{\rho_j}{\rho_{j+1}} \right) + \left( \frac{-\bar{R}_j}{2\bar{k}\delta_j} \right) \right]. \quad (2.36)$$

For constant density, equation (2.36) reduces to

$$\beta_{j+1} = \beta_j \exp \left( \frac{-\bar{R}_j}{2\bar{k}\delta_j} \right). \quad (2.37)$$

In reality, the stacked data are always scaled by some unknown factor  $s$ , in which case equation (2.37) becomes

$$\beta_{j+1} = \beta_j \exp \left( \frac{-s\bar{R}_j}{2\bar{k}\delta_j} \right). \quad (2.38)$$

Equation (2.38) allows the recursive computation of the shear velocities from a  $P$ - $SV$  stacked section, using the averaged geometry parameters  $k_{ij}$  and  $\delta_{ij}$ . These parameters can be computed for each sample and trace offset by ray tracing an approximate model, constructed using either RMS-stacking or well-log velocities. A flowchart for the inversion process is shown in Figure 2.4. Because the stacked data have a lowcut filter applied to them, the inversion process can only recover a lowcut-filtered version of the velocity log. To overcome this, the method described by Galbraith and Millington (1979) is used, in which the approximate model is lowpass filtered and added to the lowcut-filtered results of the velocity inversion. The scalar  $s$  is here determined by repeatedly performing the inversion, each time modifying  $s$  until an appropriate value is found.

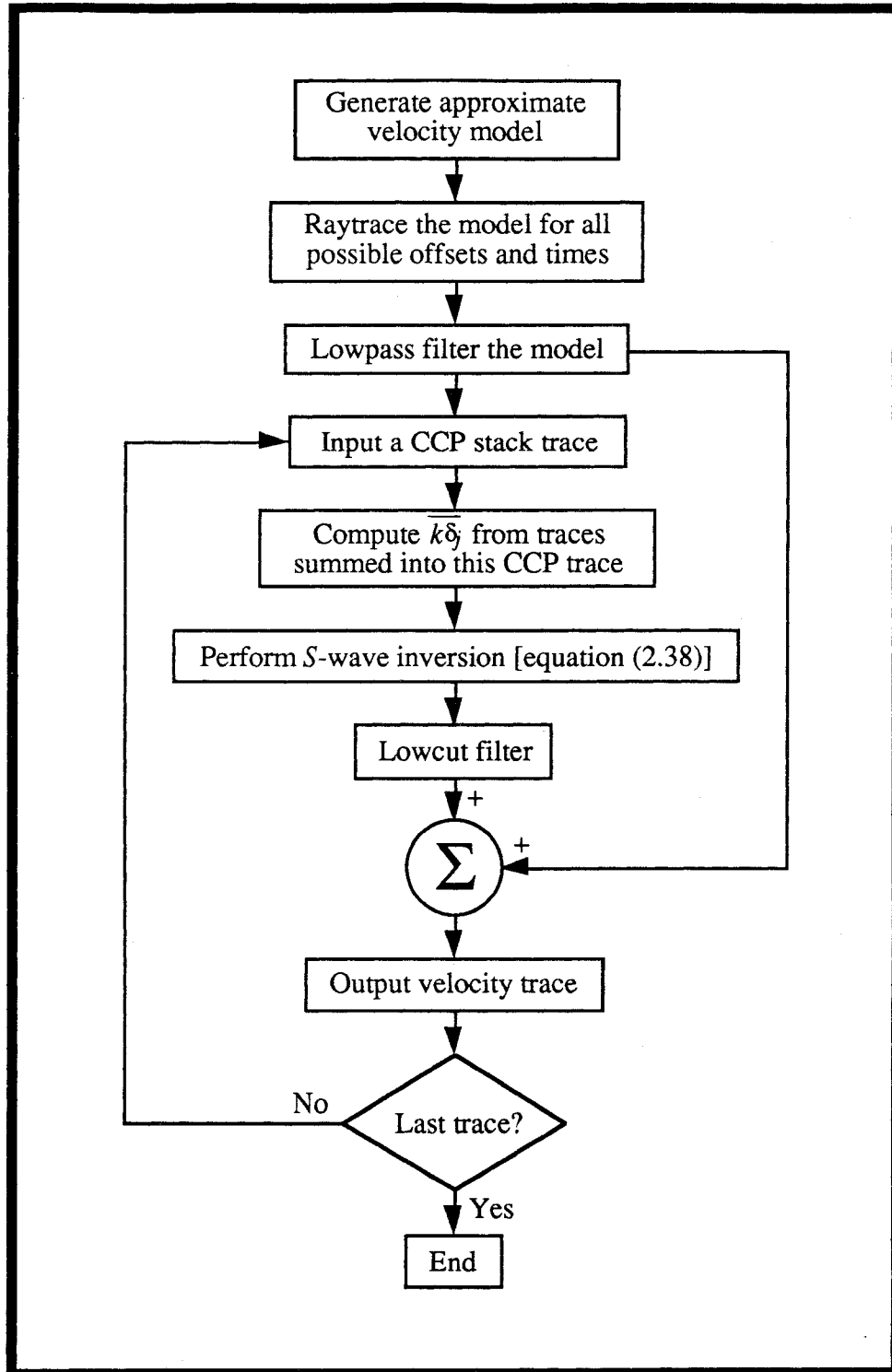


FIG. 2.4. Flowchart for the *P-SV* poststack velocity inversion algorithm.

## Chapter 3 - Birefringence analysis for *P-SV* data

### 3.1 Introduction

As demonstrated by Alford (1986) and many others since, the presence of anisotropy in the earth can lead to substantial complications in the processing of both surface and VSP shear data. In recent years there has also been much interest in the analysis of vertical shear-wave splitting, or birefringence, as a potential tool for detecting the presence of aligned vertical fracturing within reservoirs (e.g., Winterstein and Meadows, 1991). Most of the data obtained for the purpose of anisotropy studies have been acquired using multiple polarizations of the source, usually *SV* and *SH*, recorded into three-component geophones. This allows the use of Alford's four-component rotation analysis (Alford, 1986) for determining the orientation of the natural coordinate system [see Winterstein (1990) for definition]. It has been shown (Thomsen, 1988) that for data acquired with a single source polarization, such as converted-wave data, Alford's rotation method does not work.

Much work has been done using hodogram analysis methods to study *S*-wave splitting (e.g., Schulte and Edelmann, 1988; Crampin, 1989; Yardley and Crampin, 1990; McBeth, 1990). As discussed by Winterstein (1989), these methods require both very high signal-to-noise ratios and the presence of a single wavelet within the analysis window to be effective. It has also been demonstrated (Schulte and Edelmann, 1988; Slack et al., 1991) that a time separation between fast and slow wavelets of less than about one period of the dominant frequency makes direct interpretation of hodograms very difficult. Assuming a peak frequency of 25 Hz for converted-wave surface data, this implies a minimum time difference of about 40 ms. These requirements make it doubtful that hodogram analysis of converted-wave surface data is of much value.

Other two-component birefringence analysis schemes that do not involve hodograms have largely been based upon either the autocorrelation or crosscorrelation of rotated components. Naville (1986) generated the crosscorrelations between VSP first arrivals recorded at different depth levels as a function of rotation angle. In his approach the angle that visually gives the most symmetric correlation function is chosen as the proper rotation angle. Peron (1990) computed the crosscorrelation between rotated radial and transverse components for a range of rotation angles, and then analyzed three attributes from these functions: maximum correlation, time delay of maximum correlation, and a symmetry measure of correlation function relative to the maximum value. Comparison of his two-component attributes to the known orientation of the natural coordinate system for a VSP test case indicates that none of the attributes is very diagnostic.

The birefringence analysis methods presented here are somewhat similar to that of Spencer and Chi (1991); the main difference is that I rely on the modeling of crosscorrelations between rotated radial and transverse components, rather than the modeling of instantaneous polarization direction and amplitudes of the data itself.

### 3.2 Mathematical background

Shown in Figure 4.1 is a plan view of a three-component surface line for the case where vertical S-wave birefringence is assumed to occur. The direction  $S_{fast}$  indicates the polarization direction along which vertically-propagating S-waves travel at the fastest velocity  $\beta_1$ , while  $S_{slow}$ , taken to be perpendicular to  $S_{fast}$ , is the polarization along which S-waves travel at the slowest velocity  $\beta_2$ . The line is at an oblique angle  $\theta$  to the natural coordinate system, defined by the  $S_{fast}$ - $S_{slow}$  directions. If the shear waves are generated by P-SV mode conversion at depth, then in passing through an anisotropic layer of thickness  $z$  the converted S-waves will be split into fast and slow components separated by a time difference  $\delta$ :

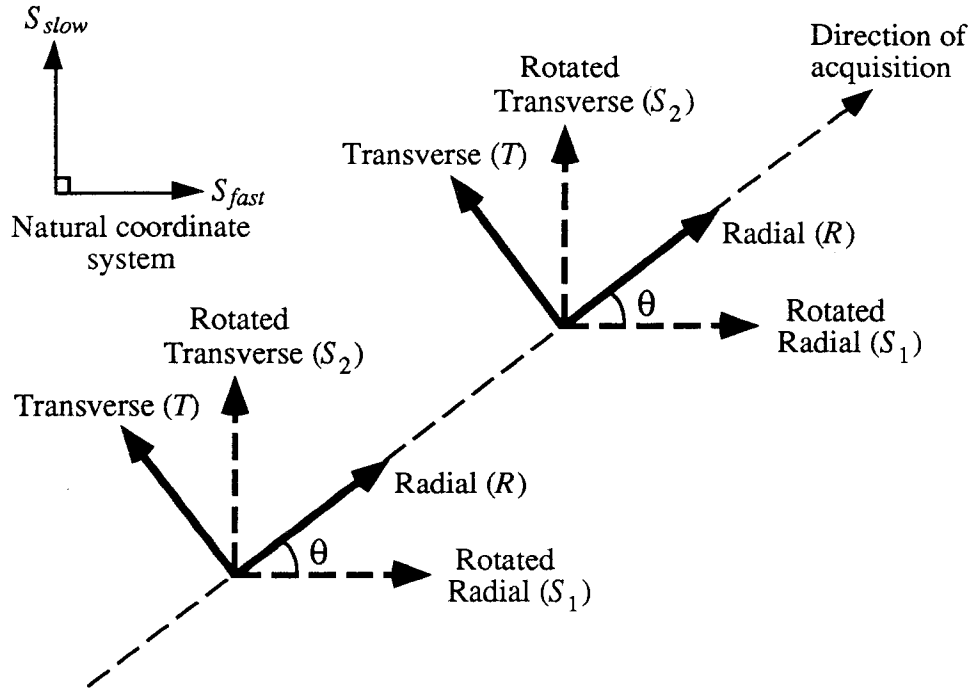


FIG. 3.1. Plan view of a multicomponent line in an area of vertical  $S$ -wave birefringence.

$$\begin{aligned}
 S_1(t) &= S(t) \cos \theta, \\
 S_2(t) &= S(t-\delta) \sin \theta, \\
 \delta &= z \left( \frac{1}{\beta_2} - \frac{1}{\beta_1} \right),
 \end{aligned} \tag{3.1}$$

where  $S$  is the amplitude of the  $SV$  signal. The recorded radial ( $R$ ) and transverse ( $T$ ) components at the receiver are given by

$$\begin{aligned}
 \begin{bmatrix} R(t) \\ T(t) \end{bmatrix} &= \begin{bmatrix} \cos \theta & \sin \theta \\ -\sin \theta & \cos \theta \end{bmatrix} \begin{bmatrix} S_1(t) \\ S_2(t) \end{bmatrix} + \begin{bmatrix} n_R(t) \\ n_T(t) \end{bmatrix} \\
 &= \begin{bmatrix} \cos \theta & \sin \theta \\ -\sin \theta & \cos \theta \end{bmatrix} \begin{bmatrix} S(t) \cos \theta \\ S(t-\delta) \sin \theta \end{bmatrix} + \begin{bmatrix} n_R(t) \\ n_T(t) \end{bmatrix}
 \end{aligned} \tag{3.2}$$

where  $n_R$  and  $n_T$  are the noise components in the radial and transverse directions. In order to recover the fast and slow components, the recorded radial and transverse components

can be rotated clockwise through an angle  $\phi$  by application of the corresponding rotation matrix;

$$\begin{aligned} \begin{bmatrix} R_\phi(t) \\ T_\phi(t) \end{bmatrix} &= \begin{bmatrix} \cos \phi & -\sin \phi \\ \sin \phi & \cos \phi \end{bmatrix} \begin{bmatrix} R(t) \\ T(t) \end{bmatrix} \\ &= \begin{bmatrix} \cos \epsilon & \sin \epsilon \\ -\sin \epsilon & \cos \epsilon \end{bmatrix} \begin{bmatrix} S_1(t) \\ S_2(t) \end{bmatrix} + \begin{bmatrix} \cos \phi & -\sin \phi \\ \sin \phi & \cos \phi \end{bmatrix} \begin{bmatrix} n_R(t) \\ n_T(t) \end{bmatrix} \end{aligned} \quad (3.3)$$

where

$$\epsilon = \theta - \phi.$$

Equation (3.3) without the noise term has been published by a number of authors (e.g., Garotta and Granger, 1986; Thomsen, 1988). Ignoring the noise term, when  $\theta = \phi$  equation (3.3) reduces to

$$\begin{bmatrix} S_1(t) \\ S_2(t) \end{bmatrix} = \begin{bmatrix} \cos \theta & -\sin \theta \\ \sin \theta & \cos \theta \end{bmatrix} \begin{bmatrix} R(t) \\ T(t) \end{bmatrix} \quad (3.4)$$

or (Thomsen, 1988):

$$\begin{bmatrix} S(t) \\ S(t-\delta) \end{bmatrix} = \begin{bmatrix} 1 & -\tan \theta \\ 1 & \cot \theta \end{bmatrix} \begin{bmatrix} R(t) \\ T(t) \end{bmatrix}. \quad (3.5)$$

As discussed by Thomsen (1988), equation (3.5) is unstable whenever  $\theta = 0$  or  $\pm\pi/2$ . Division by  $\sin \theta$  and  $\cos \theta$  to obtain equation (3.5) from equation (3.4) results in a constant scale factor being applied to the rotated data and is unnecessary, as any subsequent scaling will mask this. Equation (3.4) is then adequate, and shows that the fast and slow shear components can be separated by a simple geophone rotation if the angle  $\theta$  is known.

For the four-component case where both *SV* and *SH* sources of equal strength are used, the resulting matrix equation is always stable (Alford, 1986), and an energy optimization algorithm can be used to determine the orientation of the natural coordinate

system. Examples of this technique can be found in Winterstein and Meadows (1991) and references therein.

The autocorrelations  $A_R$  and  $A_T$  of each of the rotated components is given by

$$\begin{aligned}
 A_R(t, \phi) &= [R_\phi \otimes R_\phi](t) \\
 &= [S_1(t) \cos \epsilon + S_2(t) \sin \epsilon + n_R(t) \cos \phi - n_T(t) \sin \phi] \\
 &\quad \otimes [S_1(t) \cos \epsilon + S_2(t) \sin \epsilon + n_R(t) \cos \phi - n_T(t) \sin \phi] \\
 &= [S_1 \otimes S_1](t) \cos^2 \epsilon + [S_2 \otimes S_2](t) \sin^2 \epsilon + [S_1 \otimes S_2 + S_2 \otimes S_1](t) \sin \epsilon \cos \epsilon \\
 &\quad + [n_R \otimes n_R](t) \cos^2 \phi + [n_T \otimes n_T](t) \sin^2 \phi - [n_R \otimes n_T + n_T \otimes n_R](t) \sin \phi \cos \phi
 \end{aligned} \tag{3.6}$$

$$\begin{aligned}
 A_T(t, \phi) &= [T_\phi \otimes T_\phi](t) \\
 &= [-S_1(t) \sin \epsilon + S_2(t) \cos \epsilon + n_R(t) \sin \phi + n_T(t) \cos \phi] \\
 &\quad \otimes [-S_1(t) \sin \epsilon + S_2(t) \cos \epsilon + n_R(t) \sin \phi + n_T(t) \cos \phi] \\
 &= [S_1 \otimes S_1](t) \sin^2 \epsilon + [S_2 \otimes S_2](t) \cos^2 \epsilon - [S_1 \otimes S_2 + S_2 \otimes S_1](t) \sin \epsilon \cos \epsilon \\
 &\quad + [n_R \otimes n_R](t) \sin^2 \phi + [n_T \otimes n_T](t) \cos^2 \phi + [n_R \otimes n_T + n_T \otimes n_R](t) \sin \phi \cos \phi,
 \end{aligned} \tag{3.7}$$

where  $\otimes$  represents correlation, and the signal and noise components have been assumed to be uncorrelated, i.e.,

$$\begin{aligned}
 S_1 \otimes n_R &= S_2 \otimes n_R = n_R \otimes S_1 = n_R \otimes S_2 = 0, \\
 S_1 \otimes n_T &= S_2 \otimes n_T = n_T \otimes S_1 = n_T \otimes S_2 = 0 \text{ for all } t.
 \end{aligned}$$

The summed autocorrelation function  $A$  is given by equations (3.6) and (3.7) as

$$\begin{aligned}
 A(t) &= A_R(t, \phi) + A_T(t, \phi) \\
 &= [S_1 \otimes S_1](t) + [S_2 \otimes S_2](t) + [n_R \otimes n_R](t) + [n_T \otimes n_T](t).
 \end{aligned} \tag{3.8}$$

It is seen from equation (3.8) that there is no change in the total energy as the rotation angle  $\phi$  (or  $\epsilon$ ) is modified. The crosscorrelation function  $X$  between the rotated radial and

transverse components is given by

$$\begin{aligned}
X(t, \phi) &= [R_\phi \otimes T_\phi](t) \\
&= [S_1(t) \cos \epsilon + S_2(t) \sin \epsilon + n_R(t) \cos \phi - n_T(t) \sin \phi] \\
&\quad \otimes [-S_1(t) \sin \epsilon + S_2(t) \cos \epsilon + n_R(t) \sin \phi + n_T(t) \cos \phi] \\
&= [S_2 \otimes S_2 - S_1 \otimes S_1](t) \frac{\sin 2\epsilon}{2} + [S_1 \otimes S_2](t) \cos^2 \epsilon - [S_2 \otimes S_1](t) \sin^2 \epsilon \\
&\quad + [n_R \otimes n_R - n_T \otimes n_T](t) \frac{\sin 2\phi}{2} + [n_R \otimes n_T](t) \cos^2 \phi - [n_T \otimes n_R](t) \sin^2 \phi.
\end{aligned} \tag{3.9}$$

The crosscorrelation function defined by equation (3.9) is seen to have an obvious dependency upon rotation angle.

The autocorrelation  $C$  of the shear signal within a window of length  $L$  is given by (Kanasewich, 1981);

$$\begin{aligned}
C(t) &= [S \otimes S](t) \\
&= \frac{1}{L} \int_{-\frac{L}{2}}^{\frac{L}{2}} S(t+\tau) S(\tau) d\tau.
\end{aligned} \tag{3.10}$$

The  $S$ -wave correlations are then given by

$$[S_1 \otimes S_1](t) = C(t) \cos^2 \theta, \tag{3.11a}$$

$$\begin{aligned}
[S_2 \otimes S_2](t) &= \frac{\sin^2 \theta}{L} \int_{-\frac{L}{2}}^{\frac{L}{2}} S(t+\tau-\delta) S(\tau-\delta) d\tau \\
&= \frac{\sin^2 \theta}{L} \int_{-\frac{L}{2}+\delta}^{\frac{L}{2}+\delta} S(t+\tau) S(\tau) d\tau \\
&= C(t) \sin^2 \theta \text{ for } \delta \ll L,
\end{aligned} \tag{3.11b}$$

$$[S_1 \otimes S_2](t) = \frac{\sin 2\theta}{2L} \int_{-\frac{L}{2}}^{\frac{L}{2}} S(t+\tau) S(\tau-\delta) d\tau$$

$$\begin{aligned}
&= \frac{\sin 2\theta}{2L} \int_{\frac{L-\delta}{2}}^{\frac{L+\delta}{2}} S(t+\delta+\tau) S(\tau) d\tau \\
&= C(t+\delta) \frac{\sin 2\theta}{2} \text{ for } \delta \ll L,
\end{aligned} \tag{3.11c}$$

$$\begin{aligned}
[S_2 \otimes S_1](t) &= \frac{\sin 2\theta}{2L} \int_{\frac{L}{2}}^{\frac{L}{2}} S(t+\tau-\delta) S(\tau) d\tau \\
&= C(t-\delta) \frac{\sin 2\theta}{2} \text{ for } \delta \ll L.
\end{aligned} \tag{3.11d}$$

Using equations (3.11), equations (3.8) and (3.9) can be rewritten as

$$A(t) = C(t) + [n_R \otimes n_R](t) + [n_T \otimes n_T](t) \tag{3.12}$$

and

$$\begin{aligned}
X(t, \phi) &= -C(t) \cos 2\theta \frac{\sin 2\epsilon}{2} + [C(t+\delta) \cos^2 \epsilon - C(t-\delta) \sin^2 \epsilon] \frac{\sin 2\theta}{2} \\
&\quad + [n_R \otimes n_R - n_T \otimes n_T](t) \frac{\sin 2\phi}{2} + [n_R \otimes n_T](t) \cos^2 \phi - [n_T \otimes n_R](t) \sin^2 \phi.
\end{aligned} \tag{3.13}$$

The function defined by equation (3.13) can be broken into even and odd components  $X_e$  and  $X_o$  (Claerbout, 1976):

$$\begin{aligned}
X(-t, \phi) &= -C(-t) \cos 2\theta \frac{\sin 2\epsilon}{2} + [C(-t+\delta) \cos^2 \epsilon - C(-t-\delta) \sin^2 \epsilon] \frac{\sin 2\theta}{2} \\
&\quad + [n_R \otimes n_R - n_T \otimes n_T](-t) \frac{\sin 2\phi}{2} + [n_R \otimes n_T](-t) \cos^2 \phi - [n_T \otimes n_R](-t) \sin^2 \phi \\
&= -C(t) \cos 2\theta \frac{\sin 2\epsilon}{2} + [C(t-\delta) \cos^2 \epsilon - C(t+\delta) \sin^2 \epsilon] \frac{\sin 2\theta}{2} \\
&\quad + [n_R \otimes n_R - n_T \otimes n_T](t) \frac{\sin 2\phi}{2} + [n_T \otimes n_R](t) \cos^2 \phi - [n_R \otimes n_T](t) \sin^2 \phi,
\end{aligned} \tag{3.14}$$

and

$$X_e(t, \phi) = \frac{X(t, \phi) + X(-t, \phi)}{2}$$

$$\begin{aligned}
&= -C(t) \cos 2\theta \frac{\sin 2\varepsilon}{2} + [C(t+\delta) + C(t-\delta)] \frac{\sin 2\theta \cos 2\varepsilon}{4} \\
&+ [n_R \otimes n_R - n_T \otimes n_T](t) \frac{\sin 2\phi}{2} + [n_R \otimes n_T + n_T \otimes n_R](t) \frac{\cos 2\phi}{2}, \quad (3.15)
\end{aligned}$$

$$\begin{aligned}
X_o(t) &= \frac{X(t, \phi) - X(-t, \phi)}{2} \\
&= [C(t+\delta) - C(t-\delta)] \frac{\sin 2\theta}{4} + \frac{[n_R \otimes n_T - n_T \otimes n_R](t)}{2}. \quad (3.16)
\end{aligned}$$

The odd part of the crosscorrelation is seen from equation (3.16) to be completely independent of the rotation angle  $\phi$ , but is strongly dependent upon the natural-coordinate-system angle  $\theta$  and time delay  $\delta$ .

If the noise components on the two channels are negligible, or are similar but uncorrelated, then with sufficient fold

$$\begin{aligned}
[n_R \otimes n_T](t) &\Rightarrow 0, [n_T \otimes n_R](t) \Rightarrow 0, \text{ and} \\
[n_R \otimes n_R](t) &\Rightarrow [n_T \otimes n_T](t) \Rightarrow N(t),
\end{aligned}$$

where  $N$  is the average noise autocorrelation function. Equations (3.12), (3.13), (3.15), and (3.16) then become:

$$A(t) \equiv C(t) + 2N(t) \text{ for all } \phi, \quad (3.17)$$

$$X(t, \phi) \equiv -C(t) \cos 2\theta \frac{\sin 2\varepsilon}{2} + [C(t+\delta) \cos^2\varepsilon - C(t-\delta) \sin^2\varepsilon] \frac{\sin 2\theta}{2}, \quad (3.18)$$

$$X_e(t, \phi) \equiv -C(t) \cos 2\theta \frac{\sin 2\varepsilon}{2} + [C(t+\delta) + C(t-\delta)] \frac{\sin 2\theta \cos 2\varepsilon}{4}, \quad (3.19)$$

$$X_o(t) \equiv [C(t+\delta) - C(t-\delta)] \frac{\sin 2\theta}{4} \text{ for all } \phi. \quad (3.20)$$

These equations are the basis for the birefringence analysis methods discussed in the following section.

### 3.3 Birefringence analysis algorithms

The solution of equations (3.18), (3.19), and (3.20) for the time delay  $\delta$  and natural-coordinate-system angle  $\theta$  is greatly simplified if the autocorrelation function  $C$  is known or can be reasonably approximated. One way that this can be done is to assume that the total autocorrelation function  $A$  given by equation (3.17) is a scaled version of  $C$ , i.e.,

$$C(t) \cong a A(t) ,$$

where  $a$  is an unknown scalar. Using this assumption, estimates of delay and rotation angle can be determined from equations (3.18), (3.19), and (3.20).

The most robust measure of birefringence appears to be  $X_o$ , the odd part of the crosscorrelation function. Even for large noise levels and/or some degree of correlation between radial and transverse noise components, the noise correlation function should be nearly symmetric about zero lag;  $X_o$  therefore quickly approaches equation (3.20). Because the estimated values for  $C$  are at best off by a scale factor, it is not possible to recover  $\theta$  from equation (3.20). An analysis method for estimating  $\delta$  using  $X_o$  is presented in Section 3.3.1.

The least robust measure of birefringence appears to be  $X_e$ , the even part of the autocorrelation function [(equation (3.15))]. The noise terms include the sum of the noise-component crosscorrelation with its conjugate; if the noise crosscorrelation function is non-zero and symmetric, then this sum will be non-zero. It was also found in experimentation that the sensitivity of  $X_e$  to variations in  $\theta$  and  $\delta$  is relatively small and easily masked by the noise terms. For this reason, no further work was done using equation (3.19) as an estimator.

In order to simultaneously recover both the lag and rotation angle, forward modeling of the entire crosscorrelation function  $X$  can be performed. This method was found to give the best overall results, and can accurately recover both the correct time lag

and rotation angle if sufficient signal-to-noise and/or fold is available. The modeling of  $X$  using equation (3.18) is developed in Section 3.3.2.

### 3.3.1 Modeling the odd part of the crosscorrelation function

If the prediction function  $\widehat{X}_o$  for a given value of  $\delta$  is defined as

$$\begin{aligned}\widehat{X}_o(t, \delta) &= s(\delta) [A(t+\delta) - A(t-\delta)] \\ &= s(\delta) F(t, \delta),\end{aligned}\tag{3.21}$$

where  $s$  is unknown, then the normalized prediction error energy is given by

$$E(\delta) = \frac{\int_{\frac{L}{2}}^{\frac{L}{2}} [X_o(t) - \widehat{X}_o(t, \delta)]^2 dt}{\int_{\frac{L}{2}}^{\frac{L}{2}} X_o^2(t) dt} = \frac{\int_{\frac{L}{2}}^{\frac{L}{2}} [X_o(t) - s(\delta) F(t, \delta)]^2 dt}{\int_{\frac{L}{2}}^{\frac{L}{2}} X_o^2(t) dt}.\tag{3.22}$$

Minimizing the prediction error energy w.r.t. the scalar  $s$  gives

$$s(\delta) = \frac{\int_{\frac{L}{2}}^{\frac{L}{2}} X_o(t) F(t, \delta) dt}{\int_{\frac{L}{2}}^{\frac{L}{2}} F^2(t, \delta) dt}.\tag{3.23}$$

Substituting equation (3.23) for  $s$  into equation (3.22) gives

$$E(\delta) = 1 - \sigma^2(\delta)\tag{3.24}$$

where  $\sigma$  is the energy-normalized crosscorrelation sum (Neidell and Taner, 1971):

$$\sigma(\delta) = \frac{\int_{-\frac{L}{2}}^{\frac{L}{2}} X_o(t) F(t,\delta) dt}{\sqrt{\int_{-\frac{L}{2}}^{\frac{L}{2}} X_o^2(t) dt \int_{-\frac{L}{2}}^{\frac{L}{2}} F^2(t,\delta) dt}} . \quad (3.25)$$

The normalized prediction error [equation (3.24)] varies from a value of 1 for no prediction to 0 for perfect prediction. Rather than using this as a measure of fit, the function  $\sigma$  [equation (3.25)], which varies between  $\pm 1$ , or the signal-to-noise variance ratio  $S/N$ , defined by Gulunay (1991) as

$$S/N = \frac{\sigma}{1-\sigma} , \quad (3.26)$$

can be used. The  $S/N$  parameter is found to be a much more sensitive measure of fit, as demonstrated by Figure 3.5.

### 3.3.2 Modeling the total crosscorrelation function

Forward modeling of the total crosscorrelation function  $X$  can be performed in order to estimate both the lag and rotation angle. For this case the prediction function  $\hat{X}$  is defined as

$$\hat{X}(t,\phi,\theta,\delta) = s(\theta,\delta) G(t,\phi,\theta,\delta) , \quad (3.27)$$

where  $s$  is again unknown, and

$$G(t,\phi,\theta,\delta) = -A(t) \cos 2\theta \frac{\sin 2\epsilon}{2} + [A(t+\delta) \cos^2\epsilon - A(t-\delta) \sin^2\epsilon] \frac{\sin 2\theta}{2} . \quad (3.28)$$

The prediction error energy is given by

$$E(\theta, \delta) = \frac{\int_{-\frac{\pi}{2}}^{\frac{\pi}{2}} \int_{\frac{L}{2}}^{\frac{L}{2}} [X(t, \phi) - \widehat{X}(t, \phi, \theta, \delta)]^2 dt d\phi}{\int_{-\frac{\pi}{2}}^{\frac{\pi}{2}} \int_{\frac{L}{2}}^{\frac{L}{2}} X^2(t, \phi) dt d\phi} = \frac{\int_{-\frac{\pi}{2}}^{\frac{\pi}{2}} \int_{\frac{L}{2}}^{\frac{L}{2}} [X(t, \phi) - s(\theta, \delta)G(t, \phi, \theta, \delta)]^2 dt d\phi}{\int_{-\frac{\pi}{2}}^{\frac{\pi}{2}} \int_{\frac{L}{2}}^{\frac{L}{2}} X^2(t, \phi) dt d\phi}, \quad (3.29)$$

and minimizing  $E$  w.r.t.  $s$  and backsubstituting leads to

$$E(\theta, \delta) = 1 - \sigma^2(\theta, \delta), \quad (3.30)$$

where  $\sigma$  is once again the energy-normalized crosscorrelation sum:

$$\sigma(\theta, \delta) = \frac{\int_{-\frac{\pi}{2}}^{\frac{\pi}{2}} \int_{\frac{L}{2}}^{\frac{L}{2}} X(t, \phi) G(t, \phi, \theta, \delta) dt d\phi}{\left[ \int_{-\frac{\pi}{2}}^{\frac{\pi}{2}} \int_{\frac{L}{2}}^{\frac{L}{2}} X^2(t, \phi) dt d\phi \right] \left[ \int_{-\frac{\pi}{2}}^{\frac{\pi}{2}} \int_{\frac{L}{2}}^{\frac{L}{2}} G^2(t, \phi, \theta, \delta) dt d\phi \right]}. \quad (3.31)$$

A flowchart for the birefringence analysis algorithm is shown in Figure 3.2. The input to the rotation analysis is an autocorrelation function of the data within the analysis time window, as well as a sweep of crosscorrelations generated by rotating the field data in fixed increments spanning the range  $-90^\circ$  to  $90^\circ$ , then crosscorrelating the rotated radial and transverse components at each angle. Testing showed that no changes in analysis results occur for angular increments less than about  $20^\circ$ . All analysis plots presented in this dissertation were created using an angular increment of  $15^\circ$ .

The birefringence analysis is performed by sweeping through a two-dimensional set of natural-coordinate-system angle/time delay values and computing  $\sigma(\theta, \delta)$ , using equation (3.31), for each  $\theta$ - $\delta$  pair. The resulting 2-D correlation surface is then contour-plotted to

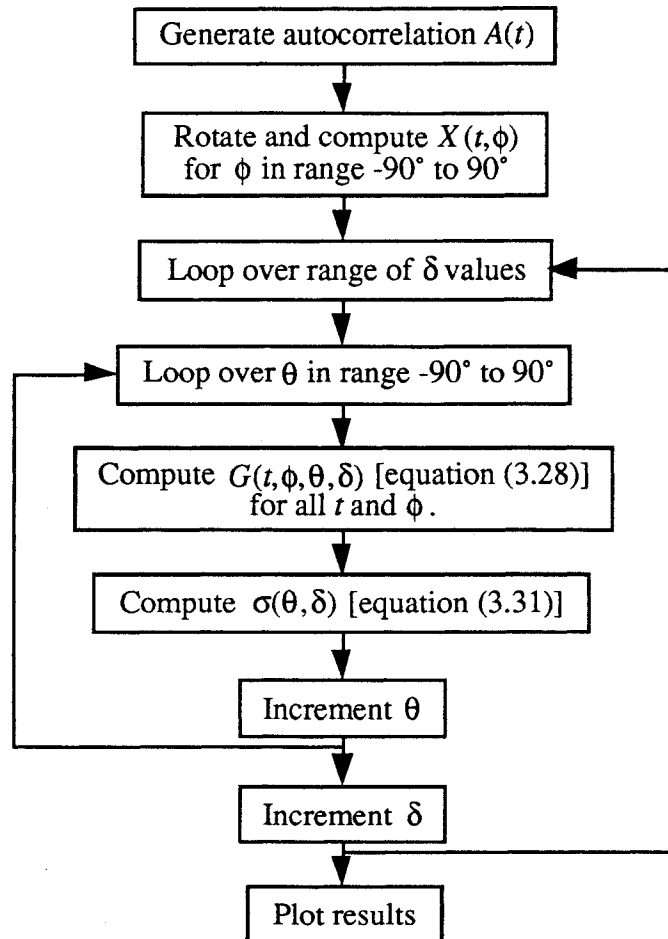
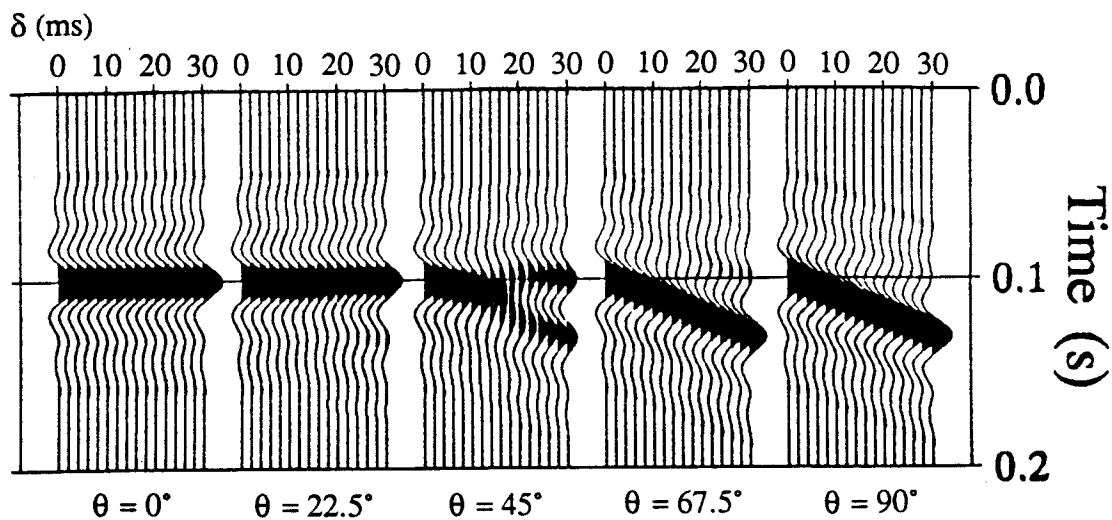


FIG. 3.2. Flowchart for the birefringence analysis algorithm of Section 3.3.2.

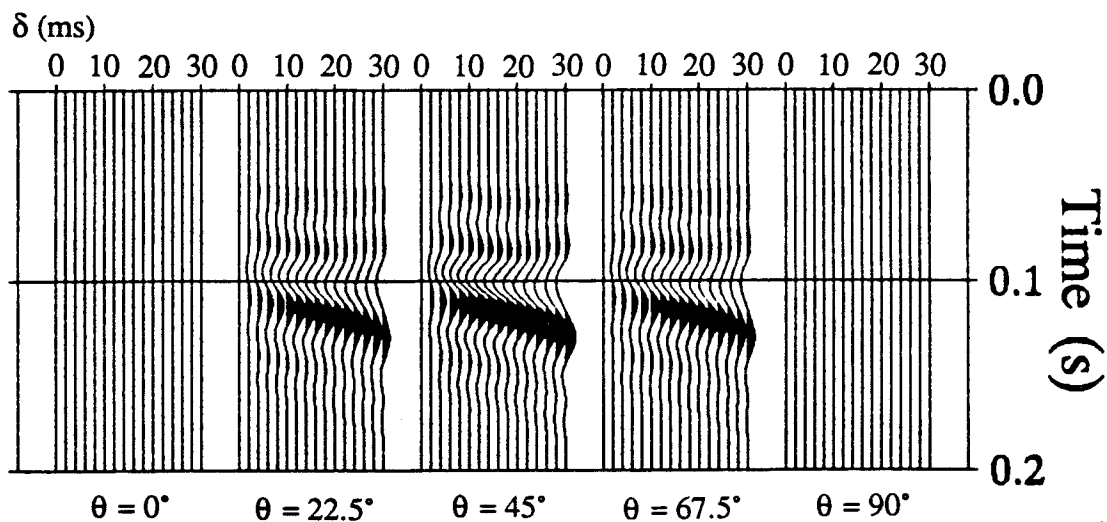
enable picking of the most probable values of coordinate-system angle and time delay. Examples of this technique are presented in the next section.

### 3.4 Application of birefringence analysis

The birefringence analysis techniques described in Sections 3.3.1 and 3.3.2 were initially tested on the synthetic data shown in Figure 3.3. Varying amounts of band-limited random noise were added to evaluate the robustness of the second method ( $\theta$ - $\delta$  analysis). The results are presented in Section 3.4.1.



(a)



(b)

FIG. 3.3. Synthetic data created for differing natural-coordinate-system angle  $\theta$  and varying amounts of time lag  $\delta$ : (a) radial component; (b) transverse component.

The  $\theta$ - $\delta$  analysis was also performed on data from two lines in the Carrot Creek, Alberta survey (Chapter 6); results are presented in Section 3.4.2.

### 3.4.1 Analysis of synthetic data

The initial synthetic data were generated using a single zero-phase wavelet with frequency spectrum 6/10-35/45 Hz. Radial and transverse components were synthesized for various values of angle  $\theta$  and time delay  $\delta$  using equation (3.2).

The radial and transverse components, total autocorrelation  $A$  and crosscorrelations  $X$  between rotated radial and transverse components are displayed in Figure 3.4 for the case of  $\theta=-30^\circ$  and  $\delta=4$  ms. Shown in Figure 3.5 is the result of applying  $\delta$  analysis (Section 3.3.1) to this data set, using both the energy-normalized crosscorrelation sum  $\sigma$  [equation (3.25)] and signal-to-noise variance ratio  $S/N$  [equation (3.26)]. The  $S/N$  measure (Figure 3.5b) is seen to give much better resolution than the crosscorrelation sum (Figure 3.5a), and is used in all other birefringence analysis plots in this dissertation. It is seen in Figure 3.5b that there is a very obvious peak in the  $S/N$  curve at  $\delta=4$  ms, as expected. In further testing it was found that the  $\theta$ - $\delta$  analysis (Section 3.3.2) was also able to accurately indicate the correct lag values; therefore no further work will be shown using the  $\delta$  analysis method.

Shown in Figure 3.6 are the contoured  $S/N$  surfaces obtained by applying  $\theta$ - $\delta$  analysis (Section 3.3.2) to synthetic data created using a number of different natural-coordinate-system angles and time lags. Contours indicate values ranging from 99% to 49% of the maximum computed value in decrements of 10%. The location of the maximum computed value is indicated in each example by the symbol '+'.

It is seen from Figure 3.6a that there is no detectable difference between having no birefringence ( $\delta=0$ ), in which case there is no preferred orientation of the natural coordinate system, and having the line fall along one of the principal axes ( $\theta=0$  or  $\pm 90^\circ$ ), in which case the time lag is indeterminate. This result is to be expected as both situations give no  $S$ -wave splitting, and data is only present on the radial channel (Figure 3.3).

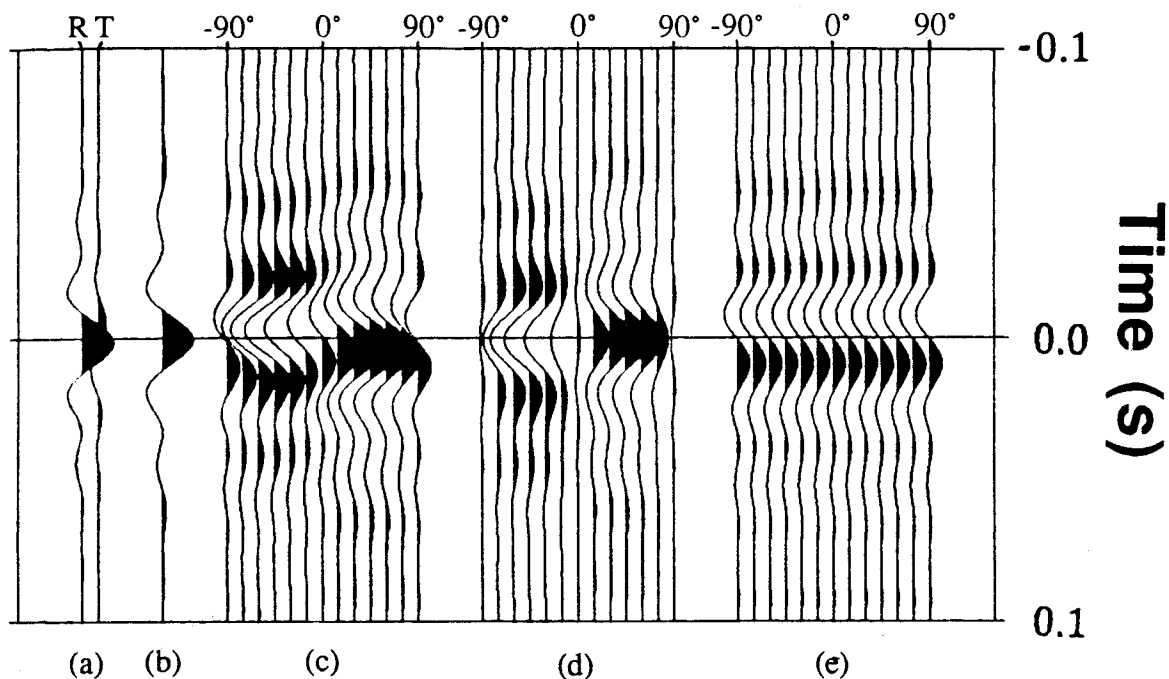
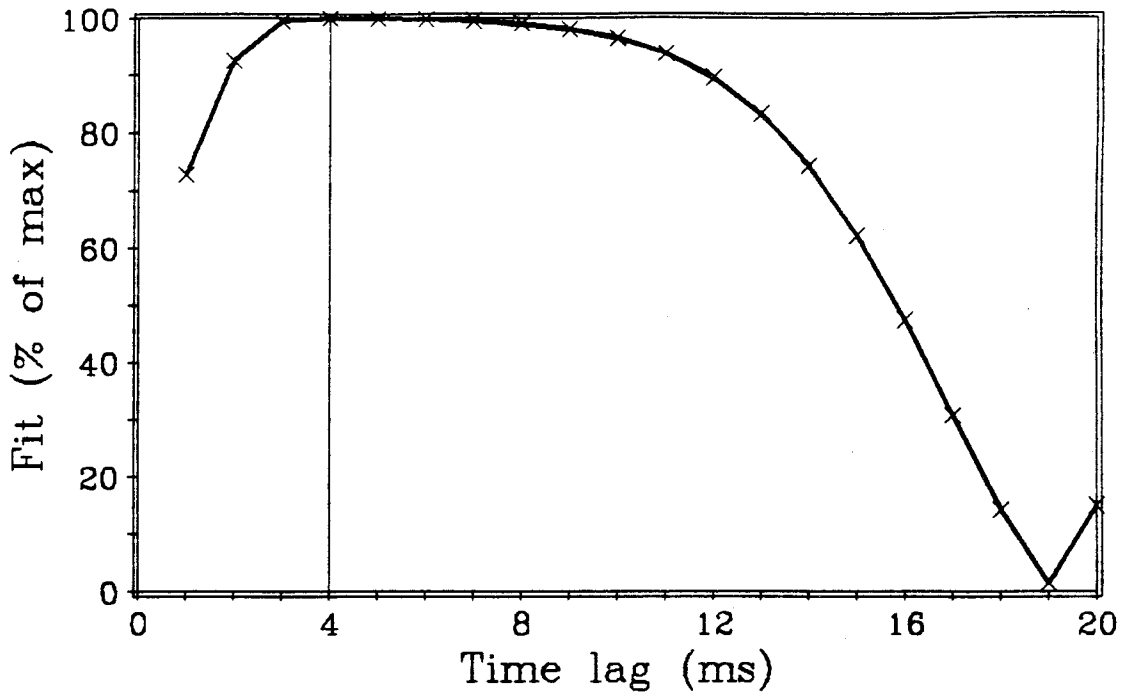


FIG. 3.4. Synthetic data created for natural-coordinate-system-angle  $\theta = -30^\circ$  and time lag  $\delta = 4$  ms: (a) radial (R) and transverse (T) data; (b) total autocorrelation  $A$ ; (c) crosscorrelation  $X$  between rotated radial and transverse components for various rotation angles  $\phi$ ; (d) even part of (c); (e) odd part of (c).

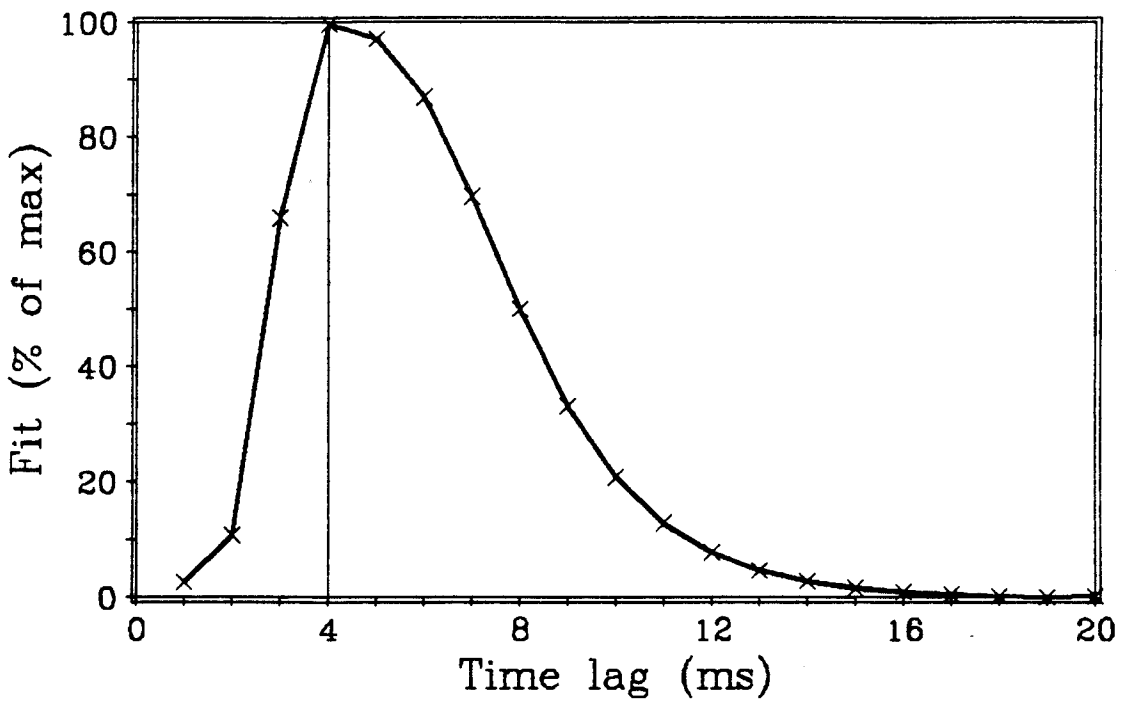
Time lags of less than 2 ms can be resolved (Figure 3.6b), but the orientation of the natural coordinate system is poorly defined for lags of 2 ms and less. As the lag increases the location of the maximum value is more pronounced; lags greater than 2 ms allow the angle  $\theta$  to be accurately determined. It is seen from Figure 3.6f that differences between positive and negative values of  $\theta$  can also be measured, and that angles of  $10^\circ$  and less can be resolved if sufficient time lag is present.

The  $\theta$ - $\delta$  analysis method was also tested on synthetic data with varying signal-to-noise power ratios ( $SNR$ ), i.e.,

$$SNR = \frac{C(0)}{N(0)}, \quad (3.32)$$

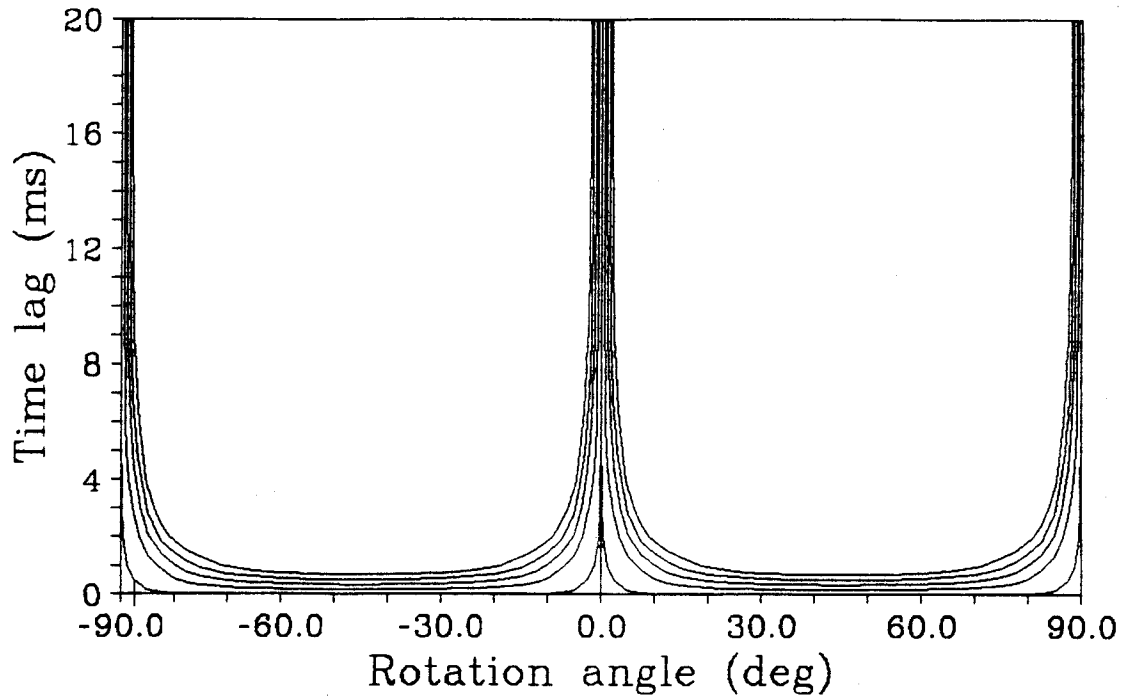


(a)

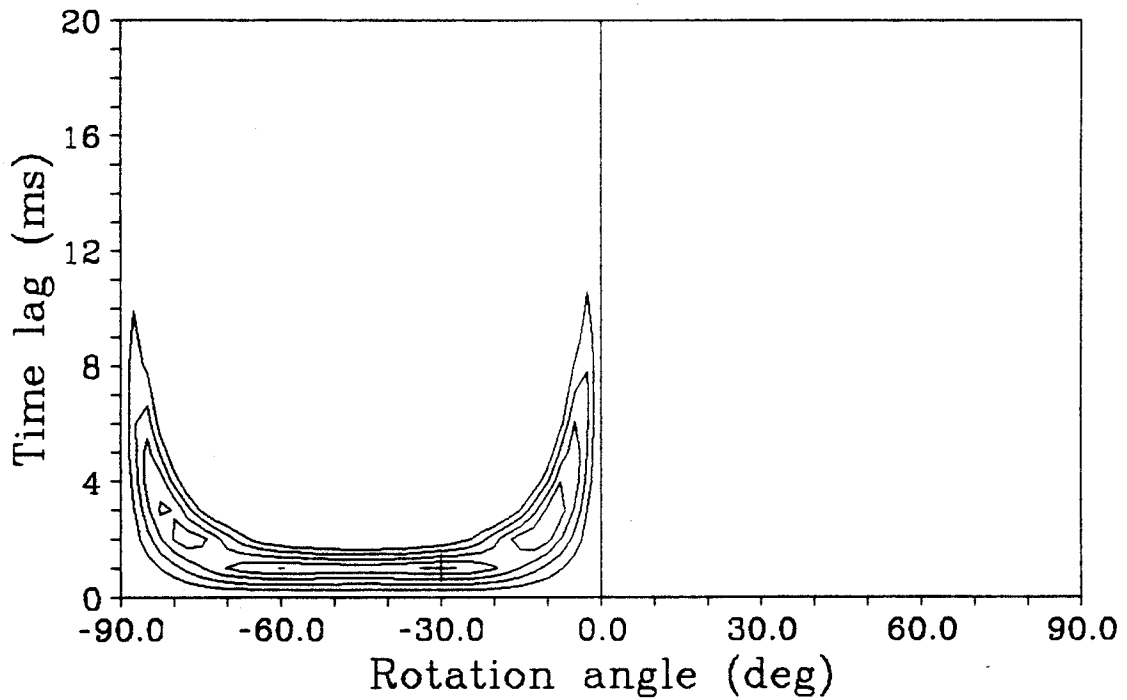


(b)

FIG. 3.5. Time-delay analysis described in Section 3.3.1 applied to synthetic data in Figure 3.4: (a) energy-normalized crosscorrelation sum  $\sigma$  vs. time lag; (b) signal-to-noise variance ratio  $S/N$  [equation (3.26)] vs. time lag.

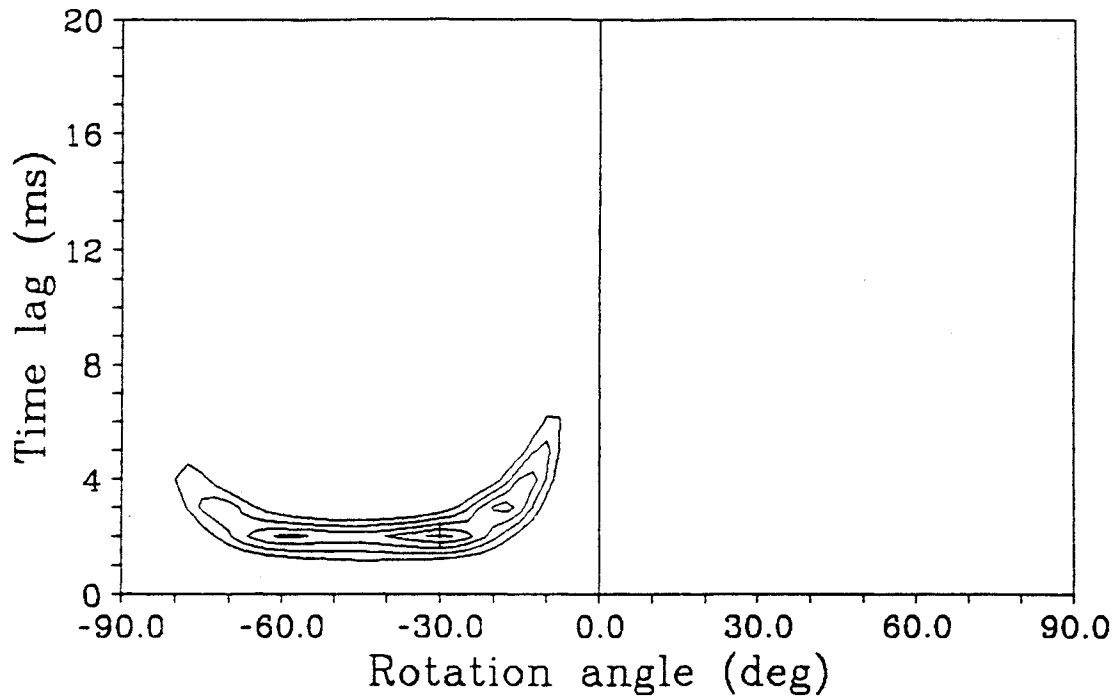


(a)

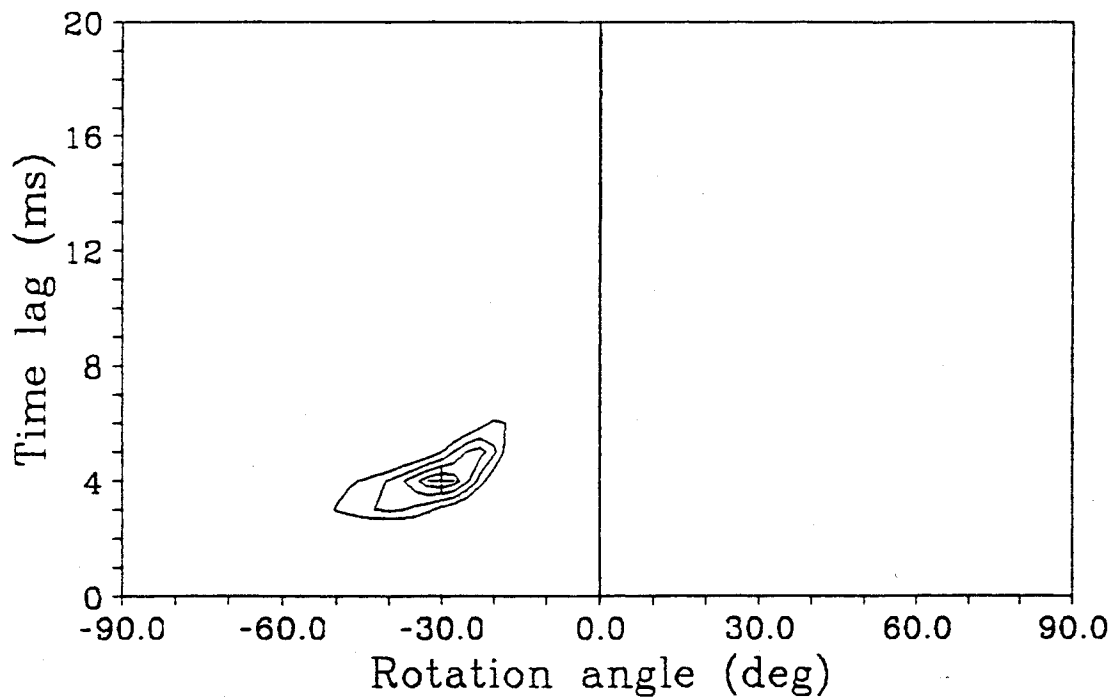


(b)

FIG. 3.6.  $\theta$ - $\delta$  analysis described in Section 3.3.2 applied to noise-free synthetic data: (a)  $\theta = -30^\circ$ ,  $\delta = 0$  ms; (b)  $\theta = -30^\circ$ ,  $\delta = 1$  ms; (c)  $\theta = -30^\circ$ ,  $\delta = 2$  ms; (d)  $\theta = -30^\circ$ ,  $\delta = 4$  ms; (e)  $\theta = -30^\circ$ ,  $\delta = 8$  ms; (f)  $\theta = 10^\circ$ ,  $\delta = 4$  ms.

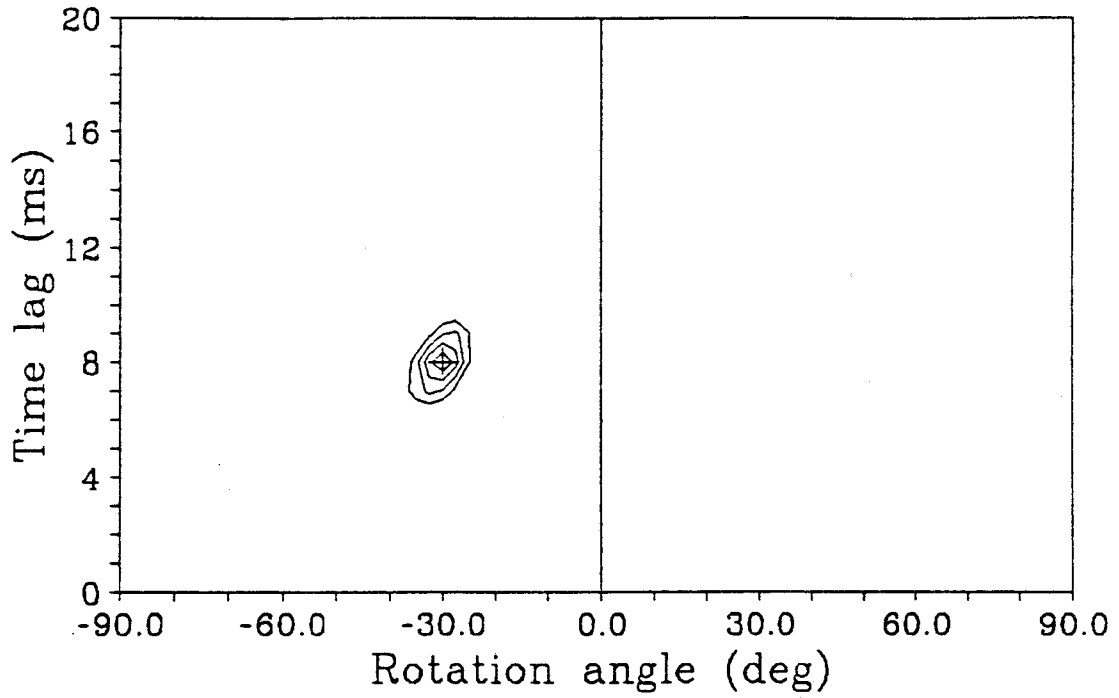


(c)

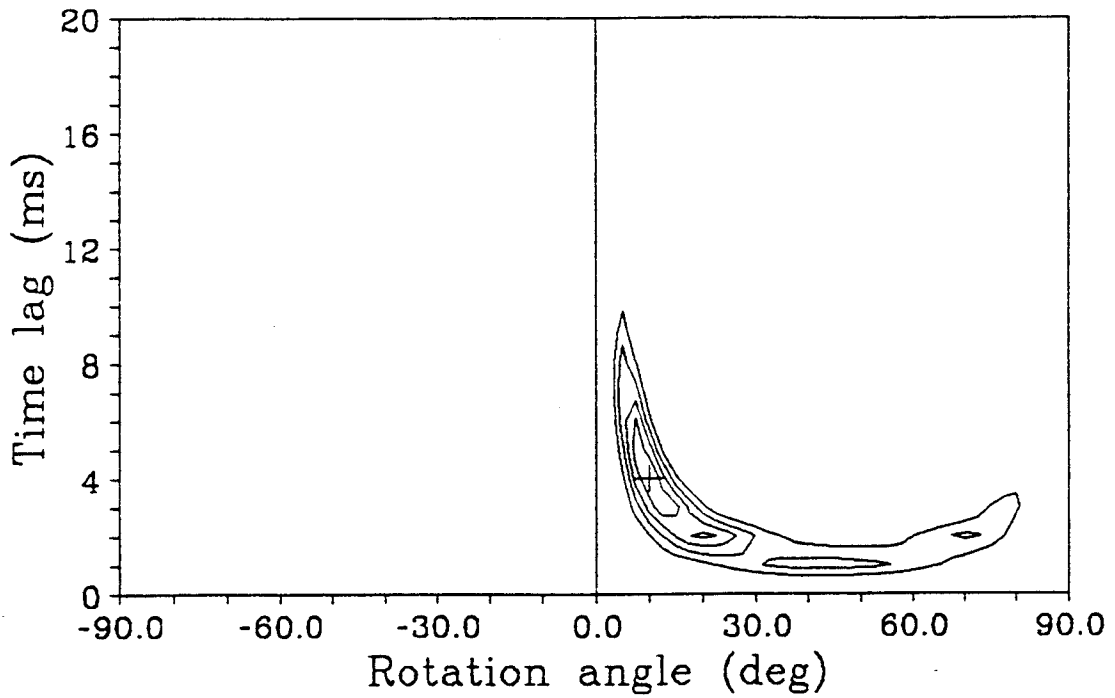


(d)

FIG. 3.6.  $\theta$ - $\delta$  analysis described in Section 3.3.2 applied to noise-free synthetic data: (a)  $\theta = -30^\circ$ ,  $\delta = 0$  ms; (b)  $\theta = -30^\circ$ ,  $\delta = 1$  ms; (c)  $\theta = -30^\circ$ ,  $\delta = 2$  ms; (d)  $\theta = -30^\circ$ ,  $\delta = 4$  ms; (e)  $\theta = -30^\circ$ ,  $\delta = 8$  ms; (f)  $\theta = 10^\circ$ ,  $\delta = 4$  ms.



(e)



(f)

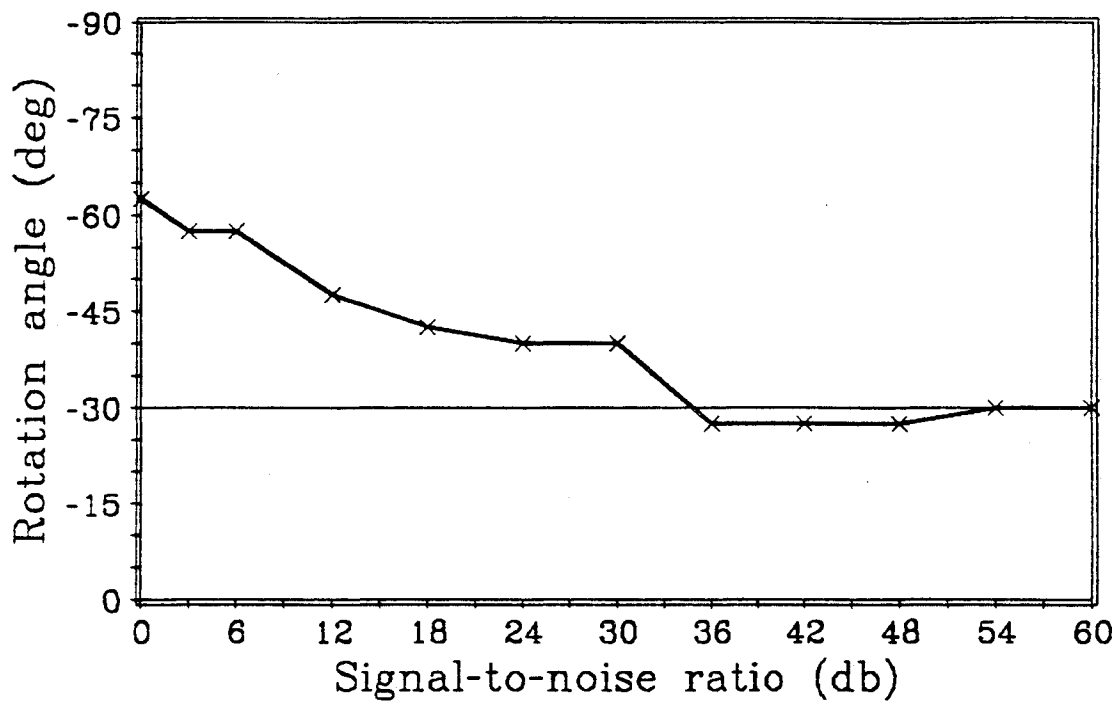
FIG. 3.6.  $\theta$ - $\delta$  analysis described in Section 3.3.2 applied to noise-free synthetic data: (a)  $\theta=-30^\circ$ ,  $\delta=0$  ms; (b)  $\theta=-30^\circ$ ,  $\delta=1$  ms; (c)  $\theta=-30^\circ$ ,  $\delta=2$  ms; (d)  $\theta=-30^\circ$ ,  $\delta=4$  ms; (e)  $\theta=-30^\circ$ ,  $\delta=8$  ms; (f)  $\theta=10^\circ$ ,  $\delta=4$  ms.

where  $C$  is the signal autocorrelation [equation (3.10)] and  $N$  is the noise autocorrelation. A 500 ms reflectivity sequence was generated by bandpass-filtering a random-number sequence. The noise in each test case was also generated using a random-number generator; each noise sequence was bandpass-filtered to the signal bandwidth and scaled to the appropriate amplitude. The errors in angle  $\theta$  and delay  $\delta$  as a function of signal-to-noise ratio for  $\theta=-30^\circ$  and  $\delta=4$  ms are shown in Figure 3.7. An  $SNR$  of 36 db is needed to accurately determine both the time-delay and the natural-coordinate-system angle.

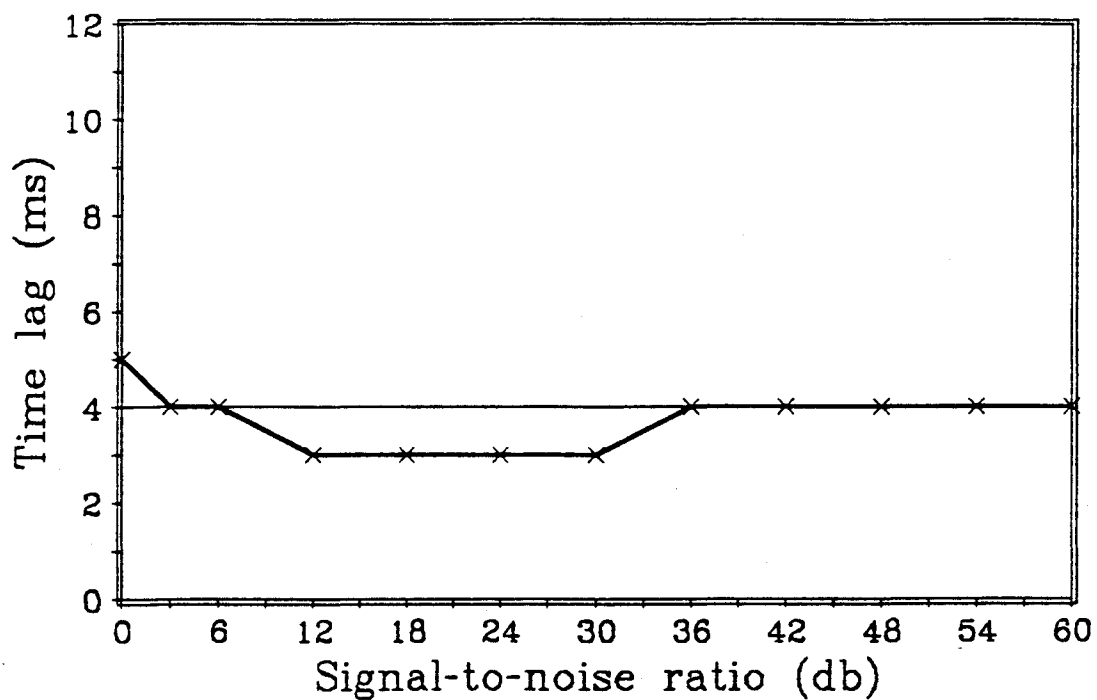
A second group of tests was run in order to assess the effect of fold on the analysis. A number of synthetic data sets were generated, all having a signal-to-noise power ratio of 0 db; this probably represents an  $SNR$  level at the lower limit of what is usually found on converted-wave field records. The autocorrelations and crosscorrelations were computed from each data set and stacked to give a single result. The analysis was then performed on these stacked values. The errors in angle and delay time as a function of stack fold for  $\theta=-30^\circ$  and  $\delta=4$  ms are shown in Figure 3.8. An approximate fold of 60 is needed to achieve a time-delay within  $\pm 1$  ms of the correct value, while a fold of about 40 gives the natural-coordinate-system angle to within  $\pm 5^\circ$ . These fold limits would usually be achieved by averaging the analysis across a single record.

### 3.4.2 Analysis of data from Carrot Creek, Alberta

Two three-component lines were acquired by Polyseis Research Inc. in the Carrot Creek area of Alberta using the acquisition parameters listed in Table 6.1. The location map (Figure 6.1) shows that the two lines are oriented at azimuths that differ by approximately  $9^\circ$ . Sample radial- and transverse-component records for line CC-SW-01 are displayed in Figures 6.3 and 6.4; a sample record for line CC-SW-02 is shown in Figure 3.9. It is seen from these displays that the transverse records for line CC-SW-01 have very little recognizable shear-wave signal, while those of line CC-SW-02 do have

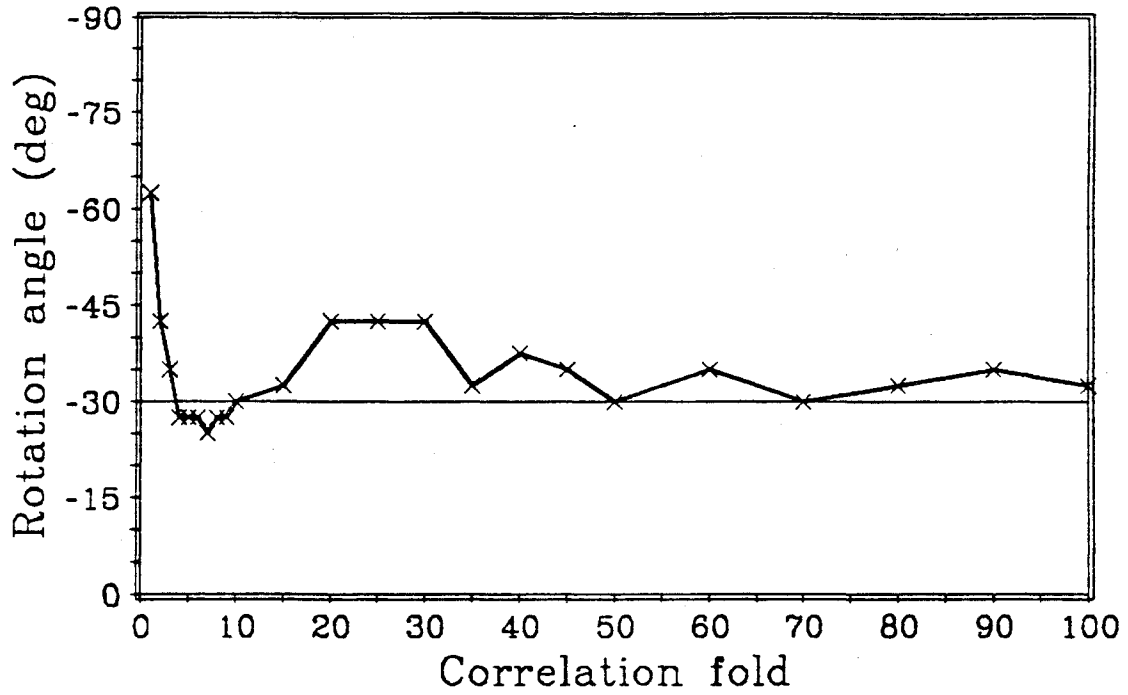


(a)

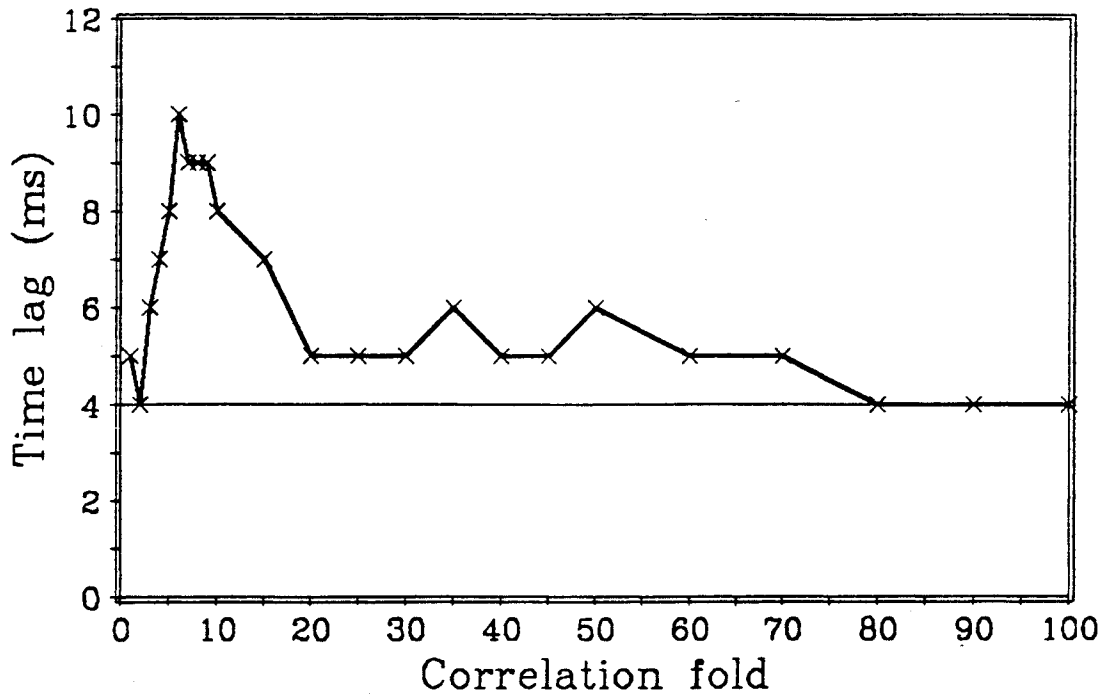


(b)

FIG. 3.7. Values of (a) the angle  $\theta$  and (b) the delay time  $\delta$  obtained by  $\theta$ - $\delta$  analysis vs. signal-to-noise power ratio ( $SNR$ ) for  $\theta = -30^\circ$  and  $\delta = 4$  ms.



(a)



(b)

FIG. 3.8. Values of (a) the angle  $\theta$  and (b) the delay time  $\delta$  obtained by  $\theta$ - $\delta$  analysis vs. correlation fold for  $\theta = -30^\circ$ ,  $\delta = 4$  ms, and  $SNR = 0$  db.

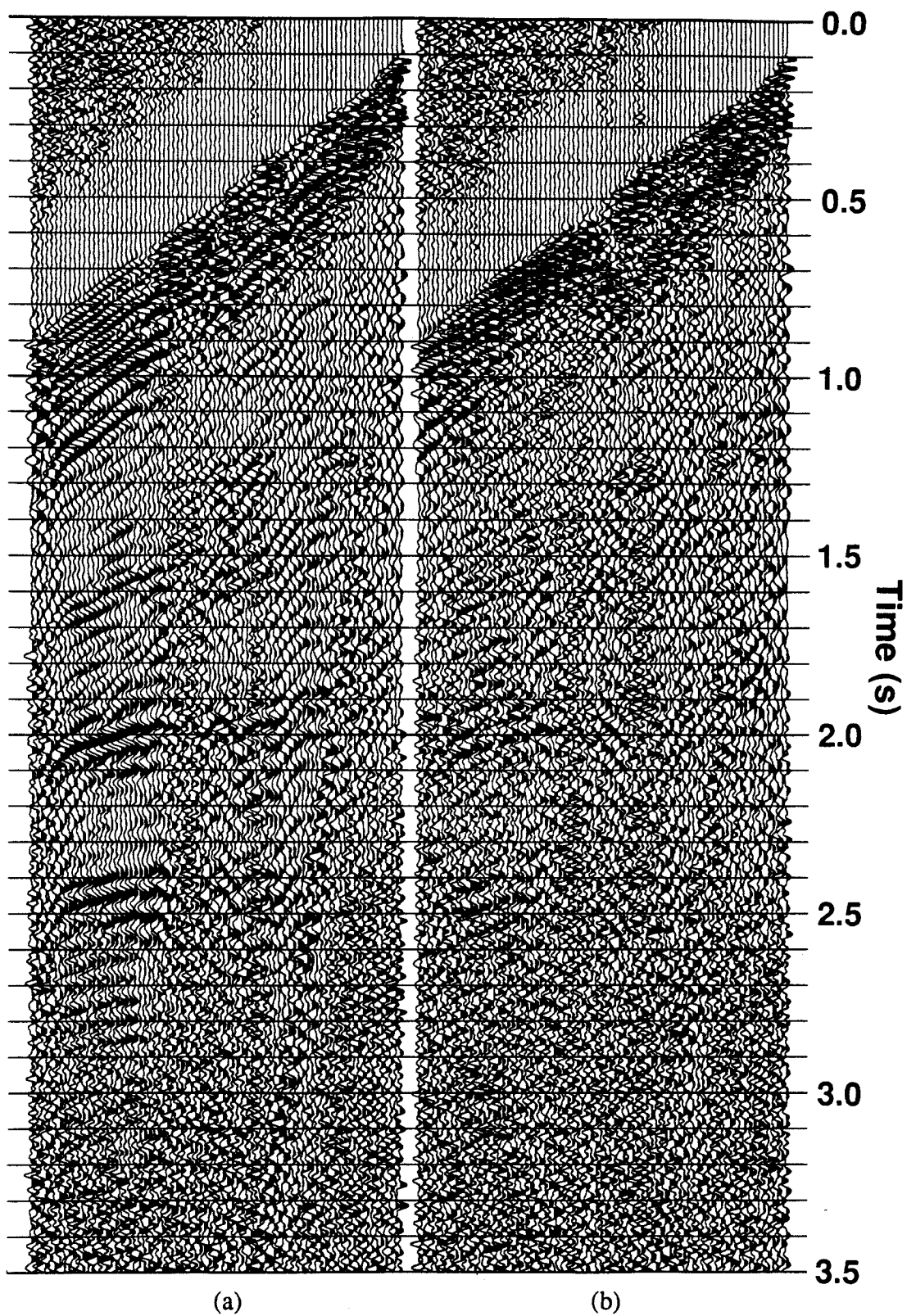


FIG. 3.9. Horizontal-component records for VP 107 of line CC-SW-02: (a) radial; (b) transverse. A 50/60 Hz highcut filter and 800 ms AGC have been applied.

weak events that correlate to reflections on the radial record. This indicates that some amount of birefringence is present in the area, and that line CC-SW-01 lies along a principal axis of the natural coordinate system.

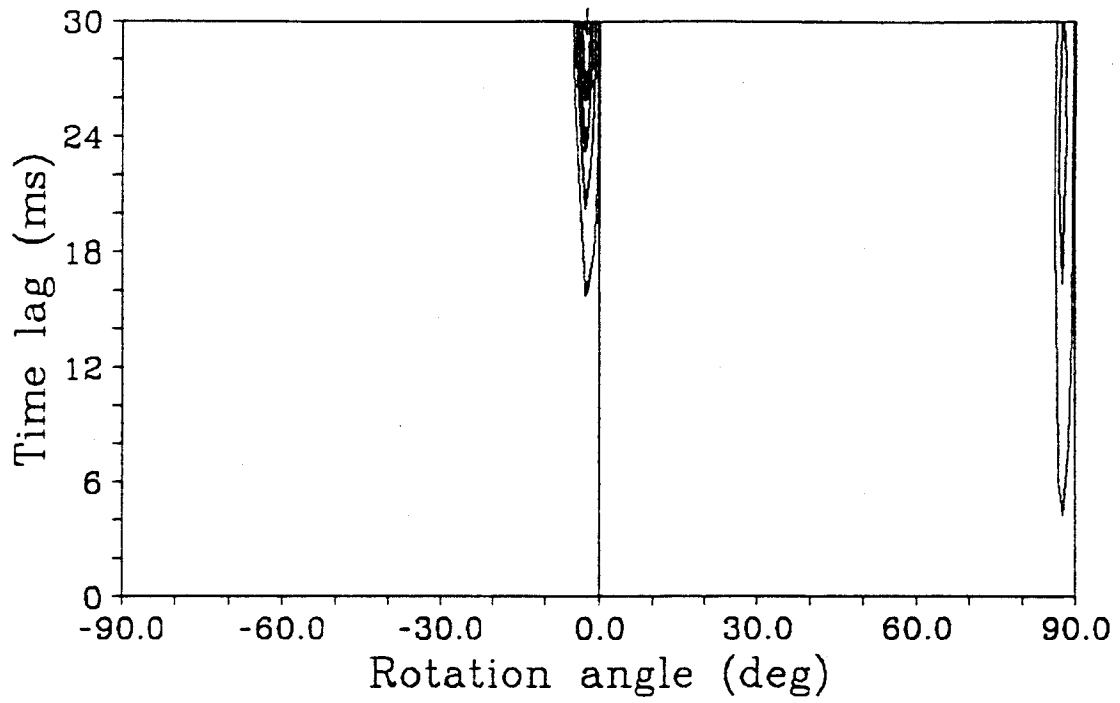
A  $\theta$ - $\delta$  analysis averaged over five 80-trace field records was run on each of the two lines (Figure 3.10). The analysis window was offset-limited to 850-2550 m and time-limited to include the stronger events falling within 1800-2600 ms. The crosscorrelation fold obtained for both cases was about 180. The result for line CC-SW-01 (Figure 3.10a) indicates that either no *S*-wave splitting occurs in the area, or that the line falls on a principal axis. The analysis for line CC-SW-02 (Figure 3.10b) has a peak at  $\theta \approx 11^\circ$  and  $\delta \approx 8$  ms. The angle indicated by the rotation analysis is consistent with the difference in the azimuths of the two lines. It should be noted that the acquisition polarity of the radial and transverse components was assumed to be correct. A relative reversal of the polarity between the two components would change the sign of the natural-coordinate-system angle, giving a result that is inconsistent between the two lines.

### 3.5 Discussion

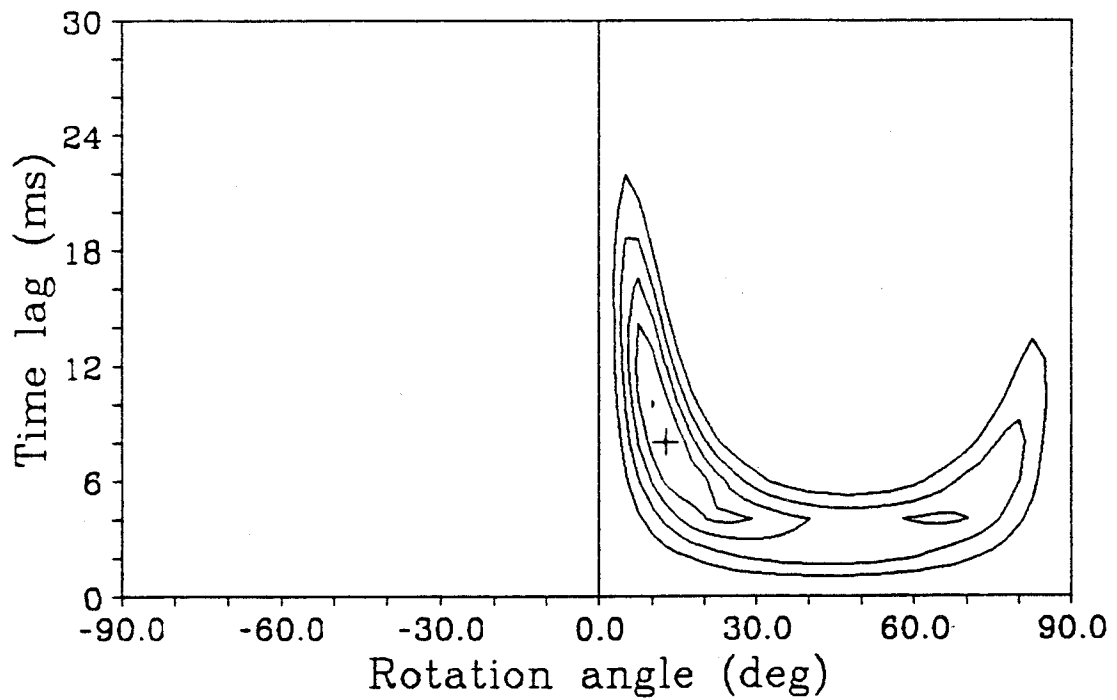
The birefringence analysis methods presented here have the following main advantages over other rotation analysis algorithms.

- 1) Because only crosscorrelations are used, they are robust in the presence of noise, and do not require that only a single event fall within the analysis time window. They are therefore more appropriate for converted-wave data than hodogram analysis.

- 2) They can be applied prestack, before any static analysis has been done. Because the correlations used are between rotated radial and transverse components of the same receiver, any static delay for that receiver will probably be common to both shear components. This makes the analysis largely independent of any static problems present in the data.



(a)



(b)

FIG. 3.10.  $\theta$ - $\delta$  analysis applied to Carrot Creek data: (a) CC-SW-01; (b) CC-SW-02.

3) They can be performed on two-component data, as opposed to Alford rotation which requires four-component data.

A potential problem with the methods shown here is that it is assumed that the autocorrelation of the input traces is equal to the autocorrelation of the shear signal. In noisy data where the bandwidth of the noise is greater than that of the signal, this is obviously not true.

One possible solution is to use the averaged crosscorrelations between radial and transverse traces from adjacent receivers, rather than autocorrelations from the same receiver, to estimate  $C$ . The result would better represent the autocorrelation of the signal, as opposed to the signal and noise. This has the disadvantage of making the analyses sensitive to uncorrected static variations between adjacent receivers.

A second way to reduce the problem is to prefilter the input data to a bandwidth roughly equal to that of the signal. The autocorrelation of the filtered data is then more likely to be a scaled version of the autocorrelation of the shear signal. This approach was used in performing birefringence analysis on the Carrot Creek field data.

Finally, birefringence analysis could be performed after stack, using traces with a higher signal-to-noise ratio. Great care must be taken in processing the data in order to maintain the same scaling between radial- and transverse-component stack sections. Also, because prestack deconvolution could potentially affect the rotation analysis, the data would initially have to be stacked without deconvolution. This necessitates the rerunning of much of the processing flow on the data after rotation, and makes poststack analysis less attractive.

A problem with any two-component birefringence analysis method is that no estimate can be obtained if the converted-wave line falls along a principal axis of the natural coordinate system. Four-component analysis techniques, such as Alford rotation, do not have this problem.

## Chapter 4 - Dip moveout for *P-SV* data

### 4.1 Introduction

The difficulties introduced by recording data over dipping reflectors have been known for some time for the conventional (*P-P*) case. Levin (1971) derived equations that show how the reflection point for data from a single dipping interface is displaced away from the midpoint. This displacement produces a dispersal, or smearing, of the data within a common-midpoint gather. The dispersal changes with offset and reflector dip, and gives rise to an increase in the apparent normal-moveout (NMO) velocity needed to flatten a dipping event. This apparent velocity for a single dipping layer is given by (Dix, 1955; Levin, 1971)

$$V_{app} = \frac{V}{\cos \theta}, \quad (4.1)$$

where  $V_{app}$  is the apparent velocity,  $V$  is the true medium velocity and  $\theta$  is the reflector dip. If data with more than one dip are present at any two-way time and common-midpoint location, then only one dip can be optimally stacked. The apparent stacking velocities do not give correct estimates of the sub-surface interval velocities, and are inappropriate for migrating the data. The movement of the reflection point away from the midpoint with increasing dip and offset causes the dipping data to be attenuated by the stacking process (Judson et al., 1978). Poststack migration, which assumes zero-offset data, will not properly image any dipping, non-zero-offset data that survives stacking, as these data are displaced away from the true zero-offset position.

Dip moveout (DMO) attempts to overcome these problems by removing from a data set any non-zero offset effects, thereby roughly creating for any offset the equivalent zero-offset data. In this way prestack migration is approximated by a zero-offset mapping, carried out by the DMO process, that is followed by poststack zero-offset migration. The

idea of applying DMO to  $P$ - $P$  data was first introduced by Judson et al. (1978) using a wave-equation approach, and initially met with limited technical success. The method was clarified and extended by Yilmaz and Claerbout (1980) in the form of partial prestack migration, but again gave restricted results. Deregowski and Rocca (1981) derived the zero-offset mapping equation for the  $P$ - $P$  case using a geometric optics approach, and used it to generate time-domain "smear stack" impulse responses for the  $P$ - $P$  DMO operator. They were also able to generate asymptotic forms of the DMO operator in  $f$ - $k$  space. Bolandi et al. (1982) later derived a finite-difference method for applying the DMO process by "offset continuation." Hale (1984) devised a Fourier-transform algorithm, and showed it to be numerically accurate for all dip angles in a constant-velocity medium. Hale's method requires a transform that cannot be implemented using the FFT, and is not generally used. Other methods using integral-summation algorithms, in which impulse response functions are generated and summed (Deregowski, 1985), or log-stretch algorithms (Bale and Jakubowicz, 1987; Biondi and Ronen, 1987; Notfors and Godfrey, 1987) have been more computationally effective. Most DMO algorithms make use of the constant velocity DMO equation. Approximate solutions for the multiple layer case have been derived (Deregowski and Rocca, 1981; Hale, 1983; Deregowski, 1985), but are not in wide-spread use.

Sections 4.2 and 4.3 of this chapter are concerned with the behavior of  $P$ - $SV$  mode-converted data in areas of dip. Analytic expressions for the dispersal and apparent stacking slowness for the  $P$ - $SV$  case are derived. It is found that these differ from the  $P$ - $P$  case, meaning that conventional DMO is not appropriate for  $P$ - $SV$  data. In Section 4.4, an exact zero-offset mapping (DMO) equation is derived for the  $P$ - $SV$  case using two methods; a geometric optics approach similar to that of Deregowski and Rocca (1981), and a much simpler proof using Snell's Law. This equation is implemented using an integral-summation algorithm (Deregowski, 1985) to apply DMO to some synthetic data.

## 4.2 Conversion-point dispersal for $P$ - $SV$ data

Dispersal within a CMP gather for  $P$ - $P$  data is defined by Levin (1971) as the distance  $\Delta$  along a dipping reflector that the true reflection point moves away from the zero-offset reflection point. For the  $P$ - $P$  case, it can be shown (Levin, 1971) that this dispersal is given by

$$\Delta = \frac{h^2}{d} \cos \theta \sin \theta, \quad (4.2)$$

where

$2h$  = total source-to receiver offset.

$\theta$  = dip angle of the reflector.

$d$  = distance from the surface CMP location to the zero-offset reflection point on the dipping interface.

From equation (4.2), the magnitude of the dispersal within a CMP gather is seen to be symmetric about zero-dip; exchanging the positions of the source and receiver produces the same dispersal value.

Using similar definitions, it is possible to set up the problem for  $P$ - $SV$  data. The goal here is to derive from basic geometry an expression for  $\Delta$  for the converted-wave case. Figure 4.1 shows  $P$ -wave energy being mode-converted by a dipping reflector and recorded by a multicomponent receiver. The velocity along the path  $\overline{SC}$  is  $\alpha$ , and the velocity along the path  $\overline{CR}$  is  $\beta$ . The  $P$ - $SV$  dispersal is here defined as the movement  $\Delta$  within a CCP gather away from the zero-offset conversion point in the source direction. From Figure 4.1, it can be seen that this dispersal is given by

$$\Delta = \delta \cos \theta, \quad (4.3)$$

where  $\delta$  is the horizontal surface displacement away from the CCP position in the source direction. The following relations can be obtained from simple geometry;

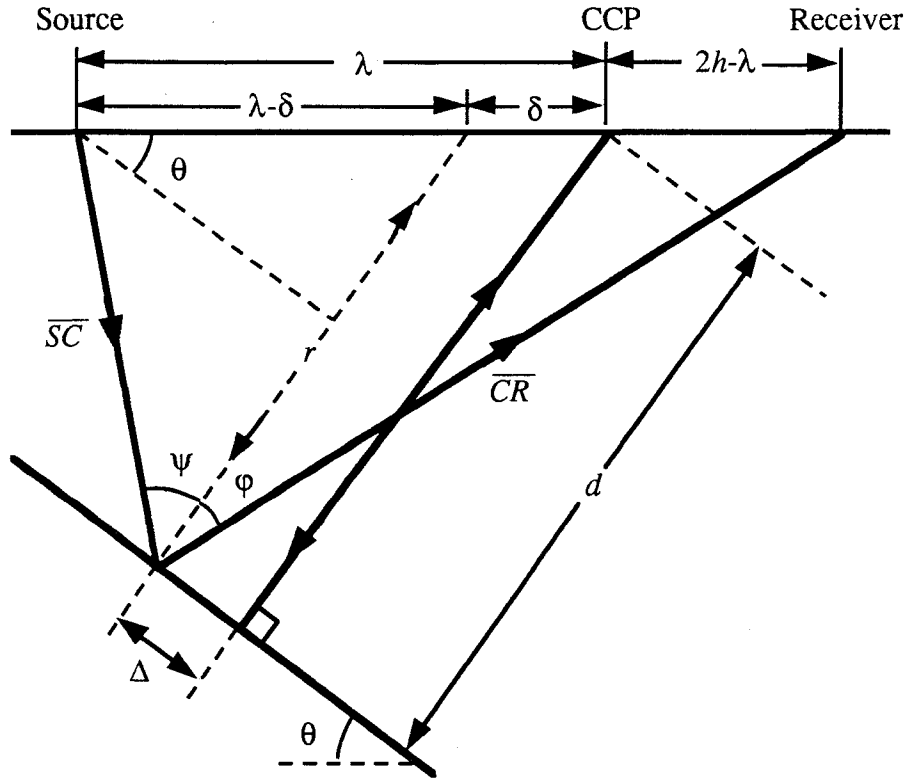


FIG. 4.1. Raypath geometry for conversion from a dipping reflector.

$$\overline{SC} = \sqrt{(d - \lambda \sin \theta)^2 + (\lambda - \delta)^2 \cos^2 \theta} , \quad (4.4)$$

$$\overline{CR} = \sqrt{[d + (2h - \lambda) \sin \theta]^2 + [2h - (\lambda - \delta)]^2 \cos^2 \theta} , \quad (4.5)$$

and

$$\tan \phi = \frac{[2h - (\lambda - \delta)] \cos \theta}{d + (2h - \lambda) \sin \theta} ,$$

which can be rearranged to give

$$(\lambda - \delta) = 2h - \frac{d + (2h - \lambda) \sin \theta}{\cos \theta} \tan \phi . \quad (4.6)$$

From Snell's Law, the ray parameter must be constant for both the incident and reflected rays at the conversion point, giving

$$\frac{\sin \psi}{\alpha} = \frac{\sin \phi}{\beta}$$

or

$$\tan \phi = \frac{\sin \psi}{\sqrt{\gamma^2 - \sin^2 \psi}}, \quad \gamma = \frac{\alpha}{\beta}. \quad (4.7)$$

It can be seen from Figure 4.1 that

$$\begin{aligned} \sin \psi &= \frac{(\lambda - \delta) \cos \theta}{\overline{SC}} \\ &= \frac{(\lambda - \delta) \cos \theta}{\sqrt{(d - \lambda \sin \theta)^2 + (\lambda - \delta)^2 \cos^2 \theta}}, \end{aligned} \quad (4.8)$$

using equation (4.4). Substituting this result into equation (4.7) gives

$$\tan \phi = \frac{(\lambda - \delta) \cos \theta}{\sqrt{\gamma^2 (d - \lambda \sin \theta)^2 + (\gamma^2 - 1)(\lambda - \delta)^2 \cos^2 \theta}}, \quad (4.9)$$

and, using equation (4.9), equation (4.6) becomes

$$(\lambda - \delta) = 2h - \frac{(\lambda - \delta) [d + (2h - \lambda) \sin \theta]}{\sqrt{\gamma^2 (d - \lambda \sin \theta)^2 + (\gamma^2 - 1)(\lambda - \delta)^2 \cos^2 \theta}}. \quad (4.10)$$

Rationalizing equation (4.10) and collecting terms gives the following quartic equation for  $(\lambda - \delta)$ ;

$$\begin{aligned} &(\gamma^2 - 1)[(\lambda - \delta) - 4h] \cos^2 \theta (\lambda - \delta)^3 \\ &+ \left\{ \gamma^2 (d - \lambda \sin \theta)^2 + (\gamma^2 - 1)4h^2 \cos^2 \theta - [d + (2h - \lambda) \sin \theta]^2 \right\} (\lambda - \delta)^2 \\ &- 4h\gamma^2 (d - \lambda \sin \theta)^2 (\lambda - \delta) + 4h^2 \gamma^2 (d - \lambda \sin \theta)^2 = 0. \end{aligned} \quad (4.11)$$

For small offset-to-depth ratios, where  $h \ll d$ , an approximate solution for the dispersal can be obtained. For this case,  $\delta$  is given by

$$\delta \cong \frac{4h^2\gamma \sin \theta}{d(\gamma+1)^2} \left[ 1 + \frac{2h(\gamma-1)}{d(\gamma+1)} \sin \theta \right], \quad h \ll d. \quad (4.12)$$

Using equation (4.3), the dispersal becomes

$$\Delta_{p-sv} \cong \left( \frac{h^2}{d} \sin \theta \cos \theta \right) \frac{4\gamma}{(\gamma+1)^2} \left[ 1 + \frac{2h(\gamma-1)}{d(\gamma+1)} \sin \theta \right],$$

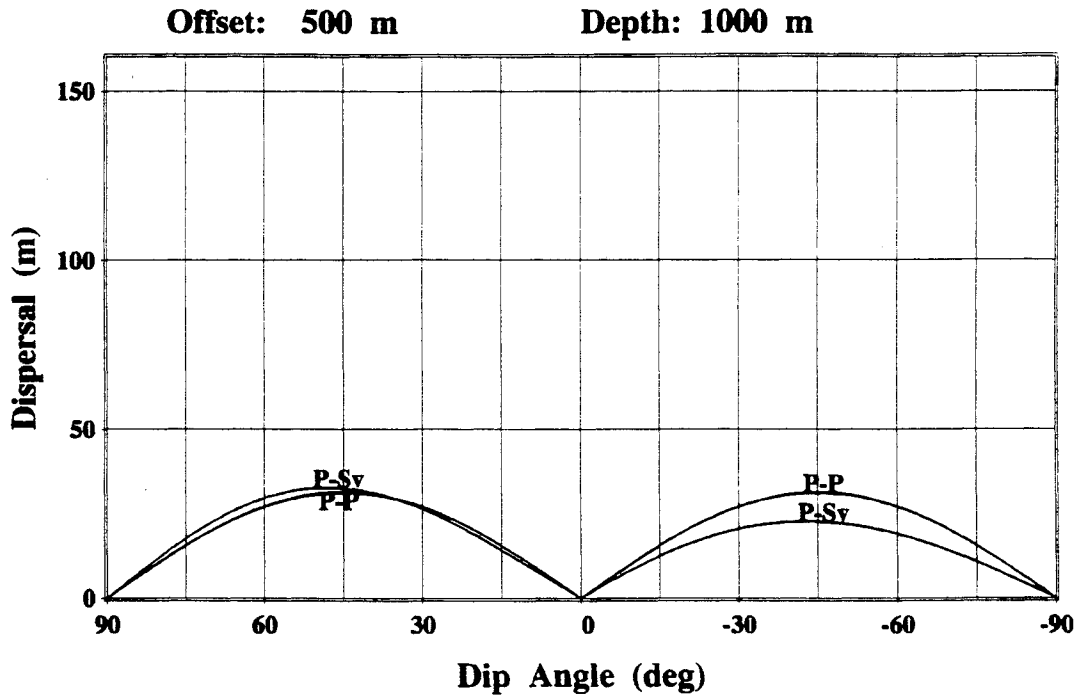
or

$$\frac{\Delta_{p-sv}}{\Delta_{p-p}} \cong \frac{4\gamma}{(\gamma+1)^2} \left[ 1 + \frac{2h(\gamma-1)}{d(\gamma+1)} \sin \theta \right], \quad (4.13)$$

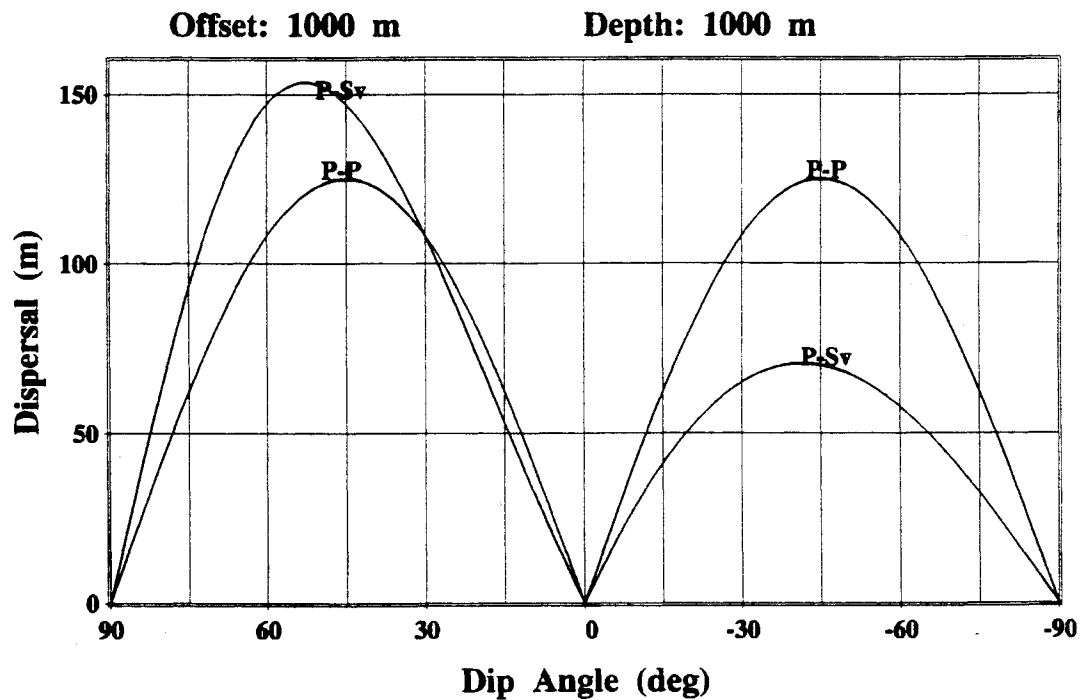
where  $\Delta_{p-p}$  is the  $P$ - $P$  dispersal of equation (4.2). Equation (4.13) shows that the  $P$ - $SV$  dispersal depends upon the sign of the dip angle through the  $\sin \theta$  term, and is therefore asymmetric about zero dip. For positive dips (down-dip conversion), the dispersal is generally larger than the  $P$ - $P$  dispersal, and for negative dips (up-dip conversion) it is smaller.

Exact values for  $P$ - $SV$  dispersal were computed by first calculating the location of the zero-dip conversion point,  $\lambda$ , using the equation given by Tessmer and Behle (1988). For each reflector dip angle, equation (4.11) was then solved to give  $\delta$ , from which the dispersal was computed using equation (4.3). Although the desired root to equation (4.11) can be found analytically, solutions were obtained using numerical methods. The results of performing these calculations for two different offset-to-depth ratios, with dip angles ranging between  $\pm 90^\circ$ , are shown in Figure 4.2. For comparison, the  $P$ - $P$  dispersal values computed using equation (4.2) are also plotted in the figure. A compressional velocity of 3000 m/s and a shear velocity of 1500 m/s were used in all computations.

As expected from equation (4.13), Figure 4.2 shows that data generated by mode conversion in the positive-dip (down-dip) direction has larger CCP dispersal than CMP



(a)



(b)

FIG. 4.2. *P-P* and *P-SV* dispersal curves for a reflector zero-offset depth of 1 km and source-to-receiver offsets of (a) 0.5 km and (b) 1.0 km.

dispersal, whereas data generated in the negative-dip (up-dip) direction has smaller CCP dispersal. Exchanging the source and receiver positions changes the sign of the dip angle, giving different dispersal values. Because any DMO operation that is applied to the converted data must correct for this CCP dispersal, the DMO operator must itself be asymmetric. This indicates that conventional  $P$ - $P$  DMO is not appropriate for  $P$ - $SV$  mode-converted data. Also, because of the expected asymmetry in the DMO operator, it is necessary to know the relative positions of the source and receiver by using signed, rather than absolute, offset information.

### 4.3 Apparent slowness for $P$ - $SV$ data

From Figure 4.1, the total source-to-receiver traveltimes is seen to be the sum of the time to travel from the source to the conversion point along the path  $\overline{SC}$  at velocity  $\alpha$ , and the time to travel from the conversion point back to the receiver along the path  $\overline{CR}$  at velocity  $\beta$ , or

$$t = \frac{\overline{SC}}{\alpha} + \frac{\overline{CR}}{\beta}. \quad (4.14)$$

Using equations (4.4) and (4.5), this becomes

$$t = \frac{\sqrt{(d - \lambda \sin \theta)^2 + (\lambda - \delta)^2 \cos^2 \theta}}{\alpha} + \frac{\sqrt{[d + (2h - \lambda) \sin \theta]^2 + [2h - (\lambda - \delta)]^2 \cos^2 \theta}}{\beta}. \quad (4.15)$$

Equation (4.15) can be simplified to

$$t^2 = \frac{2h}{(\alpha + \beta)^2} \left\{ \frac{\alpha^2}{(\lambda - \delta)} + \frac{\beta^2}{[2h - (\lambda - \delta)]} \right\} \left\{ \left[ t_0 - \left( \frac{\alpha + \beta}{\alpha \beta} \right) \delta \sin \theta \right]^2 + \left( \frac{\alpha + \beta}{\alpha \beta} \right)^2 (\lambda - \delta) [2h - (\lambda - \delta)] \right\} \quad (4.16)$$

where  $t_0$  is the zero-offset  $P$ - $SV$  traveltimes beneath the CCP location. For the zero-dip case, where  $\delta = 0$ , equation (4.16) reduces to

$$t^2 = \frac{2h}{(\alpha+\beta)^2} \left[ \frac{\alpha^2}{\lambda} + \frac{\beta^2}{(2h-\lambda)} \right] \left[ t_0^2 + \left( \frac{\alpha+\beta}{\alpha\beta} \right)^2 \lambda(2h-\lambda) \right]. \quad (4.17)$$

Even for zero-dip, equation (4.17) shows that it is not possible to obtain an exact general expression in the form of the standard NMO equation. For short offsets, however, the asymptotic approximation (Fromm et. al., 1985) can be used, i.e.,

$$\lambda \cong \frac{2\alpha h}{\alpha+\beta}.$$

Equation (4.17) then reduces to

$$t^2 \cong t_0^2 + \frac{4h^2}{\alpha\beta}. \quad (4.18)$$

Equation (4.18) is the same approximation obtained by Fromm et. al. (1985).

In order to assess the effect of reflector dip on stacking velocity, an expression for the apparent slowness can be obtained by rearranging the conventional NMO equation. In terms of slowness  $s$ , the NMO equation becomes

$$t^2 = t_0^2 + 4h^2s^2, \quad (4.19)$$

This can be rearranged to give the following expression for the apparent slowness;

$$s = \frac{\sqrt{t^2 - t_0^2}}{2h}. \quad (4.20)$$

Using equation (4.11) to compute  $\delta$  and equation (4.15) to compute  $t$ , the apparent slowness can be calculated for any dip angle by equation (4.20). The result indicates how the stacking velocity, which is the reciprocal of slowness, changes with reflector dip angle. Apparent slowness calculations for the same offset-to-depth ratios used in Figure 4.2 are

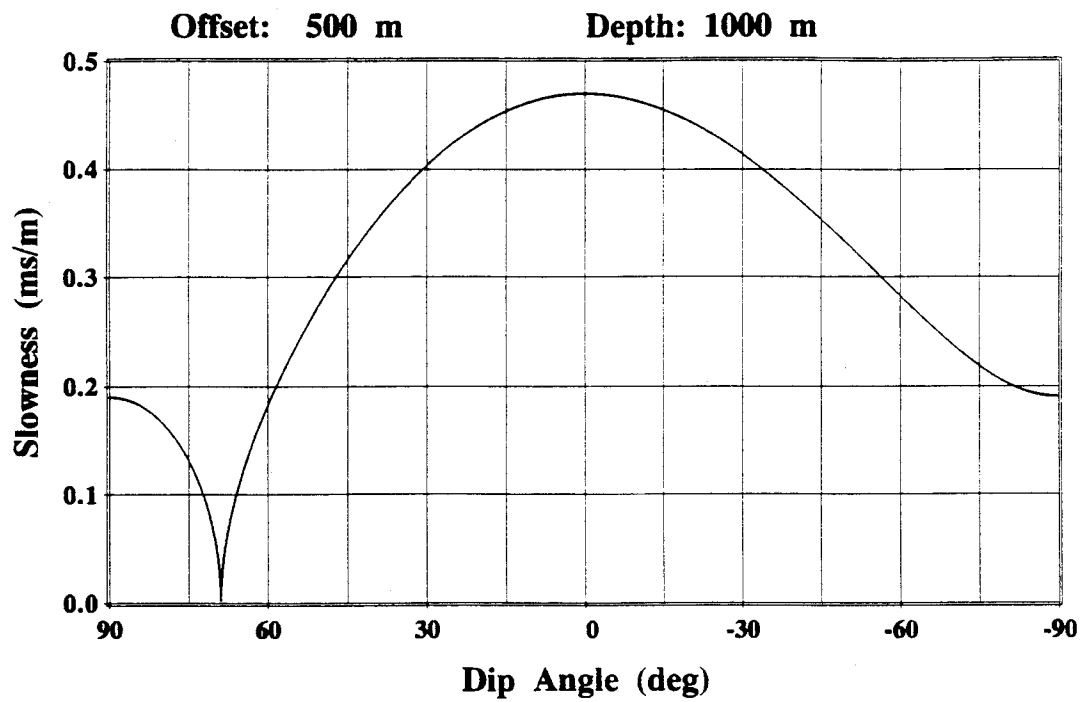
shown in Figure 4.3. From this figure, it is seen that the apparent slowness (velocity) curves for  $P$ - $SV$  data are asymmetric about zero dip. This is in contrast to the  $P$ - $P$  case, where the apparent slowness is seen from equation (4.1) to be a cosine curve, symmetric about zero dip. Also, for part of the slowness curve in the range of about  $64^\circ$  to  $90^\circ$ , the slowness becomes imaginary. This means that the total traveltime  $t$  in equation (4.20) is less than the zero-offset traveltime  $t_0$ ; something that does not happen for  $P$ - $P$  data. Events converted by a reflector with dip in this range will appear to be over-corrected within a CCP gather even before any NMO correction has been applied.

Data acquired using split spreads would see a dipping interface as having positive dip on one side of the spread, and negative dip on the other. A CCP gather containing both sides of the spread would therefore require two different apparent NMO velocities for the event, because of the asymmetry seen in Figure 4.3. Even for a single event, this suggests that it may not be possible to properly NMO-correct the gather with a single apparent stacking velocity. This, in turn, would create within a common-offset display an apparent splitting of the event into two separate events at larger offsets.

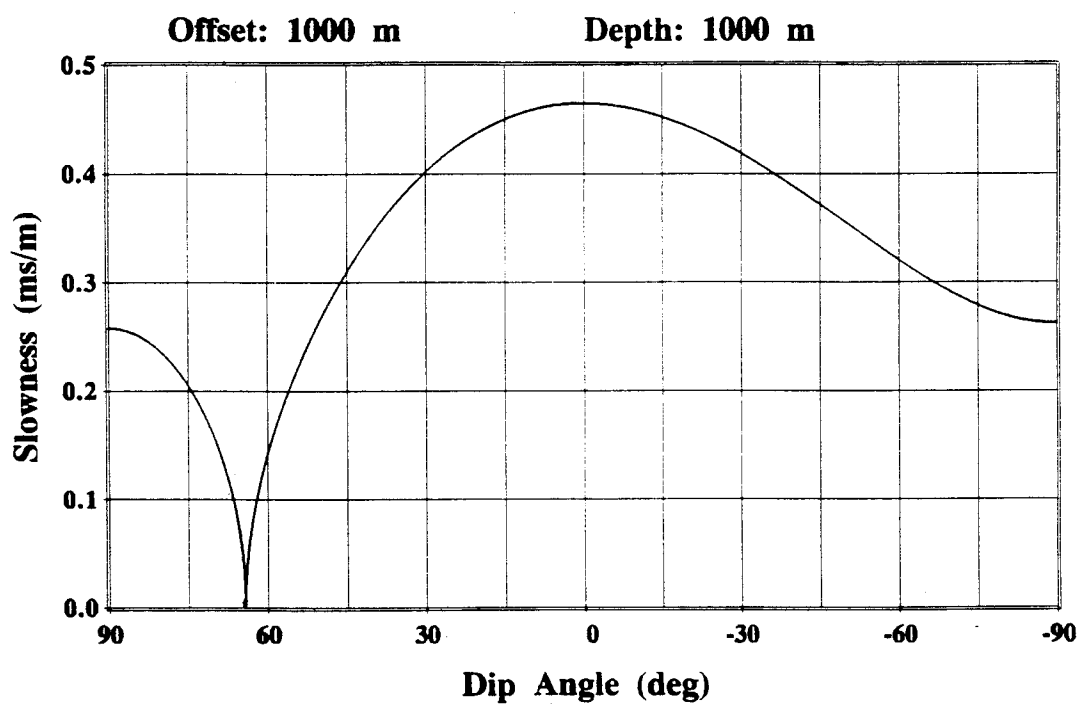
#### 4.4 $P$ - $SV$ zero-offset mapping

Two approaches to deriving the  $P$ - $SV$  zero-offset mapping (DMO) equation are presented in this section. The first method (Section 4.4.1) follows that used by Deregowski and Rocca (1981) for the  $P$ - $P$  case, in which a kinematic zero-offset-response mapping of prestack migration curves is carried out. In Section 4.4.2, the raypaths for mode-conversion from a dipping reflector are examined. The use of Snell's Law and simple geometry allow a much simpler derivation of the  $P$ - $SV$  DMO equation.

A discussion of the zero-offset mapping equation derived in Sections 4.4.1 and 4.4.2 is given in Section 4.4.3.



(a)



(b)

FIG. 4.3. Apparent *P-SV* slowness curves for a reflector zero-offset depth of 1 km and source-to-receiver offsets of (a) 0.5 km and (b) 1.0 km.

#### 4.4.1 Derivation using geometric optics

The first step in deriving the zero-offset mapping equation is to determine the locus of points from which any datum sample recorded at time  $t$  could have originated. Figure 4.4 shows the geometry being considered, in which the origin of the coordinate system is now shifted to the midpoint location. The datum sample is assumed to have been converted at the point  $C$ , which is at depth  $z$  and horizontal distance  $x$  away from the midpoint. From the figure, it is seen that the total traveltimes  $t$  must again be the sum of the traveltimes along the paths  $\overline{SC}$  and  $\overline{CR}$ ;

$$t = \frac{\overline{SC}}{\alpha} + \frac{\overline{CR}}{\beta},$$

or

$$t = \frac{\sqrt{(h+x)^2+z^2}}{\alpha} + \frac{\sqrt{(h-x)^2+z^2}}{\beta} \quad (4.21)$$

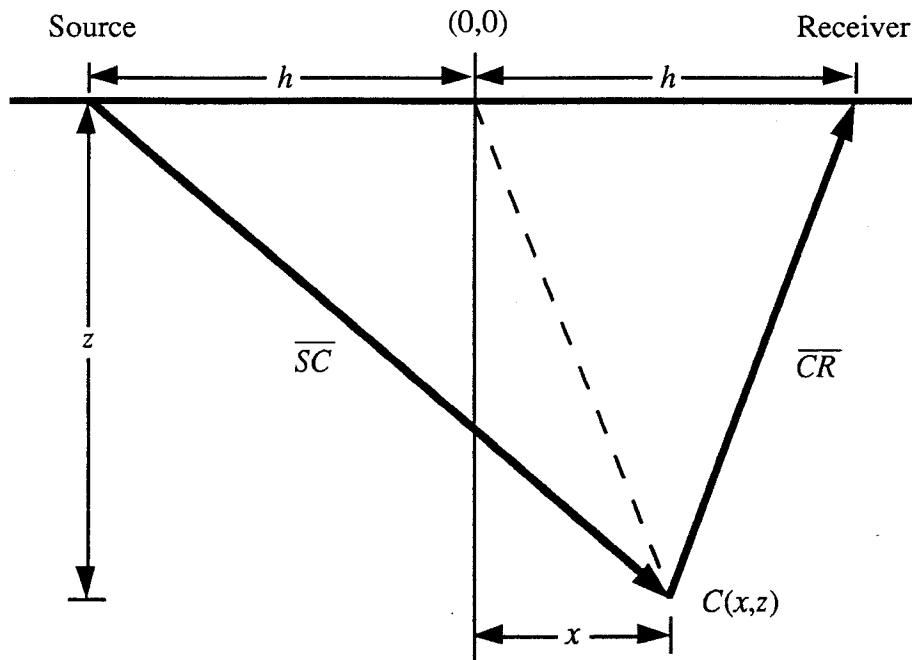


FIG. 4.4. Raypath geometry for computing the locus of points from which a datum sample could have originated.

in the new coordinate system. Rationalization and simplification of equation (4.21) gives

$$\begin{aligned} & \left(\frac{\alpha^2-\beta^2}{\alpha\beta}\right)^2(z^2+x^2+h^2)^2 - 2\left(\frac{\alpha^2+\beta^2}{\alpha\beta}\right)\left[\alpha\beta t^2+2h\left(\frac{\alpha^2-\beta^2}{\alpha\beta}\right)x\right](z^2+x^2+h^2) \\ & + \left[\alpha\beta t^2+2h\left(\frac{\alpha^2-\beta^2}{\alpha\beta}\right)x\right]^2 + 16x^2h^2 = 0. \end{aligned} \quad (4.22)$$

For the  $P$ - $P$  case, where  $\alpha = \beta = V$ , equation (4.22) reduces to the equation of an ellipse;

$$\left(\frac{x}{a}\right)^2 + \left(\frac{z}{b}\right)^2 = 1 \quad (4.23)$$

with

$$a = \frac{Vt}{2} \quad \text{and} \quad b = \frac{V\sqrt{t^2-4h^2/V^2}}{2} = \frac{Vt_n}{2},$$

where  $t_n$  is the dip-independent NMO time (Hale, 1988). Converting from depth  $z$  to two-way vertical travelttime gives the well-known migration ellipse for  $P$ - $P$  data (e.g., Deregowski and Rocca, 1981).

For the  $P$ - $SV$  case, equation (4.22) is of the form

$$A\xi^2 - 2B(x)\xi + C(x) = 0,$$

which is quadratic in the term  $\xi = z^2+x^2+h^2$ . The positive root of the equation gives physically unrealistic solutions for  $z$ , and is discarded. The remaining root simplifies to

$$\begin{aligned} z^2 + x^2 + h^2 = \\ (\alpha^2-\beta^2)^{-2} \left\{ (\alpha^2+\beta^2) \left[ \alpha^2\beta^2 t^2 + 2h(\alpha^2-\beta^2)x \right] - 2\alpha^2\beta^2 t \sqrt{\alpha^2\beta^2 t^2 + 4h(\alpha^2-\beta^2)x} \right\}. \end{aligned} \quad (4.24)$$

This equation generates the depth migration locus for a datum point recorded at time  $t$  and half-offset  $h$ , at a distance  $x$  away from the midpoint. Converting from vertical depth  $z$  to two-way vertical time  $t_z$ , where

$$t_z = \frac{z}{\alpha} + \frac{z}{\beta} = \left( \frac{\alpha + \beta}{\alpha\beta} \right) z, \quad (4.25)$$

equation (4.24) becomes

$$t_z^2 = (\alpha\beta)^{-2} \left\{ \left[ \alpha^2\beta^2 t^2 + 2h(\alpha^2 - \beta^2)x \right] \left( \frac{\alpha^2 + \beta^2}{\alpha^2\beta^2} \right) - 2r\sqrt{\alpha^2\beta^2 t^2 + 4h(\alpha^2 - \beta^2)x} \right\} - (x^2 + h^2) \left( \frac{\alpha + \beta}{\alpha\beta} \right)^2. \quad (4.26)$$

Equation (4.26) generates the raypath time migration curve for the single layer case, and could be used to implement a simple diffraction-summation-type prestack migration for *P-SV* data.

A plot of several *P-P* migration ellipses, generated using equation (4.23), for a velocity of 3000 m/s and various two-way times is shown in Figure 4.5. The location of the zero-dip reflection point, which falls at the midpoint, is plotted in the figure. A plot of several *P-SV* migration curves for  $\alpha=3000$  m/s and  $\beta=1500$  m/s and various values of  $t$  is shown in Figure 4.6. The location of the zero-dip conversion point as a function of two-way time (Tessmer and Behle, 1988) is overlain on the figure, and passes through the zero-dip location on each of the migration curves. The *P-SV* migration curves are asymmetric, with a shift in the direction of the receiver, whereas the *P-P* curves were seen to be ellipses, evenly centered on the source-to-receiver midpoint.

At this point, the prestack migration curves can be computed analytically using equation (4.24). Next, it is necessary to construct the zero-offset response to these prestack migration curves. This is conceptually equivalent to treating each prestack migration curve as a buried reflector, across which a zero-offset survey is conducted. Zero-offset migration, when applied to this zero-offset response, should regenerate the original prestack migration curves. The operation that constructs this zero-offset response curve will be the DMO mapping function for *P-SV* data.

Figure 4.7 shows the geometry by which the zero-offset reflection response is generated. Normal-incidence reflection from any point  $(x,z)$  on the locus will be recorded

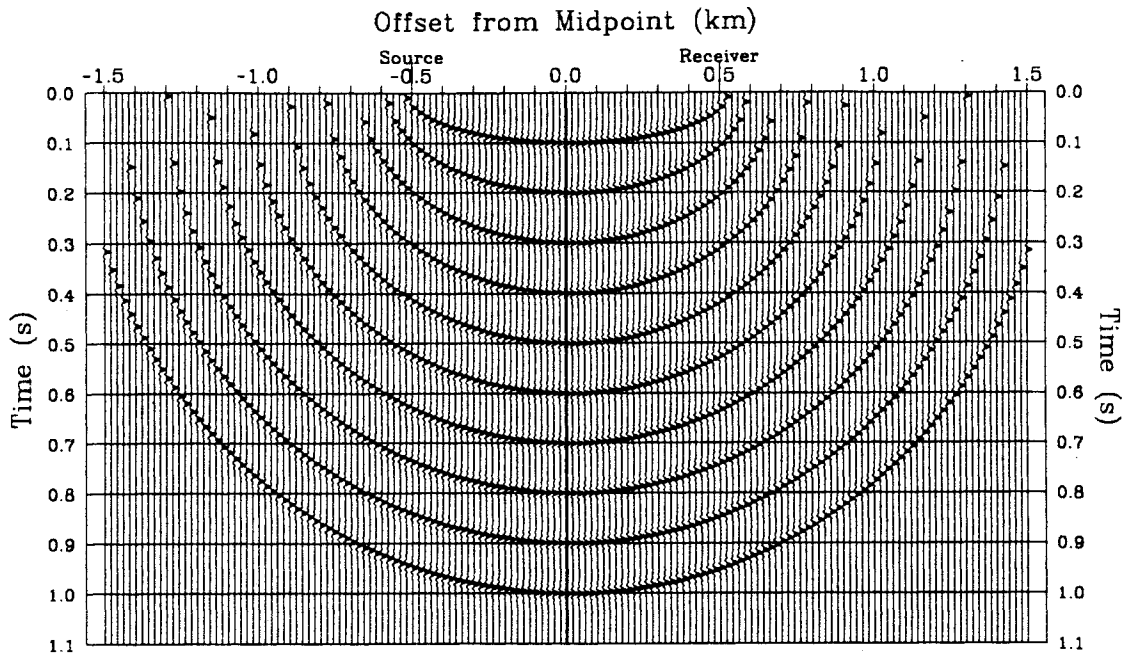


FIG. 4.5.  $P$ - $P$  migration ellipses for a source-to-receiver offset of 1 km and various two-way times. The curves were generated by placing a spike of constant amplitude at the appropriate time-offset position, then filtering with a bandpass operator.

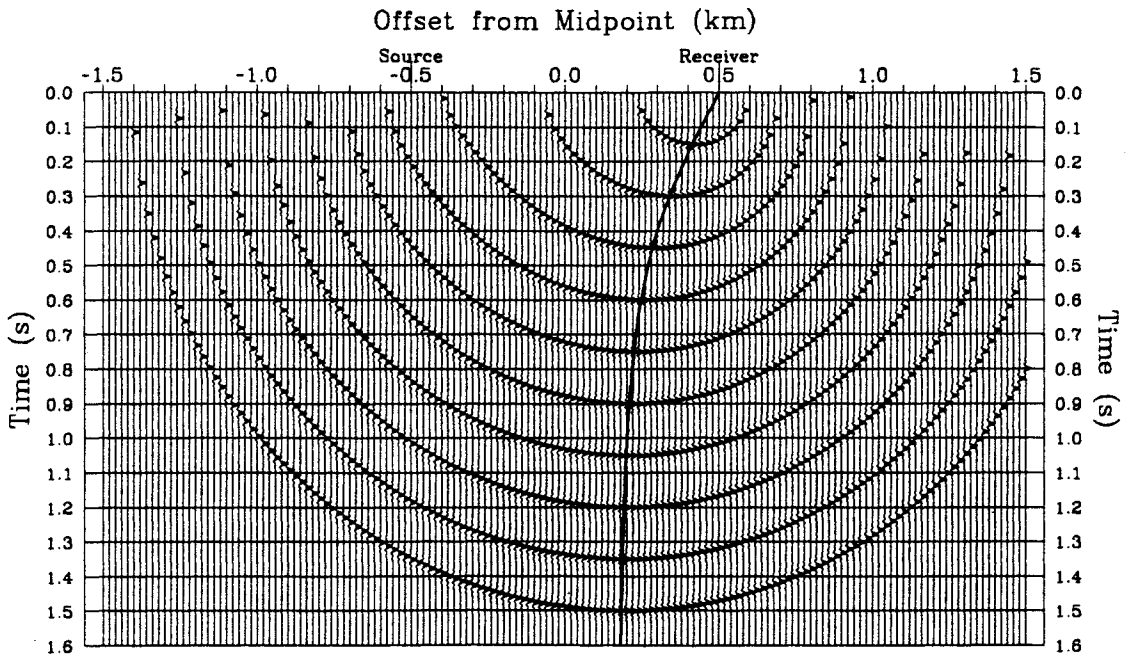


FIG. 4.6.  $P$ - $SV$  migration curves for a source-to-receiver offset of 1 km and various two-way times. The curves were generated as in Figure 4.5.

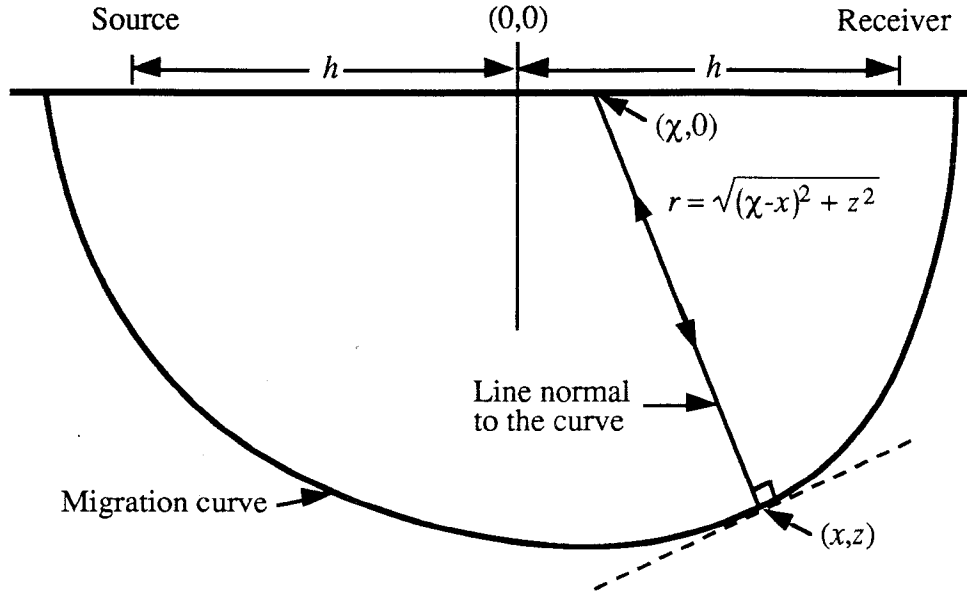


FIG. 4.7. Generation of the zero-offset response to a migration curve.

at a point  $(\chi,0)$  on the surface where the line normal to the locus at  $(x,z)$  emerges. The slope of the normal line is

$$s = -\frac{dx}{dz} = \frac{z}{x-\chi},$$

giving for  $\chi(x)$

$$\chi(x) = x + z \frac{dz}{dx}. \quad (4.27)$$

Differentiating equation (4.24) w.r.t.  $x$  gives

$$z \frac{dz}{dx} = \frac{h}{(\alpha^2 - \beta^2)} \left[ (\alpha^2 + \beta^2) - \frac{2\alpha^2\beta^2 t}{\sqrt{\alpha^2\beta^2 t^2 + 4h(\alpha^2 - \beta^2)x}} \right] - x. \quad (4.28)$$

Substitution of this result into equation (4.27) gives, after simplification,

$$\chi(x) = \frac{h}{(\alpha^2 - \beta^2)} \left[ (\alpha^2 + \beta^2) - \frac{2\alpha^2\beta^2 t}{\sqrt{\alpha^2\beta^2 t^2 + 4h(\alpha^2 - \beta^2)x}} \right]. \quad (4.29)$$

Rather than have  $\chi$  as a function of  $x$ , equation (4.29) can be inverted to give  $x(\chi)$ . This allows the computation of the distance  $x$  away from the midpoint along the migration curve as a function of the offset  $\chi$  from the midpoint along the DMO operator. The resulting equation is

$$x(\chi) = \frac{\alpha^2 \beta^2 t^2}{4h(\alpha^2 - \beta^2)} \left[ \frac{4\alpha^2 \beta^2 h^2}{[\alpha^2(h-\chi) + \beta^2(h+\chi)]^2} - 1 \right]. \quad (4.30)$$

The distance  $r$  from the zero-offset conversion point  $(x,z)$  to the point  $(\chi,0)$  on the surface is given by

$$r^2 = (\chi - x)^2 + z^2. \quad (4.31)$$

Substituting for  $z$  from equation (4.24) and  $x$  from equation (4.30), this reduces to

$$r^2 = (h^2 - \chi^2) \left[ \frac{\alpha^2 \beta^2 t^2}{2h[\alpha^2(h-\chi) + \beta^2(h+\chi)]} - 1 \right]. \quad (4.32)$$

Because both  $x$  and  $z$  have been removed from equation (4.32), the distance  $r$  can be computed without any explicit knowledge of where along the migration curve the point has been mapped from.

The zero-offset conversion time  $\tau$  will be the time to travel from the surface to the conversion point at  $(x,z)$  with velocity  $\alpha$ , plus the time to travel back from the point to the surface at velocity  $\beta$ , i.e.,

$$\tau = \frac{r}{\alpha} + \frac{r}{\beta} = \left( \frac{\alpha + \beta}{\alpha\beta} \right) r. \quad (4.33)$$

Substituting for  $r$  from equation (4.32), this becomes

$$\tau = \left( \frac{\alpha + \beta}{\alpha\beta} \right) \sqrt{(h^2 - \chi^2) \left[ \frac{\alpha^2 \beta^2 t^2}{2h[\alpha^2(h-\chi) + \beta^2(h+\chi)]} - 1 \right]}. \quad (4.34)$$

Equation (4.34) gives the exact zero-offset travelttime mapping function for the  $P$ - $SV$  constant-velocity DMO operator. For any offset  $\chi$  away from the midpoint, it allows the computation of the time  $\tau$  to which a point recorded at time  $t$  and half-offset  $h$  should be moved to apply the DMO correction, or to form the DMO operator.

#### 4.4.2 Derivation using Snell's Law

Figure 4.8 again shows  $P$ -wave energy being mode-converted by a dipping reflector and recorded by a multicomponent receiver, but with the origin shifted to the midpoint. As before, the velocity along the path  $\overline{SC}$  is  $\alpha$  and the velocity along  $\overline{CR}$  is  $\beta$ . The Law of Sines can be used to give

$$\frac{\sin \psi_p}{(h+\chi)} = \frac{\sin\left(\frac{\pi}{2} - \theta\right)}{\overline{SC}} = \frac{\cos \theta}{\overline{SC}}, \quad (4.35a)$$

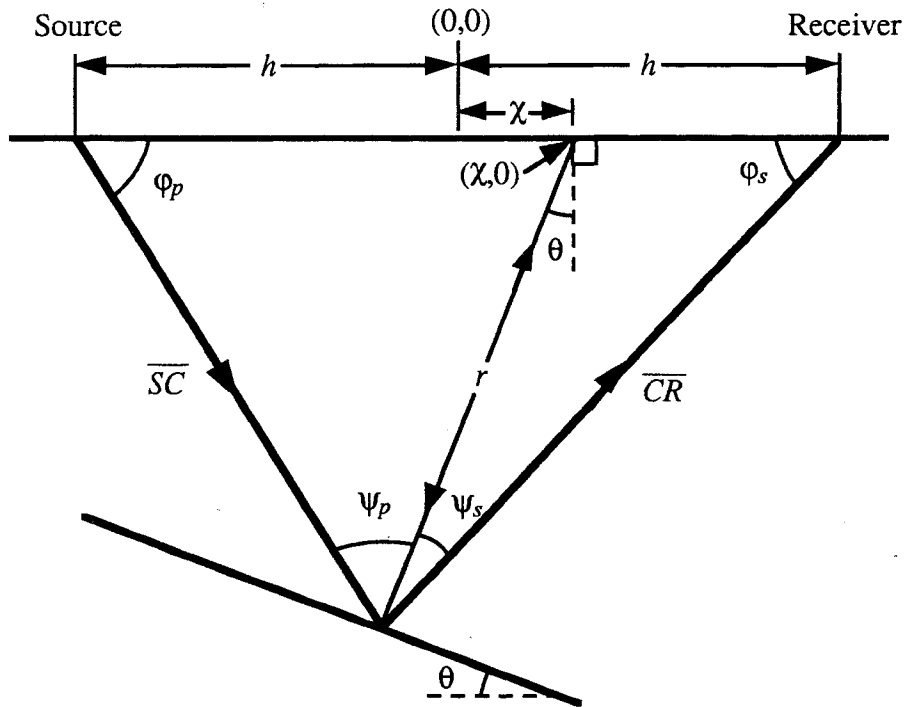


FIG. 4.8. Raypath geometry for conversion from a dipping reflector. The origin has been shifted to the source-to-receiver midpoint.

and

$$\frac{\sin \psi_s}{(h-\chi)} = \frac{\sin\left(\frac{\pi}{2} + \theta\right)}{\overline{CR}} = \frac{\cos \theta}{\overline{CR}}. \quad (4.35b)$$

From Snell's Law, the ray parameter  $p$  is constant;

$$p = \frac{\sin \psi_p}{\alpha} = \frac{\sin \psi_s}{\beta},$$

or

$$\sin \psi_s = \frac{\beta}{\alpha} \sin \psi_p. \quad (4.36)$$

Substituting for  $\sin \psi_p$  and  $\sin \psi_s$  from equations (4.35) gives

$$(h-\chi) \frac{\cos \theta}{\overline{CR}} = \frac{\beta}{\alpha} (h+\chi) \frac{\cos \theta}{\overline{SC}}$$

or

$$\overline{CR} = \frac{\alpha}{\beta} \left( \frac{h-\chi}{h+\chi} \right) \overline{SC}. \quad (4.37)$$

The total traveltime  $t$  is again given by

$$t = \frac{\overline{SC}}{\alpha} + \frac{\overline{CR}}{\beta},$$

which gives  $\overline{SC}$ , using equation (4.37), as

$$\overline{SC} = \frac{\alpha \beta^2 t (h+\chi)}{\alpha^2 (h-\chi) + \beta^2 (h+\chi)}. \quad (4.38)$$

It can be seen from Figure 4.8 that

$$\overline{SC} \cos \varphi_p + \overline{CR} \cos \varphi_s = 2h, \quad (4.39)$$

and, using the Law of Cosines, that

$$r^2 = \overline{SC}^2 + (h+\chi)^2 - 2\overline{SC}(h+\chi) \cos \varphi_p, \quad (4.40a)$$

$$r^2 = \overline{CR}^2 + (h-\chi)^2 - 2\overline{CR}(h-\chi) \cos \varphi_s. \quad (4.40b)$$

Equations (4.40) can be rearranged to give

$$\overline{SC} \cos \varphi_p = \frac{\overline{SC}^2 + (h+\chi)^2 - r^2}{2(h+\chi)}, \quad (4.41a)$$

$$\overline{CR} \cos \varphi_s = \frac{\overline{CR}^2 + (h-\chi)^2 - r^2}{2(h-\chi)}. \quad (4.41b)$$

Substituting equations (4.41) into equation (4.39) and solving for  $r$  gives

$$r^2 = \left( \frac{h^2 - \chi^2}{2h} \right) \left( \frac{\overline{SC}^2}{h+\chi} + \frac{\overline{CR}^2}{h-\chi} - 2h \right). \quad (4.42)$$

Using equations (4.37) and (4.38) to replace  $\overline{SC}$  and  $\overline{CR}$  gives, after simplification,

$$r^2 = (h^2 - \chi^2) \left[ \frac{\alpha^2 \beta^2 t^2}{2h[\alpha^2(h-\chi) + \beta^2(h+\chi)]} - 1 \right]. \quad (4.43)$$

Equation (4.43) is identical to equation (4.32). The two-way traveltimes  $\tau$  is given by equations (4.33) and (4.43) as

$$\tau = \left( \frac{\alpha + \beta}{\alpha \beta} \right) \sqrt{(h^2 - \chi^2) \left[ \frac{\alpha^2 \beta^2 t^2}{2h[\alpha^2(h-\chi) + \beta^2(h+\chi)]} - 1 \right]}. \quad (4.44)$$

Equation (4.44) is seen to be the same result obtained in Section 4.4.1 [equation (4.34)] for the  $P$ - $SV$  zero-offset mapping equation.

#### 4.4.3 Discussion of *P-SV* DMO equation

A number of observations can be made about the *P-SV* DMO mapping equation (equation 4.34). First of all, for  $\tau$  to be real it is necessary that the term  $(h^2 - \chi^2)$  be non-negative; as with *P-P* DMO, this constrains the *P-SV* DMO curves to fall within a maximum distance of  $\pm h$  away from the midpoint. Also, for *P-P* reflection, with  $\alpha = \beta = V$ , equation (4.34) reduces to

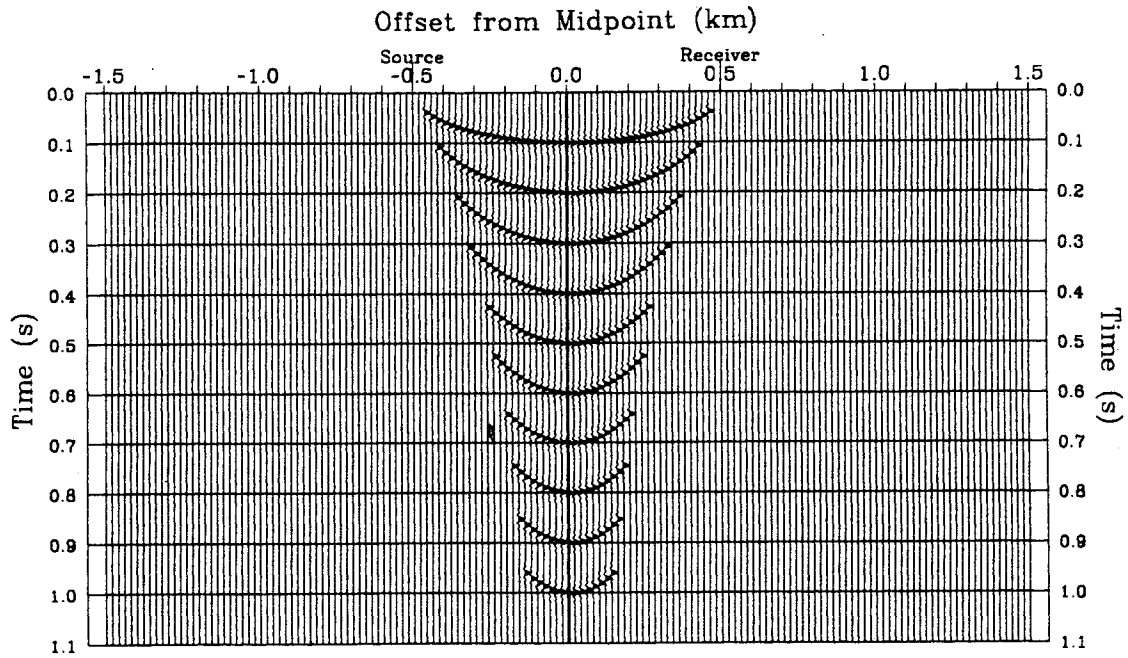
$$\tau_{p-p} = \sqrt{t^2 - \frac{4h^2}{V^2}} \sqrt{1 - \frac{\chi^2}{h^2}} = t_n \sqrt{1 - \frac{\chi^2}{h^2}}, \quad (4.45)$$

where  $t_n$  is again the NMO-corrected time (Hale, 1988). This can be rearranged to give a second ellipse;

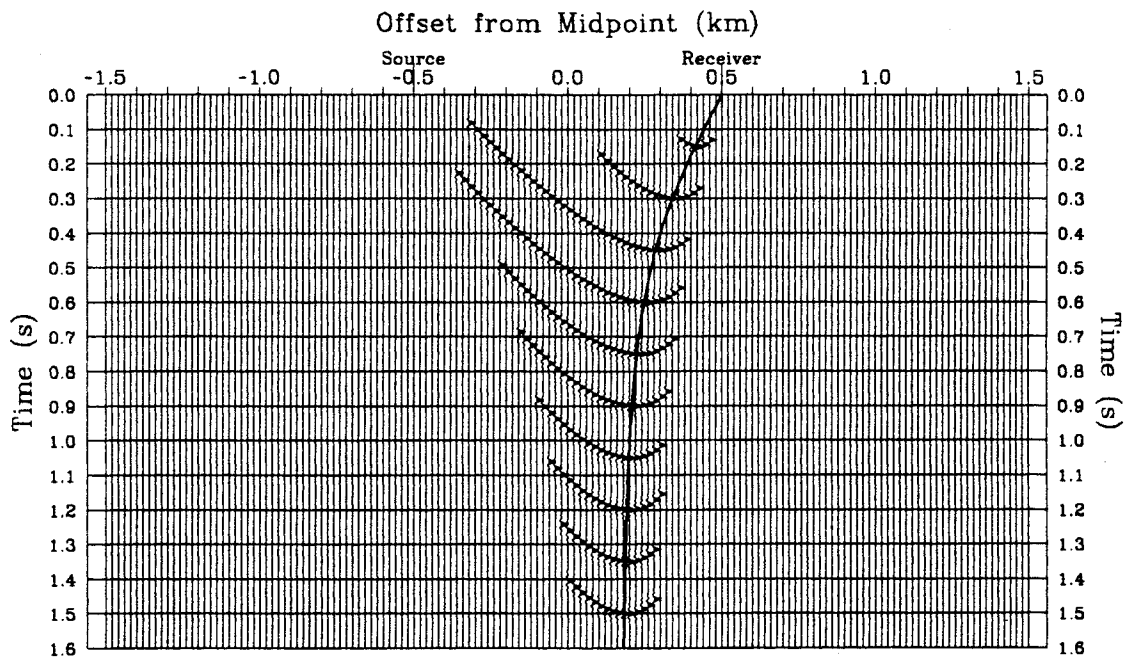
$$\left(\frac{\tau_{p-p}}{t_n}\right)^2 + \left(\frac{\chi}{h}\right)^2 = 1. \quad (4.46)$$

Equation (4.46) is the same expression for the *P-P* DMO operator given by Hale (1988); the *P-P* DMO equation is therefore a special case of equation (4.34). Shown in Figure 4.9 are the DMO curves, computed using equations (4.34) and (4.46), that correspond to the migration curves of Figures 4.5 and 4.6. The curves have all been truncated at the points corresponding to reflector dip of  $\pm 90^\circ$ , as will be discussed in Section 4.5. The location of the zero-dip reflection and conversion points are again plotted in the figure. As expected from Section 4.1, the *P-SV* DMO curves are asymmetric about zero dip, whereas the *P-P* DMO curves are perfectly symmetric.

The cascade of *P-SV* DMO followed by zero-offset migration should regenerate the prestack migration curves. To confirm this, *f-k* migration (Stolt, 1978) has been applied to a *P-SV* DMO response to give the result shown in Figure 4.10. The migration velocity used was computed using equation (5.22). To within the dip limitations of the migration program, the results agree closely with the migration curves of Figure 4.6.



(a)



(b)

FIG. 4.9. DMO curves corresponding to the migration curves of (a) Figure 4.5 ( $P$ - $P$ ) and (b) Figure 4.6 ( $P$ - $SV$ ). The curves were generated as in Figure 4.5. The offset and time axes correspond to the variables  $\chi$  and  $\tau$  in equation (4.34).

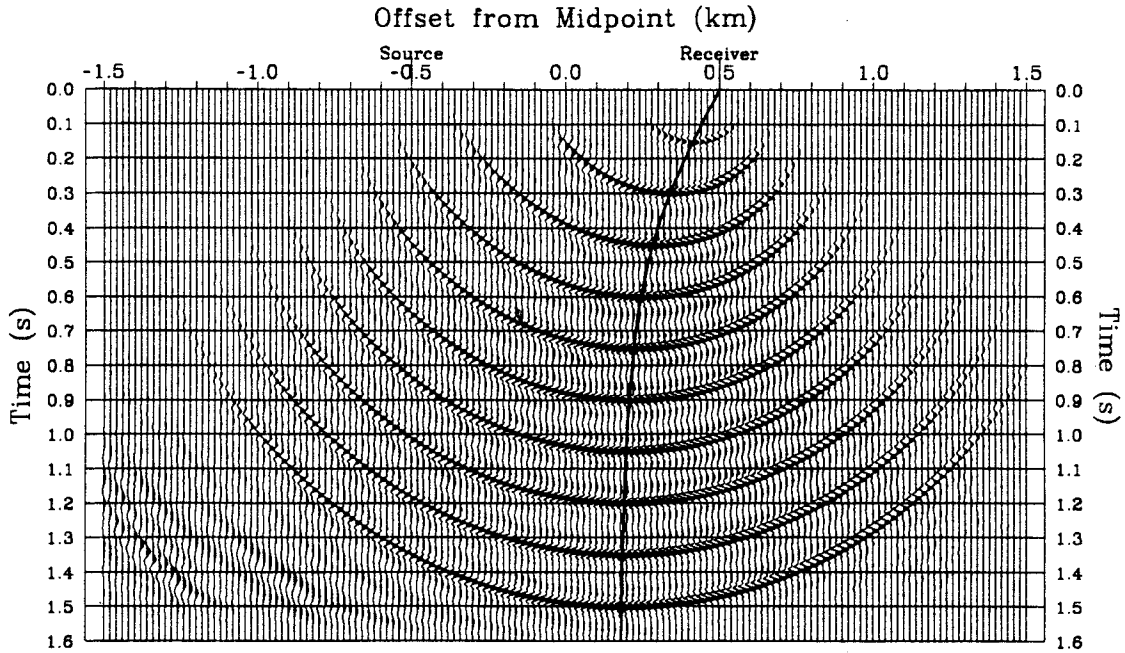


FIG. 4.10.  $f$ - $k$  migration applied to the  $P$ - $SV$  DMO curves of Figure 4.9b.

The mapping to zero offset carried out by equation (4.34) intrinsically applies a normal-moveout correction to the input data. At the location of the zero-dip conversion point, the equation reduces to an exact NMO equation for constant-velocity  $P$ - $SV$  data, or  $P$ - $P$  data if  $\alpha$  and  $\beta$  are equal. This property can be used to modify the DMO equation for application to data that has been previously NMO-corrected, as in the  $P$ - $P$  case. At the zero-dip conversion point  $\chi_0$  the DMO time is equal to the NMO-corrected time  $t_n$ :

$$t_n = \left( \frac{\alpha + \beta}{\alpha \beta} \right) \sqrt{(h^2 - \chi_0^2) \left[ \frac{\alpha^2 \beta^2 t^2}{2h[\alpha^2(h - \chi_0) + \beta^2(h + \chi_0)]} - 1 \right]}. \quad (4.47)$$

Equation (4.47) can be rearranged to give

$$t^2 = \frac{2h[\alpha^2(h - \chi_0) + \beta^2(h + \chi_0)]}{\alpha^2 \beta^2} \left[ \frac{\alpha^2 \beta^2 t_n^2}{(h^2 - \chi_0^2)(\alpha + \beta)^2} + 1 \right]. \quad (4.48)$$

After substitution for  $t^2$  using equation (4.48), equation (4.34) reduces to

$$\tau^2 = \frac{(h^2 - \chi^2)}{[\alpha^2(h - \chi) + \beta^2(h + \chi)]} \left\{ \frac{[\alpha^2(h - \chi_0) + \beta^2(h + \chi_0)]}{(h^2 - \chi_0^2)} t_n^2 + (\chi - \chi_0) (\alpha^2 - \beta^2) \left( \frac{\alpha + \beta}{\alpha\beta} \right)^2 \right\} \quad (4.49)$$

Equation (4.49) allows the application of *P-SV* DMO to NMO-corrected *P-SV* data, just as equation (4.45) allows the application of DMO to NMO-corrected *P-P* data. This extends the use of *P-SV* DMO to the general case where velocities vary with depth, provided that suitable values of  $\alpha$  and  $\beta$  are used in equation (4.49) (Section 4.8.2).

#### 4.5 Envelope of the *P-SV* DMO operator

Equation (4.34) generates the shape of the DMO curves, but it is still necessary to determine their maximum physical extents. These extents establish the minimum and maximum  $\tau$  time values, corresponding to some maximum physical dip, that the DMO operator can take on at any offset  $\chi$  away from the midpoint. This, in turn, determines the envelope of the DMO operator. For fixed velocity, differentiation of equation (4.33) gives

$$d\tau = \left( \frac{\alpha + \beta}{\alpha\beta} \right) dr. \quad (4.50)$$

From Figure 4.11, it is seen that

$$dr = d\chi \sin \theta, \quad (4.51)$$

which gives, from equation (4.50), that the slope  $s$  along the DMO curve is

$$s = \frac{d\tau}{d\chi} = \left( \frac{\alpha + \beta}{\alpha\beta} \right) \sin \theta. \quad (4.52)$$

This result relates the dip angle at the point of conversion to the slope on the DMO operator. Equation (4.34) can be differentiated w.r.t.  $\chi$  to give

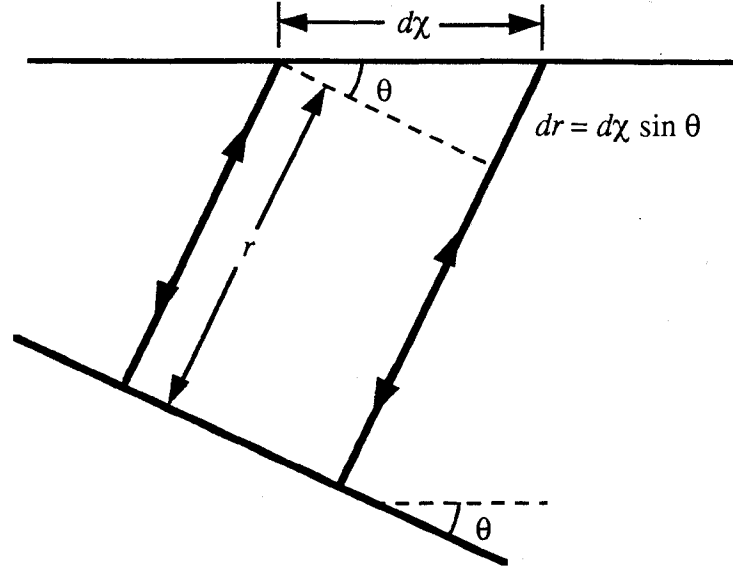


FIG. 4.11. Relationship between changes in zero-offset distance  $r$  and operator offset  $\chi$ .

$$s = \frac{1}{\tau} \left( \frac{\alpha+\beta}{\alpha\beta} \right)^2 \left\{ \chi + \frac{\alpha^2\beta^2 t^2}{4h} \frac{\alpha^2(h-\chi)^2 - \beta^2(h+\chi)^2}{[\alpha^2(h-\chi) + \beta^2(h+\chi)]^2} \right\}. \quad (4.53)$$

It is more convenient to have  $s$  defined in terms of  $\tau$ , rather than  $t$  and  $\tau$ . To do this, equation (4.34) can be inverted to give  $t(\chi, \tau)$ ;

$$t = \frac{1}{(\alpha+\beta)} \sqrt{\left[ \tau^2 + \left( \frac{\alpha+\beta}{\alpha\beta} \right)^2 (h^2 - \chi^2) \right] \left\{ \frac{2h[\alpha^2(h-\chi) + \beta^2(h+\chi)]}{h^2 - \chi^2} \right\}}. \quad (4.54)$$

This expression can be used to remove  $t$  from equation (4.53), with result

$$s = \frac{1}{2\tau} \left( \frac{\alpha+\beta}{\alpha\beta} \right)^2 \left\{ \frac{(\alpha^2 - \beta^2)(h^2 - \chi^2)^2 + \tau^2 \left( \frac{\alpha\beta}{\alpha+\beta} \right)^2 [\alpha^2(h-\chi)^2 - \beta^2(h+\chi)^2]}{(h^2 - \chi^2)[\alpha^2(h-\chi) + \beta^2(h+\chi)]} \right\}. \quad (4.55)$$

Equation (4.55) gives the slope  $s$  at any point  $(\chi, \tau)$  on the DMO operator, which can, in turn, be used to compute the dip angle at that point using equation (4.52). Alternatively, if it is desired that only dip up to some maximum angle be passed by the operator, then the slope corresponding to that dip angle can be computed using equation (4.52). Equation

(4.55) then gives a quadratic expression for  $\tau$ , with solution

$$\tau = (h^2 - \chi^2) \left\{ \frac{[\alpha^2(h-\chi) + \beta^2(h+\chi)] s \pm \sqrt{[\alpha^2(h-\chi) + \beta^2(h+\chi)]^2 s^2 - (\alpha^2 - \beta^2) \left(\frac{\alpha+\beta}{\alpha\beta}\right)^2 [\alpha^2(h-\chi)^2 - \beta^2(h+\chi)^2]}}{\alpha^2(h-\chi)^2 - \beta^2(h+\chi)^2} \right\}. \quad (4.56)$$

The two values of  $\tau$  give the minimum and maximum time that the operator can have at offset  $\chi$  away from the midpoint. Ideally, the dip aperture of the DMO operator would be set to pass all possible dips ( $\pm 90^\circ$ ). It is possible, however, that this will lead to spatial aliasing of the response at large dip angles. When this occurs, either the maximum frequency of the DMO response or the DMO dip aperture can be restricted to prevent aliasing (Beasley and Mobley, 1988). For a given maximum dip  $s_{max}$  the aliasing frequency  $f_a$  for a trace spacing of  $\Delta\chi$  is given by

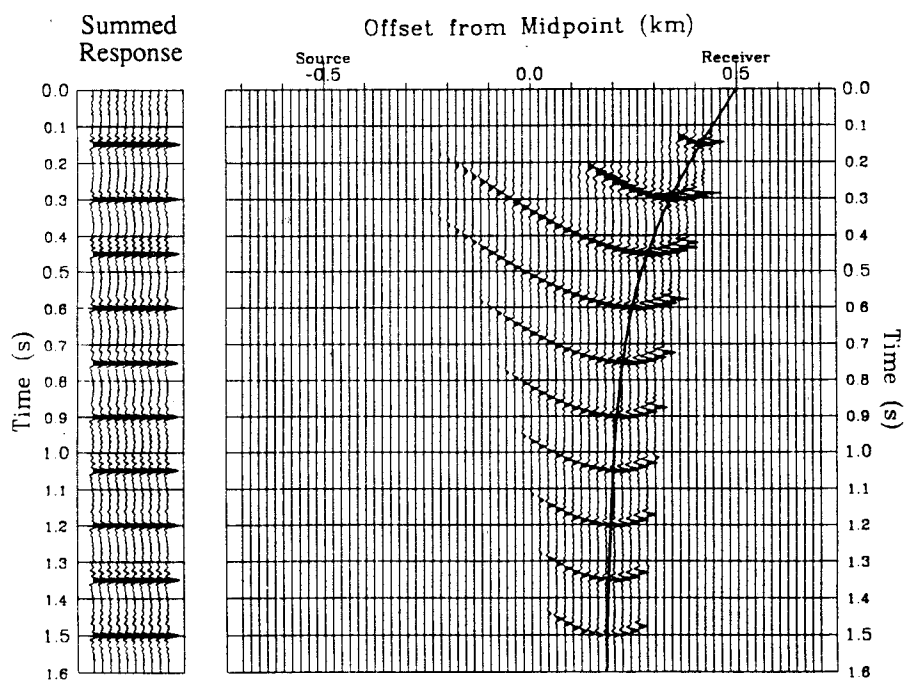
$$f_a = \frac{1}{2 s_{max} \Delta\chi}. \quad (4.57)$$

Equation (4.57) could be used to high-cut filter the DMO response to prevent aliasing for a given dip aperture. However, this involves computing and applying a time- and spatially-varying filter operator. As an alternative to this, for a given maximum data frequency  $f_{max}$  the dip  $s_a$  at which aliasing occurs can be computed;

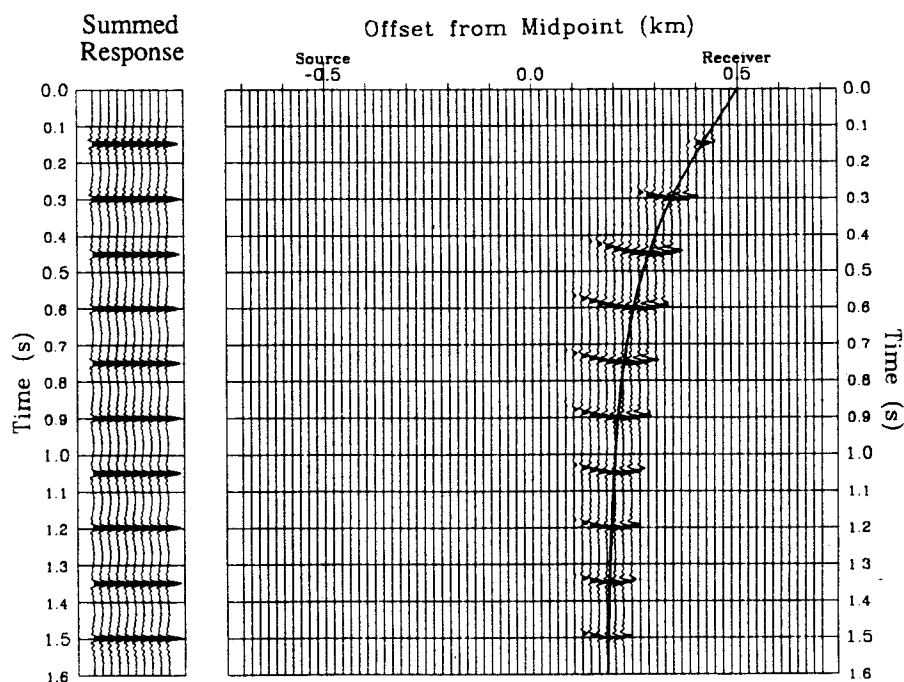
$$s_a = \frac{1}{2 f_{max} \Delta\chi}. \quad (4.58)$$

Using the value for  $s_a$  computed from equation (4.58), the envelope of the DMO response can be calculated using equation (4.56); constraining the DMO response to fall within this envelope prevents data aliasing. This second approach was used in applying  $P$ - $SV$  DMO in the examples shown in this dissertation.

To illustrate the effect that restricting the DMO dip aperture has on aliasing, Figure 4.12 shows two DMO responses that have been constrained to pass dips in the range of  $\pm 60^\circ$  and  $\pm 30^\circ$ . Aliasing occurs for dips greater than  $40^\circ$  for the trace spacing and



(a)



(b)

FIG. 4.12. *P*-*SV* DMO responses with dip apertures restricted to (a)  $\pm 60^\circ$  and (b)  $\pm 30^\circ$ .

frequency content of the wavelet used. This can be seen from the summed response plots; the aliased dips produce visible artifacts with the  $\pm 60^\circ$  aperture (Figure 4.12a), but no artifacts with the  $\pm 30^\circ$  aperture (Figure 4.12b).

For very small dip apertures, the DMO response collapses to just the trace itself, positioned along the conversion-point curve. *P-SV* DMO with a small dip aperture is therefore equivalent to performing a zero-dip conversion-point rebinning of the data. This is also true of the *P-P* case, where DMO with a small dip aperture is equivalent to CMP stacking.

#### 4.6 Location of the zero-dip conversion point

At the location of the zero-dip conversion point, the slope  $s$  along the DMO curve is zero. At this point,  $\chi$  is equal to the offset away from the midpoint of the zero-dip conversion point  $\chi_0$ . Setting  $s$  to zero in equation (4.55) leads to the following cubic equation for  $\chi_0$ ;

$$4h \left( \frac{\alpha^2 - \beta^2}{\alpha\beta} \right)^2 \chi_0^3 + \left( \frac{\alpha^2 - \beta^2}{\alpha\beta} \right) \left[ \alpha\beta t^2 - 8h^2 \left( \frac{\alpha^2 + \beta^2}{\alpha\beta} \right) \right] \chi_0^2 - 2h \left( \frac{\alpha^2 + \beta^2}{\alpha\beta} \right) \left[ \alpha\beta t^2 - 2h^2 \left( \frac{\alpha^2 + \beta^2}{\alpha\beta} \right) \right] \chi_0 + \alpha\beta t^2 h^2 \left( \frac{\alpha^2 - \beta^2}{\alpha\beta} \right) = 0. \quad (4.59)$$

It appears that all other equations for the conversion point location involve solving a quartic equation (e.g., Behle and Dohr, 1985). The desired root to equation (4.59) can be found using standard methods (e.g., Beyer, 1984). Defining

$$\eta = \frac{1}{6h} \left( \frac{\alpha\beta}{\alpha^2 - \beta^2} \right) \left[ \alpha\beta t^2 + 4h^2 \left( \frac{\alpha^2 + \beta^2}{\alpha\beta} \right) \right], \quad (4.60a)$$

$$\rho = \frac{1}{2} \left[ \eta - 2h \left( \frac{\alpha^2 + \beta^2}{\alpha^2 - \beta^2} \right) \right], \quad (4.60b)$$

$$b = h^2(\eta + \rho) + \rho \left( \frac{3\eta^2}{4} - \rho^2 \right), \quad (4.60c)$$

and

$$\Theta = \frac{1}{3} \left[ \cos^{-1} \left( -\frac{4b}{\eta^3} \right) + 4\pi \right], \quad (4.60d)$$

then the conversion point offset is given by

$$\chi_0 = \eta \cos \Theta - \rho. \quad (4.60e)$$

Equations (4.60) are found to give the same numerical values for the conversion point location as are obtained using the equation given by Tessmer and Behle (1988).

#### 4.7 *P-SV* DMO and conversion-point dispersal

In order that DMO properly convert non-zero offset data to zero-offset, the DMO operator must move data points reflected or converted from dipping reflectors a horizontal distance exactly equal to  $\delta$  in equation (4.11). Deregowski (1982) has shown that this is the case for the *P-P* DMO operator; the objective in this section is to prove that this is also true for the *P-SV* case.

To begin with, substitution of  $s$  from equation (4.52) into equation (4.55) gives

$$\begin{aligned} \tau^2 \left( \frac{\alpha\beta}{\alpha+\beta} \right) \left[ \alpha^2(h-\chi)^2 - \beta^2(h+\chi)^2 \right] - 2\tau(h^2 - \chi^2) \left[ \alpha^2(h-\chi) + \beta^2(h+\chi) \right] \sin \theta \\ + \left( \frac{\alpha+\beta}{\alpha\beta} \right) \left( \alpha^2 - \beta^2 \right) (h^2 - \chi^2)^2 = 0. \end{aligned} \quad (4.61)$$

Comparing Figures 4.1 and 4.7, it is seen that the raypath  $r$  is the same in both figures.

This gives

$$h + \chi = \lambda - \delta. \quad (4.62)$$

Using equation (4.62), equation (4.61) can be rewritten as

$$\begin{aligned}
& \tau^2 \left( \frac{\alpha\beta}{\alpha+\beta} \right) \left[ (\alpha^2 - \beta^2)(\lambda - \delta)^2 - 4h\alpha^2(\lambda - \delta) + 4h^2\alpha^2 \right] \\
& - 2\tau(\lambda - \delta) [2h - (\lambda - \delta)] \left[ 2h\alpha^2 - (\alpha^2 - \beta^2)(\lambda - \delta) \right] \sin \theta \\
& + \left( \frac{\alpha+\beta}{\alpha\beta} \right) (\alpha^2 - \beta^2)(\lambda - \delta)^2 \left[ (\lambda - \delta)^2 - 4h(\lambda - \delta) + 4h^2 \right] = 0.
\end{aligned} \tag{4.63}$$

From Figure 4.1, it can be shown that

$$r = d - \delta \sin \theta. \tag{4.64}$$

Substituting for  $r$  from equation (4.33), equation (4.64) becomes

$$\begin{aligned}
\tau &= \left( \frac{\alpha+\beta}{\alpha\beta} \right) (d - \delta \sin \theta) \\
&= \left( \frac{\alpha+\beta}{\alpha\beta} \right) [d - \lambda \sin \theta + (\lambda - \delta) \sin \theta].
\end{aligned} \tag{4.65}$$

Substituting equation (4.65) for  $\tau$  into equation (4.63) and dividing through by  $\alpha^2$  gives

$$\begin{aligned}
& [d - \lambda \sin \theta + (\lambda - \delta) \sin \theta]^2 \left[ (1 - \gamma^2)(\lambda - \delta)^2 - 4h(\lambda - \delta) + 4h^2 \right] \\
& - 2(\lambda - \delta) [2h - (\lambda - \delta)] [d - \lambda \sin \theta + (\lambda - \delta) \sin \theta] \left[ 2h - (1 - \gamma^2)(\lambda - \delta) \right] \sin \theta \\
& + (1 - \gamma^2) \left[ (\lambda - \delta)^2 - 4h(\lambda - \delta) + 4h^2 \right] (\lambda - \delta)^2 = 0.
\end{aligned} \tag{4.66}$$

After simplification and collection of terms, equation (4.66) reduces to

$$\begin{aligned}
& (\gamma^2 - 1) [(\lambda - \delta) - 4h] \cos^2 \theta (\lambda - \delta)^3 \\
& + \left\{ \gamma^2 (d - \lambda \sin \theta)^2 + (\gamma^2 - 1) 4h^2 \cos^2 \theta - [d + (2h - \lambda) \sin \theta]^2 \right\} (\lambda - \delta)^2 \\
& - 4h\gamma^2 (d - \lambda \sin \theta)^2 (\lambda - \delta) + 4h^2 \gamma^2 (d - \lambda \sin \theta)^2 = 0.
\end{aligned} \tag{4.67}$$

Equation (4.67) is seen to be the same as equation (4.11). This means that the  $P$ - $SV$  DMO operator does, in fact, exactly compensate for CCP dispersal, and repositions data points into their proper bin locations.

## 4.8 Implementation of *P-SV* dip moveout

An integral-summation algorithm (Deregowski, 1985) was implemented to test the *P-SV* DMO equations on synthetic data. The algorithm consists of first constructing a time-domain DMO response for each input trace, then summing the responses to get the final DMO result. The dip aperture was restricted to prevent operator aliasing at the maximum frequency of the input data (Section 4.5). The operator amplitude and phase corrections used are discussed in the Section 4.8.1. The method used to modify the DMO equation to handle depth-varying velocities is discussed in Section 4.8.2. Results of applying *P-SV* DMO using this algorithm to a synthetic data example are presented in Section 4.8.3.

### 4.8.1 *P-SV* operator amplitude and phase correction

To assess the effect of the DMO operator on the input data, it is necessary to analyze how the data are changed by summation across the operator width, which generates the final DMO-corrected output. Consider a point located at  $(\tau_1, \chi_1)$  on the DMO curve  $\tau = \tau(\chi)$  shown in Figure 4.13. At this point, the DMO operator is attempting to image a reflector with slope  $s_1$  equal to the slope of the tangent line. From Figure 4.13, the time at a point along the curve located a horizontal distance  $\epsilon$  away from  $(\tau_1, \chi_1)$  is seen to be

$$\tau(\chi) = \tau_1 + s_1 \epsilon + \Delta\tau. \quad (4.68)$$

Before any corrections have been applied, the amplitude at every point along the curve is equal to the amplitude at the zero-dip conversion point. The amplitude  $a_\epsilon$  at the point located a distance  $\epsilon$  away from  $(\tau_1, \chi_1)$  is therefore the same as the amplitude at  $(\tau_1, \chi_1)$ , i.e.,

$$a_\epsilon(\tau) = a_0(\tau_1) \quad \text{for } \tau \in \tau(\chi) \quad (4.69)$$

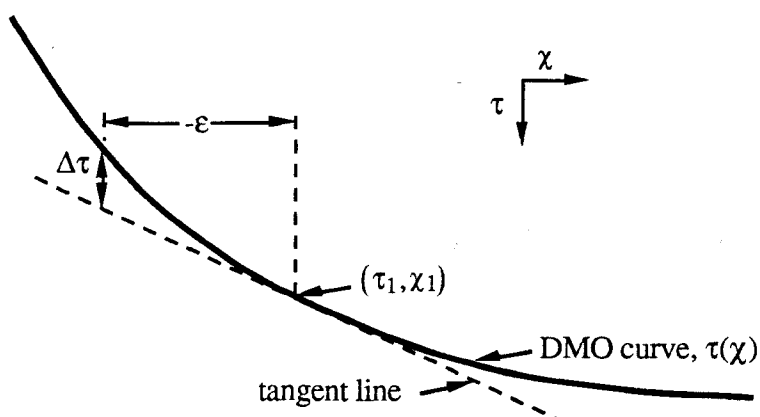


FIG. 4.13. Time difference along the DMO curve.

where  $a_0$  is the amplitude at  $\varepsilon = 0$ . As the operator moves horizontally across the dipping reflector a distance  $\varepsilon$ , the time of the reflector within the operator shifts by  $s_1\varepsilon$ . The output sample  $\bar{a}(\tau_1)$  at this location is obtained, for fixed offset, by summing horizontally across the width of the time-shifted DMO operator, i.e.,

$$\begin{aligned}\bar{a}(\tau_1) &= \int_{-\varepsilon_1}^{\varepsilon_2} a_\varepsilon(\tau_1 + s_1\varepsilon) d\varepsilon \\ &\equiv \int_{-\varepsilon_1}^{\varepsilon_2} a_0(\tau_1 - \Delta\tau) d\varepsilon,\end{aligned}\quad (4.70)$$

where  $\varepsilon_1$  and  $\varepsilon_2$  are the left and right widths of the operator about the output point, and equations (4.68) and (4.69) have been used. The time shift  $\Delta\tau$  is a function of both  $\tau$  (or  $t_n$ ) and  $\varepsilon$ , which makes an exact solution to equation (4.70) difficult. To get an approximate solution, a Taylor's series expansion in the spatial direction about the point located at  $(\tau_1, \chi_1)$  can be done;

$$\tau(\chi) = \tau_1 + \varepsilon \left( \frac{d\tau}{d\chi} \right)_{\chi_1} + \frac{\varepsilon^2}{2} \left( \frac{d^2\tau}{d\chi^2} \right)_{\chi_1} + \dots$$

$$\cong \tau_1 + s_1 \epsilon + c_1 \frac{\epsilon^2}{2}, \quad (4.71)$$

where  $s_1$  is the slope at  $(\tau_1, \chi_1)$ , given by equation (4.55), and  $c_1$  is the curvature. Equation (4.71) ignores the dependence of  $\tau$  on  $t_n$ , which is equivalent to assuming that vertical changes in the shape of the DMO curves are negligible. Using equation (4.71), the time difference  $\Delta\tau$  of equation (4.68) is given by

$$\begin{aligned} \Delta\tau &= \tau(\chi) - (\tau_1 + s_1 \epsilon) \\ &\cong c_1 \frac{\epsilon^2}{2}. \end{aligned} \quad (4.72)$$

Using this approximation, equation (4.70) becomes

$$\bar{a}(\tau_1) \cong \int_{-\epsilon_1}^{\epsilon_2} a_0(\tau_1 - c_1 \frac{\epsilon^2}{2}) d\epsilon. \quad (4.73)$$

Taking the Fourier transform of equation (4.73) and dropping the subscript on  $\tau$  gives

$$\begin{aligned} \bar{A}(\omega) &\cong \int_{-\infty}^{\infty} \left( \int_{-\epsilon_1}^{\epsilon_2} a_0(\tau - c_1 \frac{\epsilon^2}{2}) d\epsilon \right) \exp(i\omega\tau) d\tau \\ &= \int_{-\epsilon_1}^{\epsilon_2} \int_{-\infty}^{\infty} a_0(\tau - c_1 \frac{\epsilon^2}{2}) \exp(i\omega\tau) d\tau d\epsilon \end{aligned} \quad (4.74)$$

after reversing the order of integration. Evaluation of the inner integral gives

$$\begin{aligned} \bar{A}(\omega) &\cong A_0(\omega) \int_{-\epsilon_1}^{\epsilon_2} \exp\left(i\frac{\omega c_1}{2} \epsilon^2\right) d\epsilon \\ &= A_0(\omega) D(\omega), \end{aligned} \quad (4.75)$$

where  $A_0(\omega)$  is the Fourier transform of the original input. From equation (4.75), the DMO operation is seen to scale the input data by the function  $D(\omega)$ . If the width of the DMO operator about the output point is roughly the same in both directions, then

$$D(\omega) \equiv 2 \int_0^{\bar{\varepsilon}} \exp\left(i \frac{\omega c_1}{2} \varepsilon^2\right) d\varepsilon \quad (4.76)$$

where

$$\bar{\varepsilon} = \frac{\varepsilon_1 + \varepsilon_2}{2}.$$

Equation (4.76) can be rewritten as

$$\begin{aligned} D(\omega) &\equiv \sqrt{\frac{8}{\omega|c_1|}} \left( \int_0^{u_1} \cos u^2 du - i \int_0^{u_1} \sin u^2 du \right) \\ &= \sqrt{\frac{8}{\omega|c_1|}} (C(u_1) - iS(u_1)), \end{aligned} \quad (4.77)$$

where

$$u_1 = \sqrt{\frac{\omega|c_1|}{2}} \bar{\varepsilon}, \quad (4.78)$$

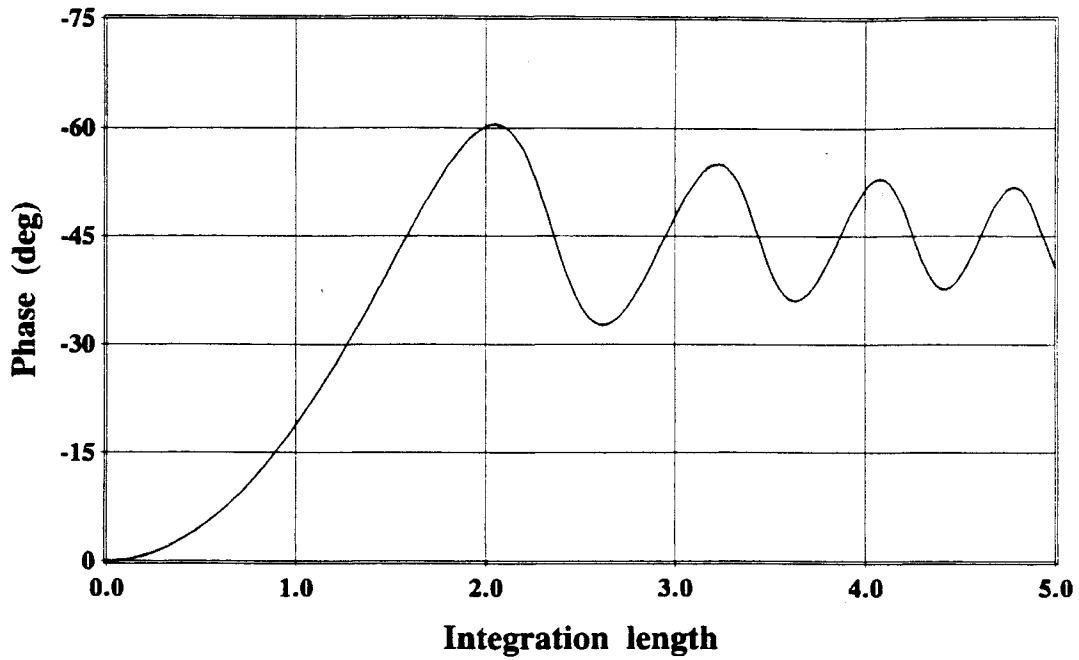
and  $C(u)$  and  $S(u)$  are the Fresnel integrals (Kreyszig, 1972). The absolute value is introduced to account for the curvature always being negative [equation (4.86)]. The phase and amplitude of  $D(\omega)$  are given by

$$\text{Phase}[D(\omega)] = -\tan^{-1} \left[ \frac{S(u_1)}{C(u_1)} \right], \quad (4.79)$$

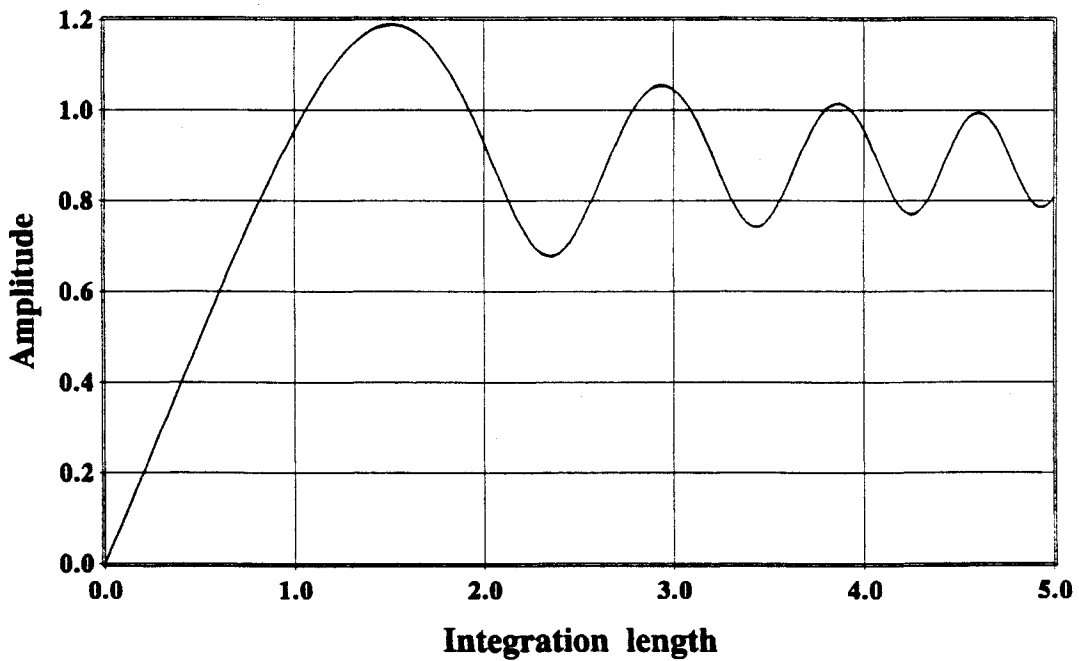
$$|D(\omega)| = \sqrt{\frac{8}{\omega|c_1|}} \sqrt{C^2(u_1) + S^2(u_1)}. \quad (4.80)$$

Figure 4.14 is a plot of the phase function given by equation (4.79), and the amplitude function given by

$$A(u_1) = \sqrt{C^2(u_1) + S^2(u_1)}, \quad (4.81)$$



(a)



(b)

FIG. 4.14. (a) Phase function of equation (4.79) and (b) amplitude function of equation (4.81) vs. the integration length,  $u_1$ .

as a function of the integration length  $u_1$ . From the figure, both functions are seen to converge to an asymptotic value.

The Fresnel integrals are known to have an analytic solution only in the limit that  $u_1$  goes to infinity, in which case

$$\text{Phase } [D(\omega)] \Rightarrow -45^\circ, \quad (4.82)$$

$$|D(\omega)| \Rightarrow \sqrt{\frac{2\pi}{\omega|c_d|}} = \frac{1}{\sqrt{f|c_d|}}. \quad (4.83)$$

The phase correction is shown by equation (4.82) to be  $45^\circ$  for a wide operator, but is less where the operator is narrow.

The phase corrections applied in this dissertation to the DMO responses were computed for each time sample by numerically solving equation (4.79) for the predicted phase at the location of the zero-dip conversion point. To reduce computation time, only the phase distortion for the dominant frequency of the data was estimated. This phase value was then removed from all frequencies and operator samples at that time by using a time-variant phase-shift filter. It was found that equation (4.79) gives a slight over-estimate of the operator phase distortion. This was compensated for by modifying  $u_1$  in equation (4.79) by a fixed scalar;

$$u_1 \Rightarrow 0.7 u_1.$$

This over-correction is not unexpected, as equation (4.79) is only approximate.

To give proper normalization, the output sample at  $(\tau_1, \chi_1)$  must be gained by the reciprocal of the asymptotic amplitude at that point, i.e.,

$$g_1 = \frac{1}{|D(\omega)|} = \sqrt{f|c_d|}. \quad (4.84)$$

If the gain  $g_0$  at the zero-dip conversion point, where the curvature is  $c_0$ , is defined as

$$g_0 = \sqrt{f|c_d|}, \quad (4.85a)$$

then the gain at any point along the DMO curve will be

$$g = \sqrt{\frac{c}{c_0}} g_0, \quad (4.85b)$$

where  $c$  is the curvature at that point. Equations (4.85) are seen to be frequency-dependent, but to reduce computation time only one gain function was computed, again using the dominant frequency of the seismic data. This function was then applied to all frequencies.

The second derivative of  $\tau$  must be computed to apply the gain function of equation (4.85). An analytical expression for this can be obtained by differentiating equation (4.55) w.r.t.  $\chi$ . After simplification, the result is

$$c \equiv \frac{d^2\tau}{d\chi^2} = -\frac{1}{\tau} \left\{ s^2 + \frac{\tau^2}{(h^2 - \chi^2)} - \frac{2(\alpha^2 - \beta^2) \left[ s\tau - \chi \left( \frac{\alpha + \beta}{\alpha\beta} \right)^2 \right]}{[\alpha^2(h - \chi) + \beta^2(h + \chi)]} \right\}, \quad (4.86)$$

where  $s$  is the first derivative, given by equation (4.55).

From energy partitioning considerations in the  $f$ - $k$  domain, Beasley and Mobley (1988) suggest that the amplitude along the DMO operator curve should be proportional to the curvature, rather than the square root of curvature [equation (4.85)]. In testing both gain functions, it was found that the gain defined by equation (4.85) was better able to preserve the amplitude of dipping events, and was used in the DMO program. Using an analysis similar to that given here, Pieprzak and Bramblett (1990) obtain a gain function for the  $P$ - $P$  case that also depends upon the square root of curvature, and conclude that it gives better results than does traditional DMO operator scaling.

The result of applying the amplitude and phase corrections discussed here can be seen in the DMO responses in Figure 4.12.

#### 4.8.2 Modification for depth-varying velocities

As discussed in Section 4.4.3, equation (4.49) allows the application of  $P$ - $SV$  DMO to NMO-corrected data if the DMO responses are constructed about the location of the zero-dip conversion point. For the multilayered case, the zero-dip conversion point can be found either by raytracing or by using some form of approximation algorithm. The DMO implementation in this dissertation uses the approximation method described in Section 2.7 [equations (2.26)].

Unlike  $P$ - $P$  DMO,  $P$ - $SV$  DMO for NMO-corrected data is velocity dependent. In order to test the sensitivity of equation (4.49) to velocity and determine a reasonable velocity function to use when applying DMO, a kinematically-correct  $P$ - $SV$  DMO response was created using raytracing for the case of vertically-inhomogenous velocity. Referring to Figure 4.15, the total source-to-receiver traveltime  $t$  is given by

$$t = \sum_{i=1}^n \frac{z_i}{\alpha_i \sqrt{1-p_1^2 \alpha_i^2}} + \sum_{i=1}^n \frac{z_i}{\beta_i \sqrt{1-p_2^2 \beta_i^2}}, \quad (4.87)$$

where  $p_1$  and  $p_2$  are the ray parameters for the down-going  $P$ -wave and up-going  $S$ -wave raypaths. The conversion point offset  $x$  from the source is

$$x = p_1 \sum_{i=1}^n \frac{\alpha_i z_i}{\sqrt{1-p_1^2 \alpha_i^2}}, \quad (4.88)$$

and the total source-receiver offset  $2h$  is

$$2h = x + p_2 \sum_{i=1}^n \frac{\beta_i z_i}{\sqrt{1-p_2^2 \beta_i^2}}. \quad (4.89)$$

The two-way vertical traveltime  $t_z$  is given by

$$t_z = \sum_{i=1}^n \left( \frac{\alpha_i + \beta_i}{\alpha_i \beta_i} \right) z_i. \quad (4.90)$$

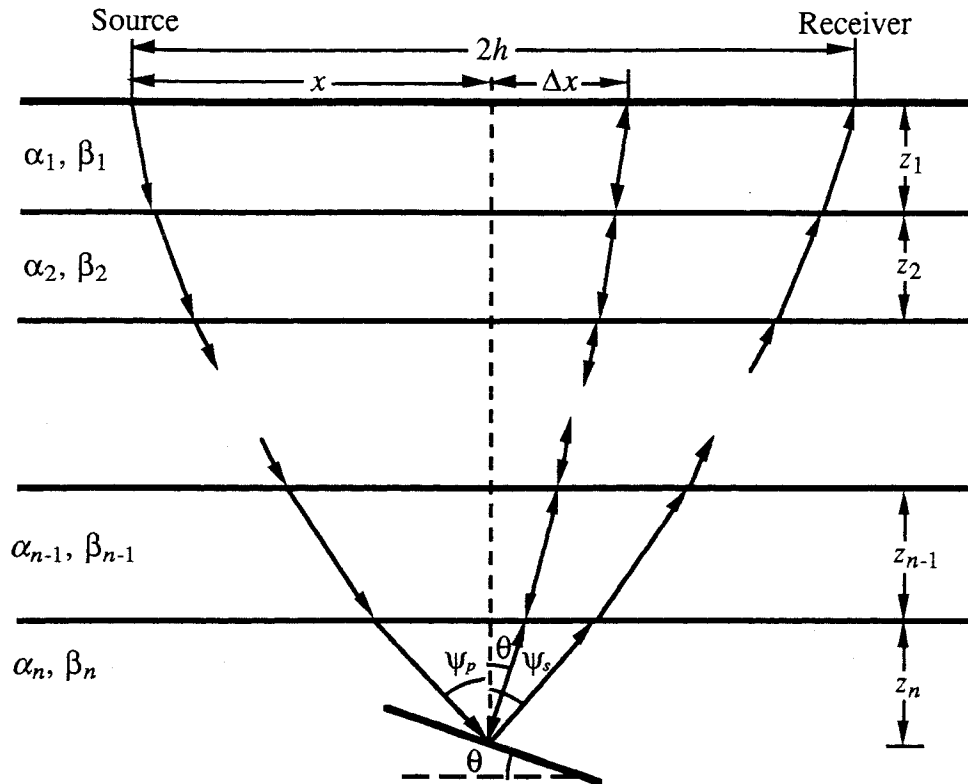


FIG. 4.15. DMO model for depth-varying velocities, consisting of a dipping reflector situated beneath a number of horizontal layers.

For given values of time  $t_z$  and offset  $x$ , equations (4.88) and (4.89) can be solved for  $p_1$  and  $p_2$ , and the traveltimes  $t$  computed using equation (4.87). A full migration response can be generated by sweeping through a range of  $t_z$  and  $x$  values.

The dip angle  $\theta$  can be computed from the two ray parameters  $p_1$  and  $p_2$ . Referring to Figure 4.15, it is seen that

$$p = \frac{\sin(\psi_p + \theta)}{\alpha_n} = \frac{\sin(\psi_s - \theta)}{\beta_n}, \quad (4.91)$$

where  $p$  is the ray parameter for mode conversion at the dipping interface. Equation (4.91) can be rearranged to give

$$\theta = \tan^{-1} \left[ \frac{\alpha_n \beta_n (p_2 - p_1)}{\alpha_n \sqrt{1 - p_2^2 \beta_n^2} + \beta_n \sqrt{1 - p_1^2 \alpha_n^2}} \right]. \quad (4.92)$$

The DMO curves are made by constructing the zero-offset response to the migration curves. Figure 4.15 has been drawn to indicate that the zero-offset down-going and up-going raypaths are coincident; this is not true in general (Section 5.2). The down-going  $P$ -wave will be incident at some small angle  $\epsilon$ , and the up-going  $S$ -wave will be converted at an angle  $\xi$  (Figure 4.16). If  $p_0$  is the ray parameter for zero-offset mode conversion at the dipping reflector, then Snell's Law gives

$$p_0 = \frac{\sin \epsilon}{\alpha_n} = \frac{\sin \xi}{\beta_n}. \quad (4.93)$$

Defining the two ray parameters  $p_\epsilon$  and  $p_\xi$  as

$$p_\epsilon = \frac{\sin(\theta + \epsilon)}{\alpha_n} \quad \text{and} \quad p_\xi = \frac{\sin(\theta - \xi)}{\beta_n}, \quad (4.94)$$

then  $p_\epsilon$  and  $p_\xi$  are given in terms of  $p_0$  by

$$p_\epsilon = \frac{\sin \theta}{\alpha_n} \sqrt{1 - p_0^2 \alpha_n^2} + p_0 \cos \theta \quad (4.95a)$$

and

$$p_\xi = \frac{\sin \theta}{\beta_n} \sqrt{1 - p_0^2 \beta_n^2} - p_0 \cos \theta. \quad (4.95b)$$

The offset  $\Delta x$  from the point of mode conversion (Figure 4.15) must be the same for the down-going and up-going zero-offset raypaths, i.e.,

$$\Delta x = p_\epsilon \sum_{i=1}^n \frac{\alpha_i z_i}{\sqrt{1 - p_\epsilon^2 \alpha_i^2}} = p_\xi \sum_{i=1}^n \frac{\beta_i z_i}{\sqrt{1 - p_\xi^2 \beta_i^2}}. \quad (4.96)$$

The value of  $p_0$  that satisfies equations (4.95) and (4.96) can be found by iteration, and the

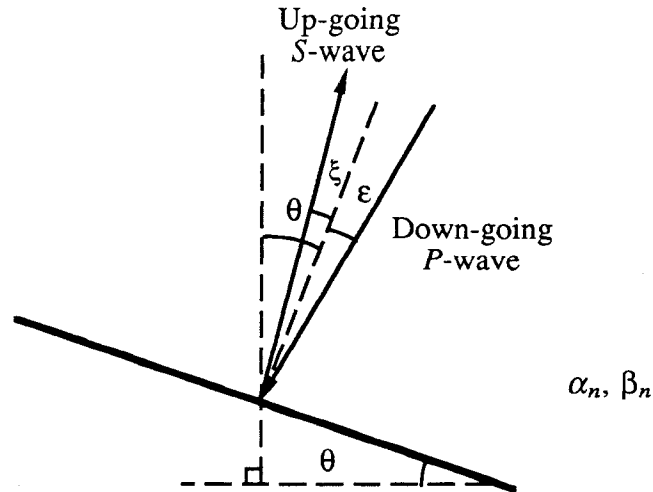


FIG. 4.16. Zero-offset mode-conversion from a dipping reflector situated beneath a number of horizontal layers.

offset  $\Delta x$  computed. The DMO midpoint-offset  $\chi$  is then given by

$$\chi = x + \Delta x - h , \quad (4.97)$$

and the zero-offset traveltime  $\tau$  is

$$\tau = \sum_{i=1}^n \frac{z_i}{\alpha_i \sqrt{1 - p_\xi^2 \alpha_i^2}} + \sum_{i=1}^n \frac{z_i}{\beta_i \sqrt{1 - p_\xi^2 \beta_i^2}} . \quad (4.98)$$

The DMO response can be constructed from the migration response by going through the following sequence for each point on the migration response:

- (1) compute the dip angle  $\theta$  from the ray parameters  $p_1$  and  $p_2$  [equation (4.92)];
- (2) find the value of  $p_0$  that satisfies equations (4.95) and (4.96);
- (3) compute the offset  $\Delta x$  using equation (4.96);
- (4) compute the DMO midpoint-offset  $\chi$  using equation (4.97);
- (5) compute the DMO zero-offset traveltime  $\tau$  using equation (4.98);
- (6) map the migration value at  $(x, t_z)$  onto the DMO point at  $(\chi, \tau)$ .

This method was applied to some test data using a velocity model (Table 4.1) consisting of four layers over a half-space. A constant  $Vp/Vs$  value was used to simplify the ray-tracing procedure; for this case the up-going and down-going raypaths are coincident (Section 5.2) and  $p_0=0$ . Equations (4.94) then reduce to

$$p_\varepsilon = \frac{\sin \theta}{\alpha_n} \quad \text{and} \quad p_\xi = \frac{\sin \theta}{\beta_n}, \quad (4.99)$$

simplifying the calculation of  $\chi$  and  $\tau$ .

The migration response computed by raytracing for a source-to-receiver offset of 1 km is shown in Figure 4.17, and the corresponding ray-traced DMO operator is shown in Figure 4.18. Across layer boundaries, the migration wavefronts display obvious discontinuities that create breaks in the DMO response curves. These breaks cannot be generated by the DMO equation developed in this chapter; the DMO algorithm can therefore only be expected to match the inner part of the ray-traced DMO response, up to the first point of discontinuity.

A DMO response generated using equation (4.49) for the same input data is shown in Figure 4.19. The response was constructed about the location of the zero-dip conversion point, approximated using equations (2.26), using average  $P$ -wave and average  $S$ -wave velocities in equation (4.49), i.e.,

$$\alpha \Rightarrow \bar{\alpha}(z) = \frac{z}{\sum_{i=1}^n \frac{z_i}{\alpha_i}} \quad \text{and} \quad \beta \Rightarrow \bar{\beta}(z) = \frac{z}{\sum_{i=1}^n \frac{z_i}{\beta_i}}, \quad (4.100)$$

where  $z$  is the depth of the zero-dip conversion point, located within the  $n$ 'th layer. The phase and amplitude corrections discussed in Section 4.8.1 have not been applied to the response displayed in Figure 4.19.

Comparison of the inner parts of the responses in Figures 4.18 and 4.19 shows that the two are in close agreement. Other DMO operators generated using RMS and interval  $P$ -

Table 4.1. Velocities used to generate the ray-traced migration and DMO responses.

Two-way <i>P-SV</i> time	<i>P</i> -wave velocity	<i>S</i> -wave velocity
300 ms	2500 m/s	1250 m/s
600 ms	3000 m/s	1500 m/s
900 ms	3500 m/s	1750 m/s
1200 ms	4000 m/s	2000 m/s
$\infty$	4500 m/s	2250 m/s

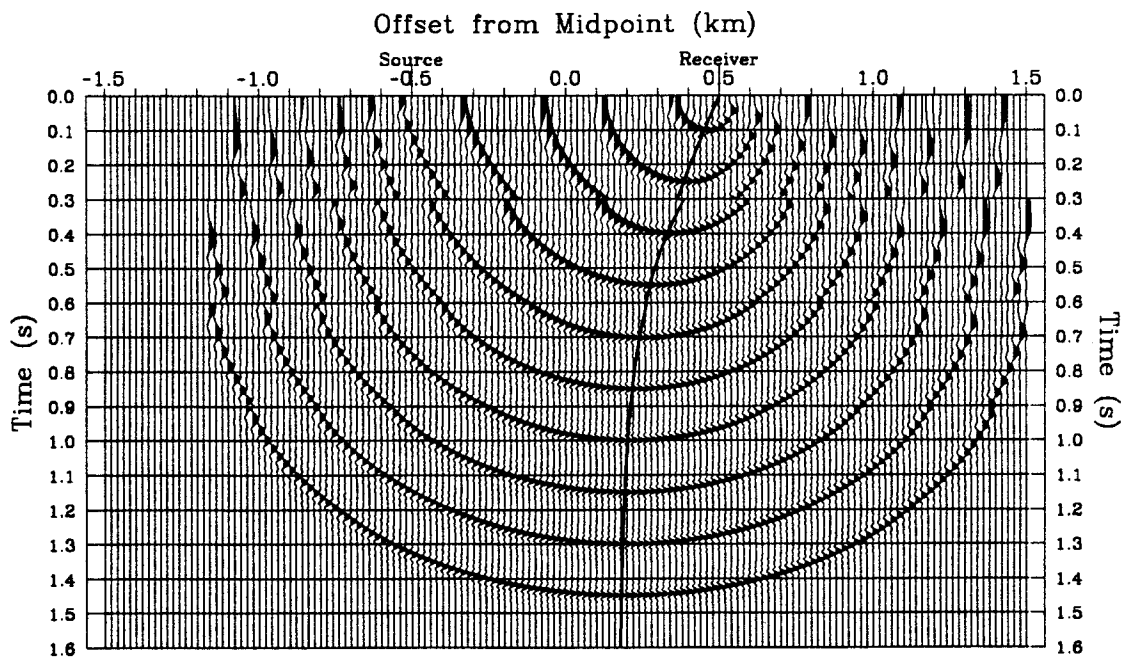


FIG. 4.17. Ray-traced *P-SV* migration response for the velocity field given in Table 4.1. The heavy line indicates the ray-traced location of the zero-dip conversion point.

and *S*-wave velocities in equation (4.49) were found to give slightly worse matches to the ray-traced operator (Figure 4.18). The differences between DMO operators were, however, small within the inner part of the DMO curves, indicating that equation (4.49) is fairly insensitive to velocity.

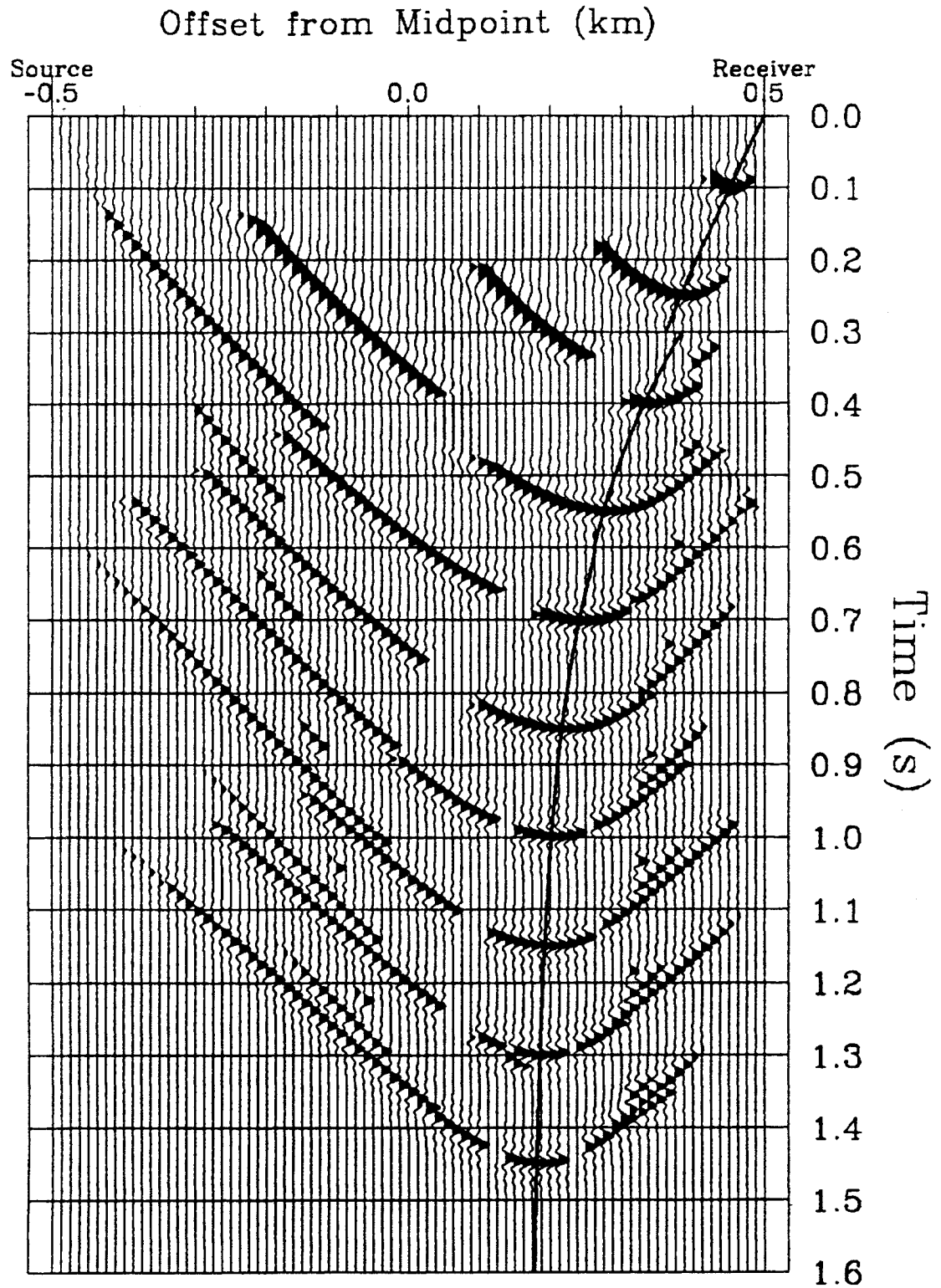


FIG. 4.18. Ray-traced *P-SV* DMO response corresponding to the migration response of Figure 4.17. The heavy line indicates the ray-traced location of the zero-dip conversion point.

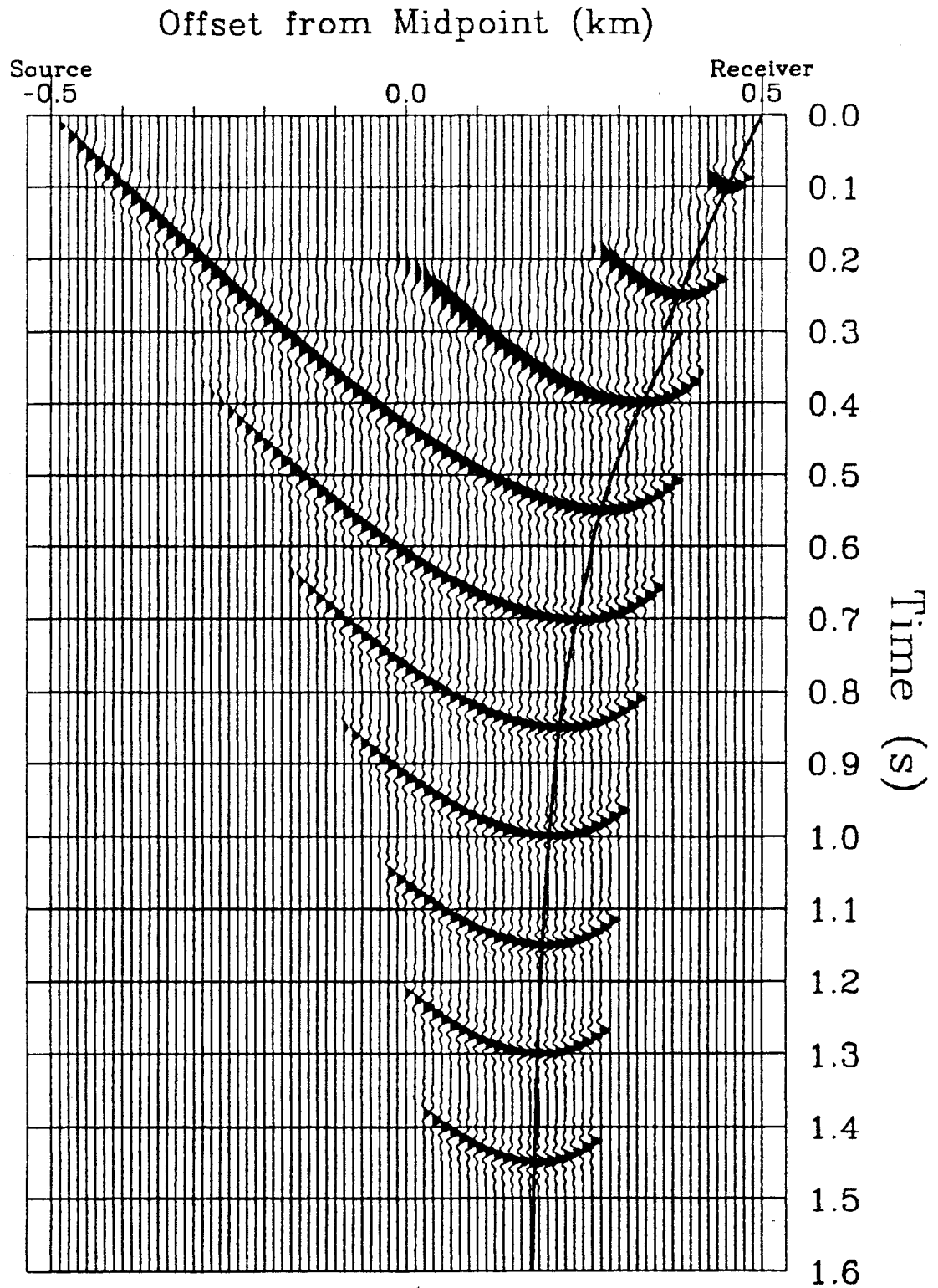


FIG. 4.19. *P-SV* DMO response computed using equation (4.49) and average *P*- and *S*-wave velocities. The heavy line indicates the ray-traced location of the zero-dip conversion point.

Because of the results obtained by comparison of various DMO responses to the response generated by raytracing, the *P-SV* DMO algorithm was implemented using average *P*- and *S*- wave velocities [equation (4.100)] in equation (4.49).

### 4.8.3 Application of *P-SV* DMO to synthetic data

A synthetic radial-component test data set was created using the Uniseis® raytracing program with the parameters listed in Table 4.2. The final data were constructed by summing six separate sets of records, giving source gathers with several reflectors having varying dips. Each of the six models was composed of a single layer having a *P*-wave velocity of 3000 m/s and an *S*-wave velocity of 1500 m/s, overlying a halfspace with a *P*-wave velocity of 3500 m/s and an *S*-wave velocity of 1750 m/s. The density in all cases was kept constant at 2200 kg/m<sup>3</sup>. The final summed data set has reflections from two flat interfaces at depths of 1 and 2 km, and from four interfaces having dips of 15°, 30°, 45°, and 60°. A *P*-wave source was used, and only *P-SV* reflections were generated by the ray-tracing program; multiple reflections were not included. The total data volume was made up of 41 split-spread records of 96-trace data. In order to better-assess the performance of the DMO operation, all AVO effects were initially removed from the data. Several NMO-corrected source gathers are shown in Figure 4.20, on which the polarity reversal between the two sides of the source spreads (Section 2.2) can clearly be seen.

The result of stacking the data volume using the asymptotic approximation (Fromm et al., 1985) is shown in Figure 4.21. It is seen from the figure that the three most-steeply-dipping reflectors have been attenuated, especially at shallow depth. Figure 4.22 is the result of stacking the data by true conversion point, accomplished by applying *P-SV* DMO with a very small dip aperture. It is seen that true CCP stacking causes the dipping layers to be more attenuated and "jittery" than does the asymptotic method (discussed later).

Table 4.2. Parameters used in generating the synthetic DMO test data.

Group interval	25 m
Source interval	50 m
Traces per record	96
Trace offsets	25 m to 1200 m, 25 m increment split-spread records
Data bandwidth	5-35 Hz
Sample rate	0.004 s

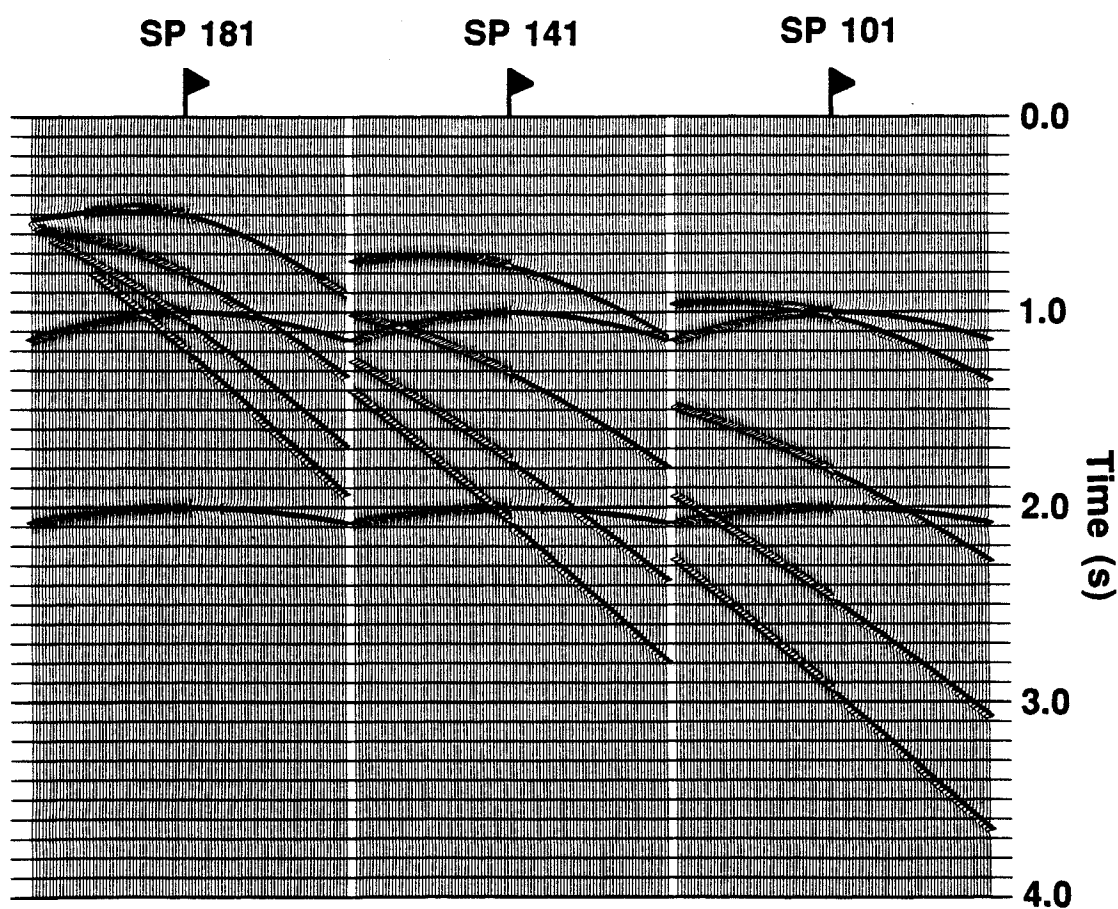


FIG. 4.20. Several NMO-corrected source gathers from the synthetic data set. All AVO effects have been removed.

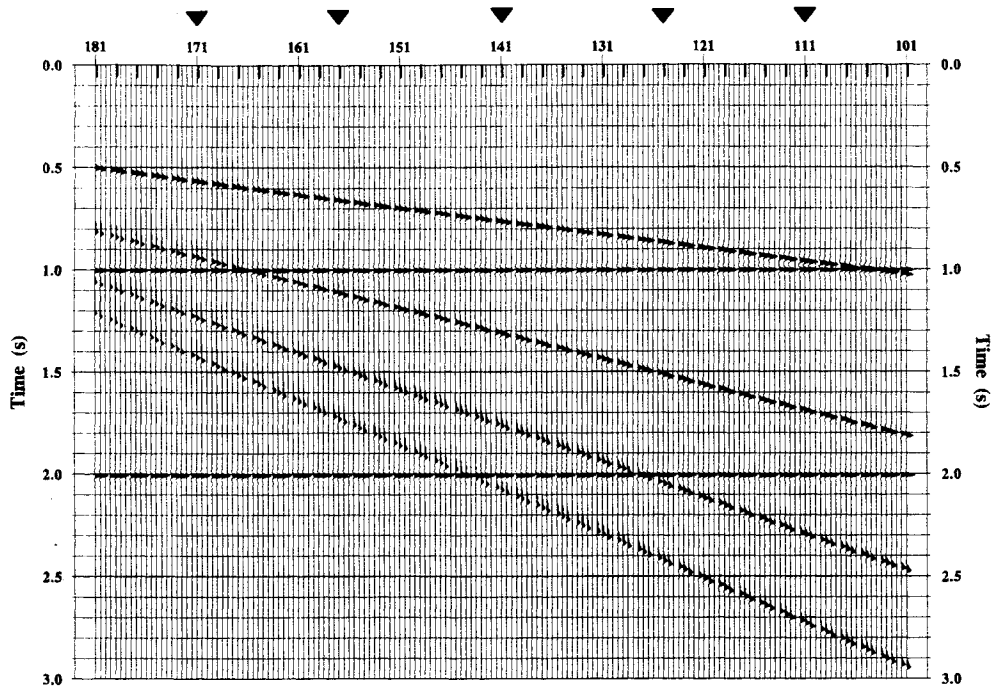


FIG. 4.21. Synthetic data stacked using the asymptotic gathering method.

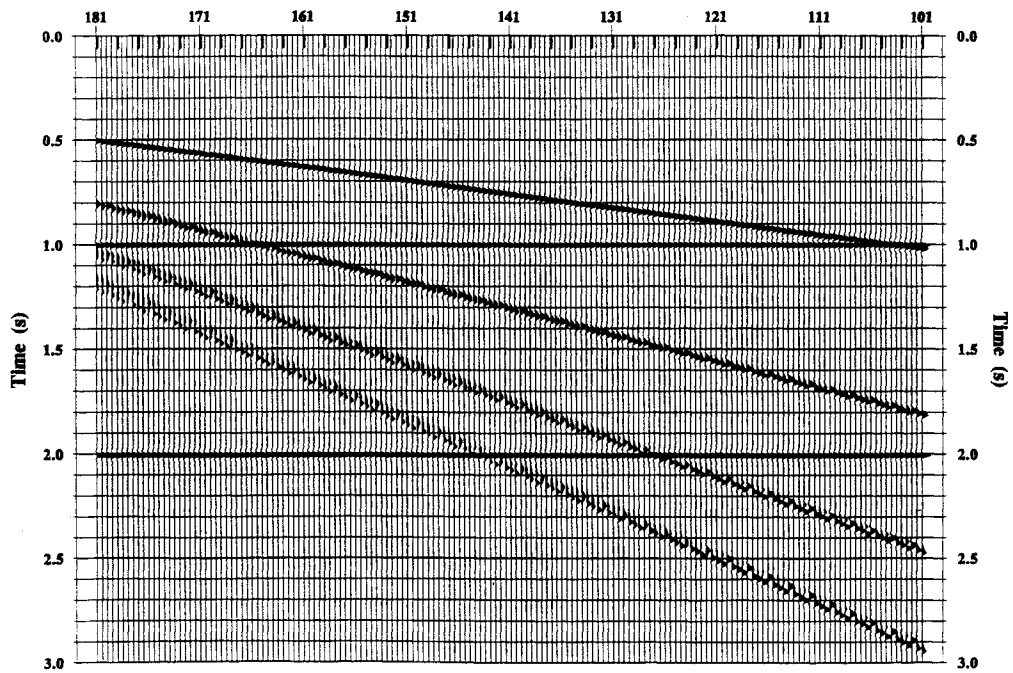


FIG. 4.22. Synthetic data stacked using true conversion-point gathering.

Figure 4.23 shows the result of applying  $P$ - $SV$  DMO to the data using a dip aperture of  $80^\circ$ . Comparing this result to Figures 4.21 and 4.22, it is seen that there is less attenuation of the dipping reflectors. Figure 4.24 shows NMO-corrected gathers taken from the positions indicated at the top of Figures 4.21 and 4.23, first after asymptotic gathering (Figure 4.24a), then after DMO has been applied in twelve constant-offset planes (Figure 4.24b). The dipping events on the asymptotic gathers are visibly overcorrected, whereas the events in the DMO gathers are nearly flat.

AVO effects are significant in  $P$ - $SV$  data; to evaluate the performance of  $P$ - $SV$  DMO in a more physically realistic case, the model data were again processed with AVO effects retained. The result of stacking this second data set using the asymptotic binning method is shown in Figure 4.25, and the section obtained by applying  $P$ - $SV$  DMO is shown in Figure 4.26. In this case, DMO is again seen to produce an improvement in the dipping events.

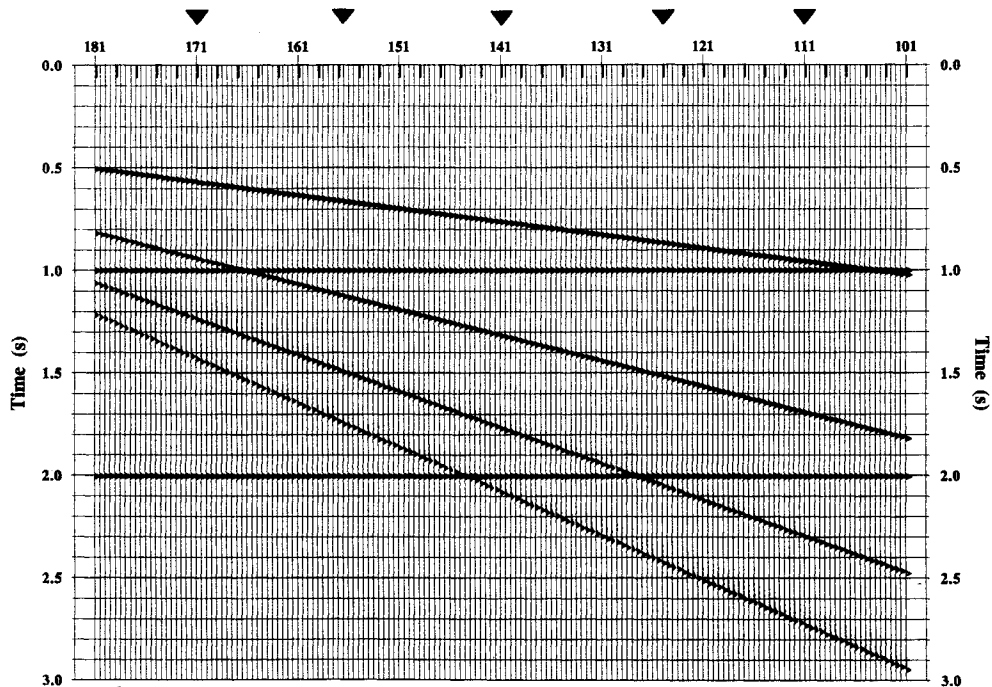
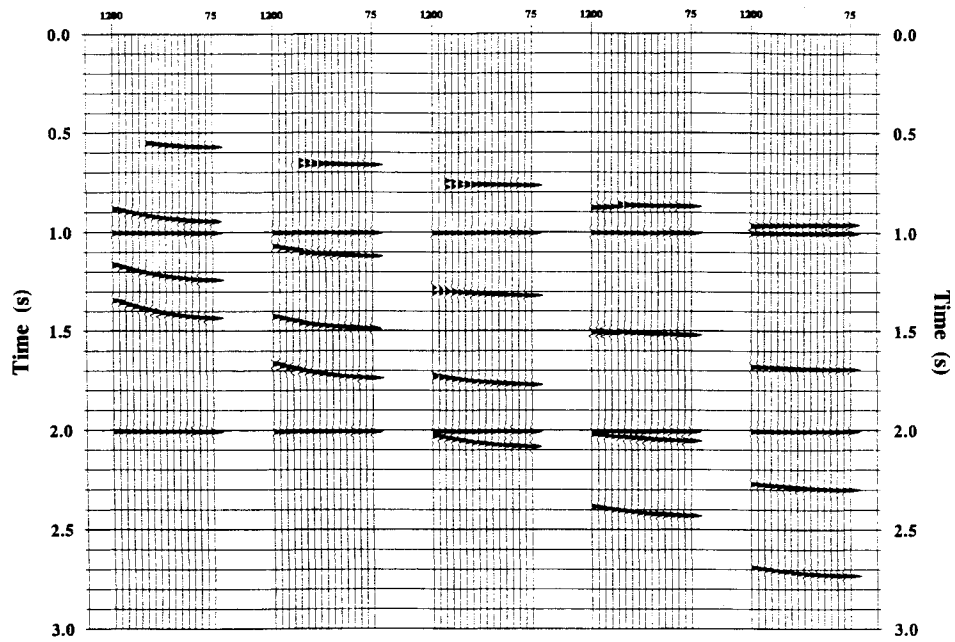
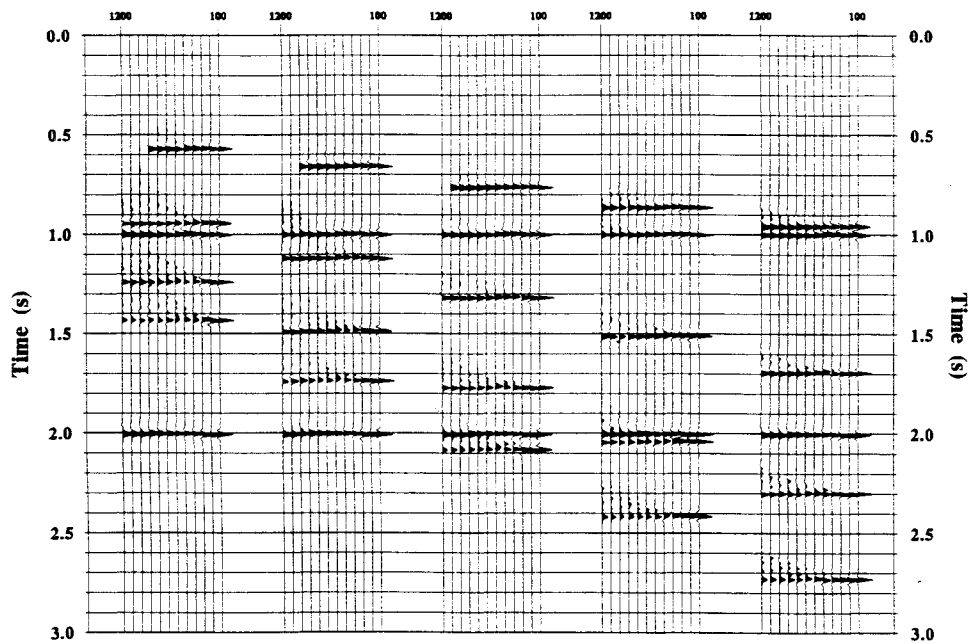


FIG. 4.23. Synthetic data stacked using  $P$ - $SV$  dip moveout.



(a)



(b)

FIG. 4.24. NMO-corrected gathers after (a) asymptotic gathering and (b)  $P$ - $SV$  DMO.

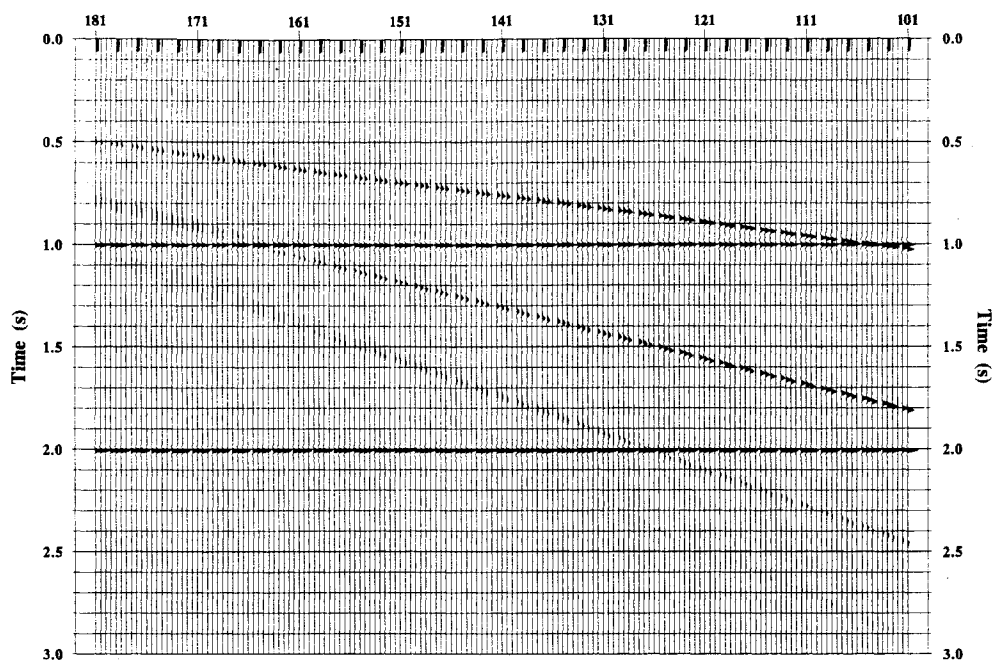


FIG. 4.25. AVO synthetic data stacked using asymptotic gathering.

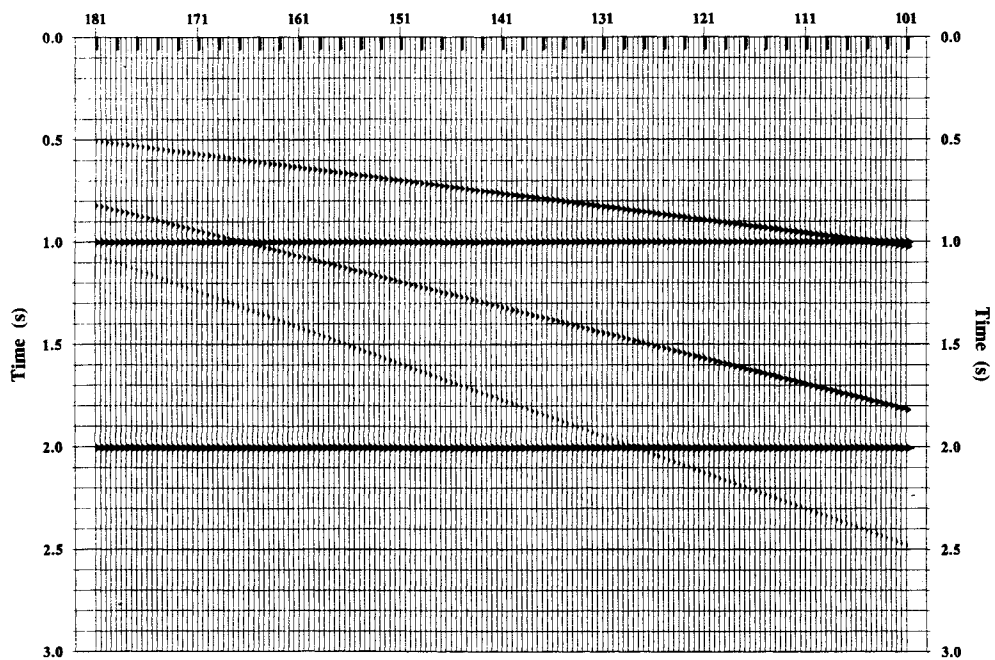


FIG. 4.26. AVO synthetic data stacked using *P-SV* dip moveout.

## 4.9 Discussion

From Figure 4.6, it can be seen that parts of the shallow migration curves correspond to conversion by transmission, rather than reflection. Because a seismic section is usually considered to be a reflection image, it may be desirable to suppress this part of the migration and DMO curves. In real data, however, the mute applied to eliminate early noise would also remove the data to which these curves would correspond, making suppression by other means unnecessary.

It is interesting to note that asymptotic binning appears to better preserve dipping data than does true CCP stacking, as can be seen from Figures 4.21 and 4.22. This appears to be due to the decrease in CCP dispersal produced by the asymptotic approximation for data converted from positive-dip interfaces. Although there is a corresponding increase in the dispersal for negative-dip data, the dispersal for positive dips is significantly greater than for negative dips, as can be seen from Figure 4.2. The overall result appears to be a net decrease in the attenuation of dipping layers that have been gathered and stacked using the asymptotic method.

As mentioned in Section 4.8.1, the phase and amplitude corrections are frequency dependent. At larger offsets, where the asymptotic gain function [equation (4.83)] is appropriate, a visible attenuation of higher frequencies can be seen on the DMO gathers of Figure 4.24b. Improved results could be achieved if the phase and amplitude corrections were made frequency-dependent, but this would greatly increase the expense of constructing the DMO operators. As an alternative to this, the "vase" method of Hale (1988) could perhaps be implemented. This method uses a shaping filter designed from a reference trace to empirically correct for operator phase and amplitude distortion, and should give improved results. It is, however, also computationally intensive.

An area for future work is to try to obtain a P-SV DMO equation that is more appropriate for depth-varying velocities. It was seen in Section 4.8.2 that the actual shape

of DMO responses can be very different from those given by equation (4.49), and that the algorithm has to be modified considerably in order to give discontinuous, multivalued DMO responses like Figure 4.18.

In summary, the problems of apparent velocity and CCP dispersal for converted-wave surface data were addressed in this chapter. A dip moveout (DMO) equation for *P-SV* data was derived, and was shown to properly account for CCP dispersal for the constant-velocity case. An integral-style *P-SV* DMO algorithm was developed, based on the DMO equation derived here, and applied to a synthetic data example. The results indicate that the DMO operation does give better reflector continuity, as expected. Other examples of applying *P-SV* DMO can be found in the following chapters.

## Chapter 5 - Poststack migration of *P-SV* data

### 5.1 Introduction

The use of appropriate normal moveout (NMO) corrections, coupled with converted-wave (*P-SV*) dip moveout (DMO), allows the construction of stack sections that are zero-offset in the kinematic sense. An obvious extension to converted-wave processing is to apply some sort of poststack migration to these sections, in order to properly position dipping reflectors and collapse diffractions. Various authors (e.g., Garotta, 1987) have shown that *P-SV* stack sections can, in practice, be migrated. However, to my knowledge, the theory of *P-SV* poststack migration has not yet been addressed, except for the constant-velocity case (Eaton et al., 1991). The purpose of this chapter is to establish the shape of *P-SV* diffractions from point scattering in a multi-layered medium, and derive a velocity function that will properly migrate them. As the migration process can be thought of as a 2-D deconvolution process in which the point-response function is removed (Brouwer et al., 1985), adequately migrating a diffraction curve is equivalent to removing the point-response function, and ensures correct migration of all other data.

To test the accuracy of the migration velocity equation presented here, poststack migration is applied to synthetic data sets containing reflections from a number of point diffractors. These data were stacked using both depth-variant binning (Eaton et al., 1990) and *P-SV* DMO (Chapter 4). The resulting DMO sections are migrated using both the migration velocity equation developed here and the RMS stacking velocities (Tessmer and Behle, 1988). A set of radial-component physical model data was also migrated to further evaluate the migration equation (Section 5.3.2). For the remainder of this chapter depth-variant binning will be abbreviated as DVB.

## 5.2 Migration velocity derivation

Consider conversion from the point diffractor shown in Figure 5.1. The point is at a distance  $x$  away from the surface common conversion point (CCP) position, where both the source and receiver are located. Energy travels from the source to the point along the path segments  $a_i$  with  $P$ -wave velocity  $\alpha_i$ , and back from the point along the path segments  $b_i$  with  $S$ -wave velocity  $\beta_i$ . The total travelttime  $t$  is given by

$$t = \sum_{i=1}^n \frac{a_i}{\alpha_i} + \sum_{i=1}^n \frac{b_i}{\beta_i}. \quad (5.1)$$

For the downward path, the ray parameter  $p_1$  is constant, and for the upward path the second ray parameter  $p_2$  is constant;

$$p_1 = \frac{\sin \theta_i}{\alpha_i} \quad \text{and} \quad p_2 = \frac{\sin \phi_i}{\beta_i} \quad \text{for all } i. \quad (5.2)$$

The total horizontal distance traveled along both up-going and down-going paths is equal to the offset  $x$ ;

$$x = \sum_{i=1}^n z_i \tan \theta_i = \sum_{i=1}^n z_i \tan \phi_i,$$

or, using equations (5.2),

$$x = p_1 \sum_{i=1}^n \frac{\alpha_i z_i}{\sqrt{1-p_1^2 \alpha_i^2}} = p_2 \sum_{i=1}^n \frac{\beta_i z_i}{\sqrt{1-p_2^2 \beta_i^2}}. \quad (5.3)$$

Within the  $i$ 'th layer

$$c = \frac{p_2}{p_1} = \frac{\sin \phi_i}{\beta_i} \frac{\alpha_i}{\sin \theta_i},$$

or

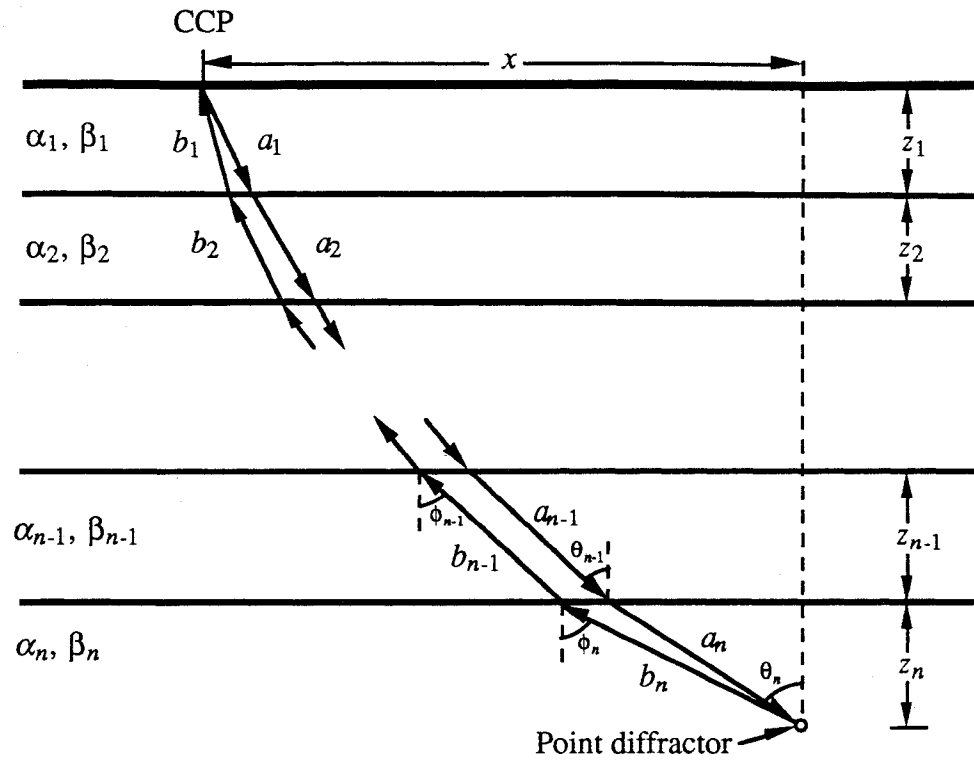


FIG. 5.1. Zero-offset raypaths traveled through a layered Earth from a point diffractor.

$$\sin \phi_i = \frac{c}{\gamma_i} \sin \theta_i, \quad (5.4)$$

where  $\gamma_i$  is the  $Vp/Vs$  ( $\alpha/\beta$ ) value for the layer and  $c$  is a constant for all layers. It is seen from equation (5.4) that the angles  $\theta_i$  and  $\phi_i$  cannot be the same for all layers if the  $Vp/Vs$  values vary with depth; the up-going and down-going raypaths then do not coincide. If the raypaths do coincide, then  $\theta_i = \phi_i$  for all  $i$ , and equation (5.4) gives

$$\gamma_i = c \quad \text{for all } i, \quad (5.5)$$

showing that the  $Vp/Vs$  value must be constant for this case. The exploding reflector model (Loewenthal et al., 1976) is, therefore, not strictly appropriate for  $P$ - $SV$  data unless the  $Vp/Vs$  value is depth-independent.

In terms of the two ray parameters, equation (5.1) can be rewritten as

$$t = \sum_{i=1}^n \frac{z_i}{\alpha_i \sqrt{1-p_1^2 \alpha_i^2}} + \sum_{i=1}^n \frac{z_i}{\beta_i \sqrt{1-p_2^2 \beta_i^2}}. \quad (5.6)$$

To obtain an approximate solution for  $t$ , a Taylor's series expansion can be performed about  $x = 0$  (the small diffractor offset case);

$$t \cong t_0 + x \left( \frac{dt}{dx} \right)_{x=0} + \frac{x^2}{2} \left( \frac{d^2t}{dx^2} \right)_{x=0} + \frac{x^3}{6} \left( \frac{d^3t}{dx^3} \right)_{x=0} + O(x^4), \quad (5.7)$$

where  $O(x^4)$  represents terms of order  $x^4$  and higher, and  $t_0$  is the two-way vertical traveltime;

$$\begin{aligned} t_0 &= \sum_{i=1}^n \left( \frac{\alpha_i + \beta_i}{\alpha_i \beta_i} \right) z_i \\ &= \sum_{i=1}^n \tau_i, \end{aligned} \quad (5.8)$$

where  $\tau_i$  is the two-way vertical traveltime through the  $i$ 'th layer. The odd-order terms in equation (5.7) must vanish because of cylindrical symmetry. The total derivative of  $t$  w.r.t.  $x$  is

$$\frac{dt}{dx} = \frac{\partial t}{\partial p_1} \frac{dp_1}{dx} + \frac{\partial t}{\partial p_2} \frac{dp_2}{dx}. \quad (5.9)$$

Differentiating equation (5.3) w.r.t.  $p_1$  and  $p_2$  gives

$$\frac{dx}{dp_1} = \sum_{i=1}^n \frac{\alpha_i z_i}{(1-p_1^2 \alpha_i^2)^{3/2}} \quad (5.10)$$

and

$$\frac{dx}{dp_2} = \sum_{i=1}^n \frac{\beta_i z_i}{(1-p_2^2 \beta_i^2)^{3/2}}. \quad (5.11)$$

Differentiating equation (5.6) w.r.t.  $p_1$  gives

$$\frac{\partial t}{\partial p_1} = p_1 \sum_{i=1}^n \frac{\alpha_i z_i}{(1-p_1^2 \alpha_i^2)^{3/2}} = p_1 \frac{dx}{dp_1}, \quad (5.12)$$

where equation (5.10) has been used. This gives

$$\frac{\partial t}{\partial p_1} \frac{dp_1}{dx} = p_1. \quad (5.13)$$

Similarly

$$\frac{\partial t}{\partial p_2} \frac{dp_2}{dx} = p_2, \quad (5.14)$$

and equation (5.9) becomes

$$\frac{dt}{dx} = p_1 + p_2. \quad (5.15)$$

Equation (5.15) shows the total horizontal slowness to be the sum of the two ray parameters. At  $x = 0$ , both ray parameters are also zero, giving

$$\left(\frac{dt}{dx}\right)_{x=0} = 0. \quad (5.16)$$

Differentiating equation (5.15) w.r.t.  $x$  results in

$$\begin{aligned} \frac{d^2 t}{dx^2} &= \frac{dp_1}{dx} + \frac{dp_2}{dx} \\ &= \left[ \sum_{i=1}^n \frac{\alpha_i z_i}{(1-p_1^2 \alpha_i^2)^{3/2}} \right]^{-1} + \left[ \sum_{i=1}^n \frac{\beta_i z_i}{(1-p_2^2 \beta_i^2)^{3/2}} \right]^{-1}, \end{aligned} \quad (5.17)$$

where equations (5.10) and (5.11) have been used. At  $x = 0$ , equation (5.17) becomes

$$\begin{aligned} \left(\frac{d^2 t}{dx^2}\right)_{x=0} &= \left( \sum_{i=1}^n \alpha_i z_i \right)^{-1} + \left( \sum_{i=1}^n \beta_i z_i \right)^{-1} \\ &= \frac{\sum_{i=1}^n \alpha_i \beta_i \tau_i}{\left( \sum_{i=1}^n \frac{\alpha_i^2 \beta_i}{\alpha_i + \beta_i} \tau_i \right) \left( \sum_{i=1}^n \frac{\alpha_i \beta_i^2}{\alpha_i + \beta_i} \tau_i \right)}. \end{aligned} \quad (5.18)$$

Differentiating equation (5.17) w.r.t.  $x$  gives

$$\begin{aligned} \frac{d^3 t}{dx^3} &= \frac{d^2 p_1}{dx^2} + \frac{d^2 p_2}{dx^2} \\ &= -3p_1 \frac{\left[ \sum_{i=1}^n \frac{\alpha_i^3 z_i}{(1-p_1^2 \alpha_i^2)^{5/2}} \right]}{\left[ \sum_{i=1}^n \frac{\alpha_i z_i}{(1-p_1^2 \alpha_i^2)^{3/2}} \right]^3} - 3p_2 \frac{\left[ \sum_{i=1}^n \frac{\beta_i^3 z_i}{(1-p_1^2 \beta_i^2)^{5/2}} \right]}{\left[ \sum_{i=1}^n \frac{\beta_i z_i}{(1-p_1^2 \beta_i^2)^{3/2}} \right]^3}, \end{aligned} \quad (5.19)$$

and

$$\left( \frac{d^3 t}{dx^3} \right)_{x=0} = 0. \quad (5.20)$$

Using equations (5.16), (5.18), and (5.20), equation (5.17) becomes

$$t = t_0 + \frac{x^2}{2} \left[ \frac{\sum_{i=1}^n \alpha_i \beta_i \tau_i}{\left( \sum_{i=1}^n \frac{\alpha_i^2 \beta_i}{\alpha_i + \beta_i} \tau_i \right) \left( \sum_{i=1}^n \frac{\alpha_i \beta_i^2}{\alpha_i + \beta_i} \tau_i \right)} \right] + O(x^4). \quad (5.21)$$

Squaring both sides of equation (5.21) gives

$$t^2 = t_0^2 + x^2 \left[ \frac{t_0 \sum_{i=1}^n \alpha_i \beta_i \tau_i}{\left( \sum_{i=1}^n \frac{\alpha_i^2 \beta_i}{\alpha_i + \beta_i} \tau_i \right) \left( \sum_{i=1}^n \frac{\alpha_i \beta_i^2}{\alpha_i + \beta_i} \tau_i \right)} \right] + O(x^4). \quad (5.22)$$

Comparing equation (5.22) to the standard equation for the diffraction hyperbola,

$$t^2 = t_0^2 + \frac{4x^2}{V_{mig}^2}, \quad (5.23)$$

where  $V_{mig}$  is the migration velocity, it is seen that for  $P$ - $SV$  data

$$V_{mig} = 2 \sqrt{\frac{\left( \sum_{i=1}^n \frac{\alpha_i^2 \beta_i}{\alpha_i + \beta_i} \tau_i \right) \left( \sum_{i=1}^n \frac{\alpha_i \beta_i^2}{\alpha_i + \beta_i} \tau_i \right)}{t_0 \sum_{i=1}^n \alpha_i \beta_i \tau_i}} \quad (5.24)$$

For the single-layer case, where  $n=1$ , equation (5.24) reduces to

$$\frac{1}{V_{mig}} = \frac{1}{2} \left( \frac{1}{\alpha} + \frac{1}{\beta} \right). \quad (5.25)$$

Equation (5.25) is the same result given by Eaton et al. (1991).

Equation (5.22) shows that, if terms of fourth-order and higher in  $x$  are ignored,  $P$ - $SV$  diffraction curves are also hyperbolic, and that a  $P$ - $SV$  stack section can be migrated using the velocity function defined by equation (5.24). This argument is only correct in a ray-theoretical sense, but it does give justification to applying poststack migration to  $P$ - $SV$  data.

Equation (5.24) can be compared to the  $P$ - $SV$  RMS velocity function given by Tessmer and Behle (1988):

$$V_{RMS} = \sqrt{\frac{\sum_{i=1}^n \alpha_i \beta_i \tau_i}{t_0}} \quad (5.26)$$

The form of the RMS and migration velocity equations is seen to be significantly different. For the case of constant  $V_p/V_s$  value, the ratio of RMS velocity to migration velocity reduces to

$$\frac{V_{RMS}}{V_{mig}} = \frac{\gamma + 1}{2\sqrt{\gamma}}, \quad \gamma = \frac{\alpha_i}{\beta_i} \text{ for all } i. \quad (5.27)$$

The function defined by equation (5.27) is plotted in Figure 5.2 for a range of  $V_p/V_s$  values. It is seen that the migration velocity is always less than the RMS velocity for this case.

### 5.3 Migration examples

In this section poststack migration is applied to two sets of synthetic  $P$ - $SV$  diffraction data (Section 5.3.1) and to a converted-wave physical model data set (Section 5.3.2). The data are migrated in each case using both the RMS velocities [equation(5.26)] and the migration velocity function defined by equation (5.24).

#### 5.3.1 Synthetic data

Two sets of synthetic data were created to evaluate the migration velocity equation. The geometry parameters used in generating synthetic shot records are summarized in Table 5.1. The total data volume in both cases consisted of 41 records of 121 traces each.

Each source record was constructed by performing 2-D ray-tracing through the two different media to compute the response to a number of point diffractors located at various depths beneath SP 181. The first sourcepoint was located at SP 101, and the last at SP 261. Diffraction amplitudes were computed using the following equation derived by Knopoff (1959);

$$A(\mathbf{r}) = \frac{\gamma^2 \sin \varphi}{\alpha(1+2\gamma^2)} \frac{A_0}{|\mathbf{r}|} \quad (5.28)$$

where

$A_0$  = initial wavelet amplitude,

$\mathbf{r}$  = source-to-receiver travelpath, and

$\varphi$  = angle between the incident and scattered rays.

The first data set was created using eight point diffractors positioned at depths ranging from 250 m to 2.0 km, embedded in a medium with  $P$ -wave velocity 3000 m/s and  $S$ -wave velocity 1500 m/s (Figure 5.3). The resulting traces were moveout corrected using

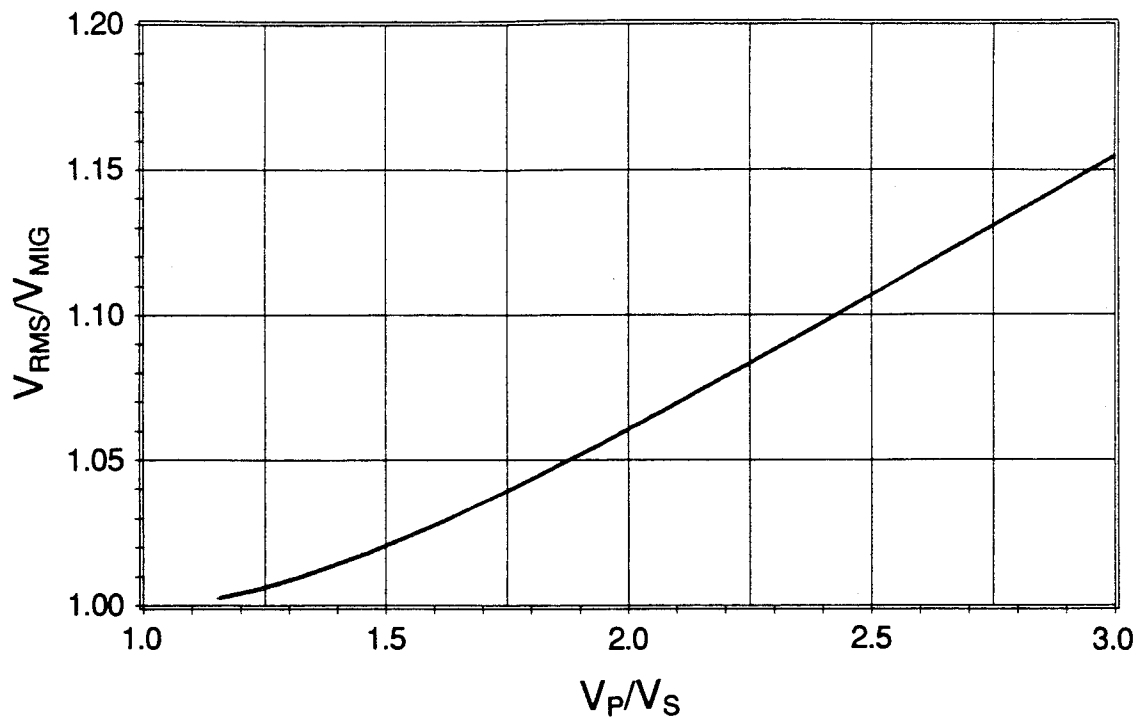


FIG. 5.2. Ratio of RMS velocity to migration velocity as a function of  $V_p/V_s$  value for the constant- $V_p/V_s$  case.

Table 5.1. Parameters used in generating the synthetic migration test data.

Group interval	25 m
Source interval	100 m
Traces per record	121
Trace offsets	0 to 1500 m, 25 m increment split-spread records
Nominal fold	15
Data bandwidth	8-35 Hz
Record length	3500 ms
Sample rate	2 ms

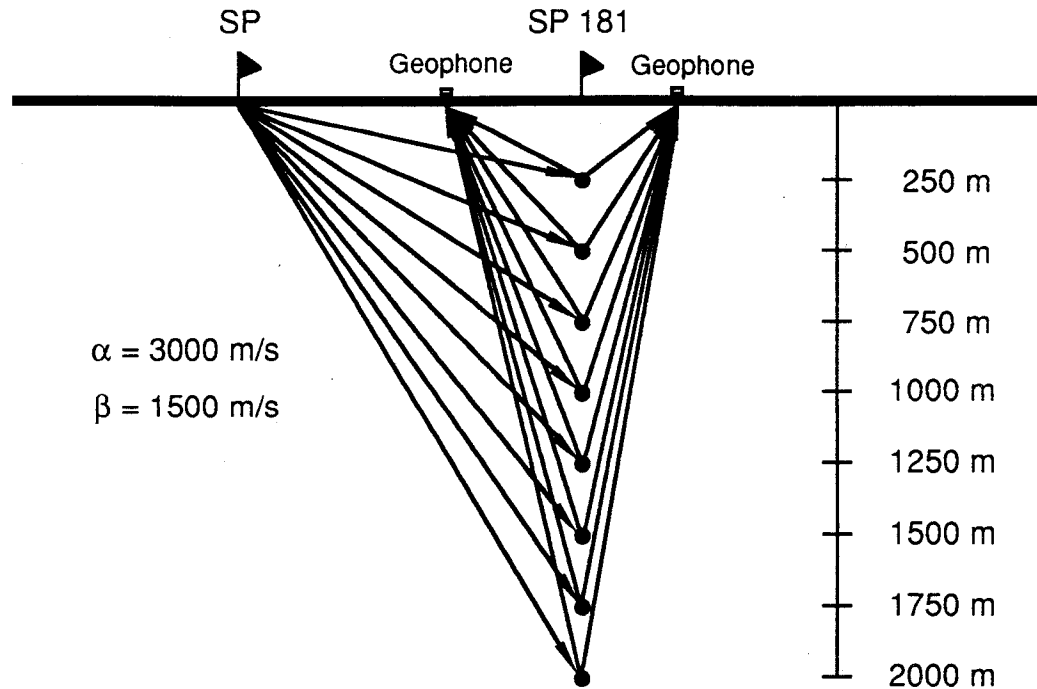


FIG. 5.3. Sample raypaths for diffracted energy received by two geophones. Diffractors are positioned at 250 m depth intervals, ranging from 250 m to 2000 m.

ray-traced NMO and scaled to compensate for spherical divergence. Several of these records are displayed in Figure 5.4.

After NMO, gain, and polarity reversal, the data were stacked using DVB and  $P$ -SV DMO, giving the results shown in Figures 5.5 and 5.6. The DMO section better preserves the diffraction tails, and was used as input to a phase-shift migration program (Gadzag, 1978) using both the RMS velocity function of equation (5.26) and the migration velocity function defined by equation (5.25). The diffractions are seen to be overmigrated using the RMS velocities (Figure 5.7a), but successfully collapsed using the migration velocity (Figure 5.7b). For this simple case equation (5.24) is exact, and the results shown in Figure 5.7b are the best that can be obtained for the geometry and wavelet bandwidth used.

As a more appropriate test of equation (5.24), a second set of synthetic records was created. The model for this case consists again of a number of point diffractors, but

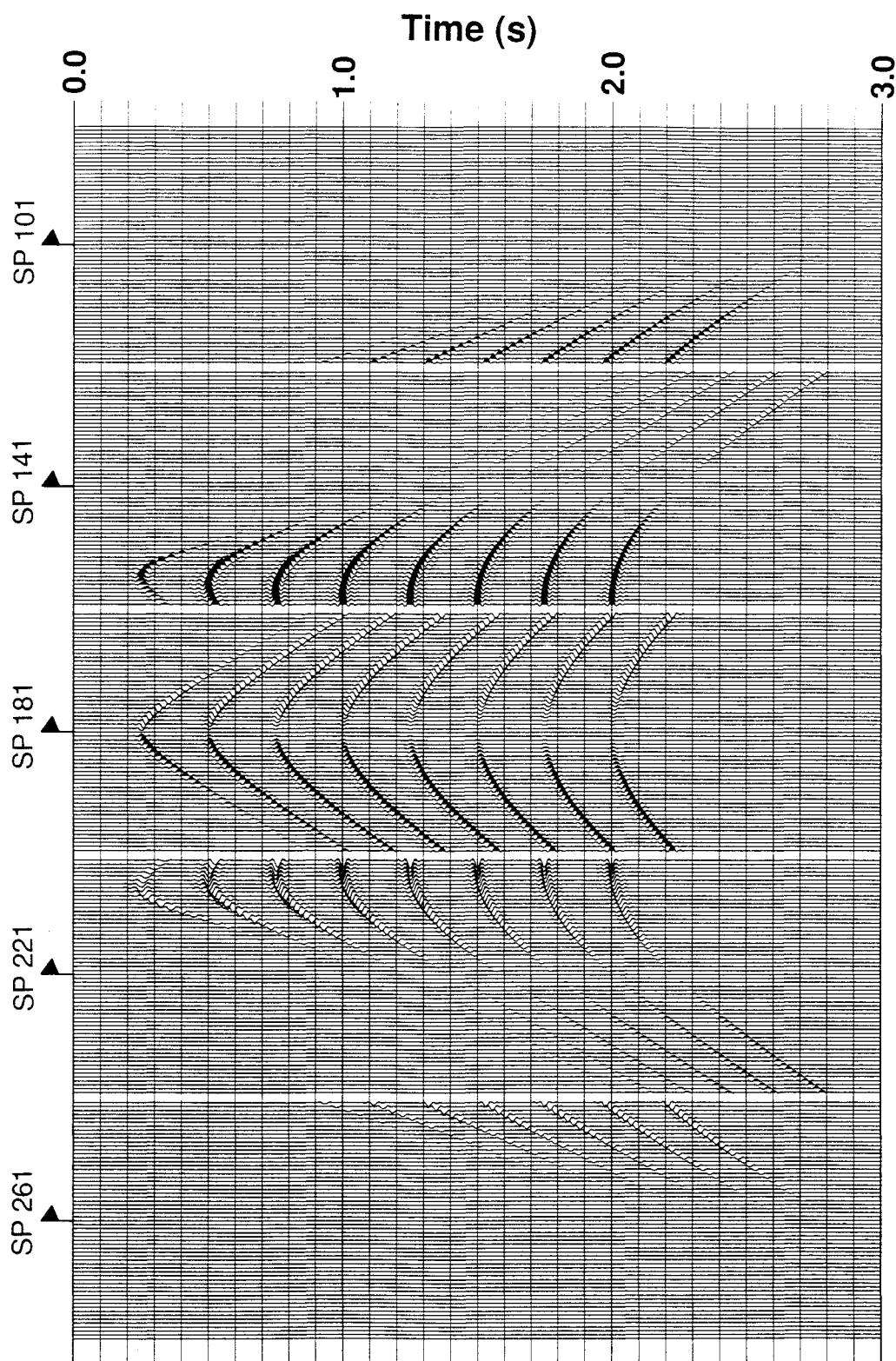


FIG. 5.4. Sample synthetic  $P$ - $SV$  records for the constant-velocity case. The data have been NMO corrected and scaled for spherical divergence. Every second trace is plotted.

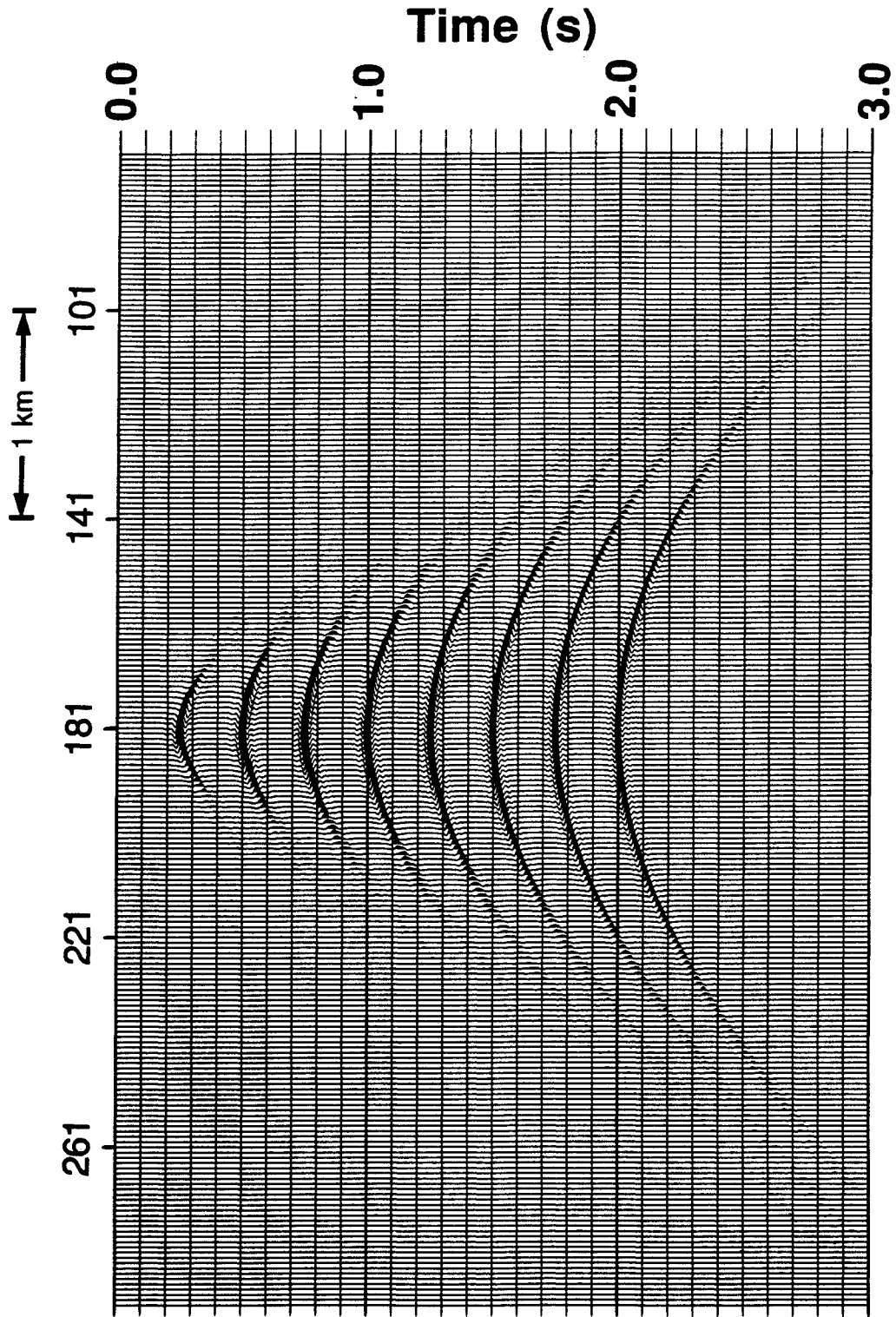


FIG. 5.5. Constant-velocity data stacked using depth-variant binning (DVB).  
Every second trace is plotted.

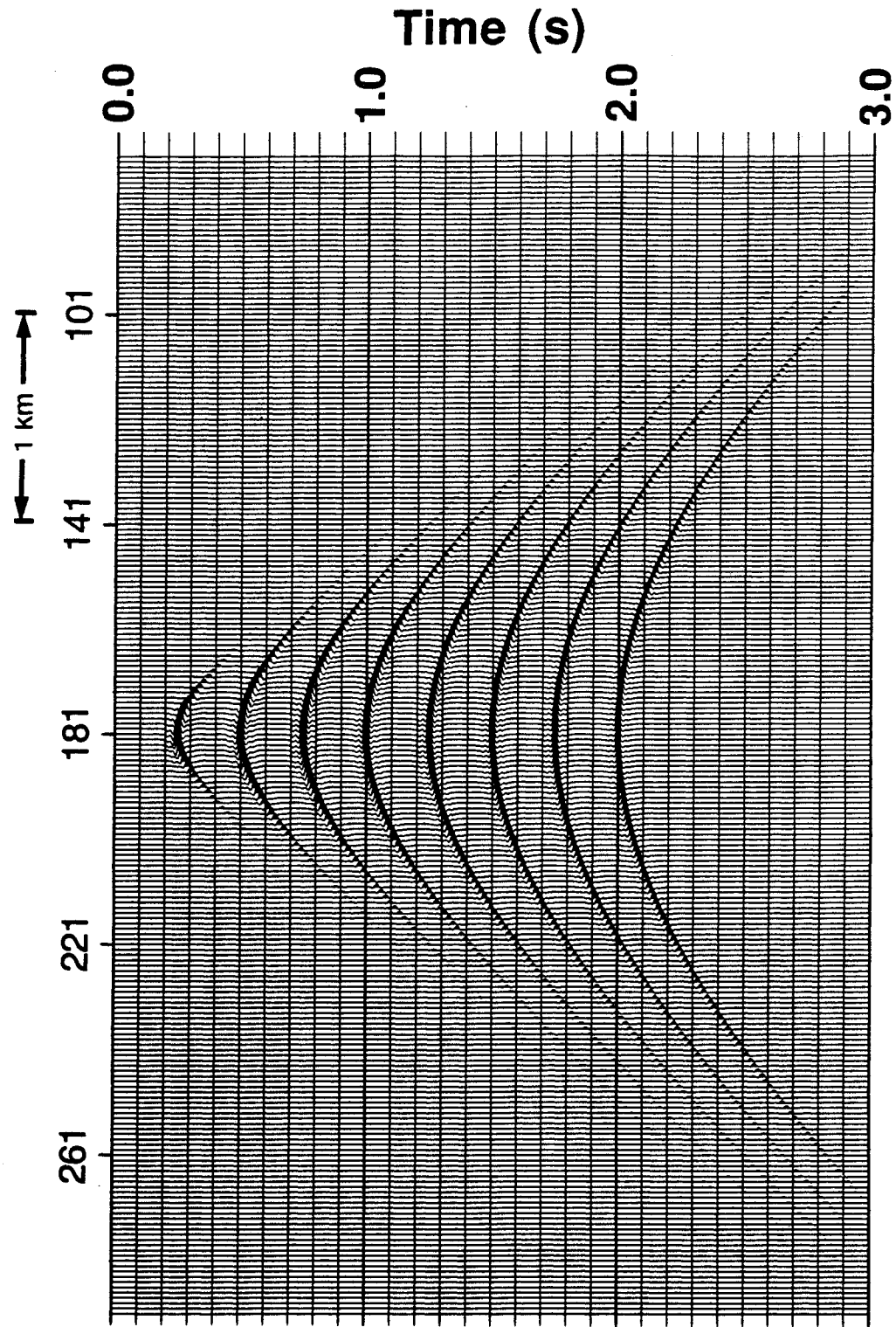


FIG. 5.6. Constant-velocity data stacked using *P-SV* DMO. Every second trace is plotted.

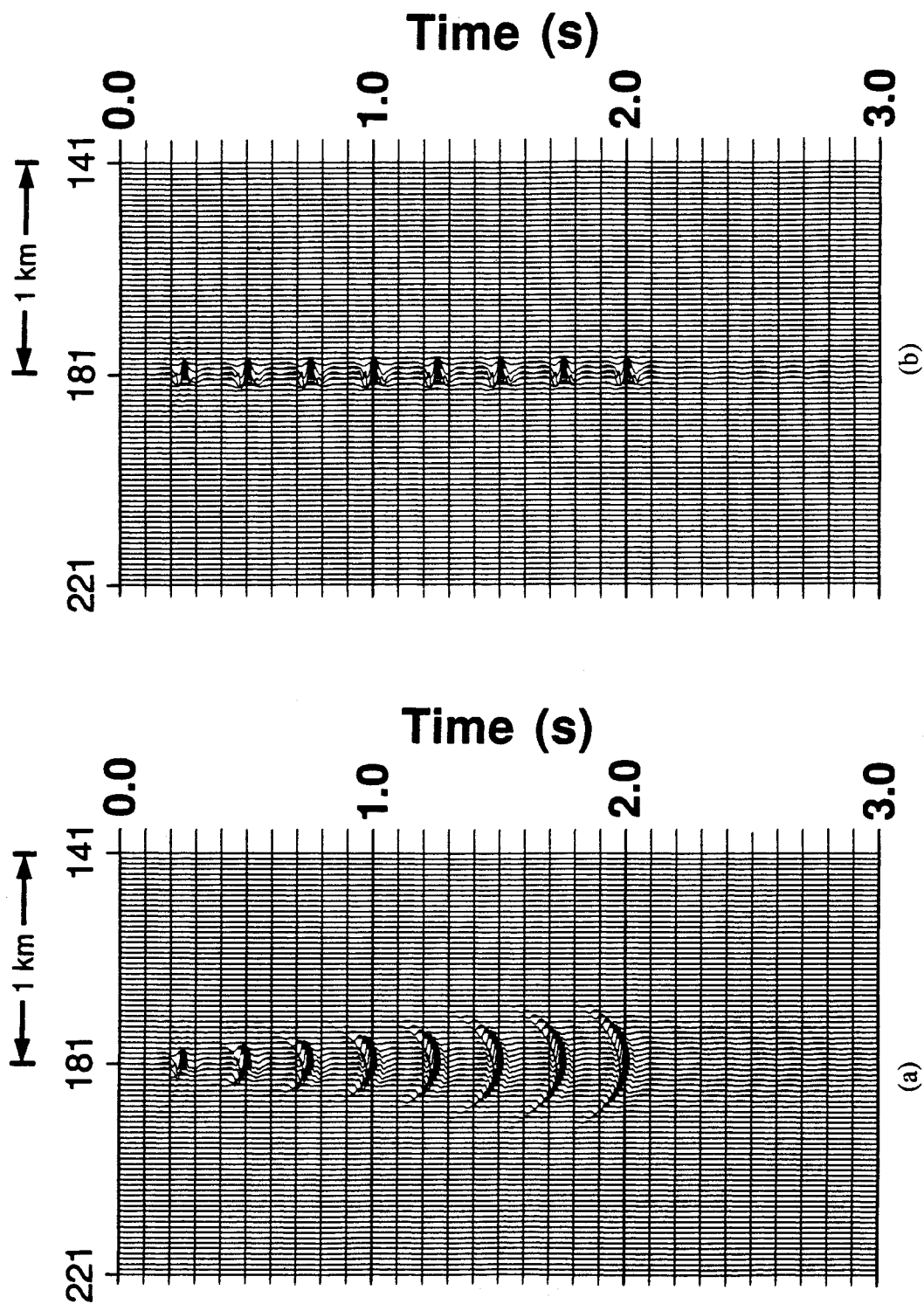


FIG. 5.7. DMO-stacked constant-velocity data migrated using: (a) the RMS velocity function; (b) the  $P$ - $SV$  migration velocity function. Every second trace is plotted.

embedded in a layered media having thirty-two different velocity intervals. The layer thickness and velocity values are based on a blocked sonic log from the Carrot Creek field of Alberta (Chapter 6), and are plotted vs. two-way  $P$ - $SV$  time in Figure 5.8. Also shown is the ratio of RMS and migration velocities, from which it is seen that the RMS velocities are about 6-11% greater than the migration velocities. Sample records are shown in Figure 5.9, again with ray-traced NMO and geometric spreading compensation applied.

The second data set was stacked using DVB (Figure 5.10) and depth-variant  $P$ - $SV$  DMO (Figure 5.11), in which the DMO response is constructed about the location of the zero-dip conversion point (Section 4.8.2). The DVB stack shows differences in curvature of the earlier (shallower) diffractions relative to the DMO section, as well as greater attenuation of the diffraction tails.

Phase shift migration applied to the DMO stack section using the RMS velocity function (Figure 5.12a) results in overmigration on the diffractions. Migration using the migration velocity function of equation (5.24) has successfully collapsed all but the last two diffractors, which are slightly undermigrated (Figure 5.12b). In further testing it was found that these two diffractions required a 2% increase in migration velocity to be completely collapsed.

### 5.3.2 Physical model data

The physical model shown in Figure 5.13 was constructed by Stewart and Marchisio (1991) to simulate a limestone reef buried beneath 1 km of shale overburden. A 2-D survey was conducted across the axis of the reef using a vertical source and vertical and radial receivers to give single-fold constant-offset sections. The scaled sourcepoint separation was 50 m, and the scaled source-to-receiver offset was 250 m. All data shown in this section have been NMO- and DMO-corrected, and filtered with a 4/8-60/70 Hz bandpass.

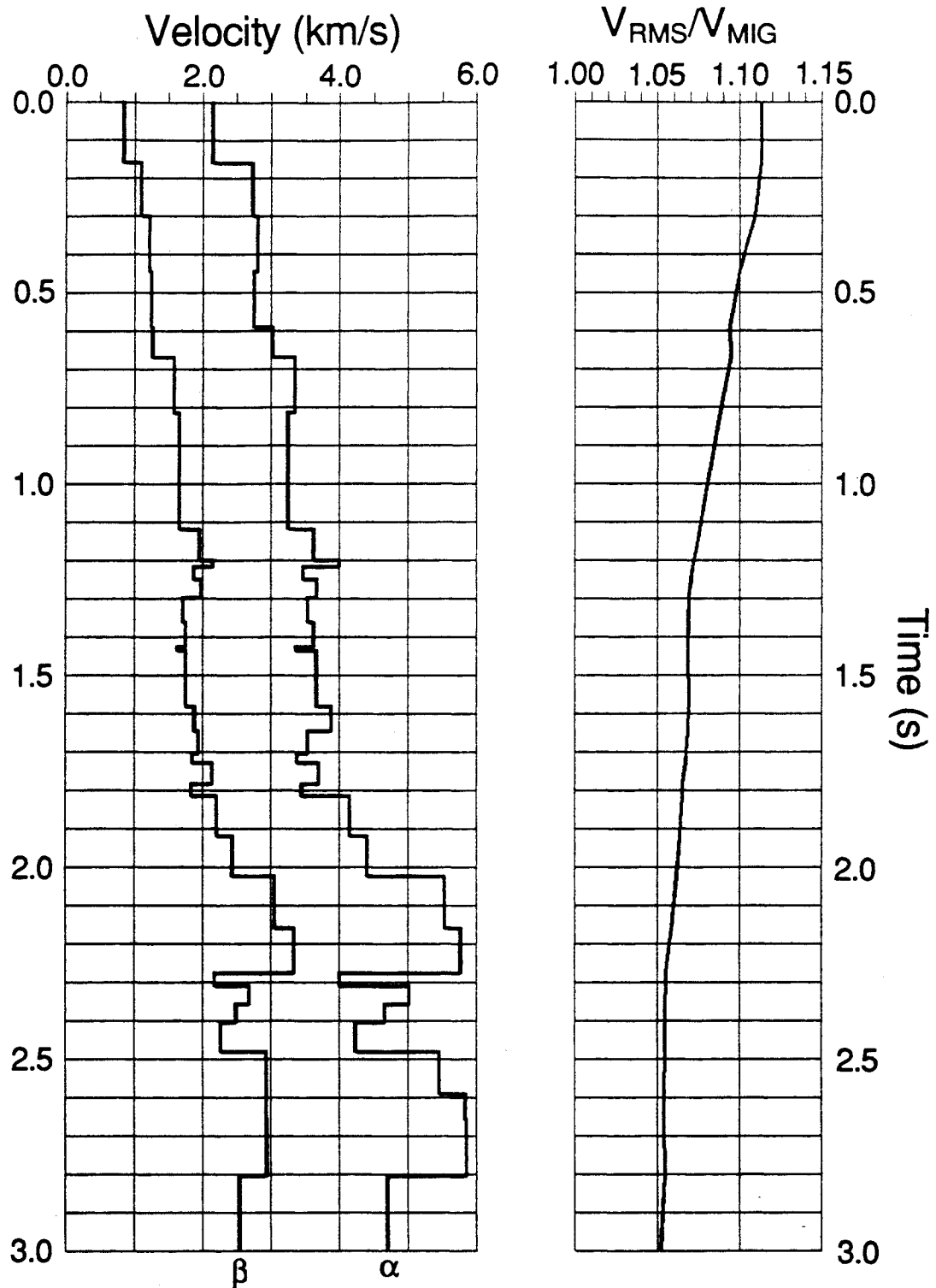


FIG. 5.8. Velocity model used to generate the second synthetic data set, plotted as a function of total two-way  $P$ - $SV$  traveltimes. The  $P$ -wave velocity function is labeled as  $\alpha$ , and the  $S$ -wave function is labeled as  $\beta$ . Also shown is the ratio of RMS and migration velocity functions for this model.

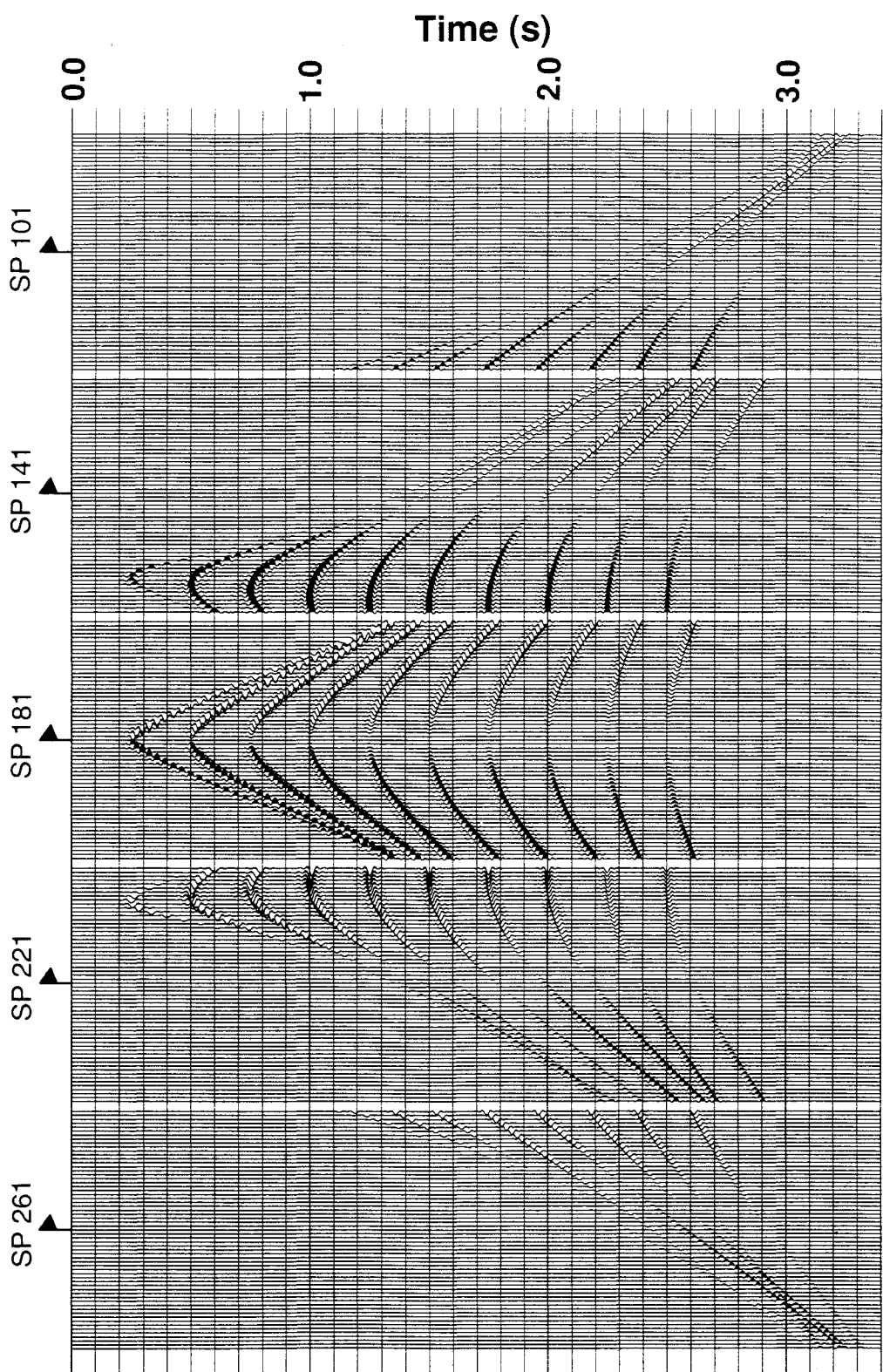


FIG. 5.9. Sample synthetic *P-SV* records for the variable-velocity case. The data have been NMO corrected and scaled for spherical divergence. Every second trace is plotted.

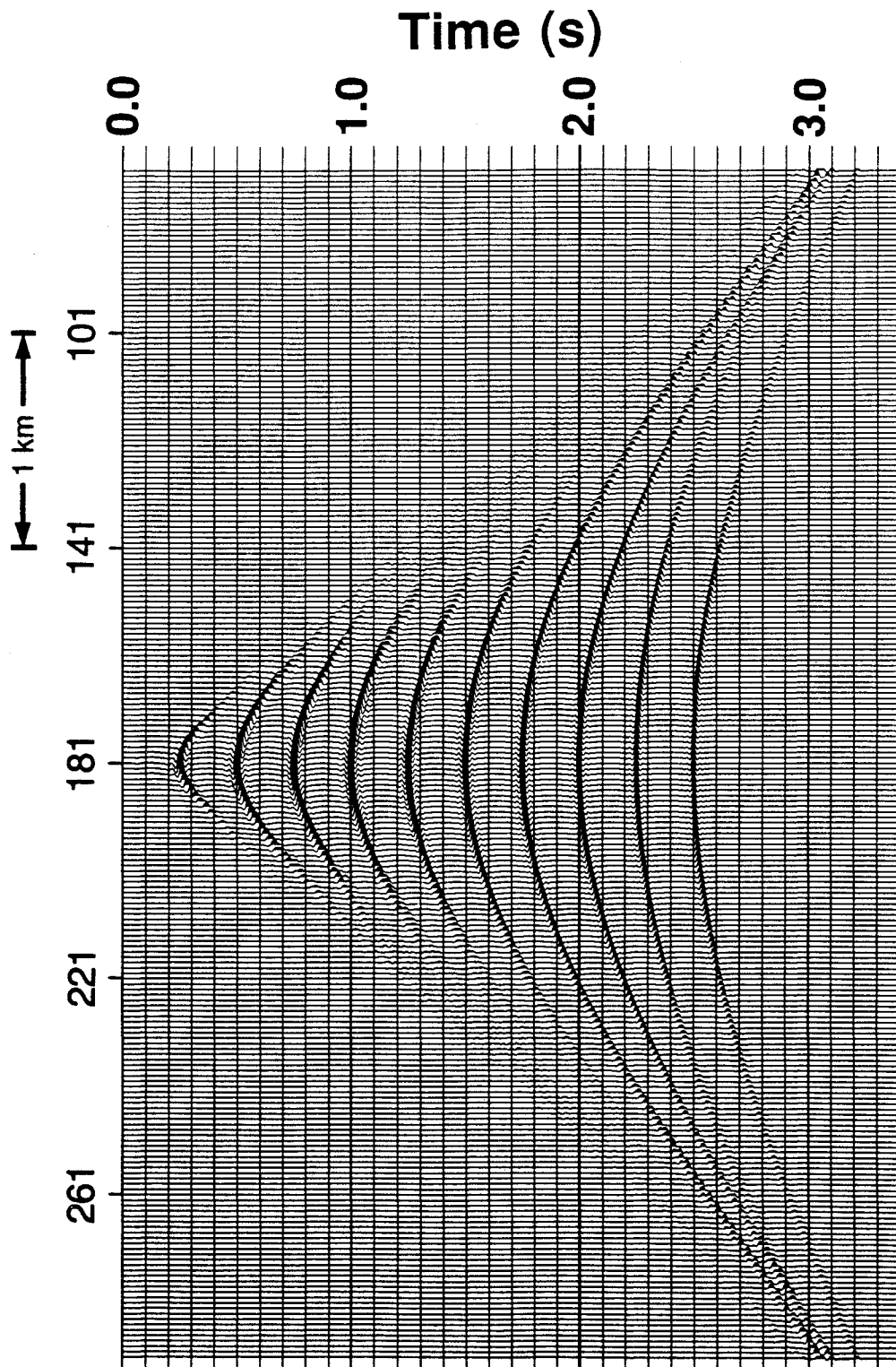


FIG. 5.10. Variable-velocity data stacked using DVB. Every second trace is plotted.

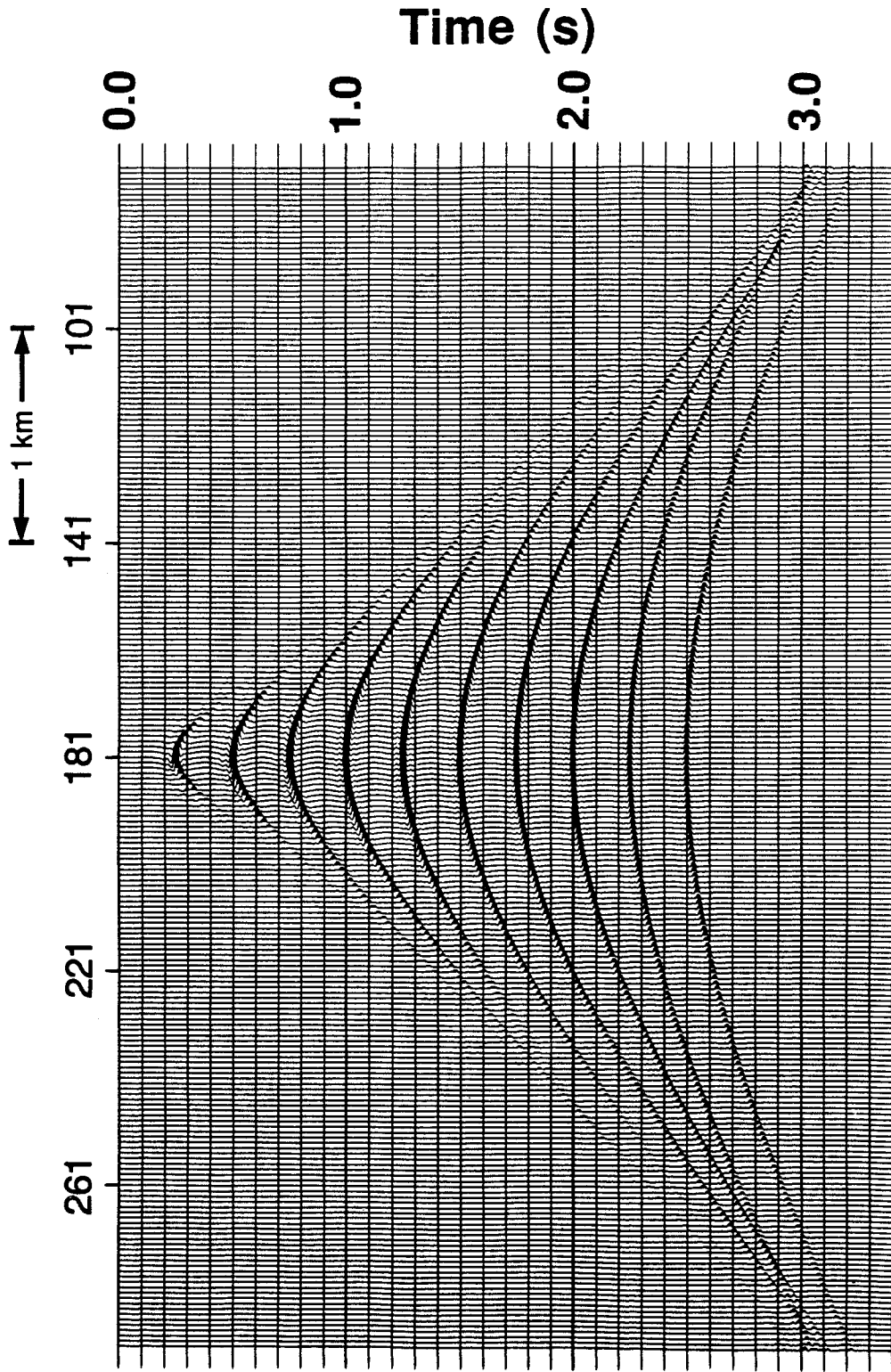


FIG. 5.11. Variable-velocity data stacked using depth-variant *P-SV* DMO. Every second trace is plotted.

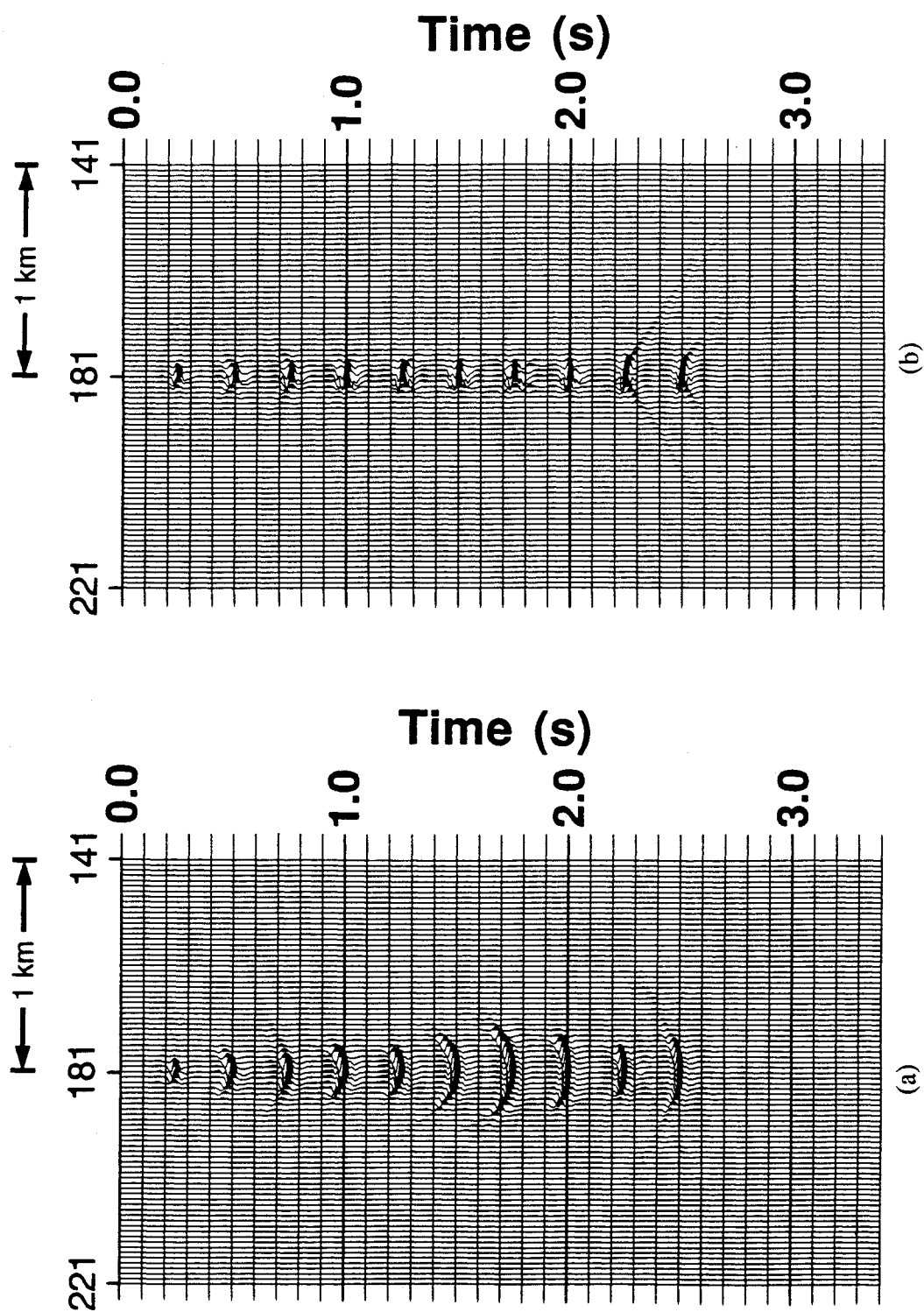


FIG. 5.12. DMO-stacked variable-velocity data migrated using: (a) the RMS velocity function; (b) the  $P$ - $SV$  migration velocity function. Every second trace is plotted.

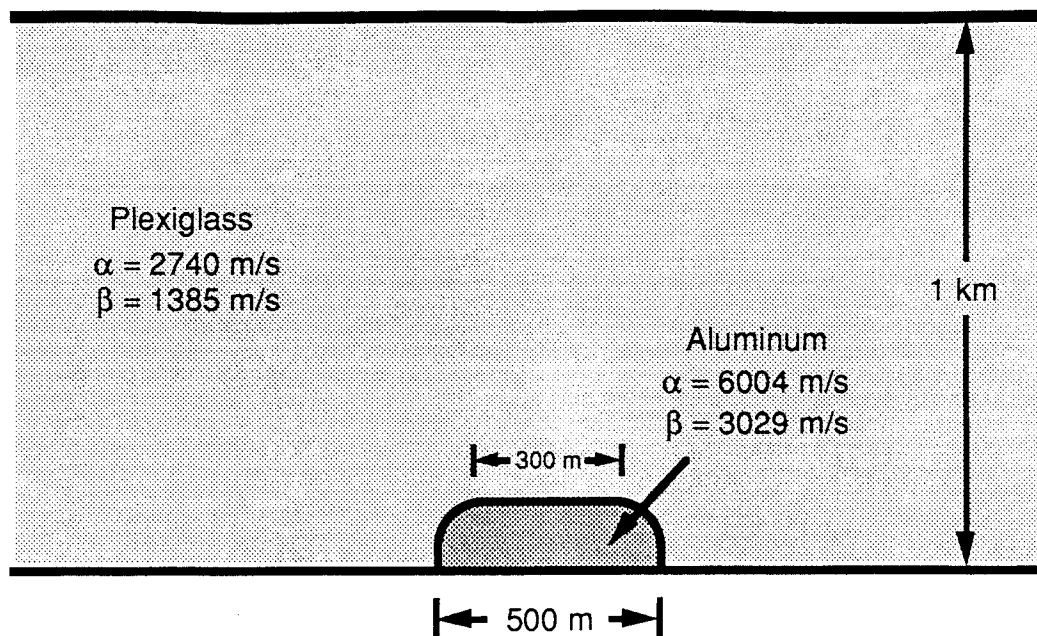


FIG. 5.13. Schematic diagram of the scaled physical model (after Stewart and Marchisio, 1991). All dimensions given are 10000 times actual size.

The vertical and radial data sets are displayed in Figures 5.14 and 5.15; events corresponding to reflected  $P$ -waves (P-P), converted  $S$ -waves (P-S), and reflected  $S$ -waves (S-S) are labeled. The mode-converted (P-S) reflection from the top of the reef shows an obvious asymmetry, and is weaker than the  $P$ -wave reflection on the vertical section (Figure 5.14), possibly because of the short offset-to-depth ratio.

The results of applying phase-shift migration to the radial section using both RMS velocities (equation 5.26) and  $P$ -SV migration velocities (equation 5.24) are shown in Figures 5.16 and 5.17 respectively. The model  $V_p/V_s$  value of 1.98 gives a difference between the two velocity functions of about 6% (Figure 5.2). The reflected  $P$ -wave (P-P) reflections appear undermigrated and the reflected  $S$ -wave (S-S) reflections appear overmigrated on both displays. Enlargements of the migrated sections around the location of the reef are shown in Figure 5.18, and show little difference between the two migrated results. The migrated vertical-component data (Figure 5.19) give better definition of the reef edges than do the migrated  $P$ -SV data, possibly because of the higher signal-to-noise

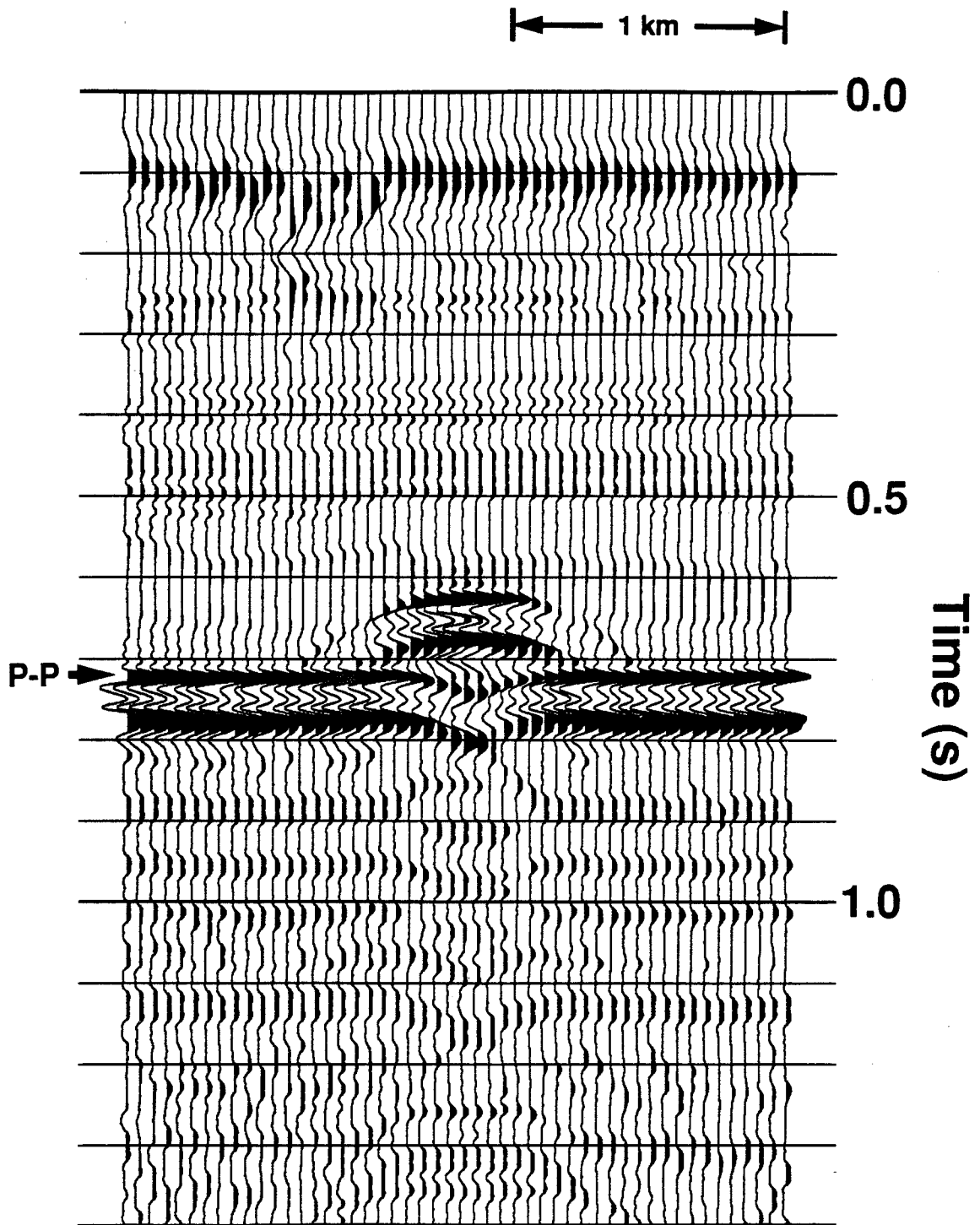


FIG. 5.14. Vertical component of physical-model data.

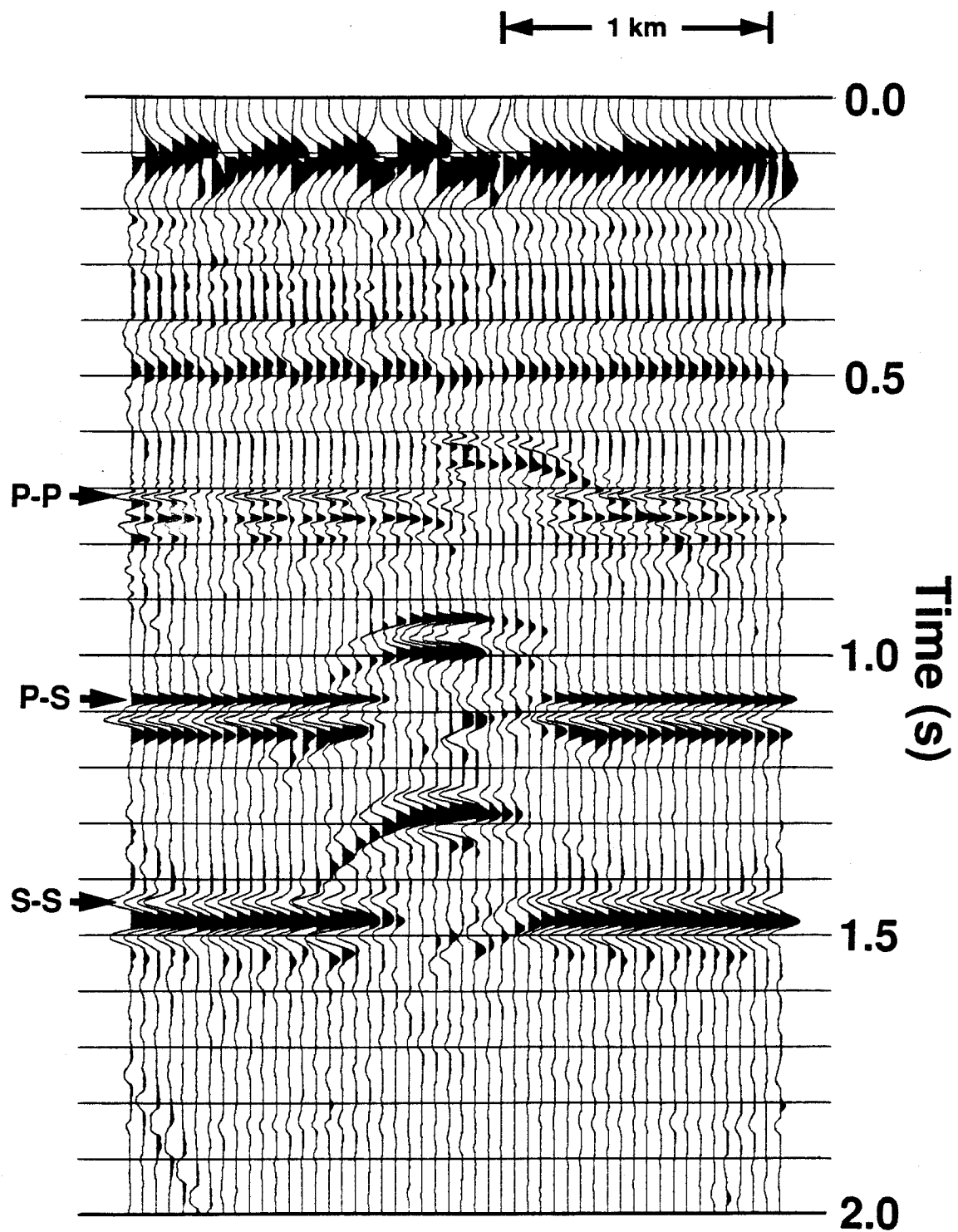


FIG. 5.15. Radial component of physical-model data.

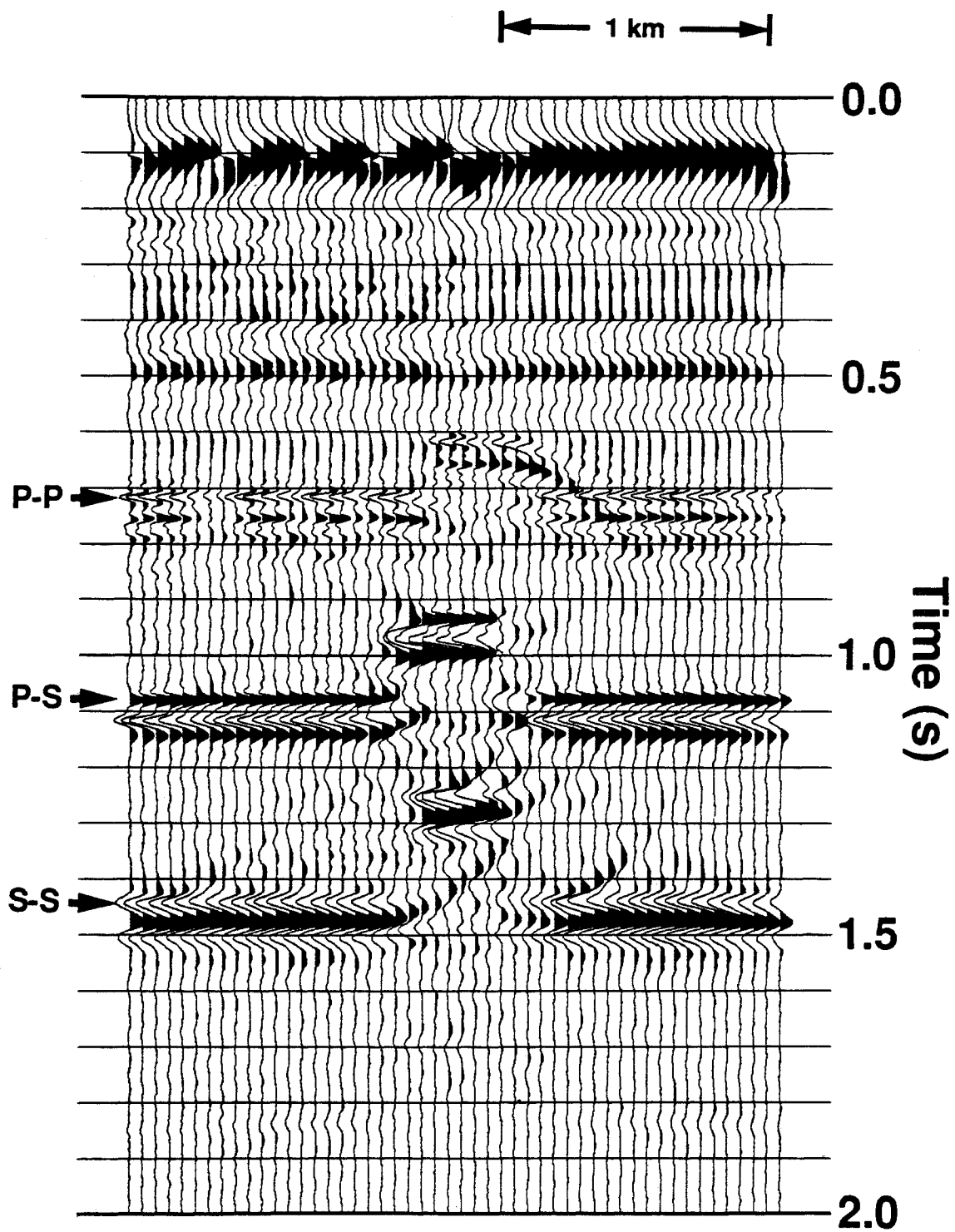


FIG. 5.16. Radial-component data migrated using the RMS velocity function.

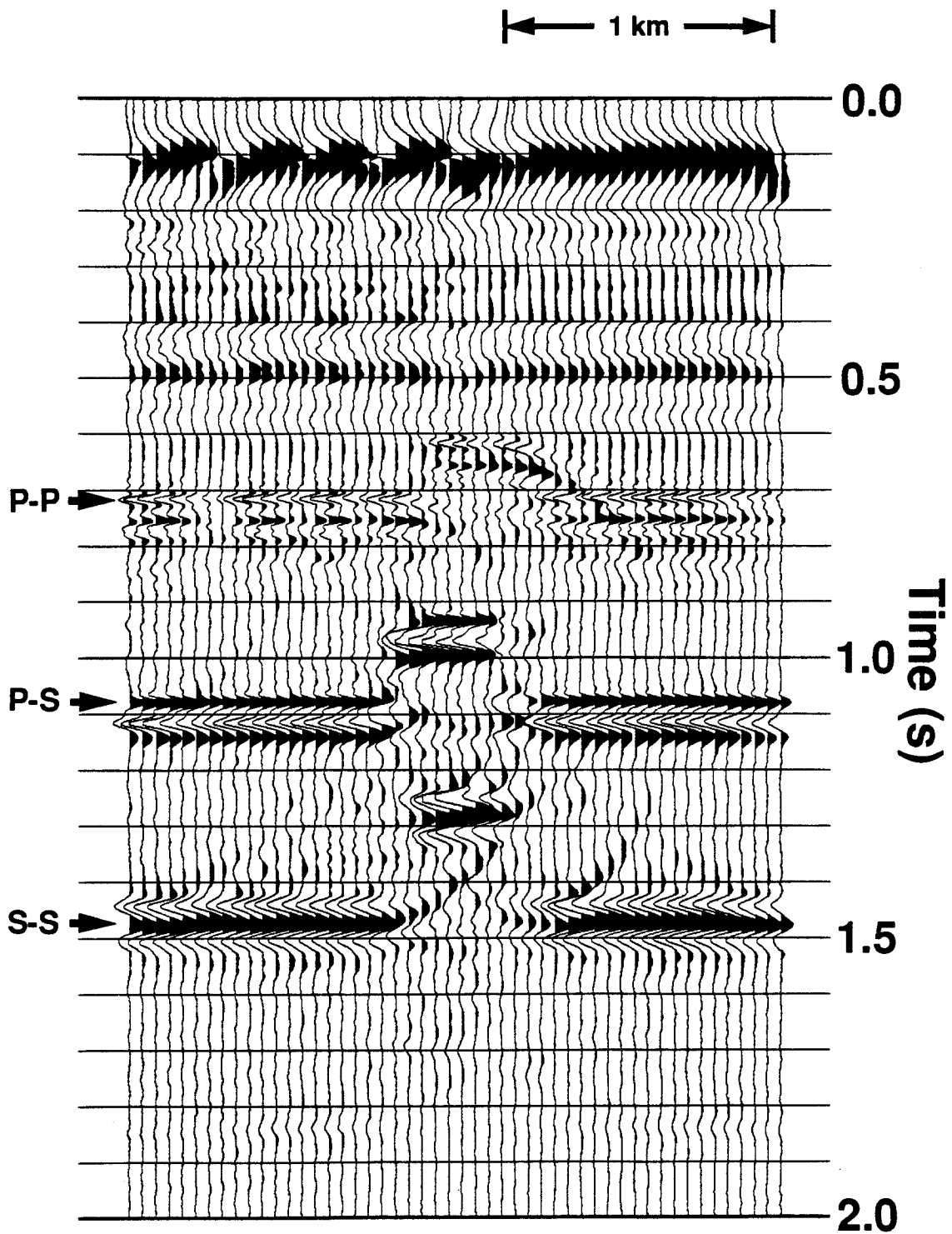
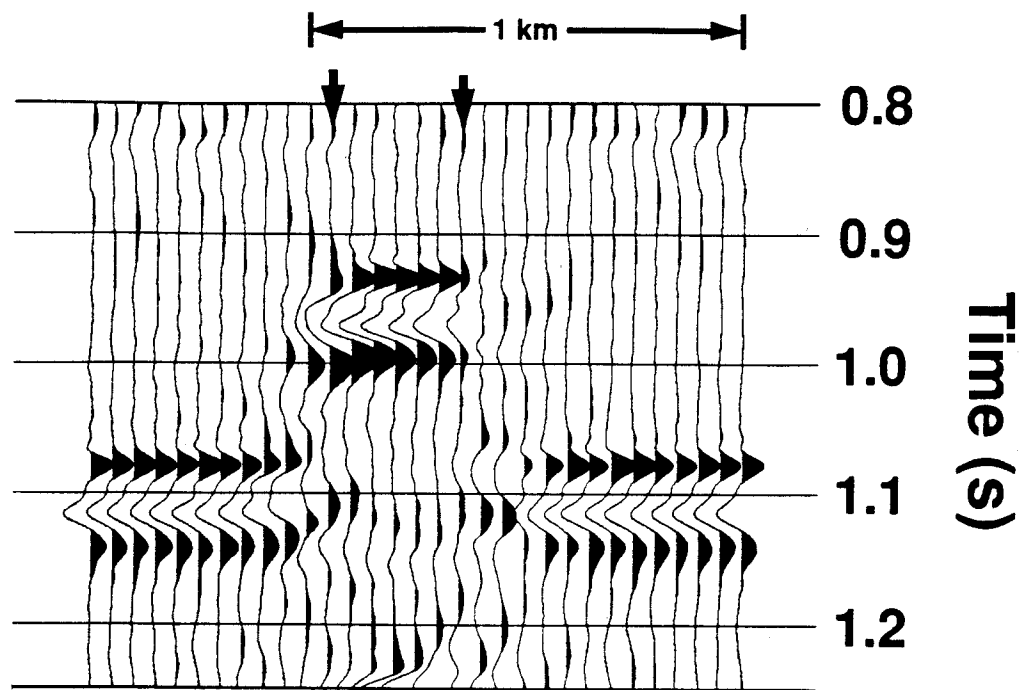
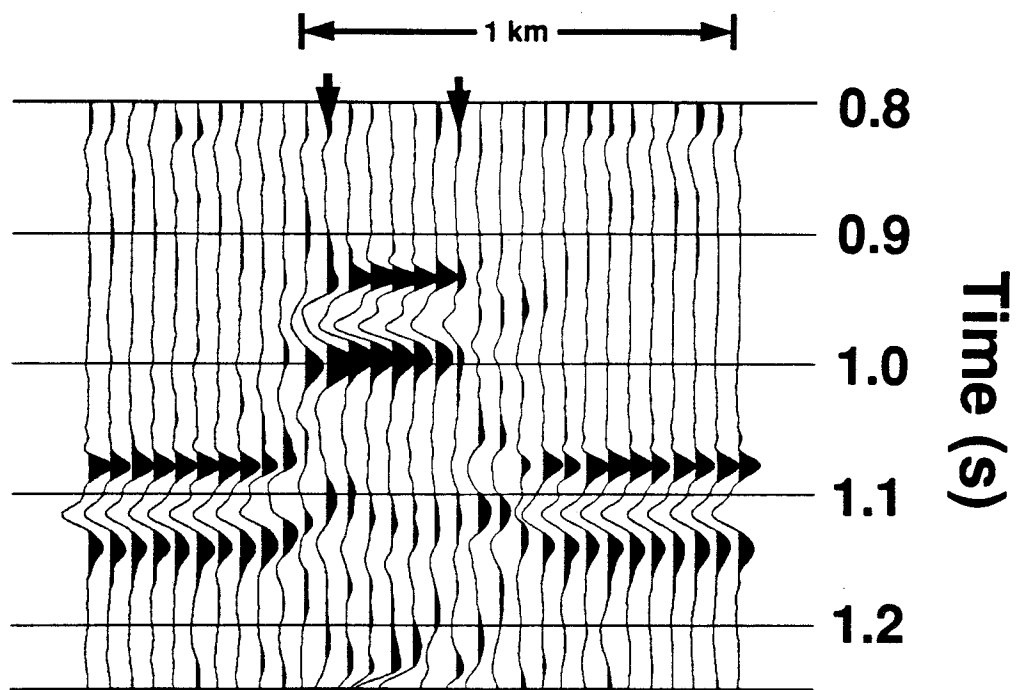


FIG. 5.17. Radial-component data migrated using the *P-SV* migration velocity function.



(a)



(b)

FIG. 5.18. Enlargements of the migrated radial-component data: (a) migrated with RMS velocities; (b) migrated with  $P$ - $SV$  migration velocities. Arrows indicate the location of reef-top edges.

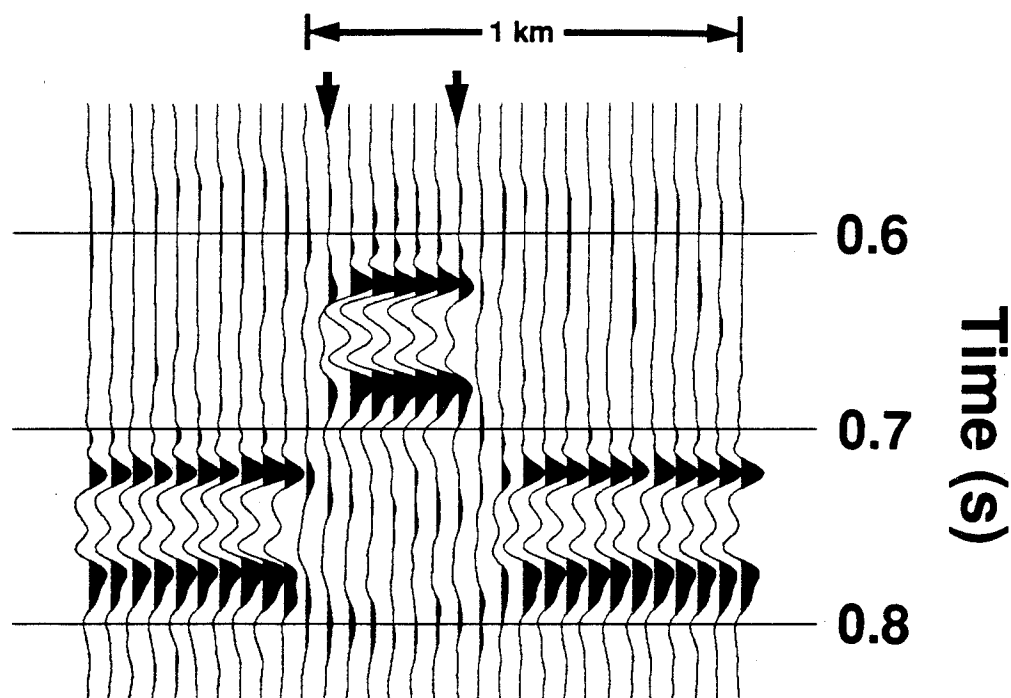


FIG. 5.19. Enlargement of the migrated vertical-component data. Arrows indicate the location of reef-top edges.

levels seen in Figure 5.14 and the greater symmetry of the  $P$ - $P$  diffraction. The migrated  $P$ - $SV$  data do, however, allow the edge of the reef to be picked with reasonable accuracy.

#### 5.4 Discussion

The undermigration of the last two diffractors in Figure 5.12b can be understood by referring to Figure 5.8. There are seen to be large changes in interval velocity after 2 seconds, where the two diffractors are positioned. Because the migration equation is a low-order approximation to the zero-offset travelpaths, it is probable that the large variations in ray parameter that would accompany large velocity changes make the higher order terms in equation (5.22) significant. The degree of undermigration is, however, seen to be small.

Although the migration velocities differ from the RMS velocities, it appears from Figure 5.8 that reducing the RMS velocities to about 94% of their value gives a reasonable estimate of the migration velocities for the deeper data. This could explain why poststack migration has been successfully applied to *P-SV* sections in the past. It should be noted that the RMS-to-migration adjustment factor is in addition to the usual ~10% reduction that would be applied to stacking velocities to obtain migration RMS velocities. This gives an expected total reduction of approximately 20% for the shallow data and 16% for the deeper data.

The lack of substantial difference between the physical-model data migrated using RMS and migration velocities can perhaps be explained by the limited dip aperture of the data. Using a peak frequency of 30 Hz, the 50 m trace separation gives aliasing of dips greater than 18°. Either velocity function is probably capable of correctly migrating data within this small aperture.

In summary, it is shown here that *P-SV* diffractions in a vertically-inhomogeneous medium are hyperbolic (neglecting fourth-order and higher terms), and an expression for their migration velocity can be obtained. The resulting velocities are found to be 6-11% less than the *P-SV* RMS velocities. Migration of DMO-corrected synthetic *P-SV* stack data using a conventional phase-shift algorithm and the appropriate migration velocities is found to adequately collapse diffractions, while migration using the RMS velocity function gives significant overmigration. Migration of physical model data shows little difference between the results obtained using RMS and *P-SV* migration velocities.

## Chapter 6 - Multicomponent processing: Carrot Creek, Alberta

### 6.1 Introduction

A three-component survey was conducted by Polyseis Research Inc. in the Carrot Creek area of Alberta in 1986, and the data have since been donated to the University of Calgary for study. The target in this area is the thin sandstone and conglomerate of the Upper Cretaceous Cardium Formation, which has been explored for successfully by using amplitude analysis (e.g., Wren, 1984) on conventional (*P-P*) data. This survey was undertaken to compare the *P*- and *S*-wave signatures across two known Cardium bars. Two lines were recorded in total, both using three-component geophones. The location and orientation of these lines are shown in Figure 6.1, and they are seen to cross two known Cardium pools, as outlined by Joiner (1989).

This chapter discusses the processing of line CC-SW-01 of the survey. The complete processing flow described in Chapter 2, with the exception of geophone rotation, has been applied to the radial component of this line.

### 6.2 Data acquisition

The field acquisition parameters are summarized in Table 6.1. The survey was carried out using a vibrator source and a 240-trace Sercel SN-348 recording system. Single three-component geophones were used at each receiver station, measuring motion in the vertical, radial (inline-horizontal), and transverse (crossline-horizontal) directions. All three geophone components were recorded on the same system, resulting in data collection from 80 receiver stations for each sourcepoint. No data were recorded at source-to-

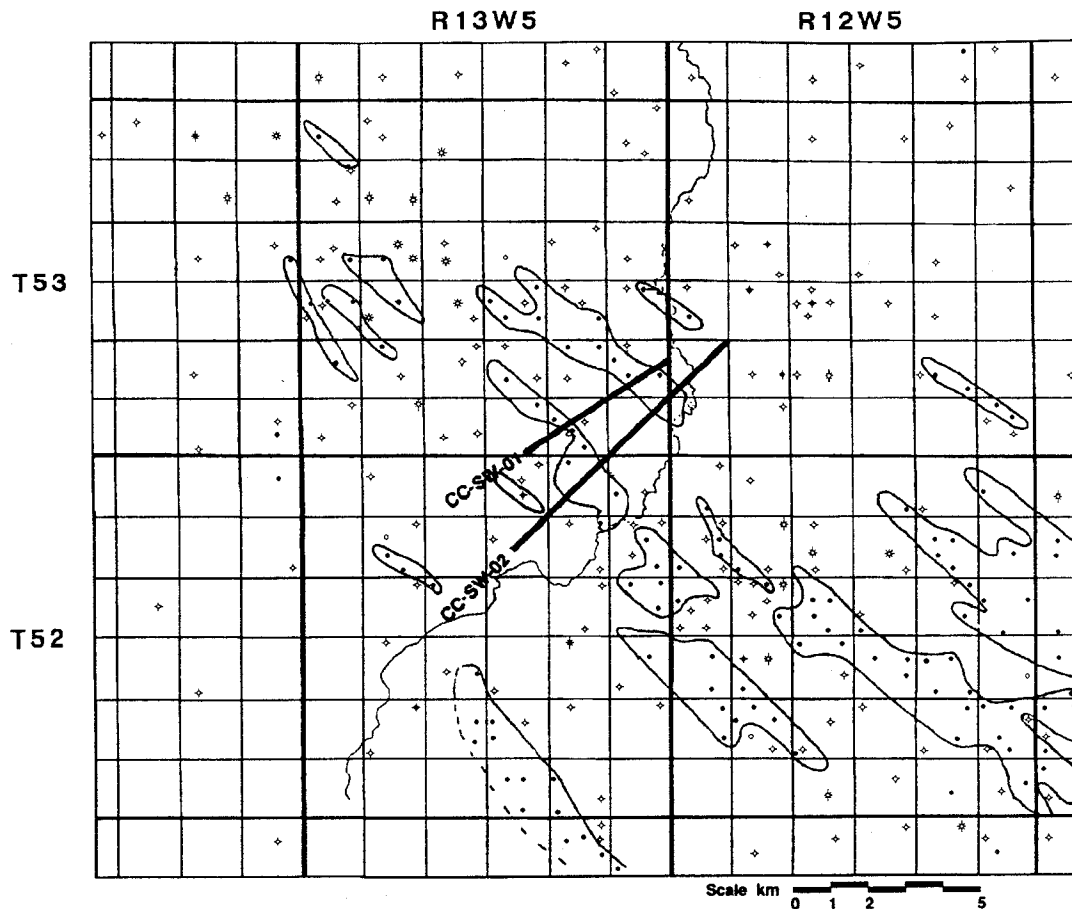


FIG. 6.1. Location map for the Carrot Creek survey. Cardium pool locations have been outlined by Joiner (1989).

Table 6.1. Field acquisition and recording parameters for the Carrot Creek survey.

Energy source	4 vibrators
Number of sweeps per VP	10
Source pattern length	30 m
Sweep frequency	10-94 Hz
Sweep length & type	6 s (linear)
Amplifier type	Sercel SN348
Number of channels	240
Sample rate	2 ms
Recording filter	Out-125 Hz
Notch filter	Out
Geophones per group	1
Type of geophones used	LRS 1033, 10 Hz
Number of groups recorded	80
Group interval	30 m
Normal source interval	60 m
Nominal CMP fold	20

receiver offsets less than 180 meters (6 groups), and the normal cable spread gives a maximum offset of slightly over 2.5 km. The nominal CMP stacking fold was 20.

Vertical-, radial-, and transverse-component gathers are shown in Figures 6.2, 6.3, and 6.4 respectively for sourcepoints spaced approximately one-third and two-thirds down the line. A time-squared gain function followed by individual trace-balance scaling has been applied to these field records. The vertical time scale on all plots of horizontal-component data shown in this chapter have been reduced to be roughly two-thirds that of the vertical component displays. As the  $V_p/V_s$  value for most sedimentary rocks is in the neighborhood of 2.0 (e.g., Tatham, 1985), plotting the converted-wave data at this scale facilitates visual correlation between  $P$ - and  $S$ -wave data sets.

In Figures 6.2, 6.3, and 6.4, all three components display low-velocity source-generated noise that travels with a linear velocity of about 340 m/s. This velocity is very close to the speed of sound in air, strongly suggesting that the noisetrain is associated with an airwave from the vibrators. The radial-component records (Figure 6.3) are seen to have good signal strength, with events that roughly correspond to those on the vertical component. These records have a second wavetrain not present on the vertical-component gathers that travels with a horizontal velocity of about 1280 m/s (discussed later). The polarity reversal between the left and right sides of the spread can be seen on the split-spread gather (Figure 6.3a). Also, large time delays occur on some traces in Figure 6.3, but no corresponding delays are found on the  $P$ -wave traces (Figure 6.2). This indicates that the  $P$ - $P$  and  $P$ - $SV$  static effects are significantly different. The transverse-component records (Figure 6.4) have little recognizable reflection signal, and no further work has been done on this component.

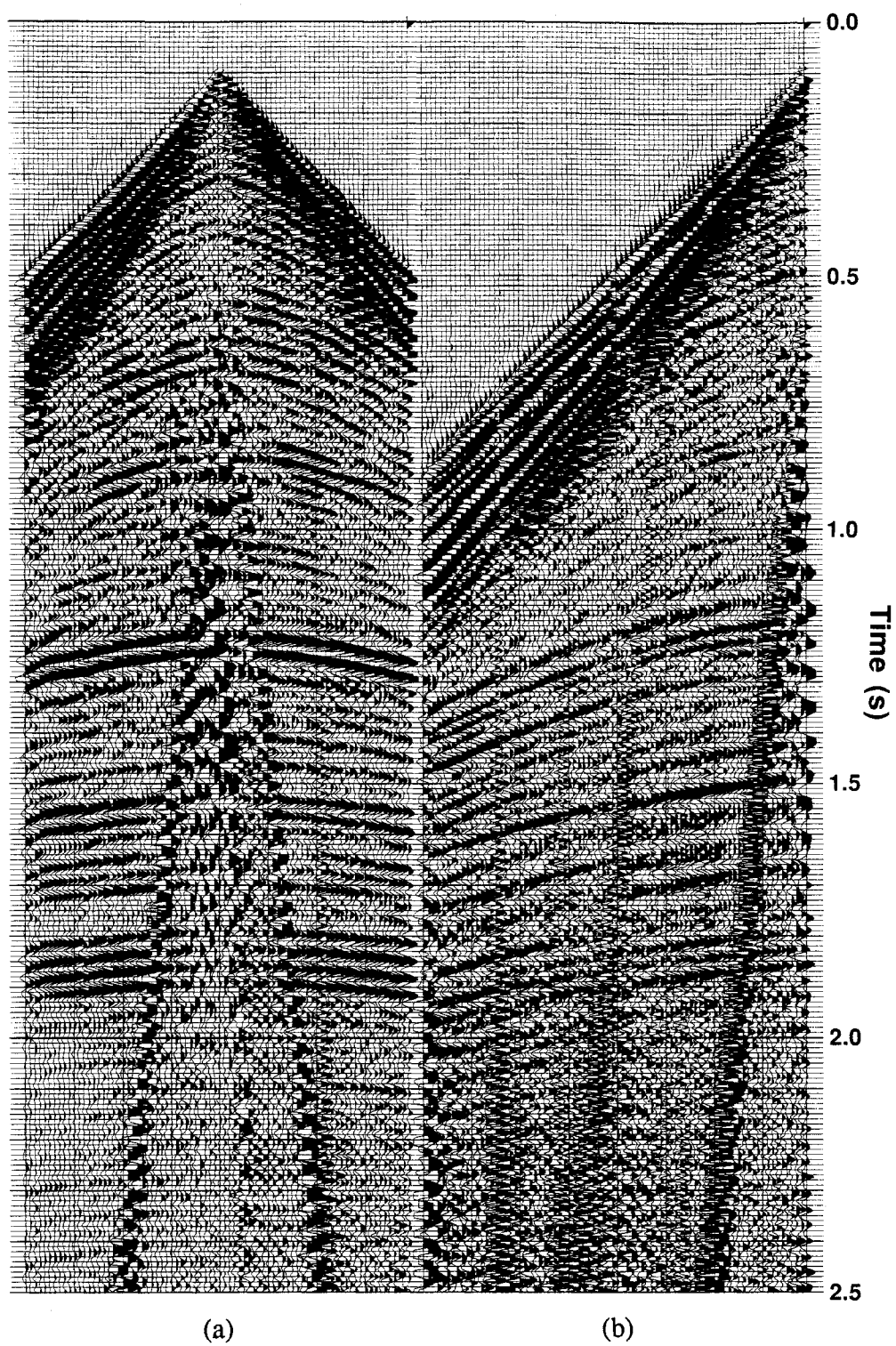


FIG. 6.2. Vertical-component records for line CC-SW-01: (a) VP 211; (b) VP 115.

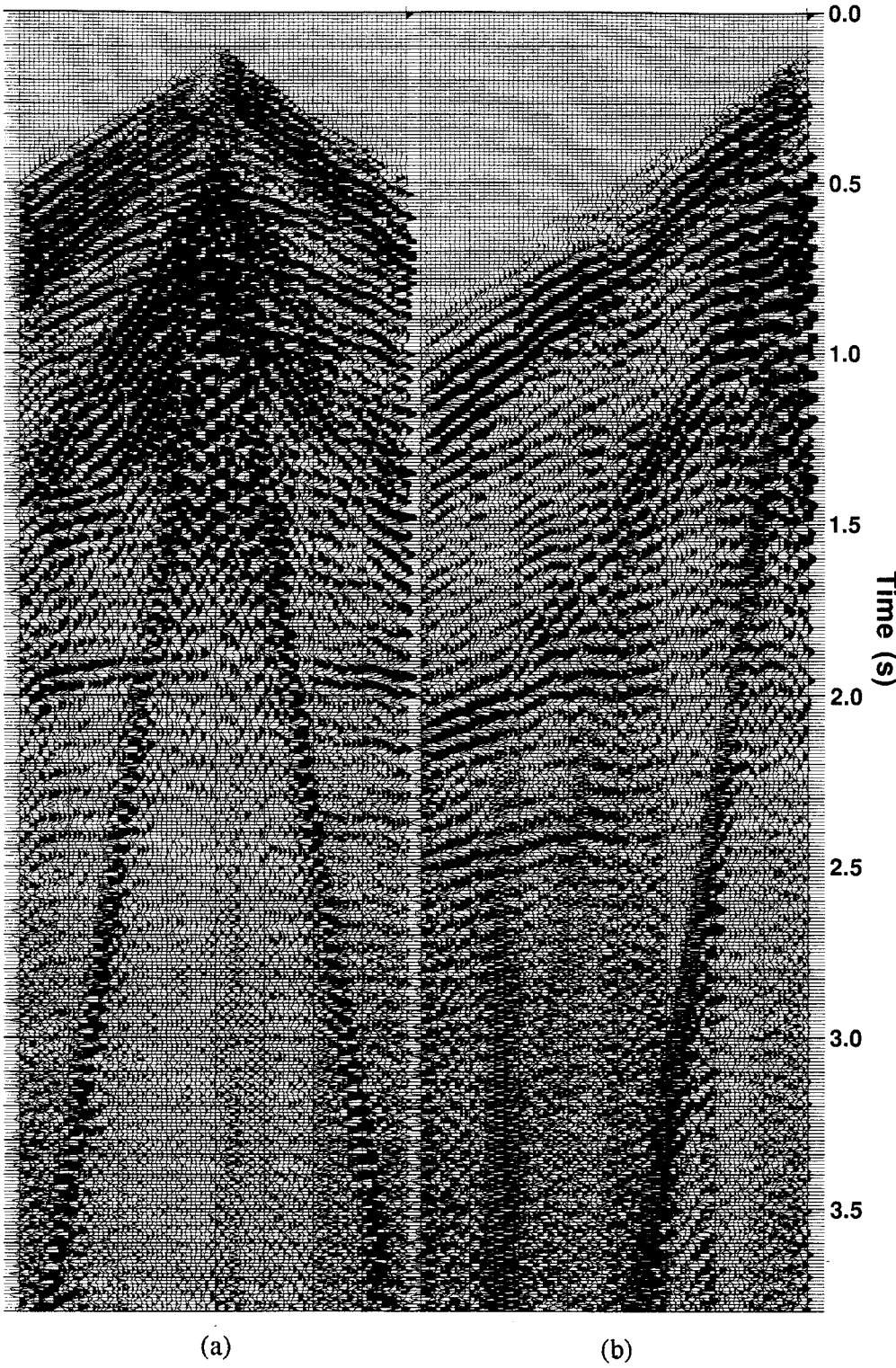


FIG. 6.3. Radial-component records for line CC-SW-01: (a) VP 211; (b) VP 115.

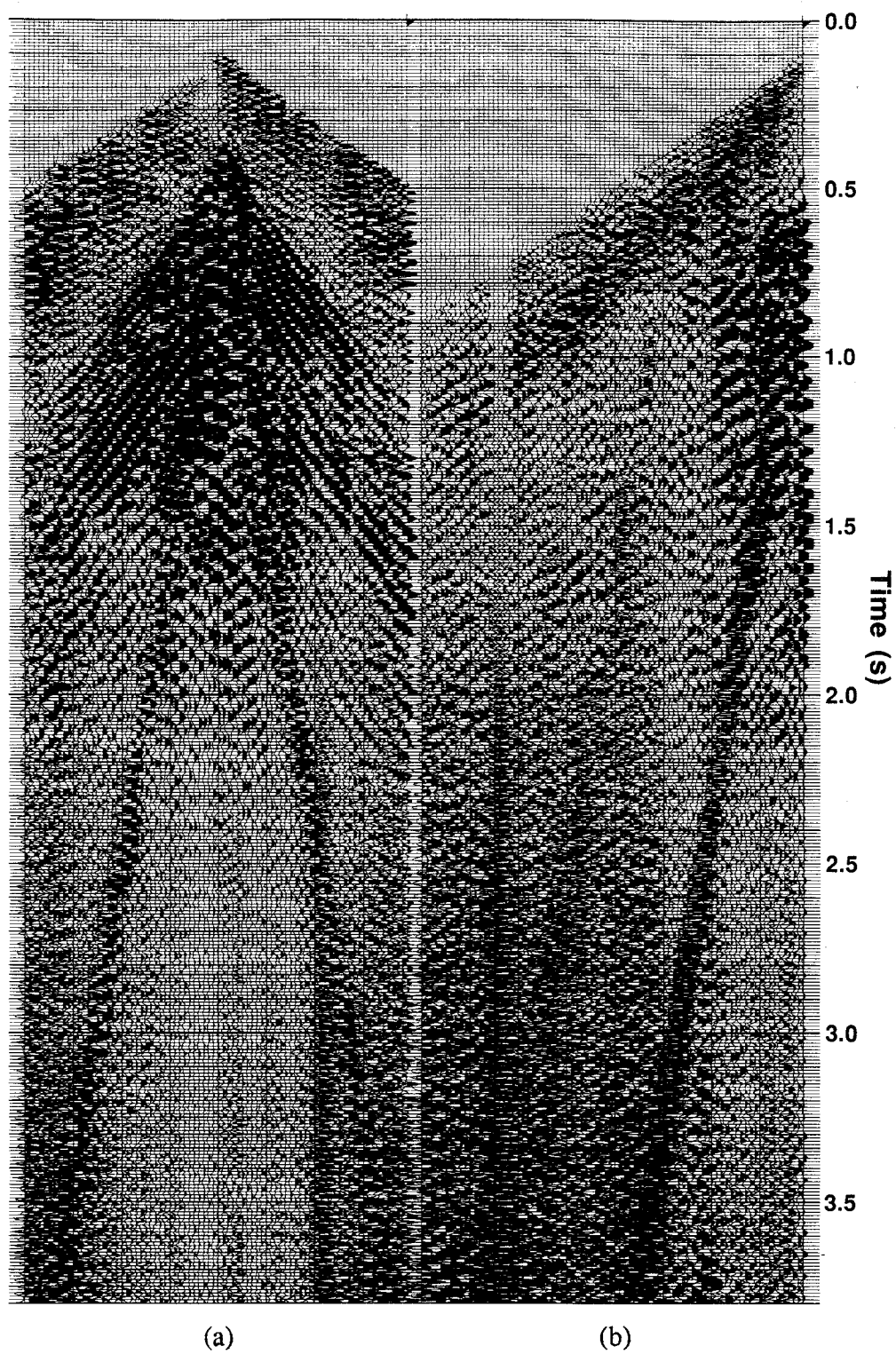


FIG. 6.4. Transverse-component records for line CC-SW-01: (a) VP 211; (b) VP 115.

### 6.3 Data processing

The vertical channel data were processed using the conventional *P*-wave processing flow outlined in Figure 6.5. The vibrator records were picked for best-guess arrival times, from which layer replacement statics were computed. Geometric spreading compensation was applied using the equation given by Newman (1973). The final *P*-wave stack section is displayed in Figure 6.6 with the northeast side on the right, and is qualitatively seen to have good overall signal strength. More noise is present in roughly the first 750 ms of data, possibly because of the smaller amount of noise attenuation provided by point receivers. On the basis of well control information in the area (1-3-53-13W5 and 11-22-49-12W5), the Cardium (Cz) reflection is at a time of about 990 ms on the *P*-wave sections, and the Precambrian (Pc) is very roughly estimated to be at 1800 ms.

A contour plot of the averaged time-variant cross-power spectra is shown in Figure 6.7. In the figure, the spectrum for a given time was computed from the average crosscorrelation of 20 adjacent stack traces; a 400 ms correlation window was used, and spectra were computed at 100 ms increments. The plot indicates a usable bandwidth of approximately 10-60 Hz for the *P*-wave data.

An *f-k* filter with a passband from -2 to +2 ms/trace and a 6 db maximum reject was applied to the final *P*-wave section, giving the result shown in Figure 6.8. Finite-difference migration (Claerbout and Doherty, 1972), followed by bandpass filtering and gain, was also performed (Figure 6.9). Shown in Figure 6.10 are enlargements of the *f-k* filtered (Figure 6.8) and migrated (Figure 6.9) sections, centered on one of the Cardium pools. A small amplitude increase can be seen in the figure at the pool location. Migration does appear to reduce the horizontal extent of the anomaly by about 45 m on each side.

The radial (*P-SV*) component was processed using the sequence shown in Figure 6.11. Because no significant reflection energy was seen on the transverse-component data,

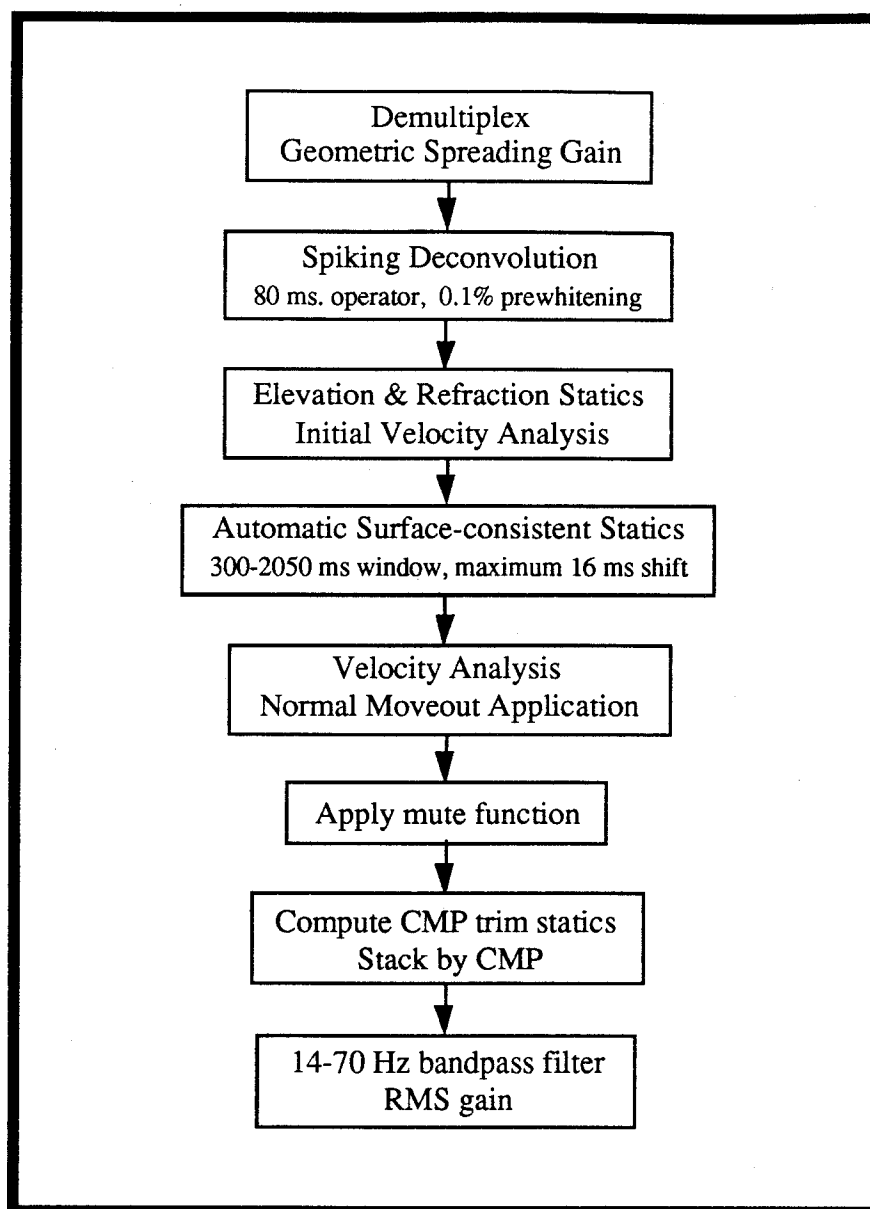


FIG. 6.5. Processing flowchart for the vertical-component ( $P$ - $P$ ) data set.

no rotation of the two horizontal components was performed. Shown in Figure 6.12 is an  $S$ -wave stack section that was created using the final  $P$ - $P$  static solution and the final  $P$ - $SV$  stacking velocities and mute function. Reflections on the section are improperly stacked, indicating that the  $P$ - $P$  statics do not correctly account for the  $P$ - $SV$  statics problems.

Common-source and common-receiver stack sections for the  $P$ - $SV$  data, with the final  $P$ - $P$

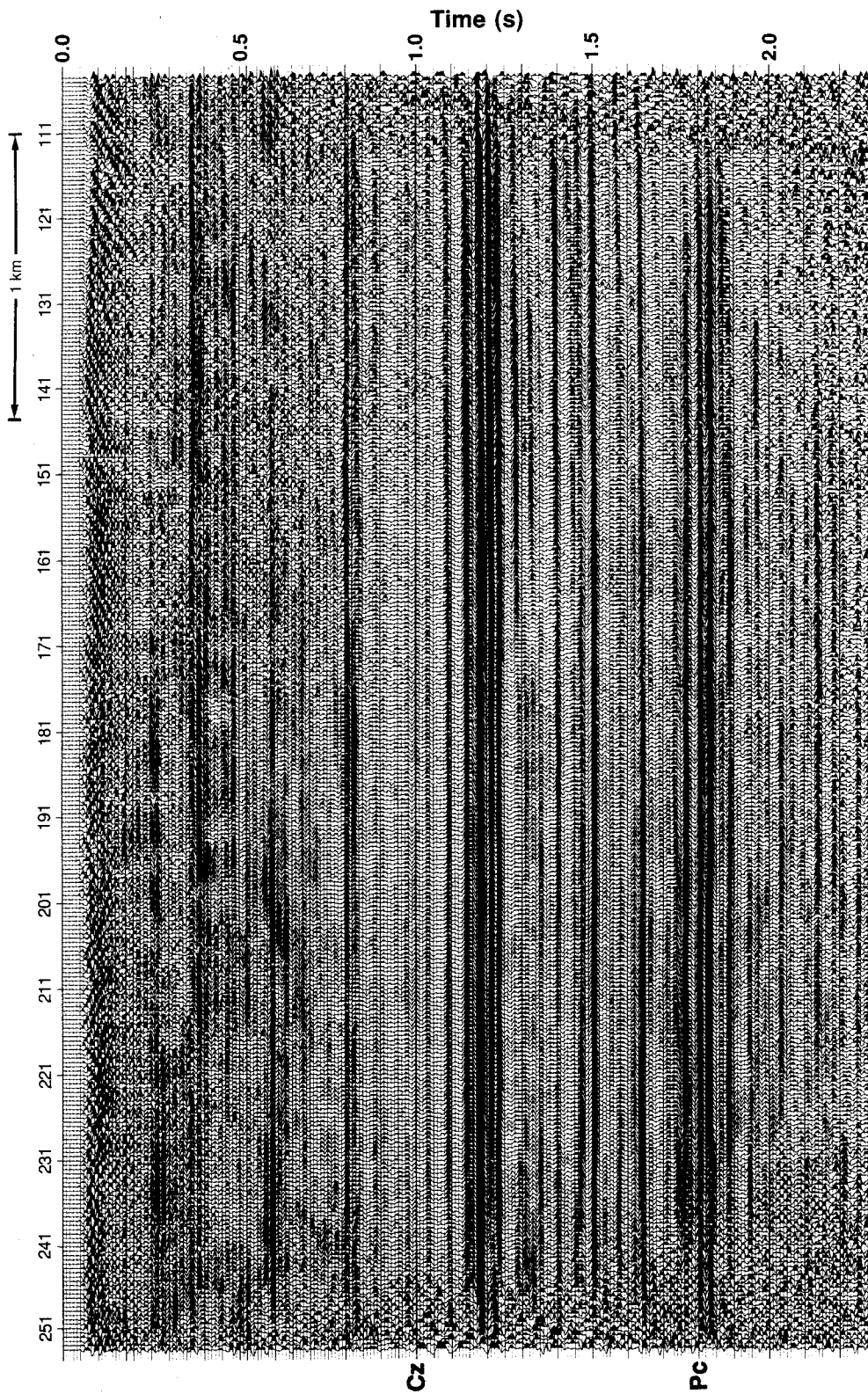


FIG. 6.6. Stack section of vertical-component data.

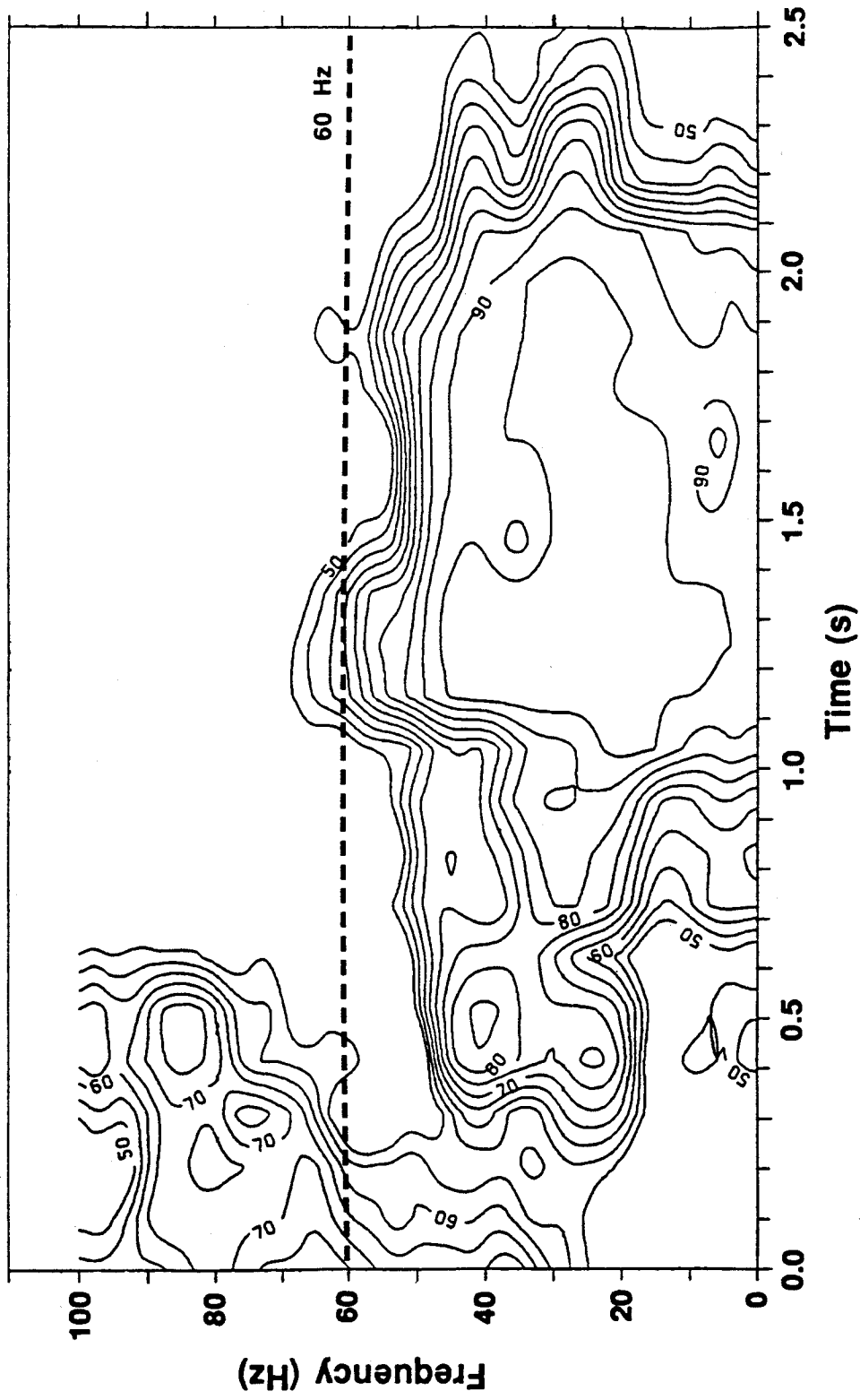


FIG. 6.7. Averaged time-variant cross-power spectra for the *P*-wave stacked data. The spectrum for a given time was computed from the average crosscorrelation of 20 adjacent stack traces. A 400 ms correlation window was used, and spectra were computed at 100 ms increments. Contours are in percentage of maximum.

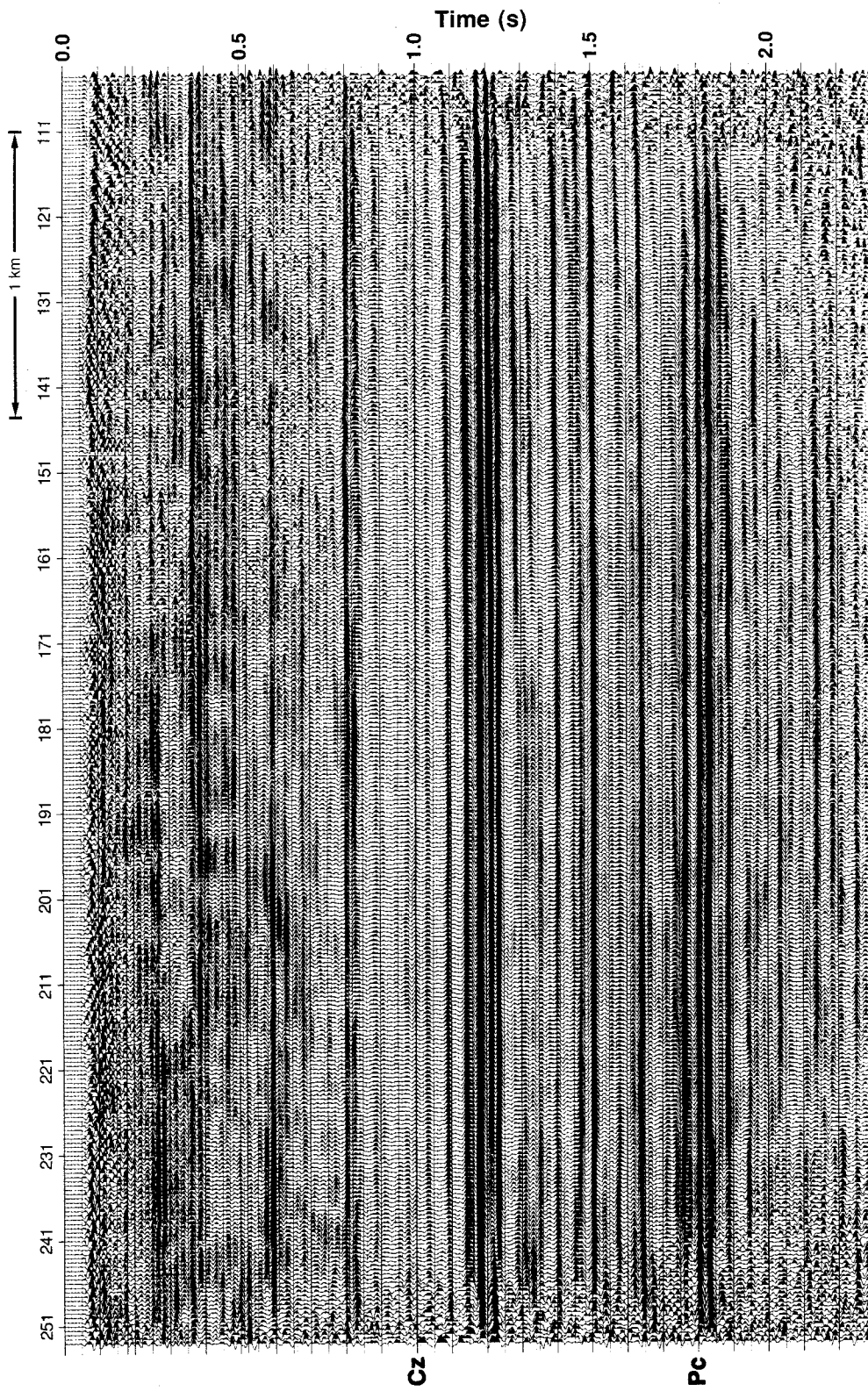


FIG. 6.8. Stack section of vertical-component data with poststack  $f-k$  filter applied.

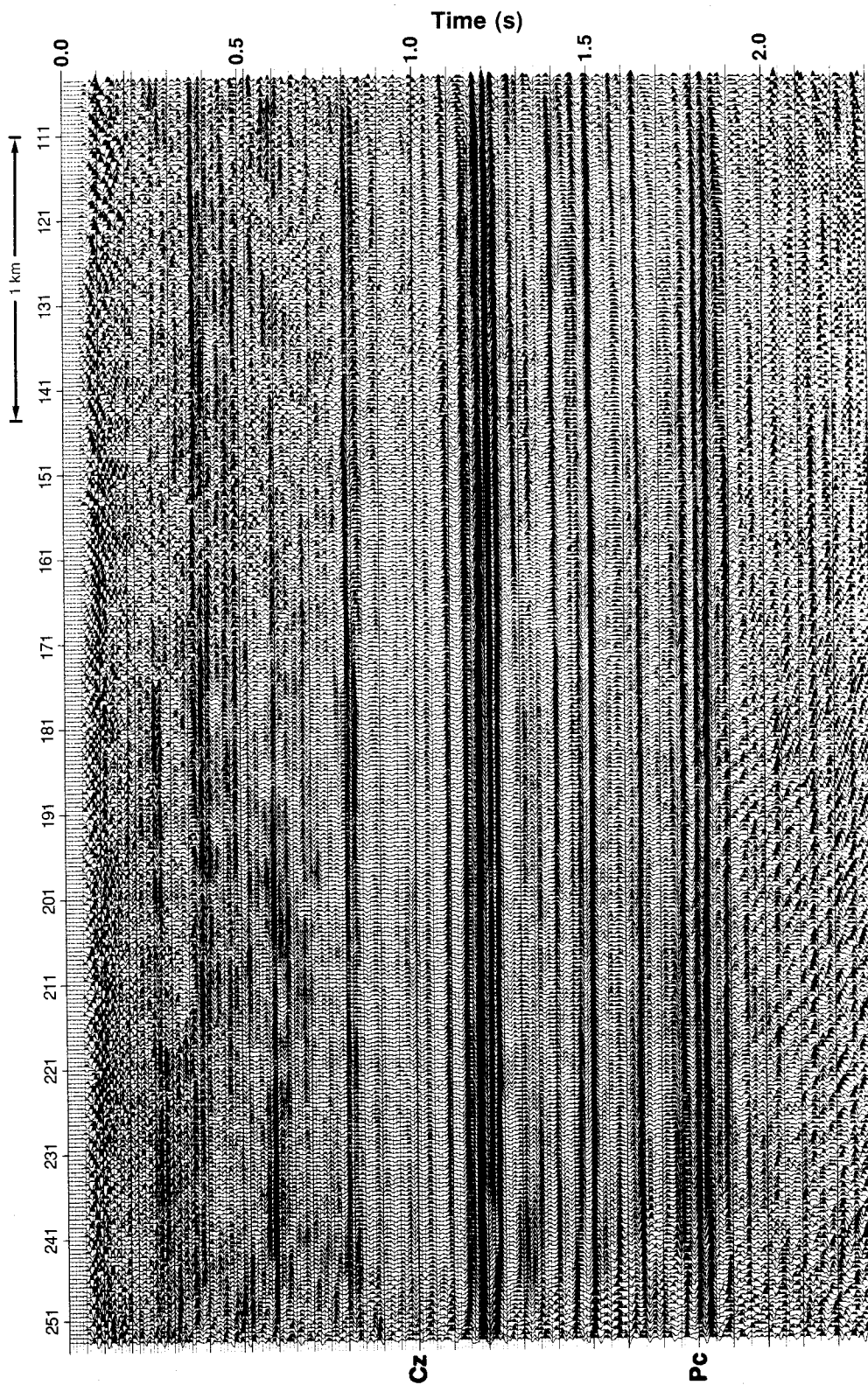
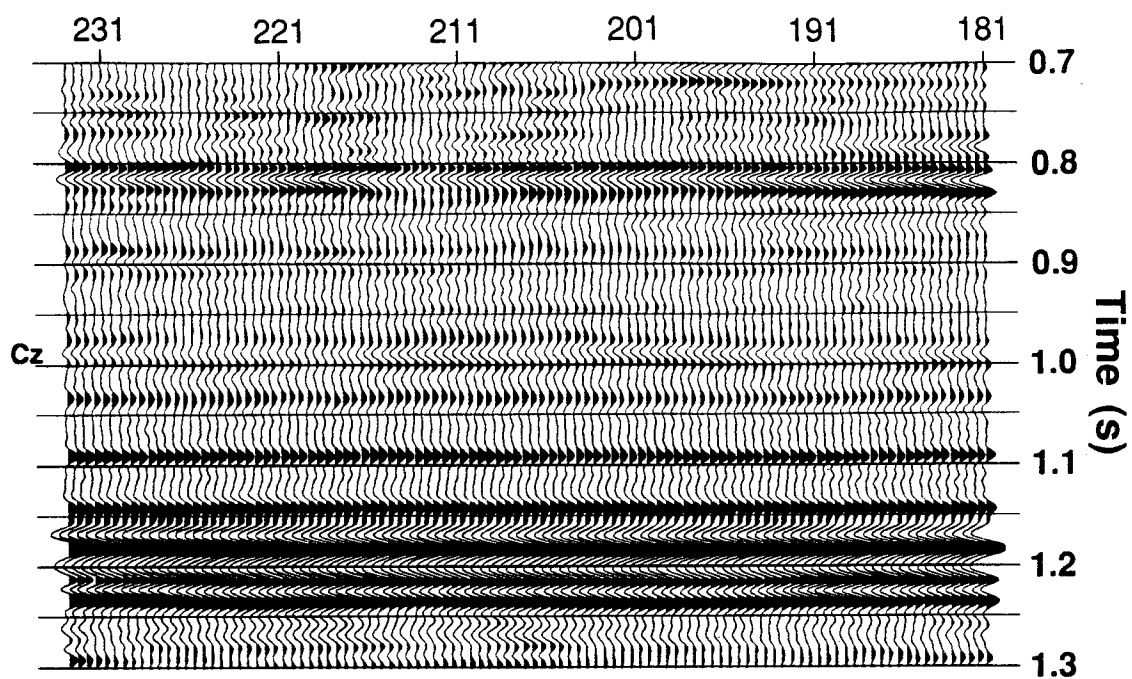
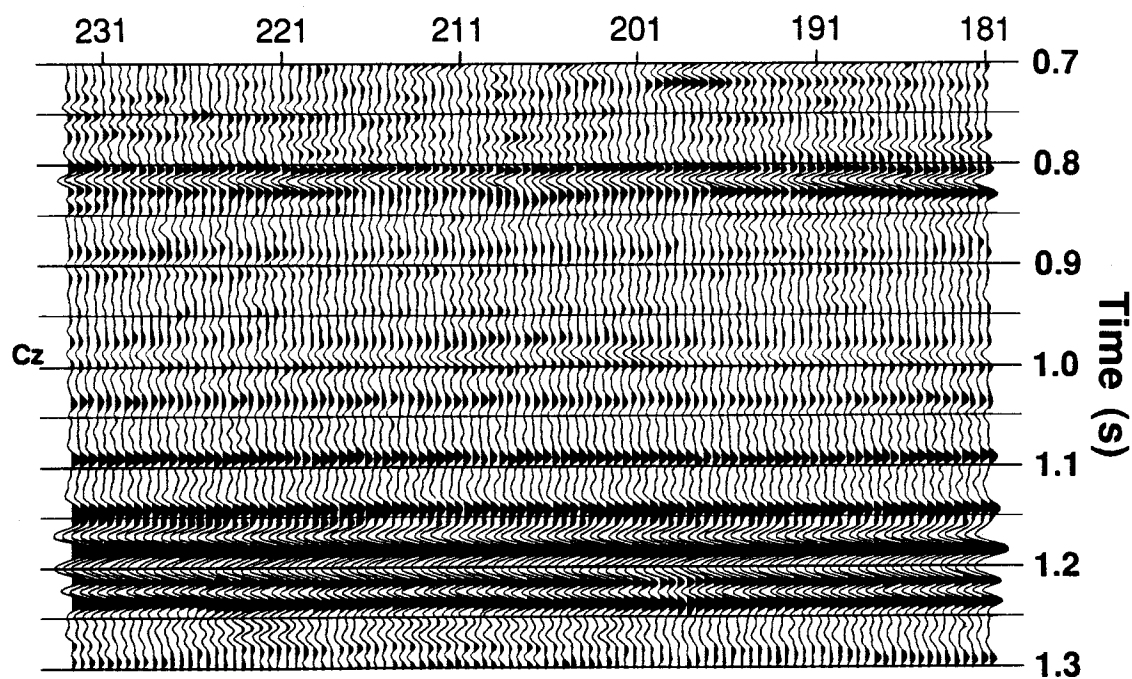


FIG. 6.9. Vertical-component section with poststack migration applied.



(a)



(b)

FIG. 6.10. Enlargement of vertical-component sections: (a) poststack  $f$ - $k$  filter; (b) poststack migration.

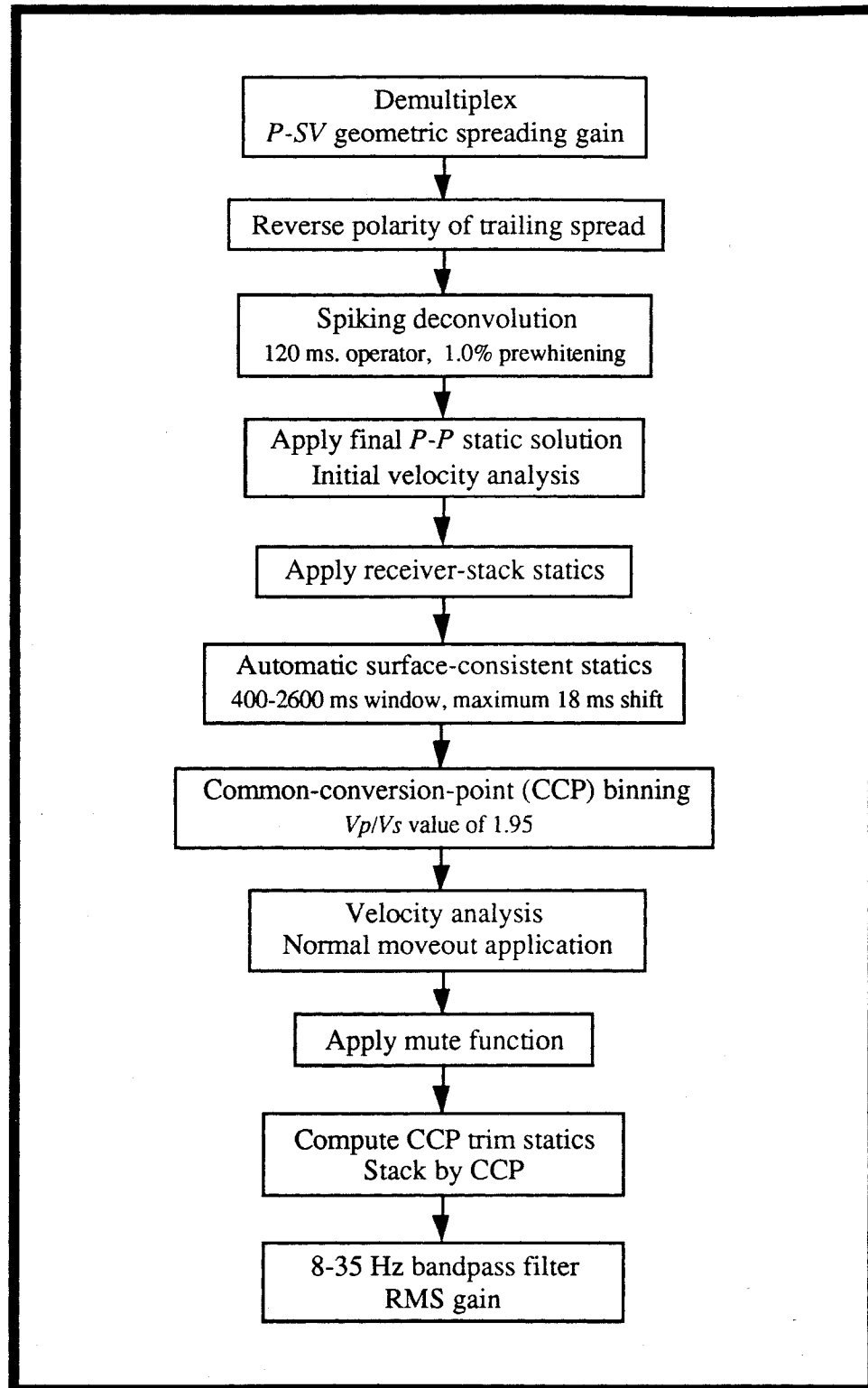


FIG. 6.11. Processing flowchart for the radial-component ( $P$ - $SV$ ) data set.

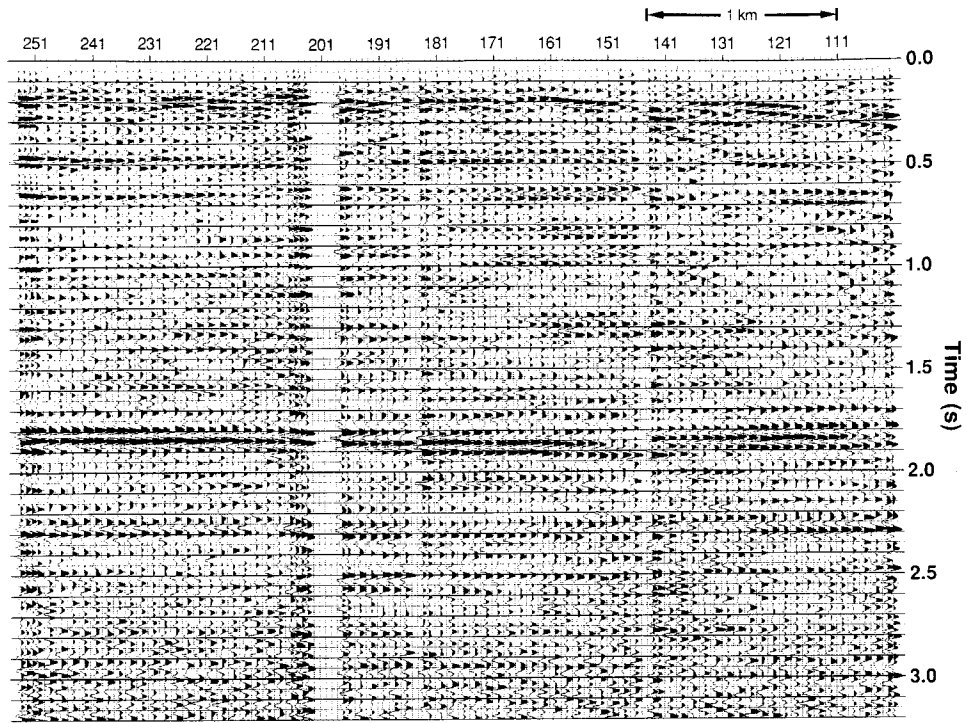


FIG. 6.12. Stack section of radial-component data with final vertical-component statics applied.

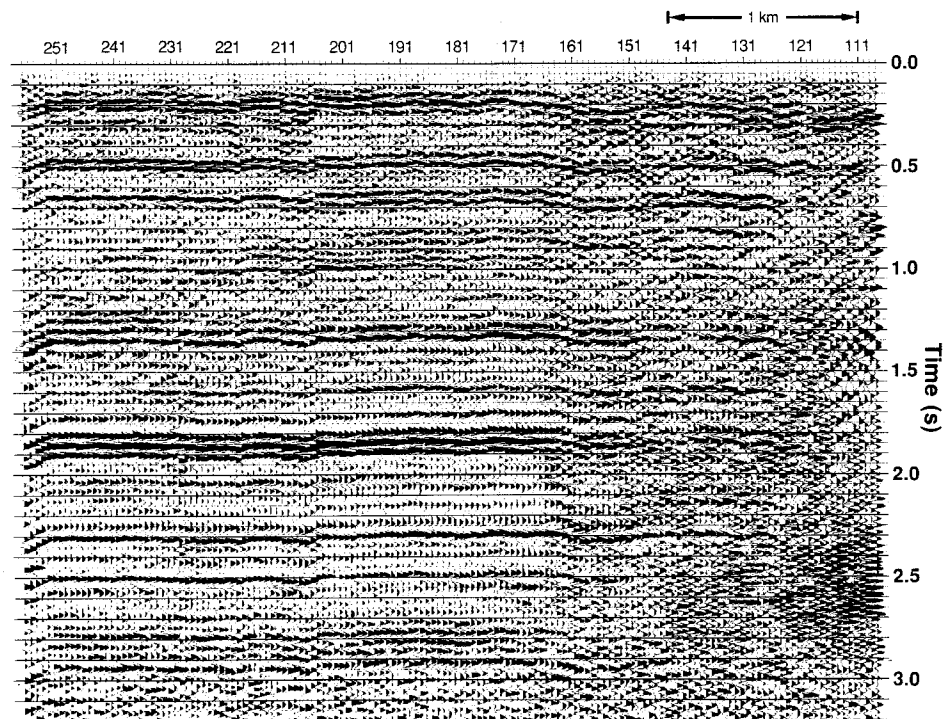
statics solution applied, are displayed in Figure 6.13. As expected (Section 2.6), there is little residual source static seen in Figure 6.13a, but residual receiver delays as large as 60 ms are visible in Figure 6.13b. Residual receiver statics were picked by hand from the common-receiver stack section and applied to the radial-component data, giving a second set of CMP and surface stacks. These new stacks were greatly improved over the previous set, showing much greater coherency with no visible source delays. A pass of automatic surface-consistent residual statics was made later in the processing sequence to remove any remaining static values. The final receiver-statics solution for both the  $P$ - $P$  and  $P$ - $SV$  data sets are plotted in Figure 6.14.

Once the statics problems were resolved, velocity analysis was done on the  $P$ - $SV$  data using conventional hyperbolic NMO curve-fitting. Sample velocity analysis plots for each of the  $P$ -wave and  $S$ -wave data sets are displayed in Figure 6.15, and demonstrate good separation between the  $P$ - $P$  and  $P$ - $SV$  stacking velocity curves. Little evidence is seen of  $P$ - $SV$  events on the  $P$ - $P$  analysis, but high-velocity semblance maximas, probably from  $P$ - $P$  events, are found on the  $P$ - $SV$  analysis. Sample common-offset stack records constructed approximately in the center of the line for each of the  $P$ - $P$  and  $P$ - $SV$  data sets are shown in Figure 6.16. The  $S$ -wave record (Figure 6.16b) indicates generally greater mode conversion with increasing offset, as expected from the Zoeppritz equations (Zoeppritz, 1919). The strong reflection located at about 1200 ms on the  $P$ -wave record (Figure 6.16a) shows a measurable decrease in amplitude with offset, but no analysis has yet been done to quantify this, or relate  $P$ - $P$  and  $P$ - $SV$  AVO effects. Some weak coherent events with large NMO overcorrection are visible on Figure 6.16b, probably from  $P$ - $P$  reflections recorded on the radial component.

After residual statics and stacking velocities were obtained, the  $P$ - $SV$  data were stacked using an approximate  $V_p/V_s$  value to give an initial  $S$ -wave section. Events were then hand-correlated between the  $P$ - $P$  and  $P$ - $SV$  stacks (Figure 6.17), and interval  $V_p/V_s$  values were computed using equation (2.29). Correlations were based upon similarities in

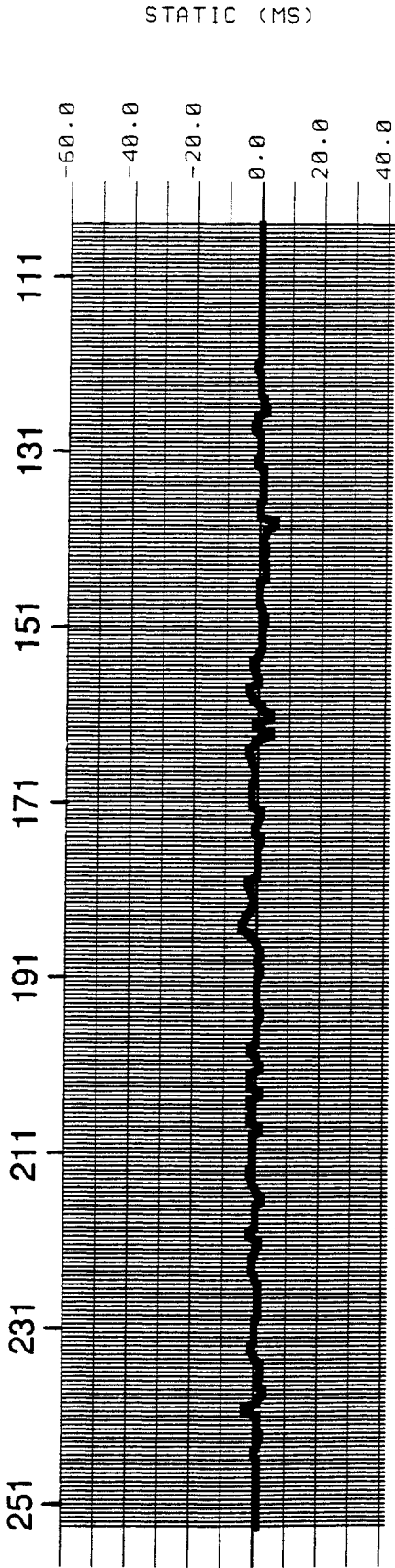


(a)

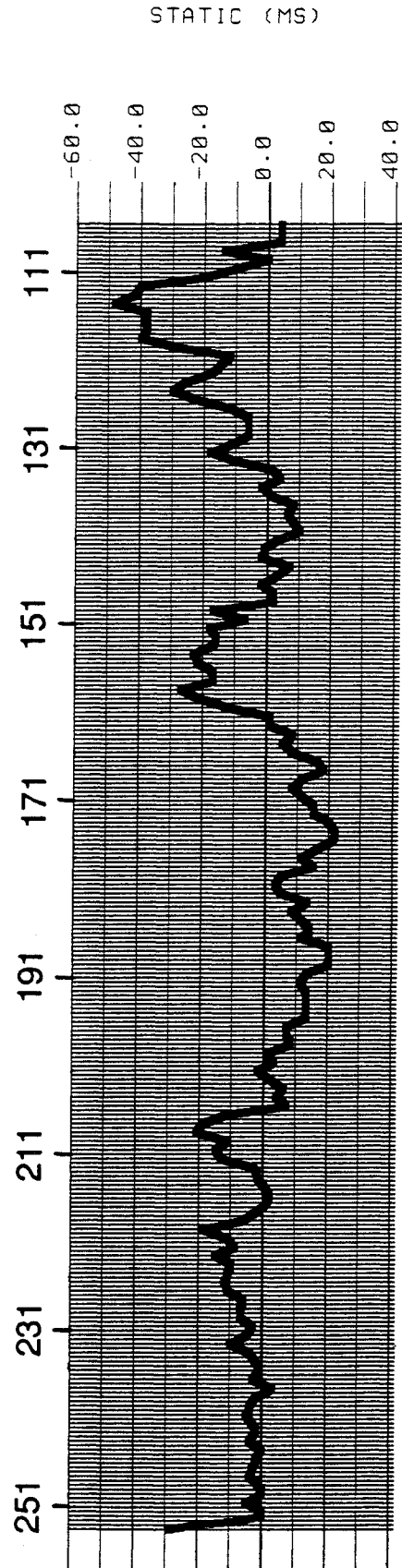


(b)

FIG. 6.13. Surface stacks of radial-component data with final  $P-P$  statics applied: (a) common source; (b) common receiver.



(a)



(b)

FIG. 6.14. Final receiver-static solutions: (a) vertical component ( $P-P$ ); (b) radial component ( $P-SV$ ).

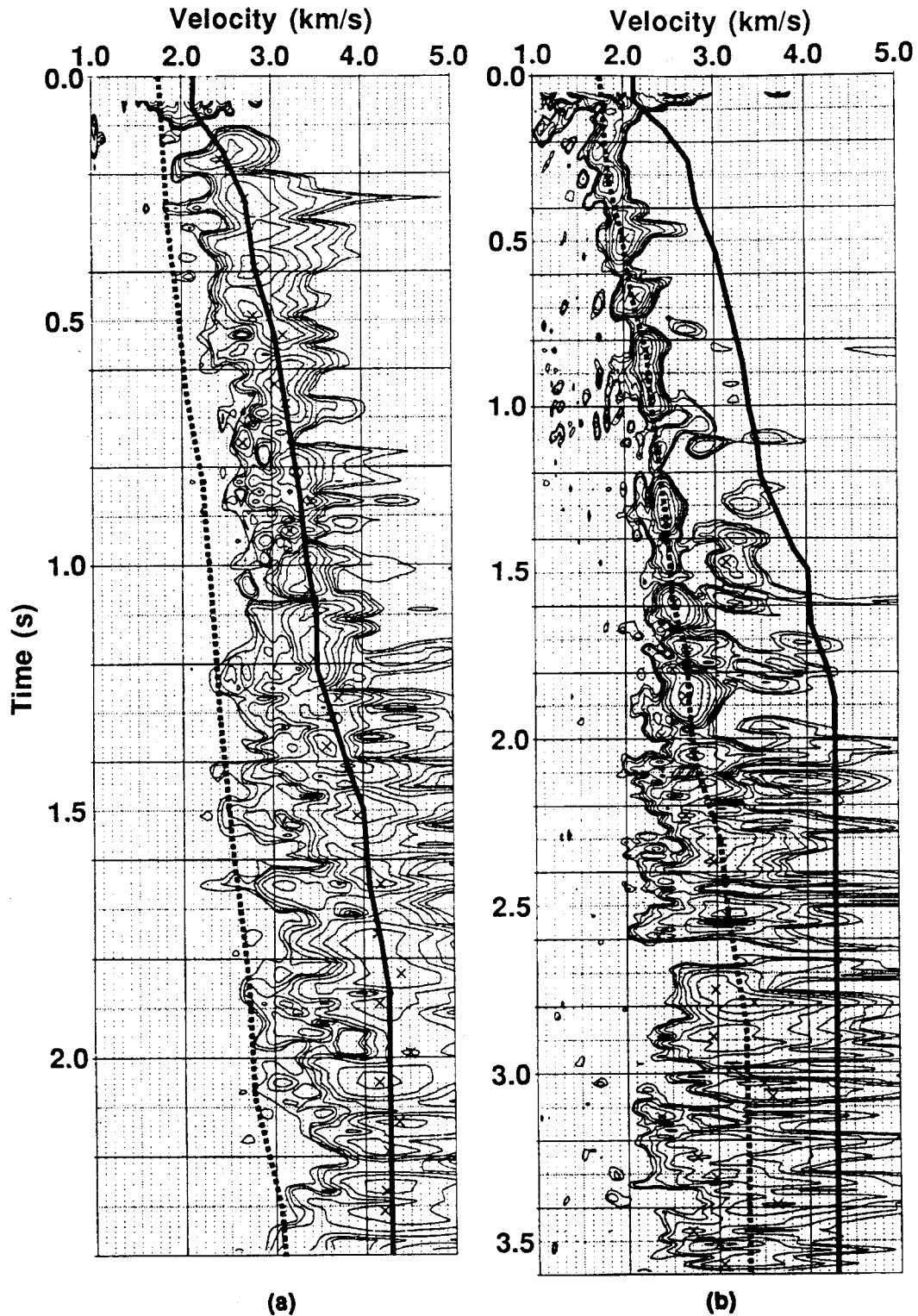


FIG. 6.15. Sample velocity analysis semblance displays: (a) vertical component ( $P$ - $P$ ); (b) radial component ( $P$ - $SV$ ). The solid line is the vertical-component NMO velocity function, and the dashed line is the radial-component NMO function.

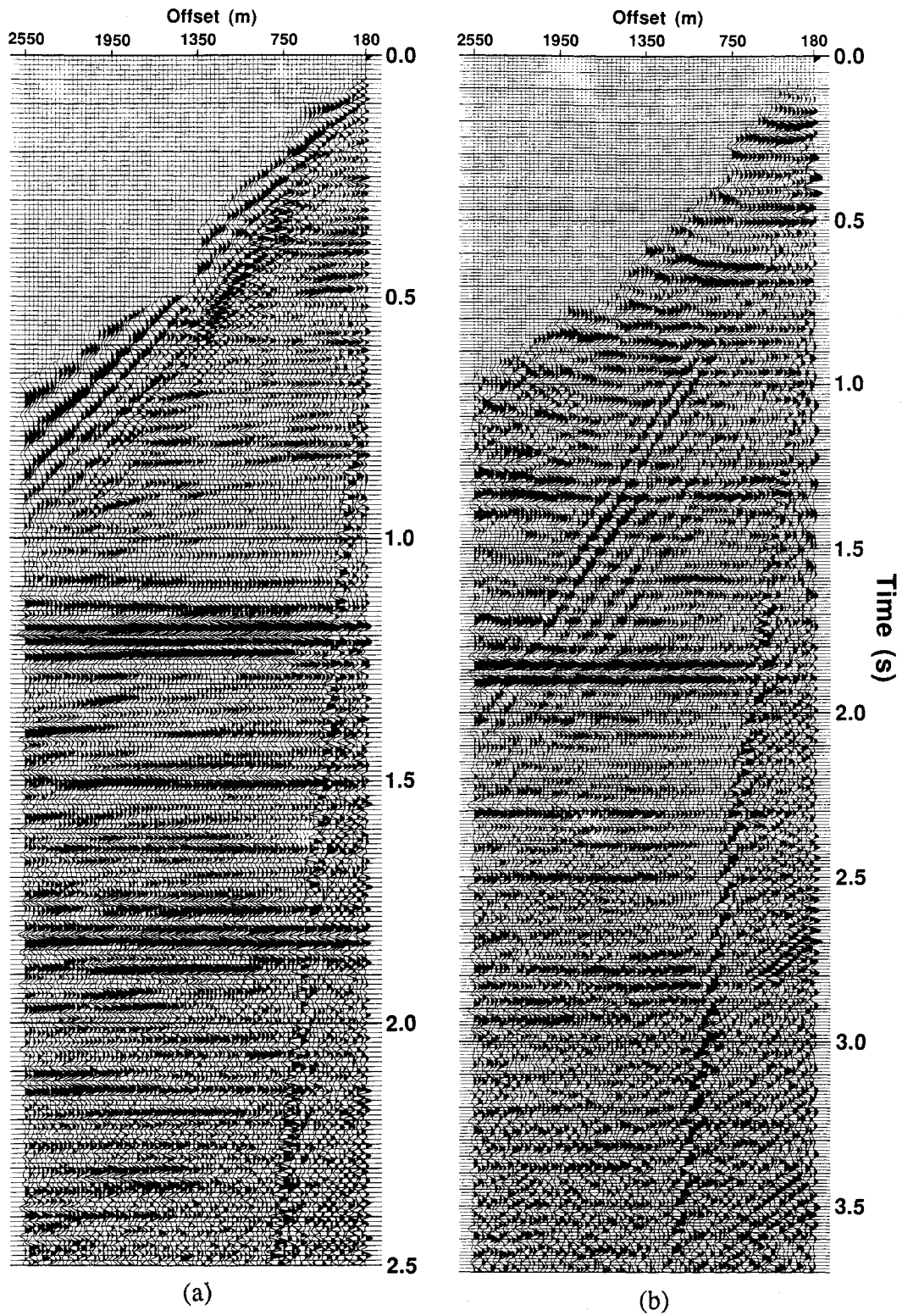


FIG. 6.16. Sample common-offset gather records: (a) vertical component ( $P$ - $P$ ); (b) radial component ( $P$ - $SV$ ).

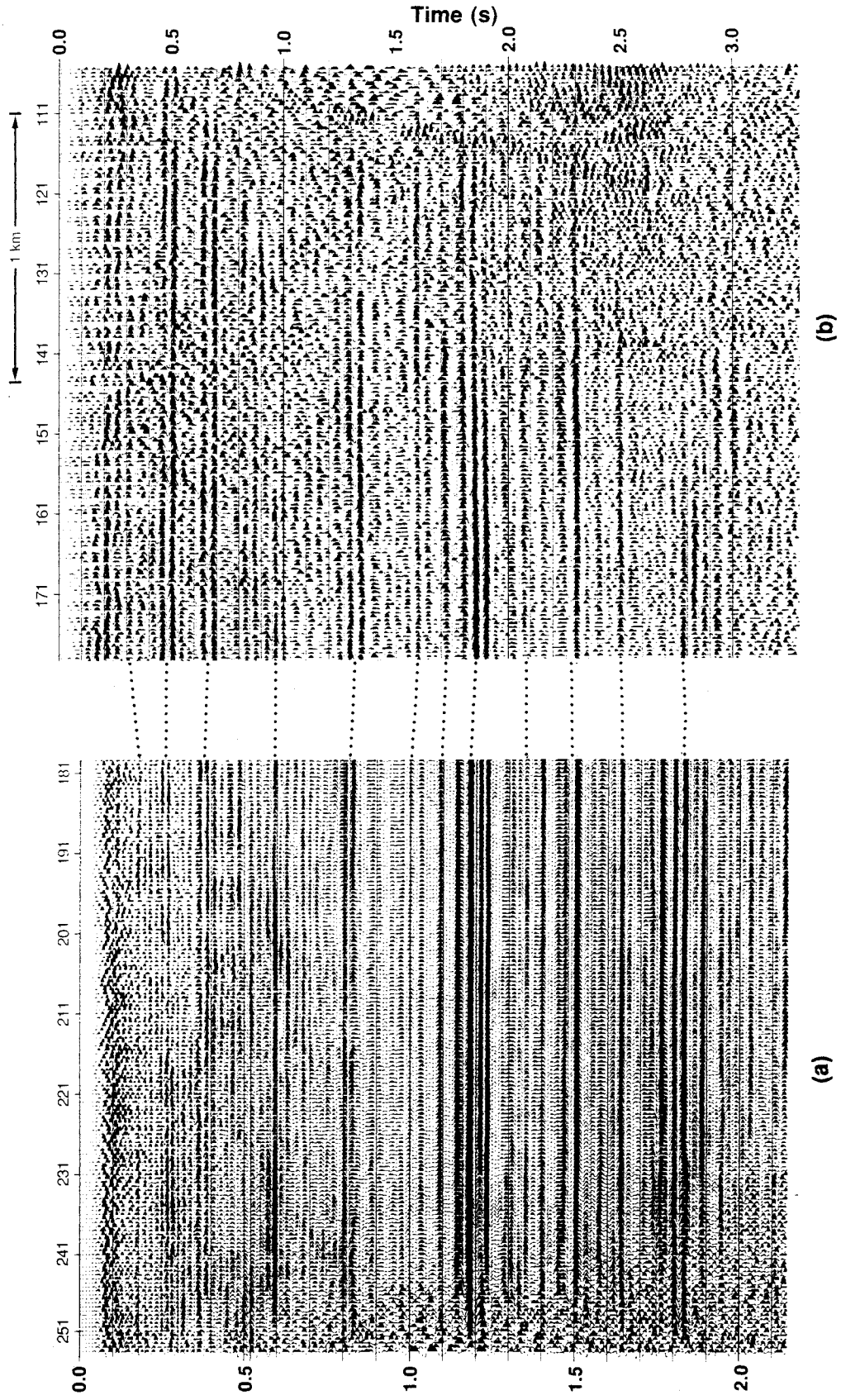


FIG. 6.17. Reflection correlation between (a) the vertical-component section and (b) the radial-component section.

reflection character, and are somewhat subjective. The results of these calculations are plotted in Figure 6.18. An average  $V_p/V_s$  down to the Cardium reflection was calculated using the values computed between events, weighed by the  $P$ - $P$  time interval over which the value was computed. The first value of 2.57 was not considered reliable, and was excluded from the calculations. This resulted in a  $V_p/V_s$  value of 1.95 for the line.

The radial-component ( $P$ - $SV$ ) data were then stacked using this average  $V_p/V_s$  value and the asymptotic approximation [equation (2.25)], giving the result displayed in Figure 6.19. On the  $S$ -wave sections, the Cardium reflection (Cz) occurs at 1600 ms, and the Precambrian (Pc) is at roughly 2800 ms. The noise level of the  $S$ -wave section is qualitatively seen to be greater than that of the  $P$ -wave section, especially for times greater than 2.0 s. Figure 6.20 is a plot of the averaged time-variant cross-power spectra between adjacent  $S$ -wave stack traces, and indicates a usable  $S$ -wave bandwidth of approximately 6-30 Hz. An  $f$ - $k$  filter with a passband from -3 to +3 ms/trace and a 6 db maximum reject was applied to the data of Figure 6.19 to give the result shown in Figure 6.21. The  $f$ - $k$  filter was found to work well at reducing section noise and improving reflector continuity.

The radial-component data were restacked using the depth-variant CCP binning method [equations (2.26)], giving the section in Figure 6.22. An  $f$ - $k$  filter identical to that used on the asymptotically-binned stack (Figure 6.21) was also applied (Figure 6.23).  $P$ - $SV$  DMO was performed (Figure 6.24), followed again by  $f$ - $k$  filtering (Figure 6.25). Poststack finite-difference migration (Claerbout and Doherty, 1972), using the velocity function defined by equation (5.24), of the  $f$ - $k$ -filtered DMO section in Figure 6.25 produced the result shown in Figure 6.26. Migration was done after  $f$ - $k$  filtering in order to reduce noise-generated artifacts on the  $S$ -wave sections.

$P$ - $SV$  velocity inversion using equation (2.38) was applied to part of the  $f$ - $k$  filtered DMO section (Figure 6.29), giving the result shown in Figure 6.31. The background velocity was constructed using  $P$ -wave velocities taken from a nearby sonic log

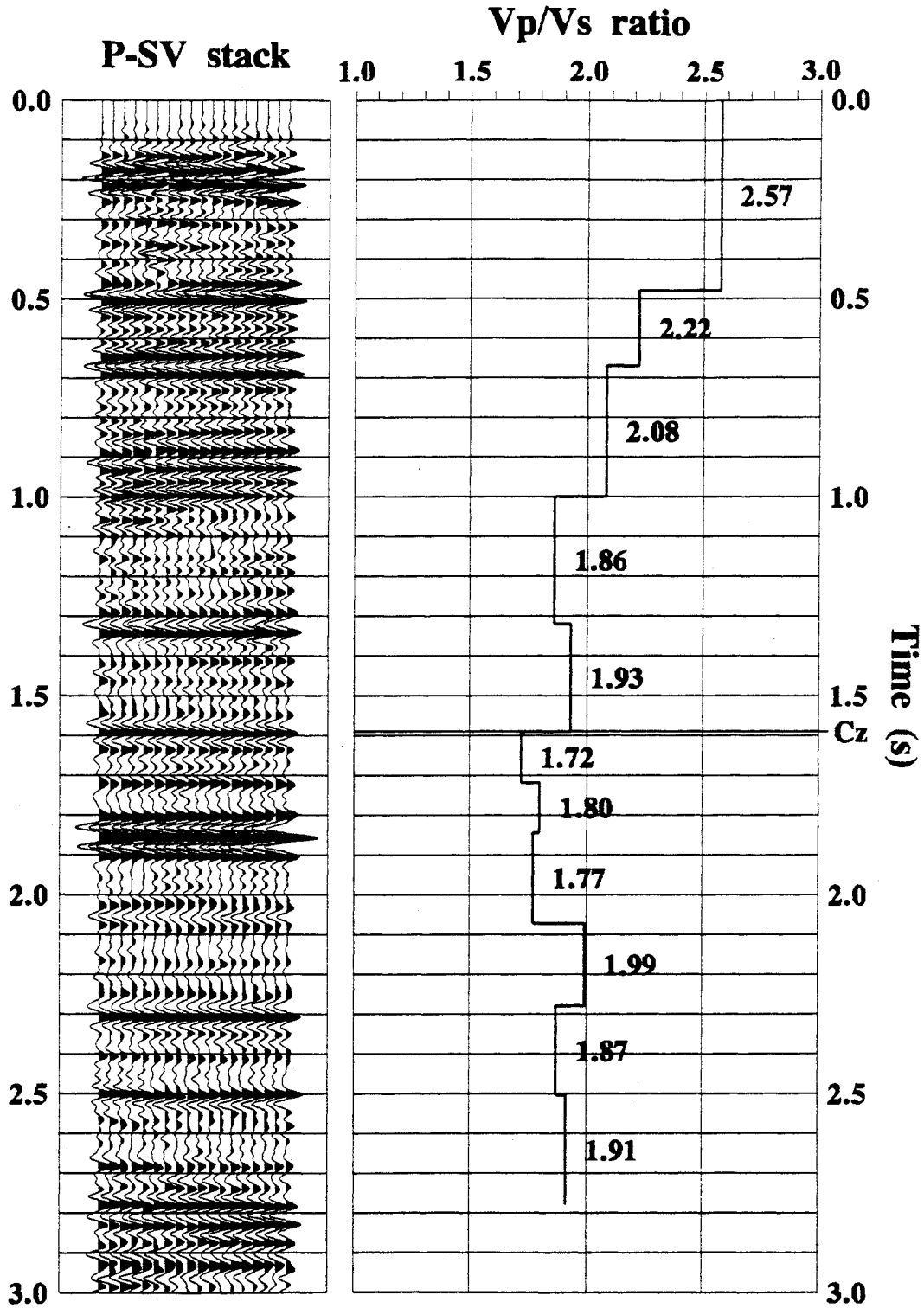


FIG. 6.18.  $V_p/V_s$  values from correlation of vertical- and radial-component reflections.

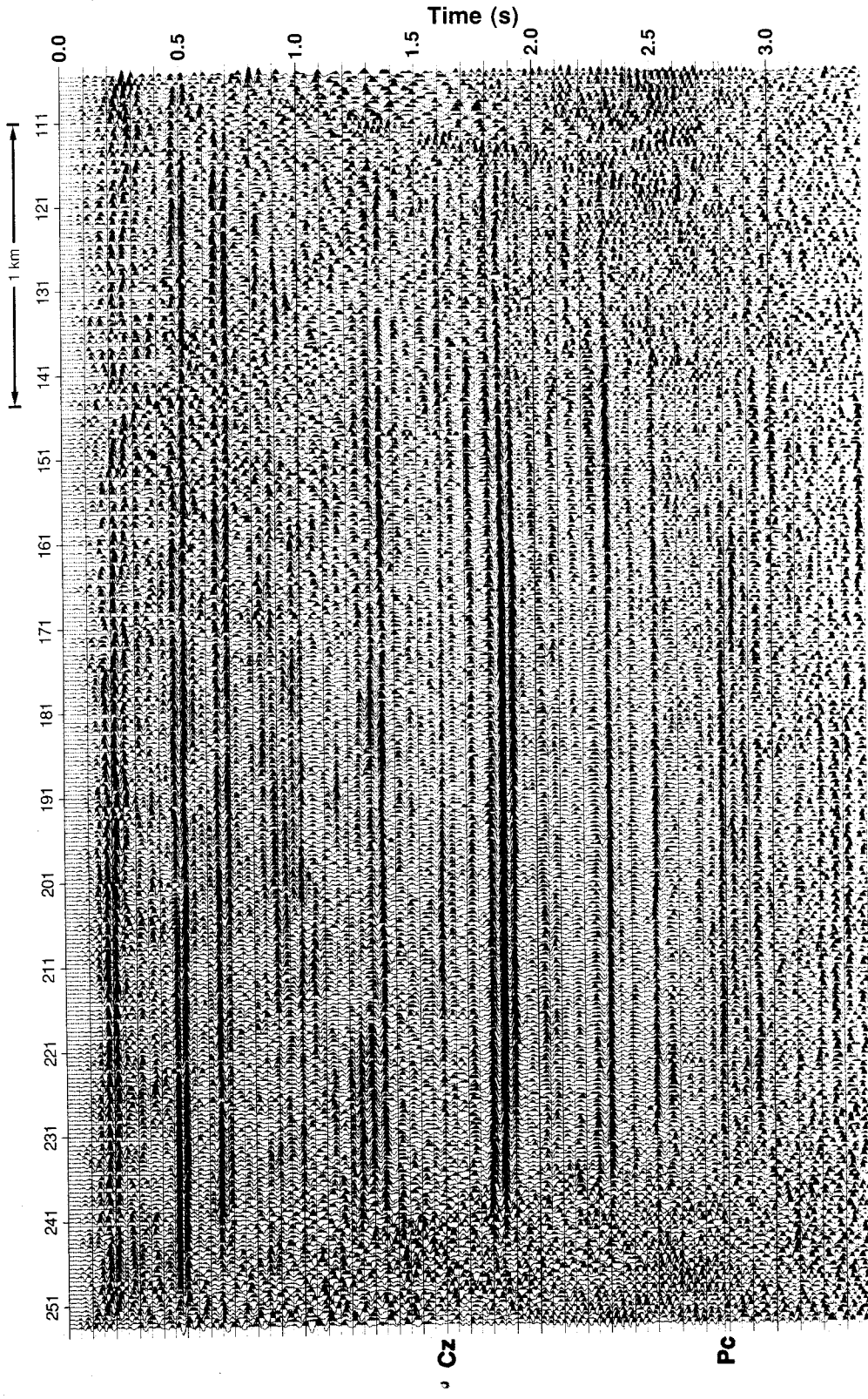


FIG. 6.19. Stack section of radial-component data with asymptotic binning.

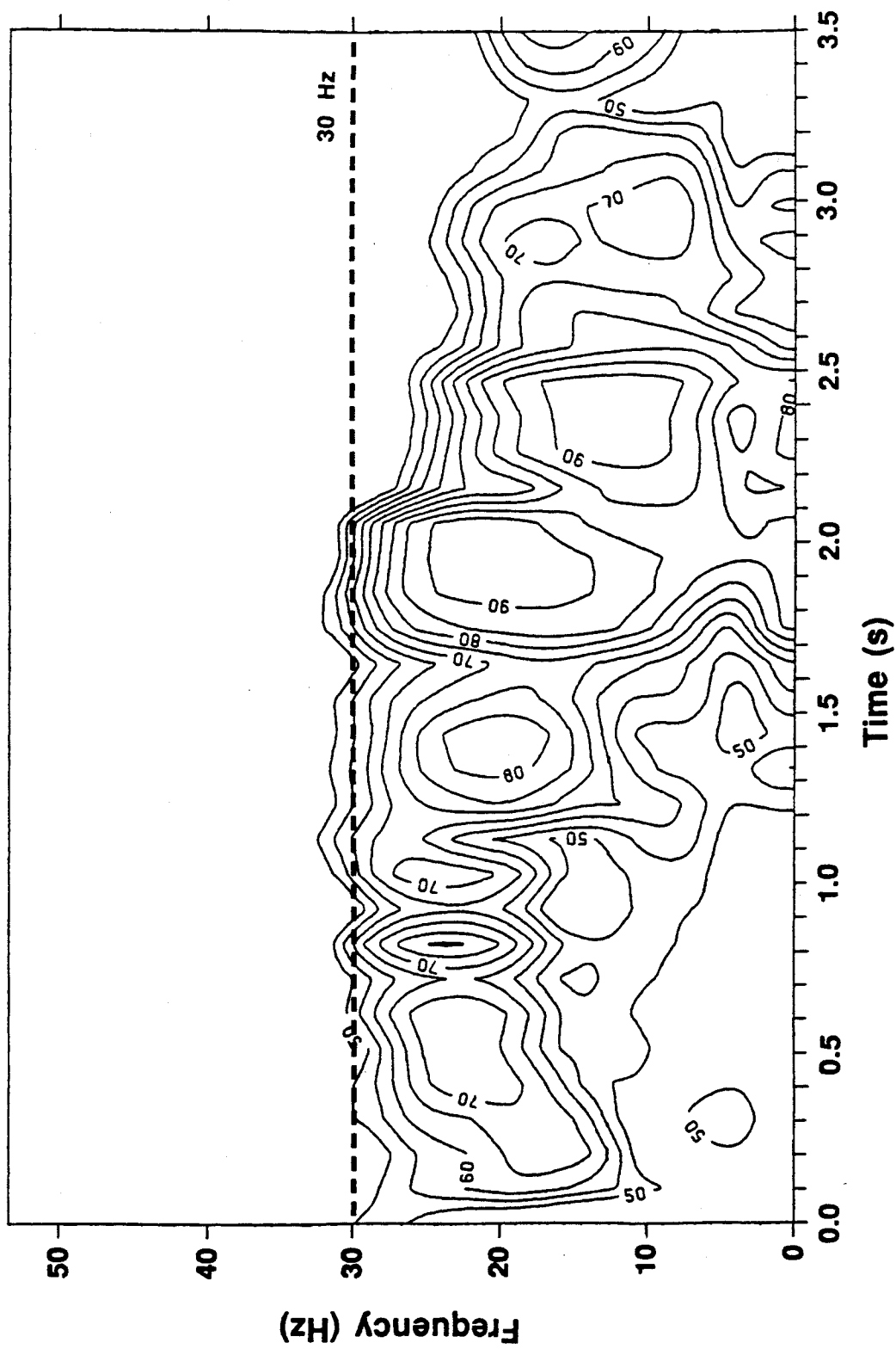


FIG. 6.20. Averaged time-variant cross-power spectra for the S-wave stacked data. Spectra were computed as in Figure 6.7. Contours are in percentage of maximum.

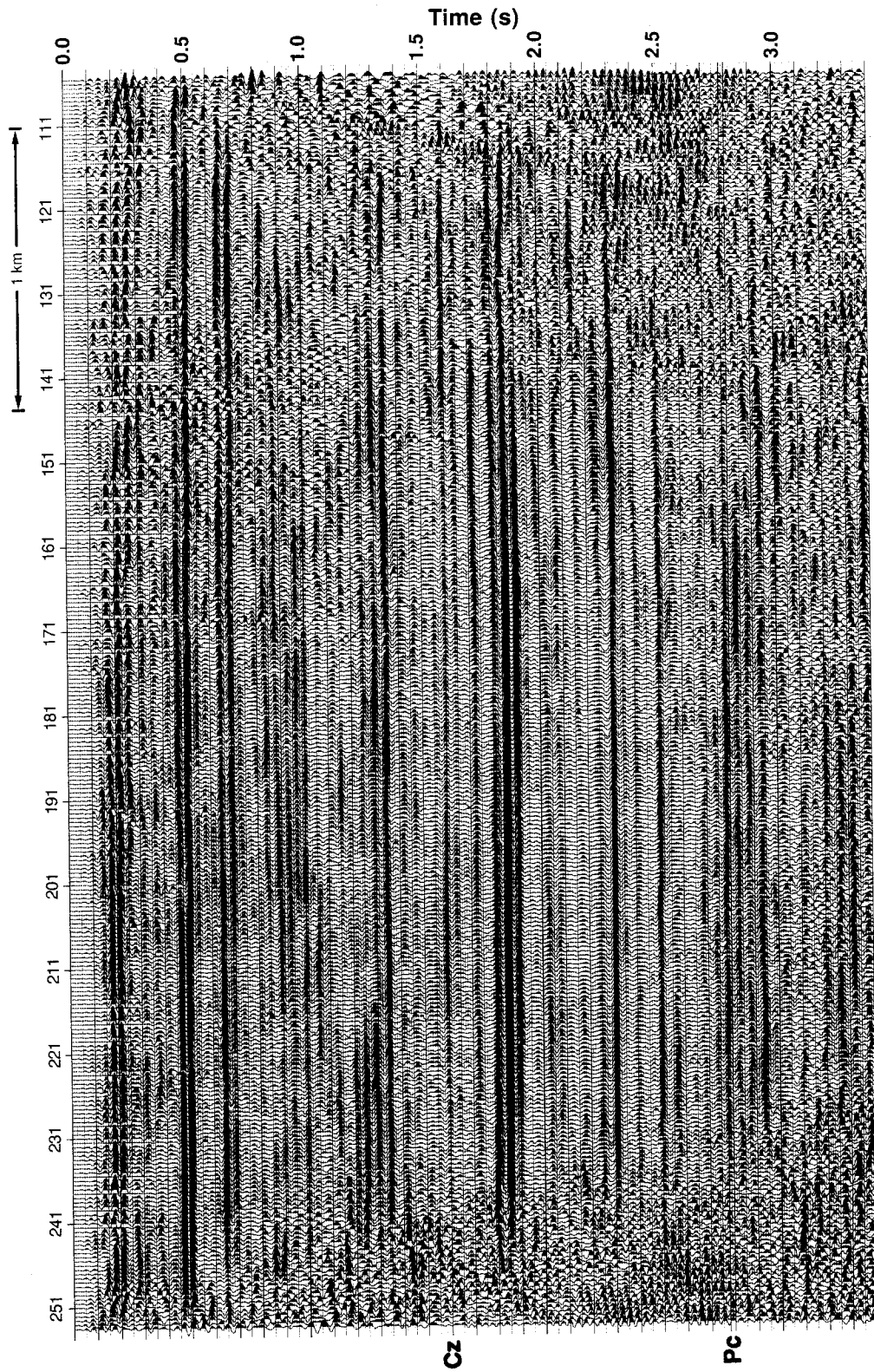


FIG. 6.21. Stack section of radial-component data with asymptotic binning and poststack  $f-k$  filter applied.

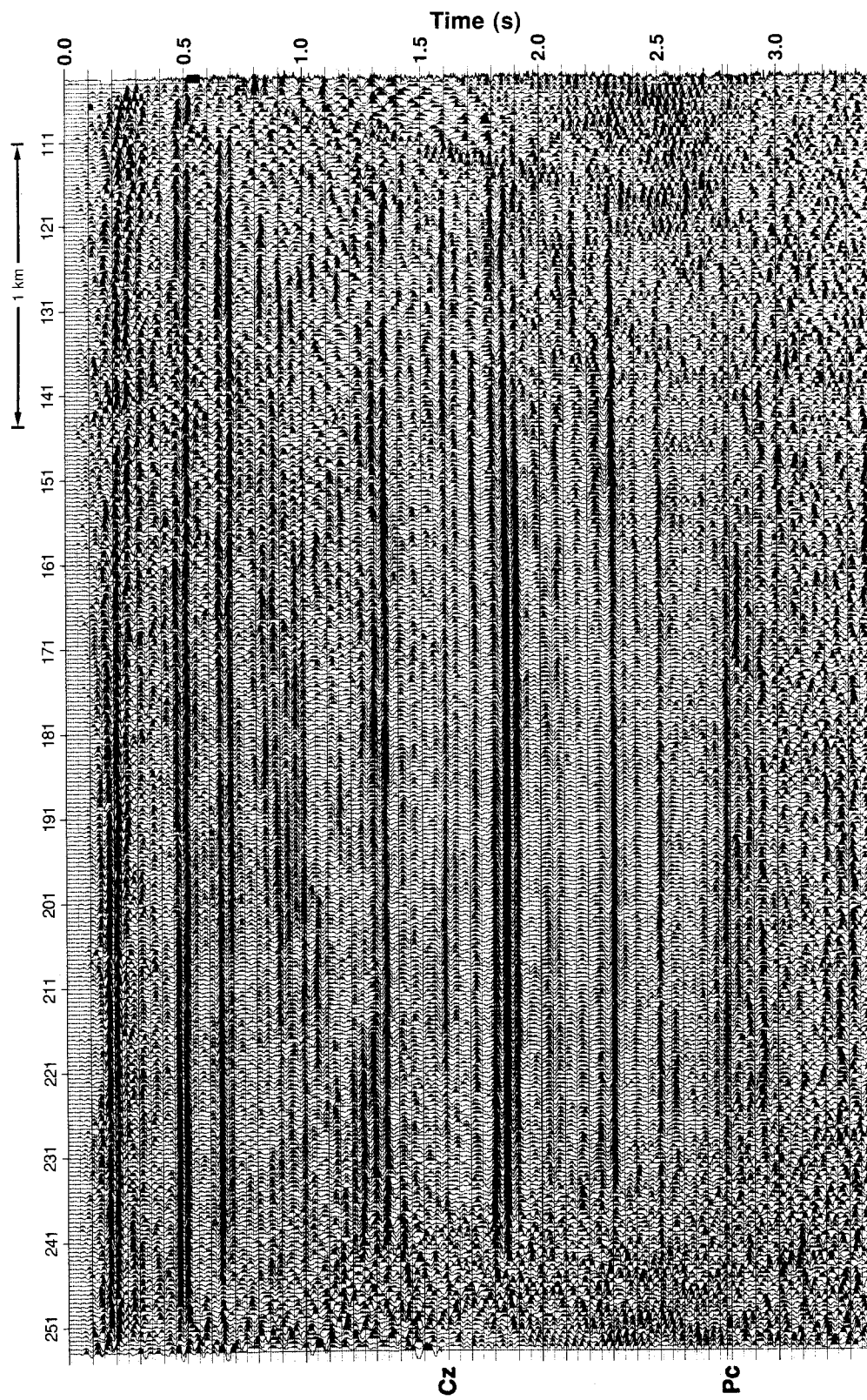


FIG. 6.22. Stack section of radial-component data with depth-variant binning.

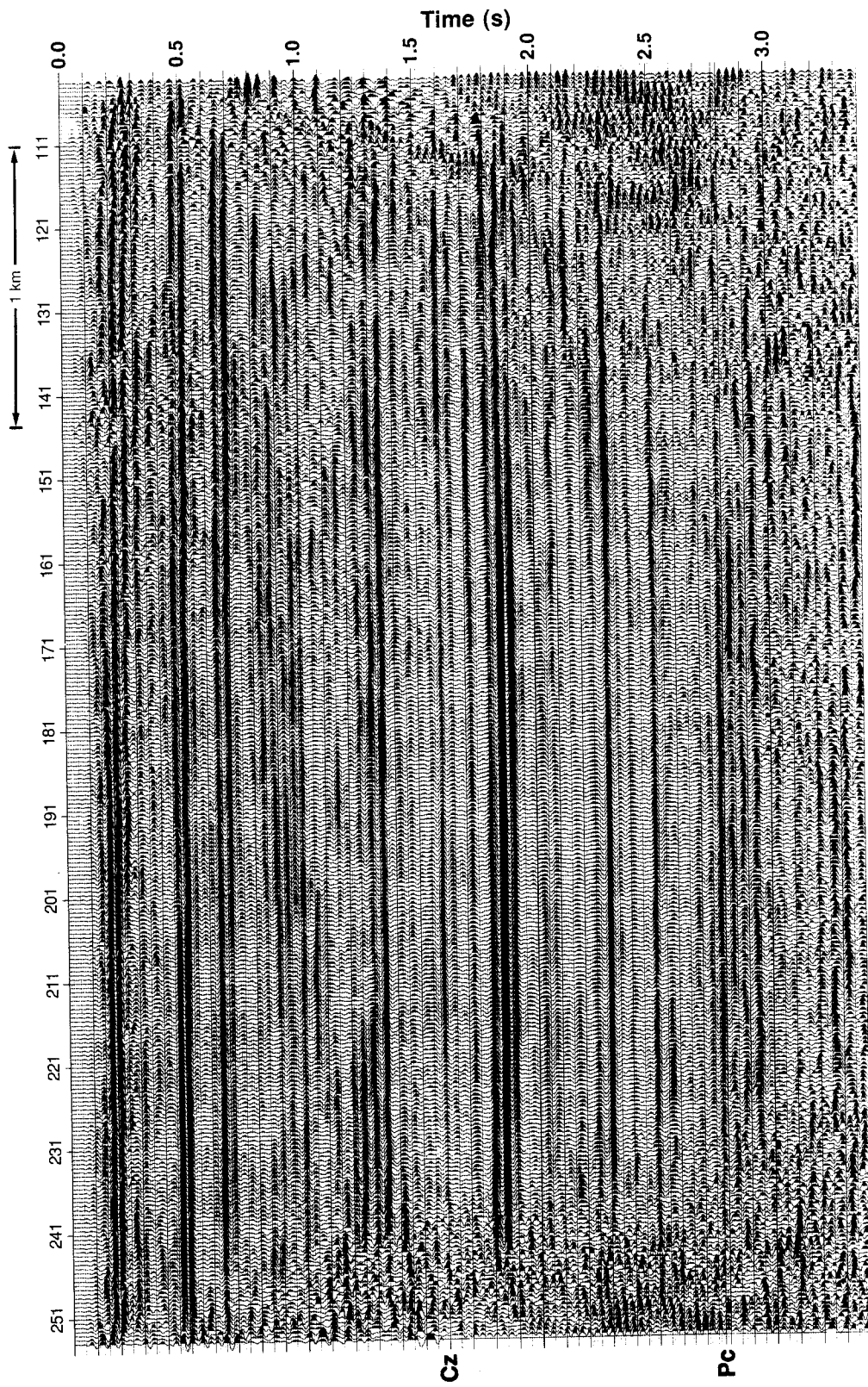


FIG. 6.23. Stack section of radial-component data with depth-variant binning and poststack  $f$ - $k$  filter applied.

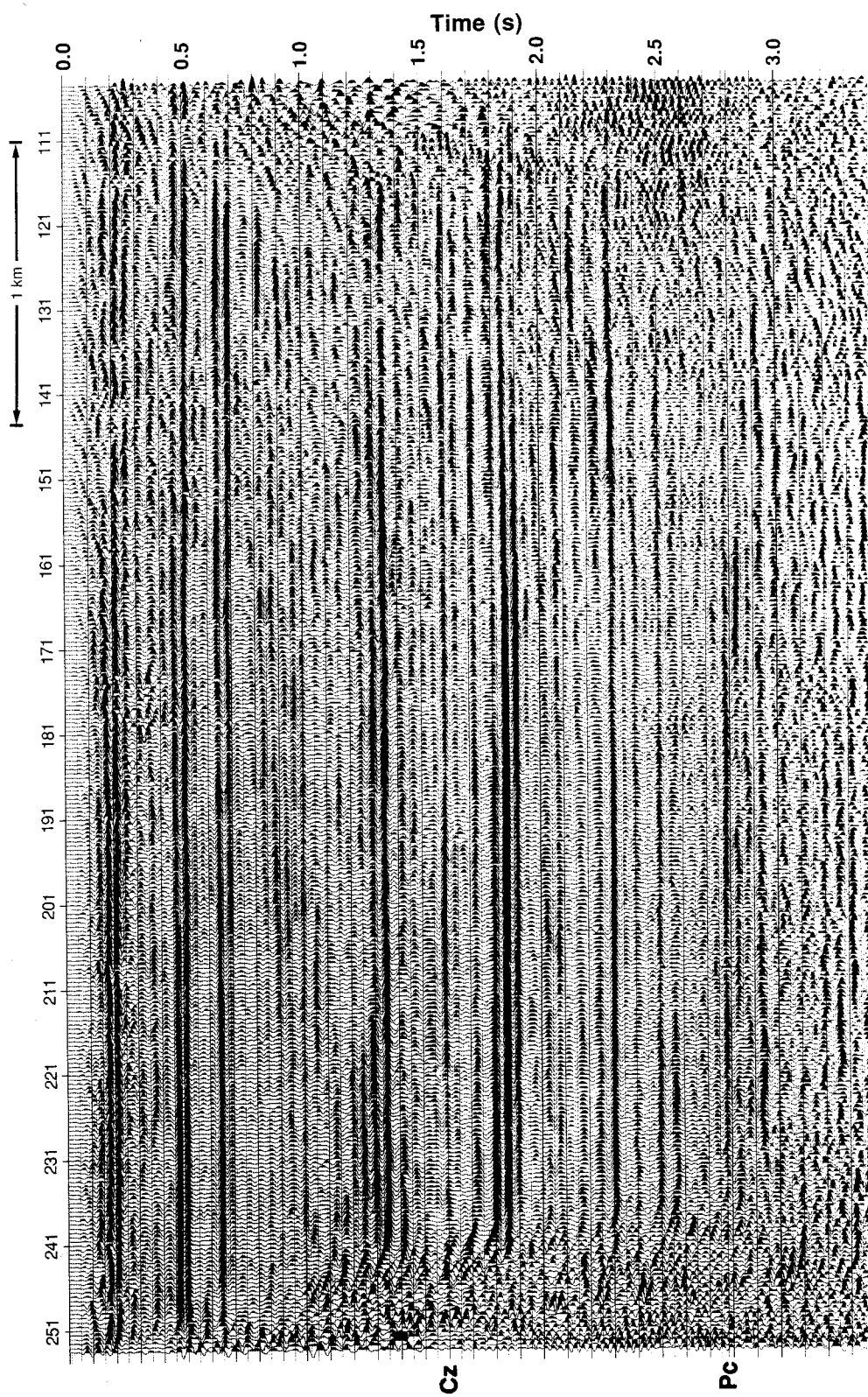


FIG. 6.24. Stack section of radial-component data with P-SV DMO.

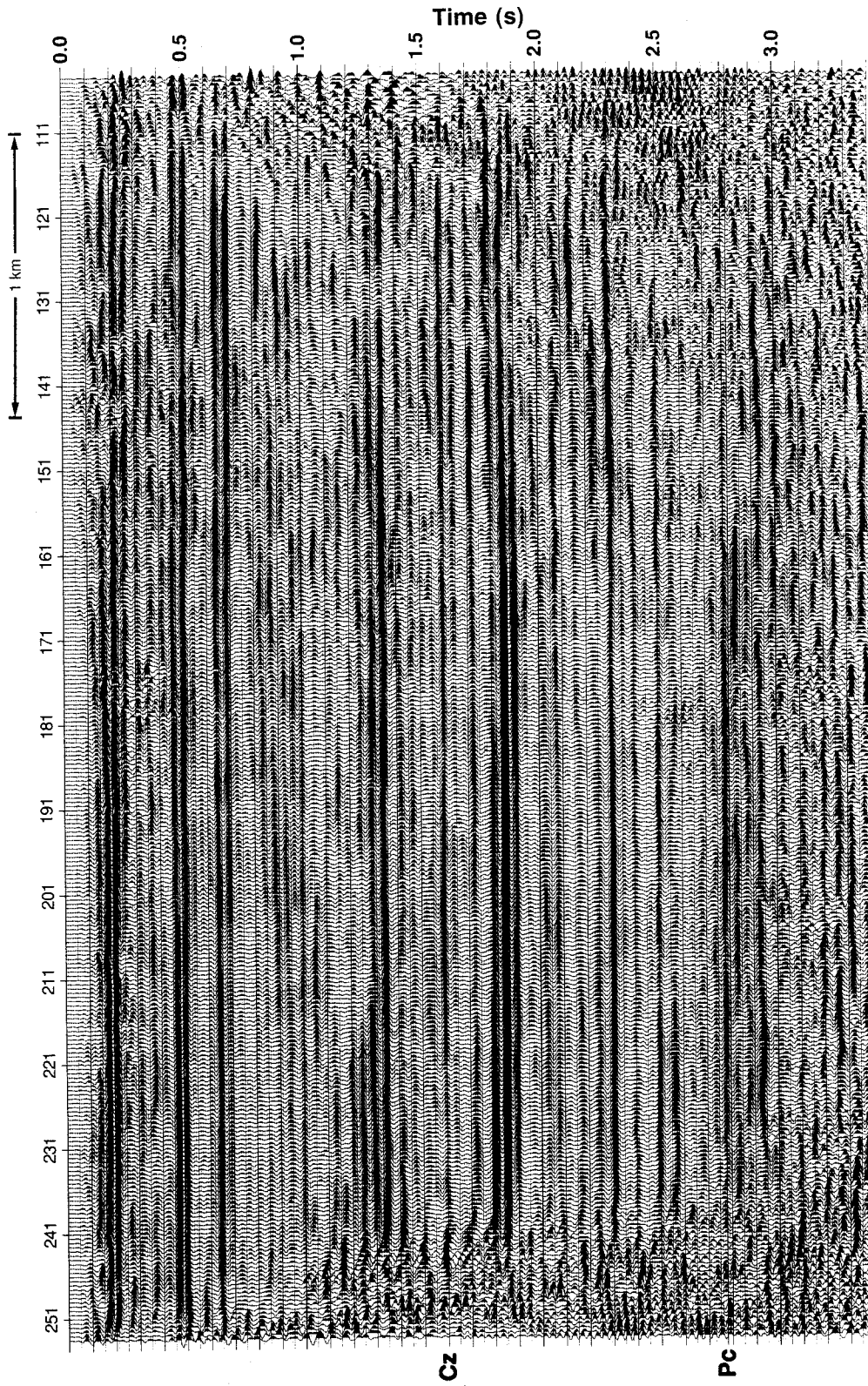


FIG. 6.25. Stack section of radial-component data with  $P$ - $SV$  DMO and poststack  $f$ - $k$  filter applied.

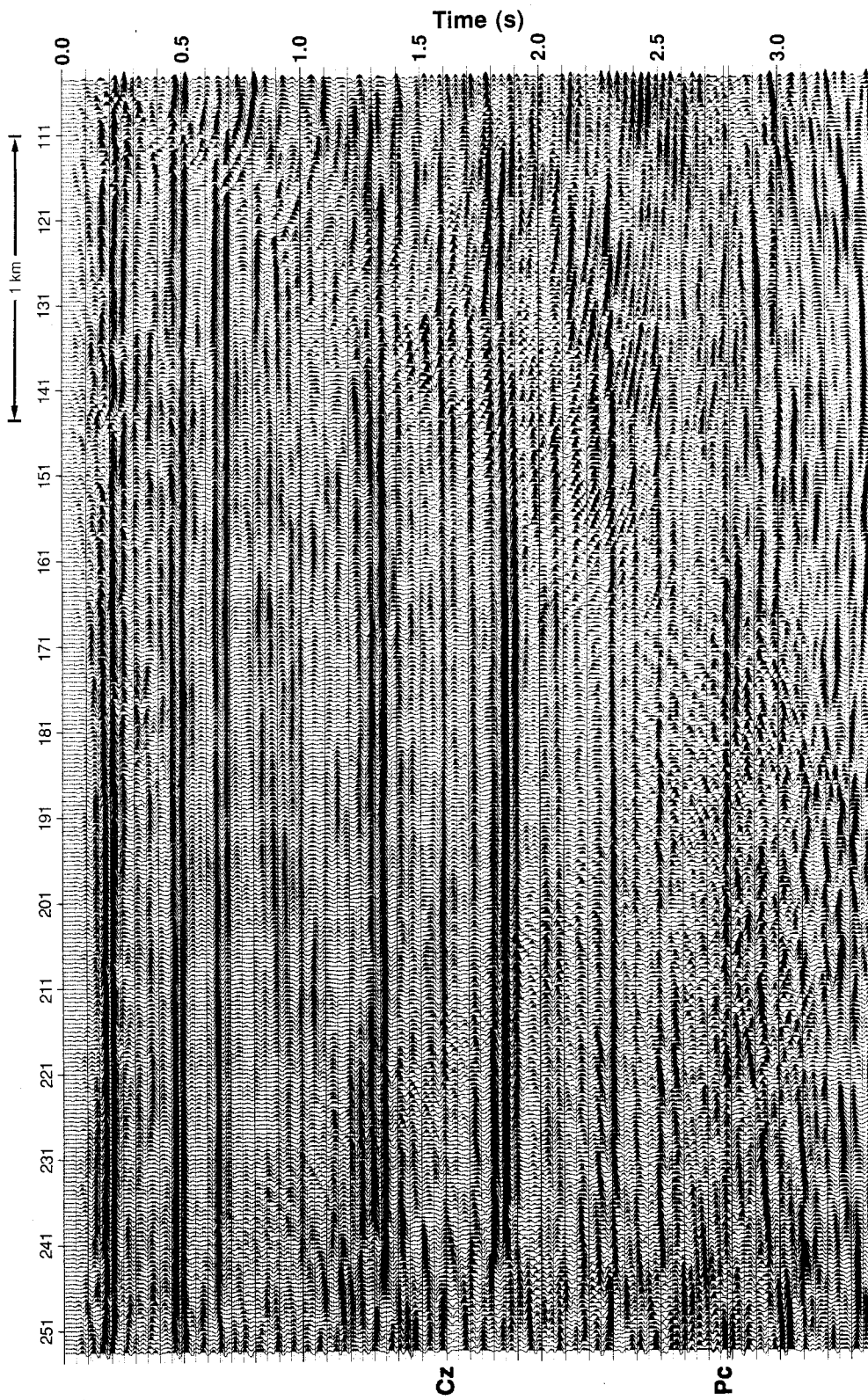


FIG. 6.26. Migrated stack section of radial-component data with  $P$ - $SV$  DMO and poststack  $f$ - $k$  filter applied.

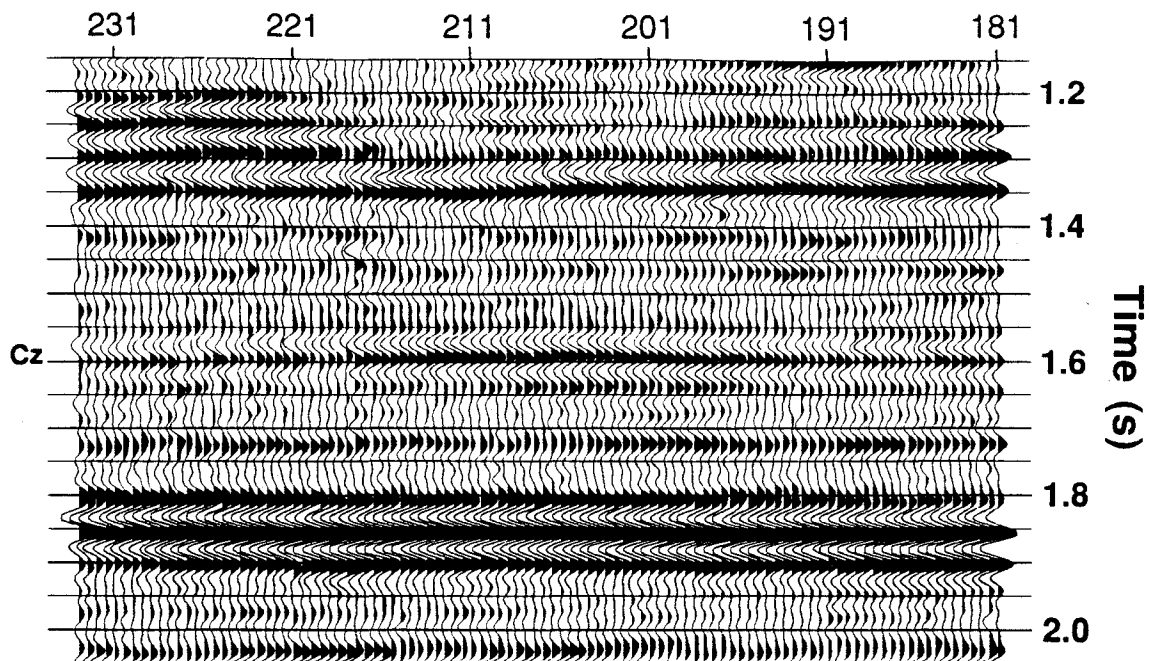


FIG. 6.27. Enlargement of radial-component section with asymptotic binning and poststack  $f$ - $k$  filter applied.

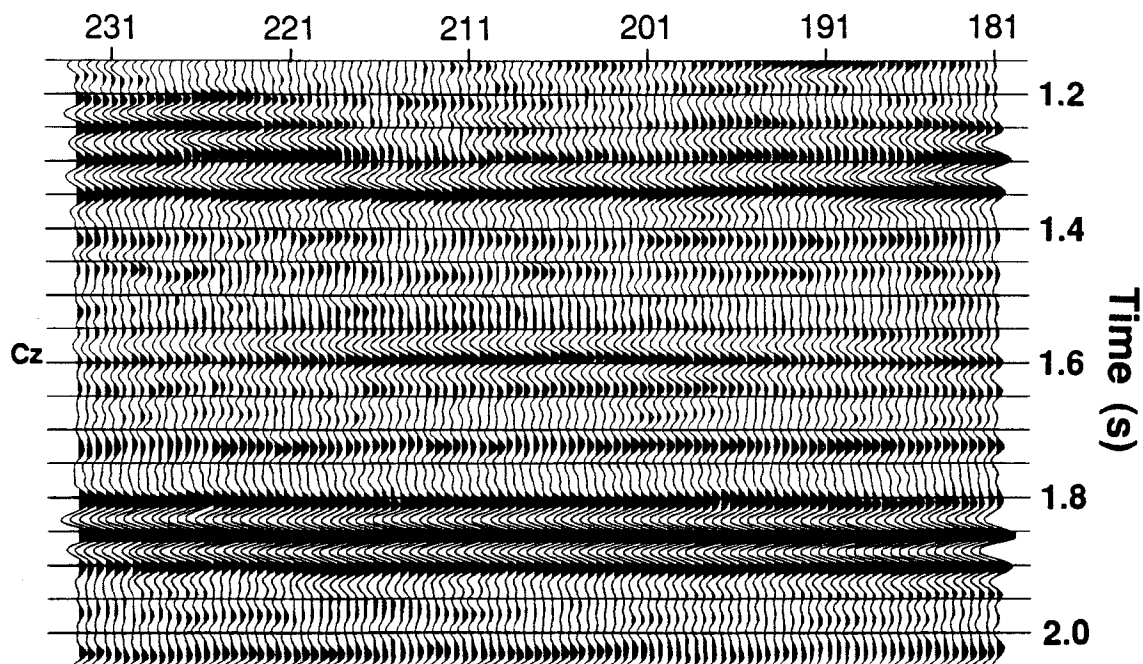


FIG. 6.28. Enlargement of radial-component section with depth-variant binning and poststack  $f$ - $k$  filter applied.

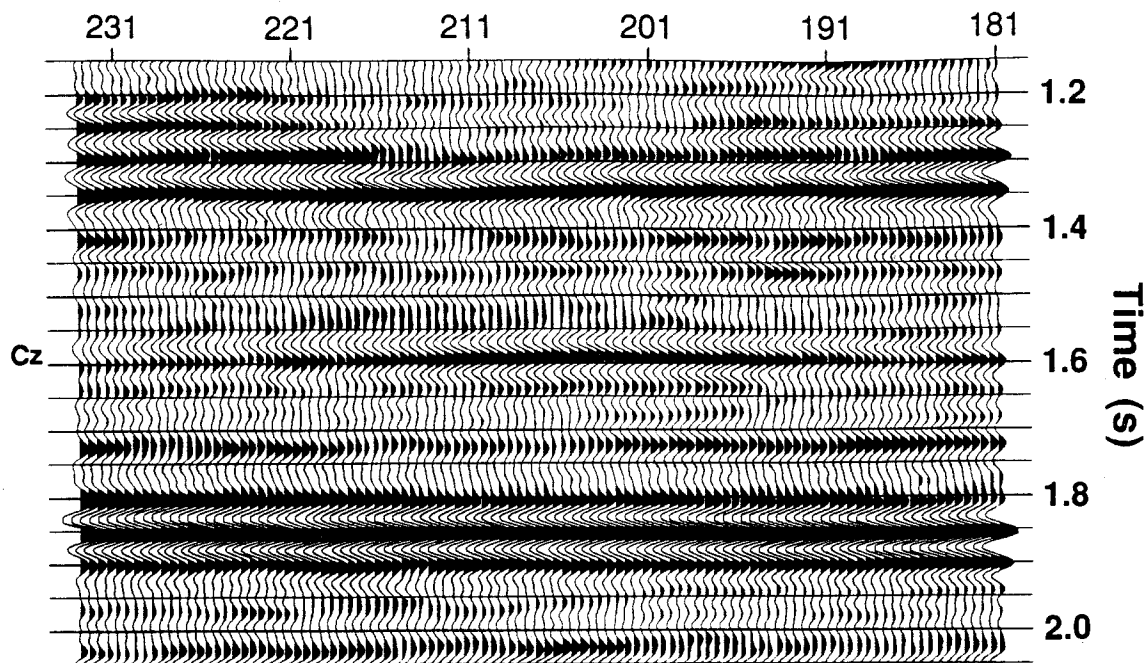


FIG. 6.29. Enlargement of radial-component section with  $P$ -SV DMO and poststack  $f$ - $k$  filter applied.

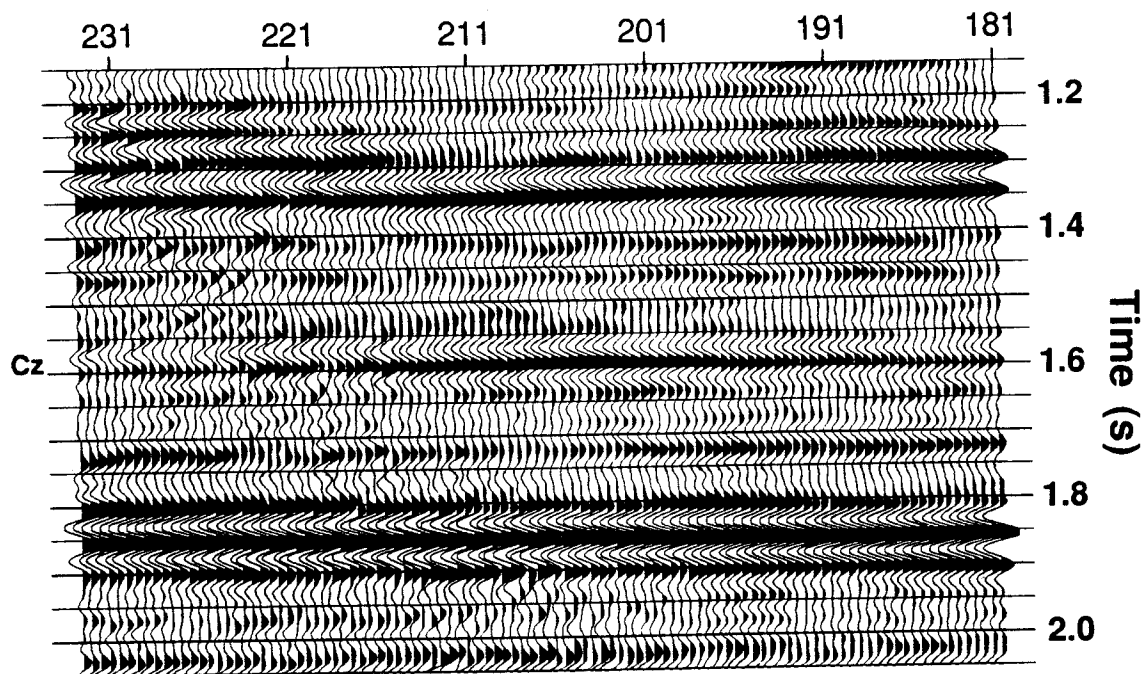


FIG. 6.30. Enlargement of migrated radial-component section with  $P$ -SV DMO and poststack  $f$ - $k$  filter applied.

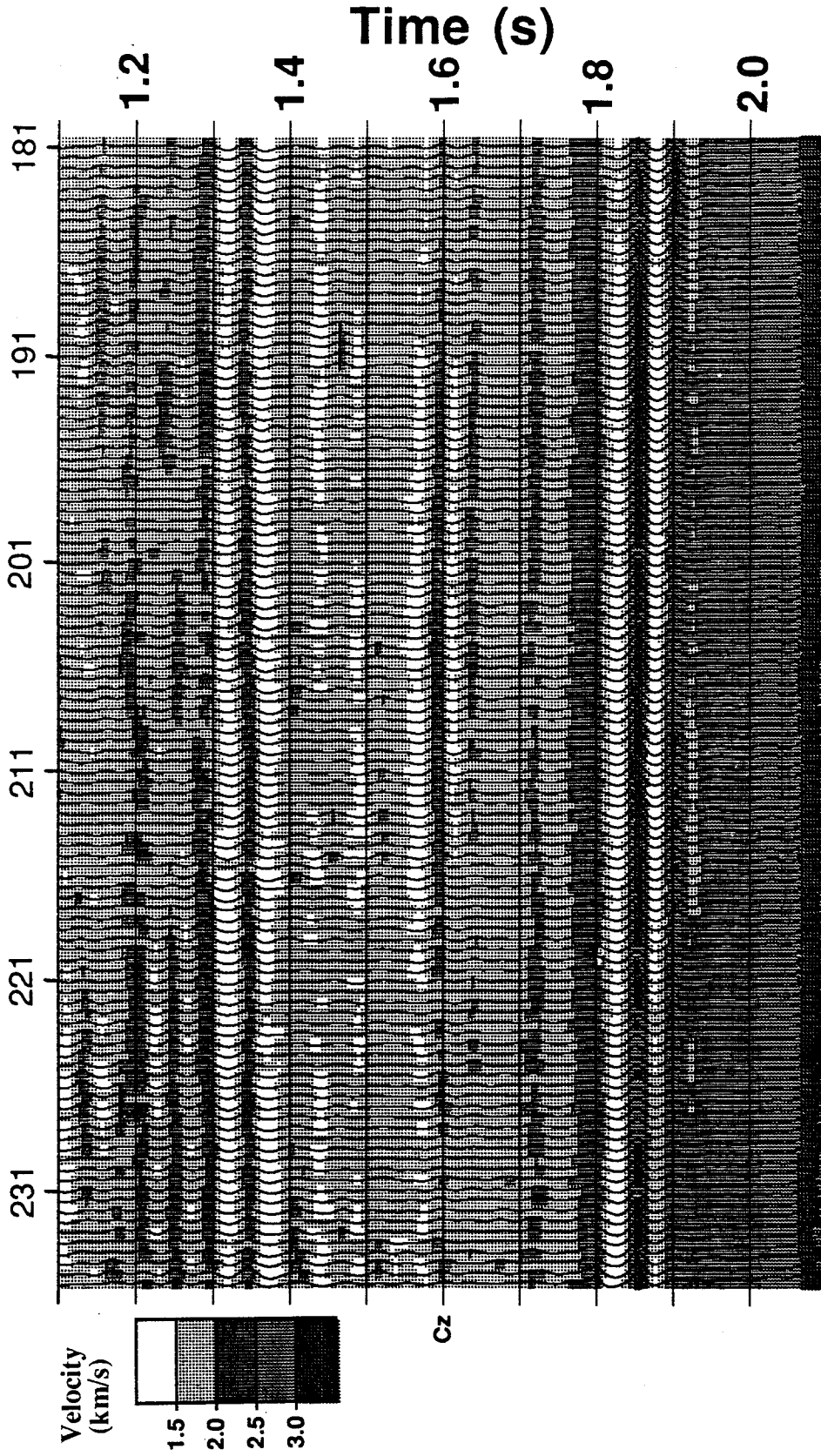


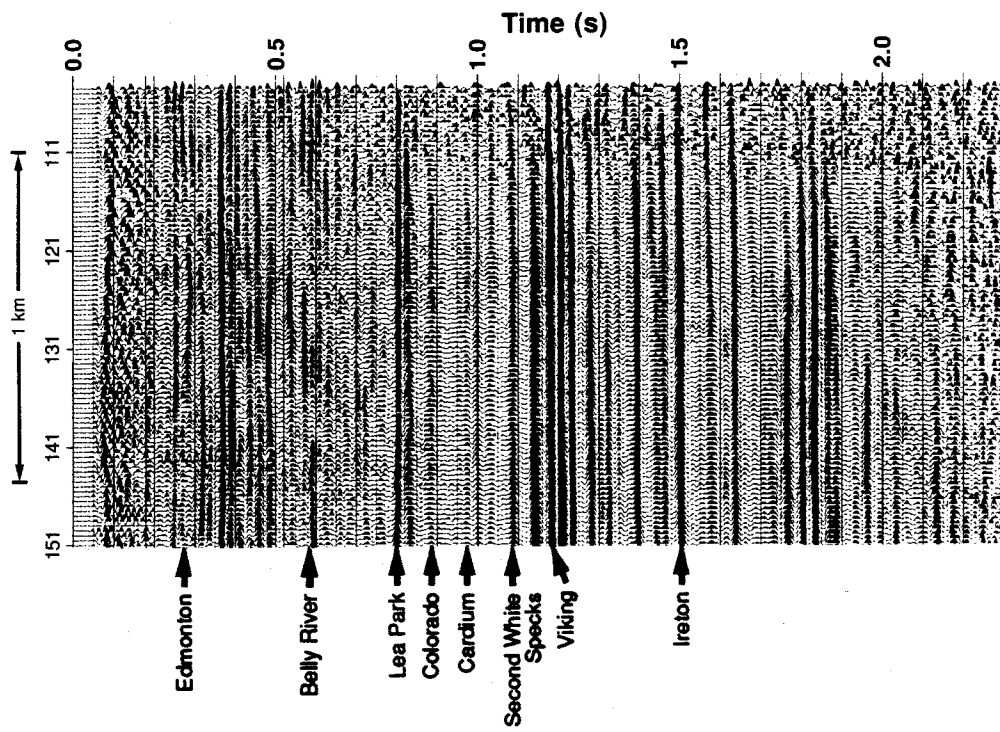
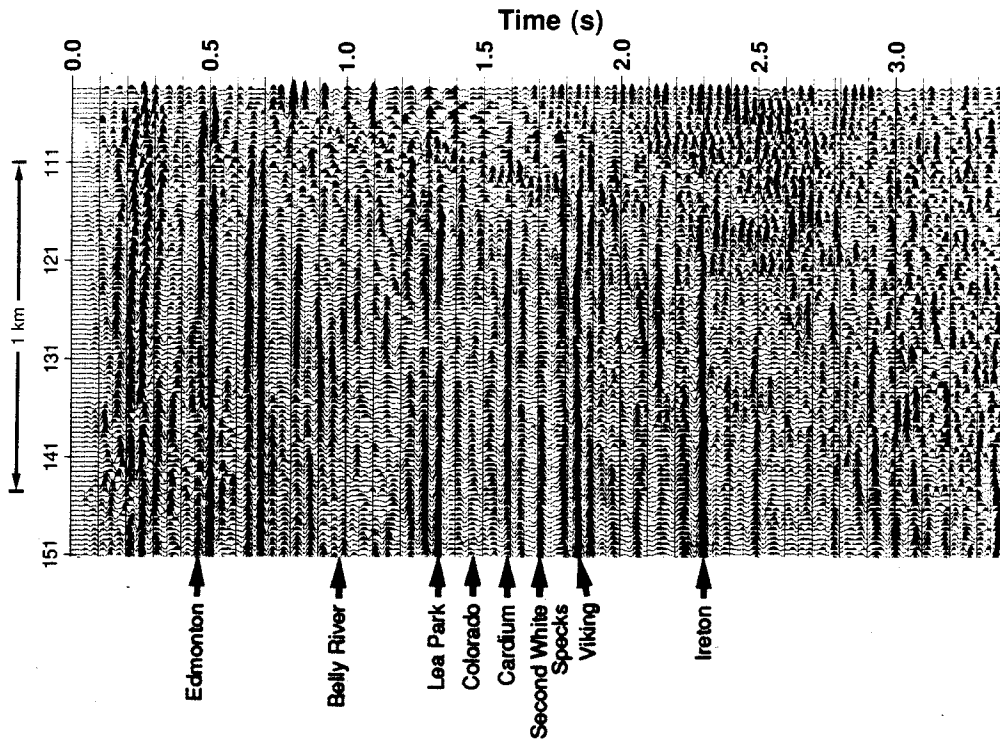
FIG. 6.31. *P-SV* velocity inversion applied to a window of the radial-component section with *P-SV* DMO and poststack *f-k* filter applied.

(1-3-53-13W5), and  $S$ -wave velocities were computed using the interval  $V_p/V_s$  values of Figure 6.18. The transition frequency between background and inversion velocities was 6 Hz.

The major reflections on the vertical- and radial-component stack sections are labeled in Figure 6.32. Reflection identification is from Nazar (1991), and is based on well control information and correlation to synthetic seismograms.

## 6.4 Discussion

The 1280 m/s wavetrains on the radial-component records (Figure 6.2) do not appear to be either ground roll [pseudo-Rayleigh wave motion; see Sheriff (1973)] or Love waves. Source-generated ground roll would give surface motion in both the vertical and horizontal directions, while Love waves should give motion mainly on the transverse component (Aki and Richards, 1980), neither of which is the case here. The presence of the wavetrain on the radial channel, coupled with its velocity, suggests that it might be refracted pure  $S$ -wave energy that has been generated by the vibrators. Studies by Edelman (1985) show that substantial amounts of shear energy are radiated by  $P$ -wave vibrators at off-vertical angles. If these shear waves are subsequently refracted in the near-surface, they should be recorded on the radial component of the receivers, as is seen here. Also, the ratio of the  $P$ -wave refraction velocity (3150 m/s) to the suspected shear-refraction velocity (1280 m/s) gives a  $V_p/V_s$  value of 2.46, which is reasonable for a shallow, compacted shale (Garotta, 1985; Tatham, 1985). A comparison of  $P$ - $P$  and  $P$ - $SV$  reflection event times for a shallow marker on the final processed sections produces an average  $V_p/V_s$  value of 2.57 for the first roughly-350 m of depth, which is supportive. Schafer (1989) gives other examples of what appear to be source-generated, refracted  $S$ -waves in dynamite data. If these are refracted  $S$ -waves, then traveltime analysis of these refractions might



(a) Major reflections as interpreted by Nazar (1991); (b)  $f-k$  filtered vertical-component stack section; (b)  $f-k$  filtered radial-component stack section.

(a)

(b)

enable the construction of an  $S$ -wave model of the near-surface, from which static corrections could be made.

The absence of reflection energy on the transverse-component records suggests either that any  $S$ -wave velocity anisotropy in this area is not significant at the frequencies found here, or that the line is positioned along one of the axes of the natural velocity coordinate system. From studies of well-breakout orientation in Western Canada, Bell and Babcock (1986) conclude that the stress gradient in the subsurface lies in a direction normal to the general orientation of the Rocky Mountains; roughly the direction of line CC-SW-01. If this stress is largely responsible for subsurface anisotropy in this area, then line CC-SW-01 roughly falls along a principle velocity axis, as indicated by the analysis done in Section 3.4.2.

From the plot of the final  $P$ - $P$  receiver static corrections (Figure 6.13a), the thickness of the near-surface weathering layer that the  $P$ -wave energy passes through is almost constant across the line. The  $P$ - $SV$  static correction plot (Figure 6.13b), however, shows that the  $S$ -wave energy encounters large variations in the thickness and/or velocity of the near-surface layer. There is no visible correlation between  $P$ - and  $S$ -wave receiver corrections, and it is not possible to scale the  $P$ -wave statics by some constant factor to give the  $S$ -wave delays.

From the frequency-analysis plots of Figures 6.8 and 6.20, the bandwidth of the  $S$ -wave data is approximately half that of the  $P$ -waves, giving less vertical resolution. There is little change in the  $P$ - $P$  bandwidth with depth, but there is a noticeable decrease in the  $P$ - $SV$  bandwidth and peak frequency, especially below the strong reflection at 1850 ms. This might indicate greater subsurface attenuation of shear waves.

Comparing the asymptotically-binned section (Figure 6.19) to the depth-variant-binned and DMO sections (Figures 6.22 and 6.24), there is little apparent difference amongst the three, apart from a progressive reduction in the background noise level. In all

cases the application of poststack  $f-k$  filtering was found to be beneficial. Both the DMO and migrated results show end-effect problems, which are reduced by the  $f-k$  filter. The enlargements in Figures 6.27, 6.28, and 6.28 show little change in the amplitude or extent of the pool between asymptotic, depth-variant, or DMO binning. This suggests that the asymptotic binning approximation is adequate for this particular target. The enlargement of the migrated section (Figures 6.30) shows a slight reduction in the horizontal extent of the  $S$ -wave Cardium bright spot, with the two sides of the anomaly each moving approximately three traces (45 m) toward the center. The velocity inversion (Figure 6.31) indicates an increase in shear velocity at the Cardium pool location. This agrees with core measurements in the area that give a higher shear velocity for the Cardium conglomerate versus the surrounding formations (Nazar, 1991).

On the  $P$ -wave sections, the Cardium shows only a minor change in amplitude at the location of the two pools, while the  $S$ -wave sections give a pronounced increase in Cardium amplitude at both pool locations. Because of this, multicomponent recording and analysis appear to provide a valuable exploration tool in this area. A study of the observed amplitude increases has been carried out by Nazar (1991). He suggests the  $P$ - $SV$  anomaly is due to event tuning and AVO effects that combine to increase the amplitude of the Cardium reflection on the  $P$ - $SV$  stack section, but not on the  $P$ - $P$  stack section.

## Chapter 7 - Multicomponent processing: Springbank, Alberta

### 7.1 Introduction

The Geophysics Field School at the University of Calgary has been acquiring conventional *P*-wave reflection data over the triangle zone (Gordy et al., 1977) in the Rocky Mountain Foothills west of Calgary for a number of years. As part of the 1990 Field School, a two-component reflection line was recorded along with a conventional *P*-wave line in this area to test the applicability of *P-SV* surveys in the presence of mild structure. The 1990 seismic program (Figure 7.1) was located at Springbank, Alberta, near the Jumping Pound gas field, and consisted of one 3 km line, FS90-1. A general discussion of the geology of the area and the overall objectives of the survey can be found in Lawton and Harrison (1992).

This chapter is concerned with the processing of the two-component data set and the conventional *P*-wave data set for line FS90-1. The *P-SV* records were found to have severe noise problems, and hopefully the results presented here will give some insight into what can be obtained from low-quality *P-SV* data. Only the most significant processing displays are shown here in order to avoid repetition of details presented in Chapter 6.

### 7.2 Data acquisition

The survey acquisition parameters are summarized in Table 7.1. A 96-channel Sercel 338HR field system was used to record the two-component data, with 48 channels allocated to each component. A three-component geophone was planted at each receiver station, but only the radial and vertical outputs were recorded. The conventional *P*-wave data were recorded with a 48-channel DFS III system, using an array of nine vertical

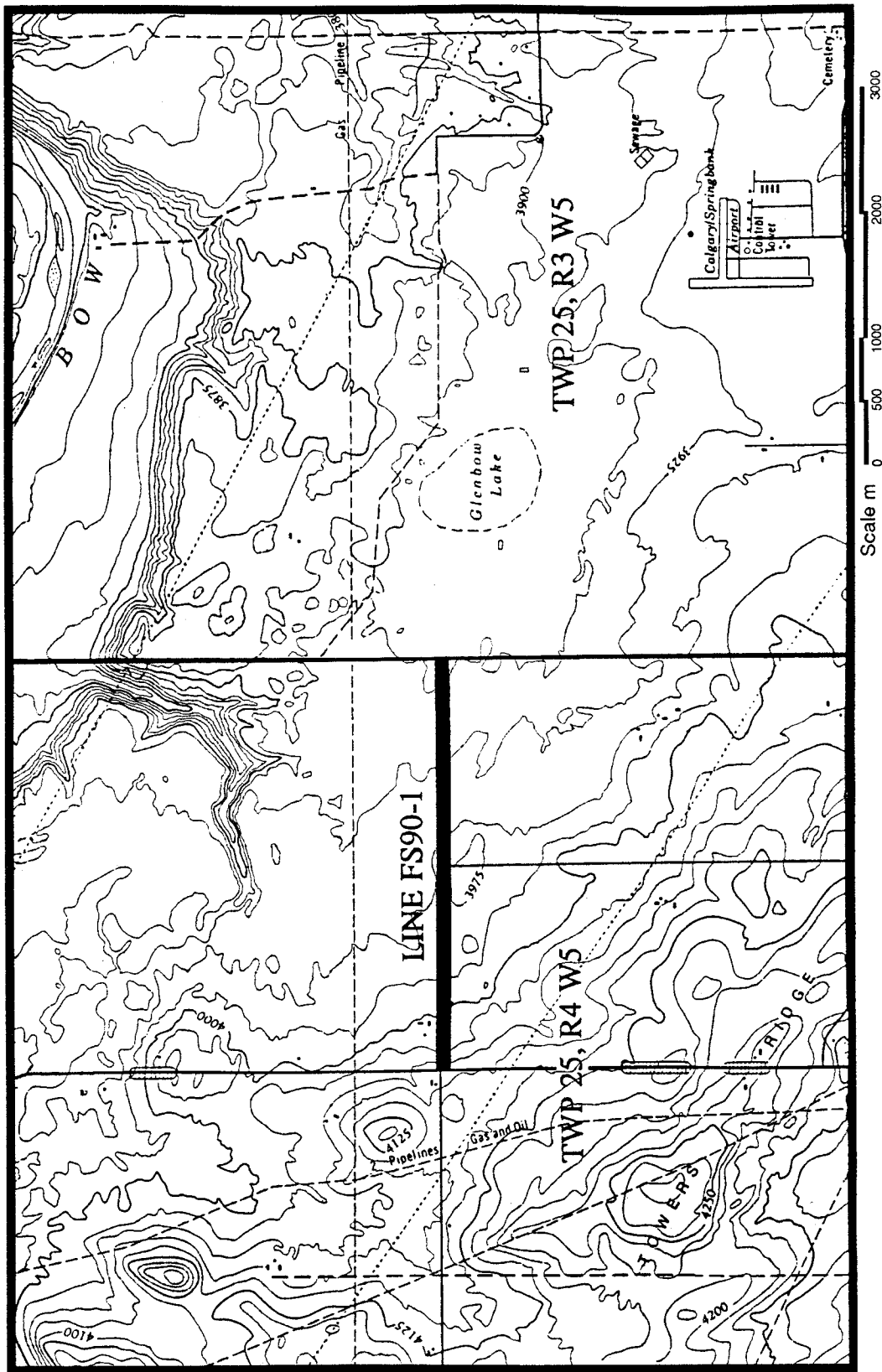


FIG. 7.1. Location map for the Springbank area showing line FS90-1. Contours are elevations in feet ASL.

Table 7.1. Field acquisition and recording parameters for line FS90-1 of the Springbank survey.

	Conventional	2-component
Energy source	Dynamite	Dynamite
Shot size (common)	1 kg	1 kg
Shot depth	10-15 m	10-15 m
Geophone array	9 over 30 m	single
Type of geophones	M.P., 14 Hz	3-C Oyo, 10 Hz
Group interval	30 m	30 m
Spread (end-on)	SP-30-1440 m	SP-30-1440 m
Instruments	DFS-III	Sercel 338HR
Channels	48	96
Low-cut filter	12 Hz, 36 db/oct	20 Hz, 12 db/oct
Notch filter	In	In
Sample interval	2 ms	2 ms
Record length	4 s	6 s

geophones spread over 30 m (one group). In summary, a total of 144 data channels was recorded simultaneously for each sourcepoint; 48 channels each of conventional ( $P$ - $P$ ), vertical ( $P$ - $P$ ), and radial ( $P$ - $SV$ ) data.

To obtain sufficient offsets for mode-conversion, an off-end spread was used for both the conventional and two-component data sets. The theoretical subsurface stacking fold was 24, but, because of a large gap in the line and the short line length, the true fold varied considerably. Representative shot gathers from SP 161 are shown in Figure 7.2. Reflections are clearly visible on the conventional and vertical gathers, but little coherent energy is seen on the radial-channel traces.

### 7.3 Data processing

The vertical ( $P$ - $P$ ) component of the two-component data set was processed using the flow shown in Figure 7.3. Double-gated (two operator design windows per trace) spiking deconvolution was applied, due to the length of the data window. The initial elevation and refraction statics solution produced a gradual drop of about 16 ms in the

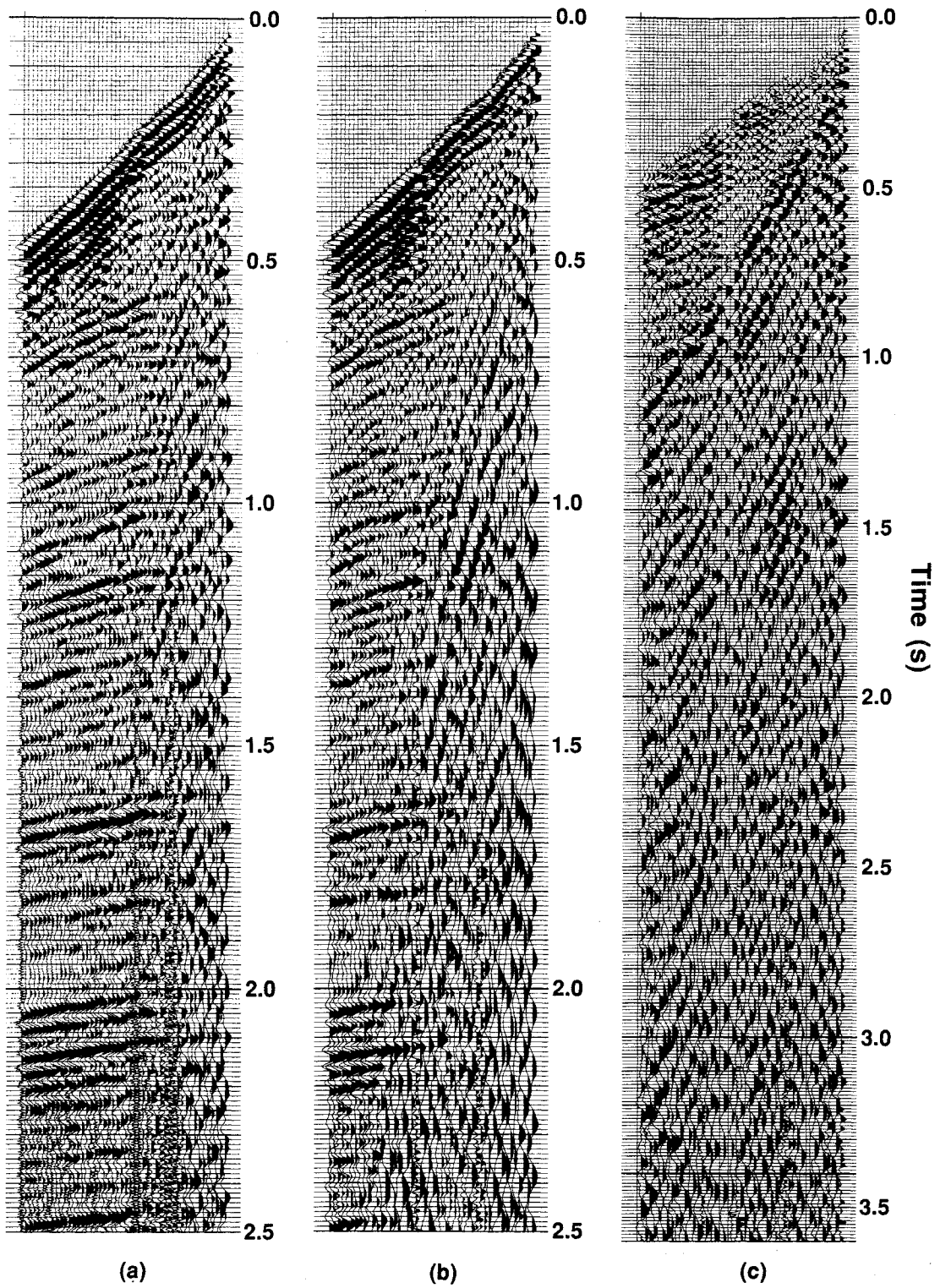


FIG. 7.2. Shot records from SP 161 of line FS90-1: (a) conventional; (b) vertical component; (c) radial component.

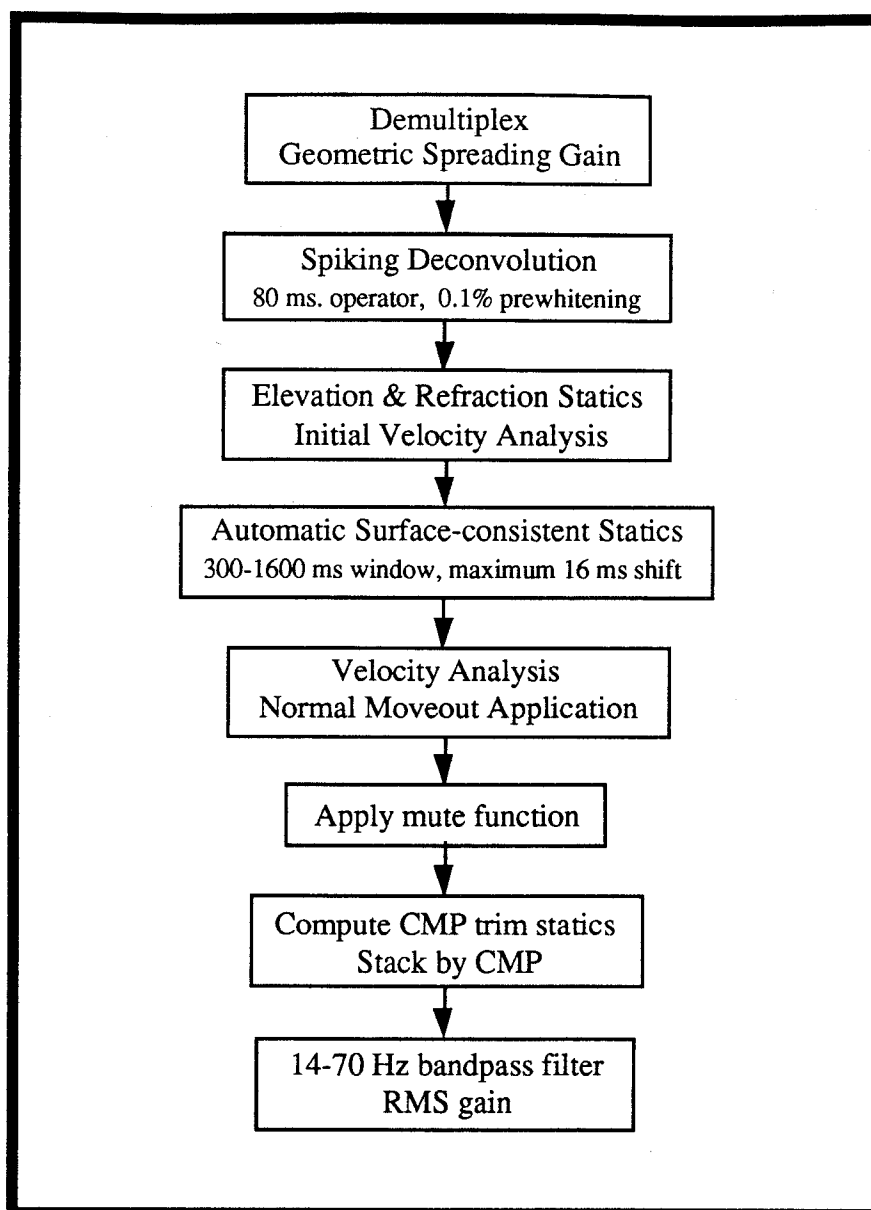


FIG. 7.3. Processing flowchart for the vertical-component ( $P$ - $P$ ) data.

structure times of the deeper events on the west end of the line. This drop was attributed to poor refraction-static control, and was removed using common-source and common-receiver stacks. The final  $P$ -wave stack section obtained is shown in Figure 7.4. To improve the signal-to-noise ratio, mainly in the shallow part of the section, an  $f$ - $x$  prediction filter (Canales, 1984) was applied to the unfiltered stack, followed by an  $f$ - $k$

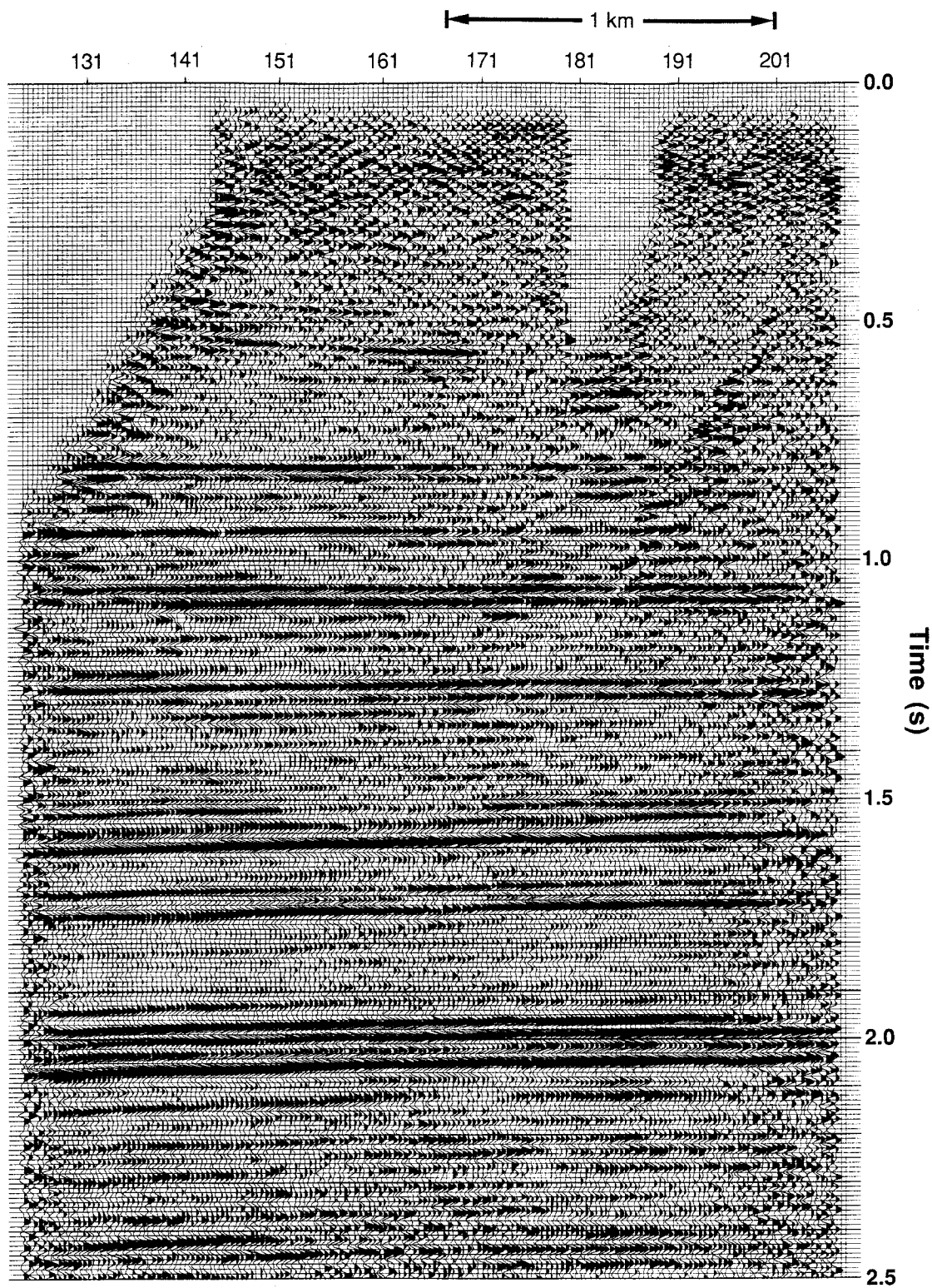


FIG. 7.4. Stack section of single-geophone vertical-component data.

filter, bandpass filter, and gain (Figure 7.5). The  $f-x$  filter prediction operators were seven points in length, designed on windows 500 ms long and 50 traces wide. The  $f-k$  filter was designed to attenuate data with dip outside of  $\pm 4$  ms/trace by 6 db.

The conventional data set was processed using the same deconvolution parameters, static solution and velocity functions as were used on the vertical component data, giving the section shown in Figure 7.6. To facilitate comparison with the final vertical-component section (Figure 7.5), identical poststack  $f-x$  and  $f-k$  filters were also applied (Figure 7.7). Except for the shallow data, the sections in Figures 7.5 and 7.7 are quite similar.

Processing of the radial ( $P-SV$ ) component data set followed the flow shown in Figure 7.8. Double-gated deconvolution was also used on the  $P-SV$  data. The final statics solution from the vertical component data set was applied to the radial component. This solution was found to be appropriate for the source statics, but residual receiver statics as large as 90 ms were later removed using common-receiver stacks. From Figure 7.9 there is again seen to be little similarity between the final  $P-P$  and  $P-SV$  receiver statics solutions. Events were correlated between the  $P-P$  and  $P-SV$  stack sections (Figure 7.10) to get interval transit times and  $V_p/V_s$  estimates [equation (2.29)]. The radial-component data were then binned using both the asymptotic method [equation (2.25)] with a  $V_p/V_s$  of 2.08, and the depth-variant binning method [equations (2.26)], giving the sections in Figures 7.11 and 7.12 respectively. The result of applying  $P-SV$  DMO is shown in Figure 7.13, and the products of applying  $f-x$  and  $f-k$  filters to the three  $P-SV$  stack sections are shown in Figures 7.14, 7.15, and 7.16. The  $f-x$  filter parameters were identical to those used on the  $P-P$  sections, while the  $P-SV$   $f-k$  filter was designed to attenuate data outside of  $\pm 4$  ms of dip by 9 db. Due of the poor quality of the  $P-SV$  sections,  $P-SV$  migration and inversion were not performed. Common-offset stack records from SP 151 for each of the conventional, vertical-channel, and radial-channel data sets are displayed in Figure 7.17. A number of major  $P-P$  and  $P-SV$  reflections are identified in Figure 7.18.

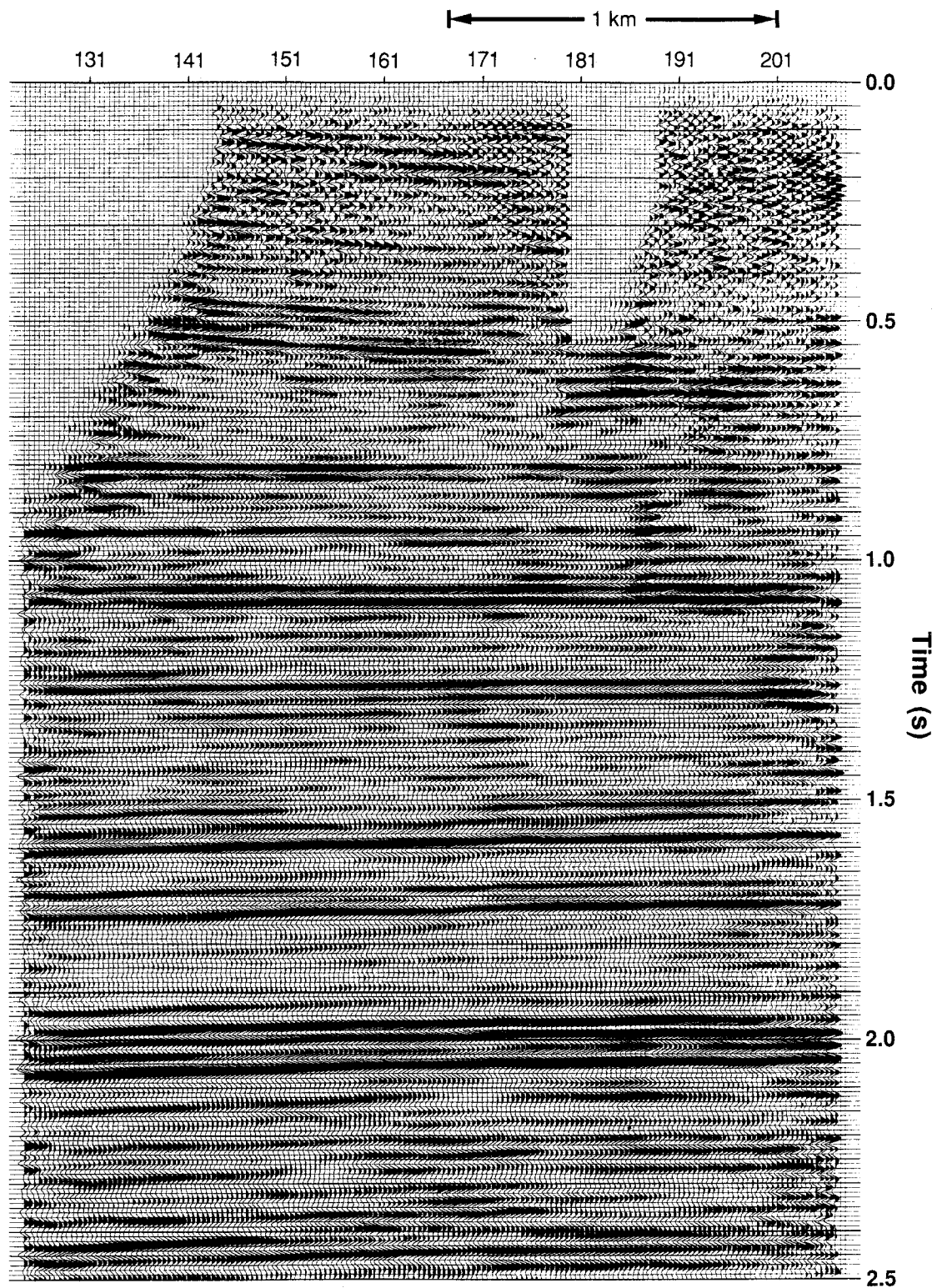


FIG. 7.5. Stack section of single-geophone vertical-component data with poststack  $f$ - $x$  and  $f$ - $k$  filters applied.

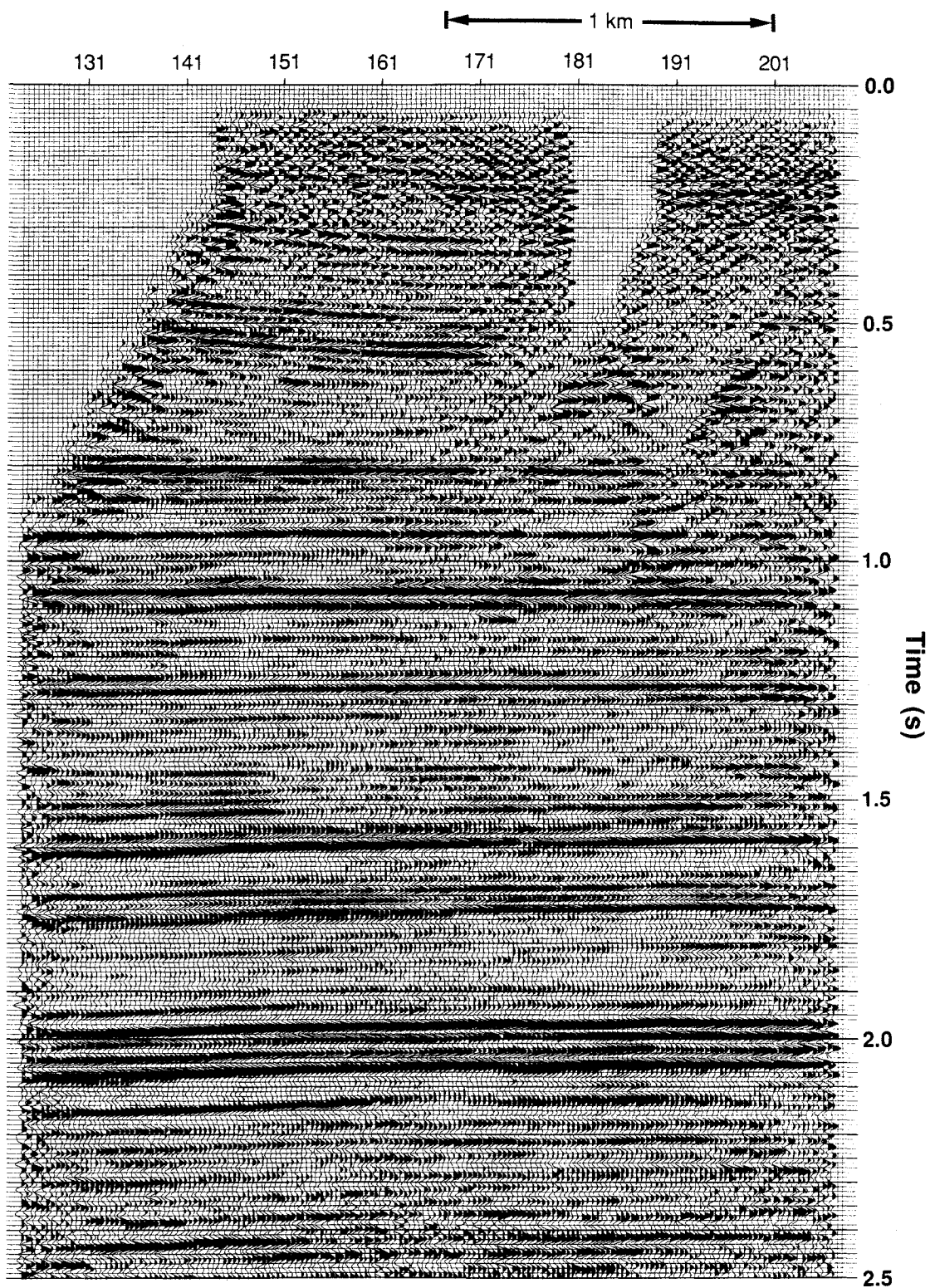


FIG. 7.6. Stack section of conventional vertical-component data.

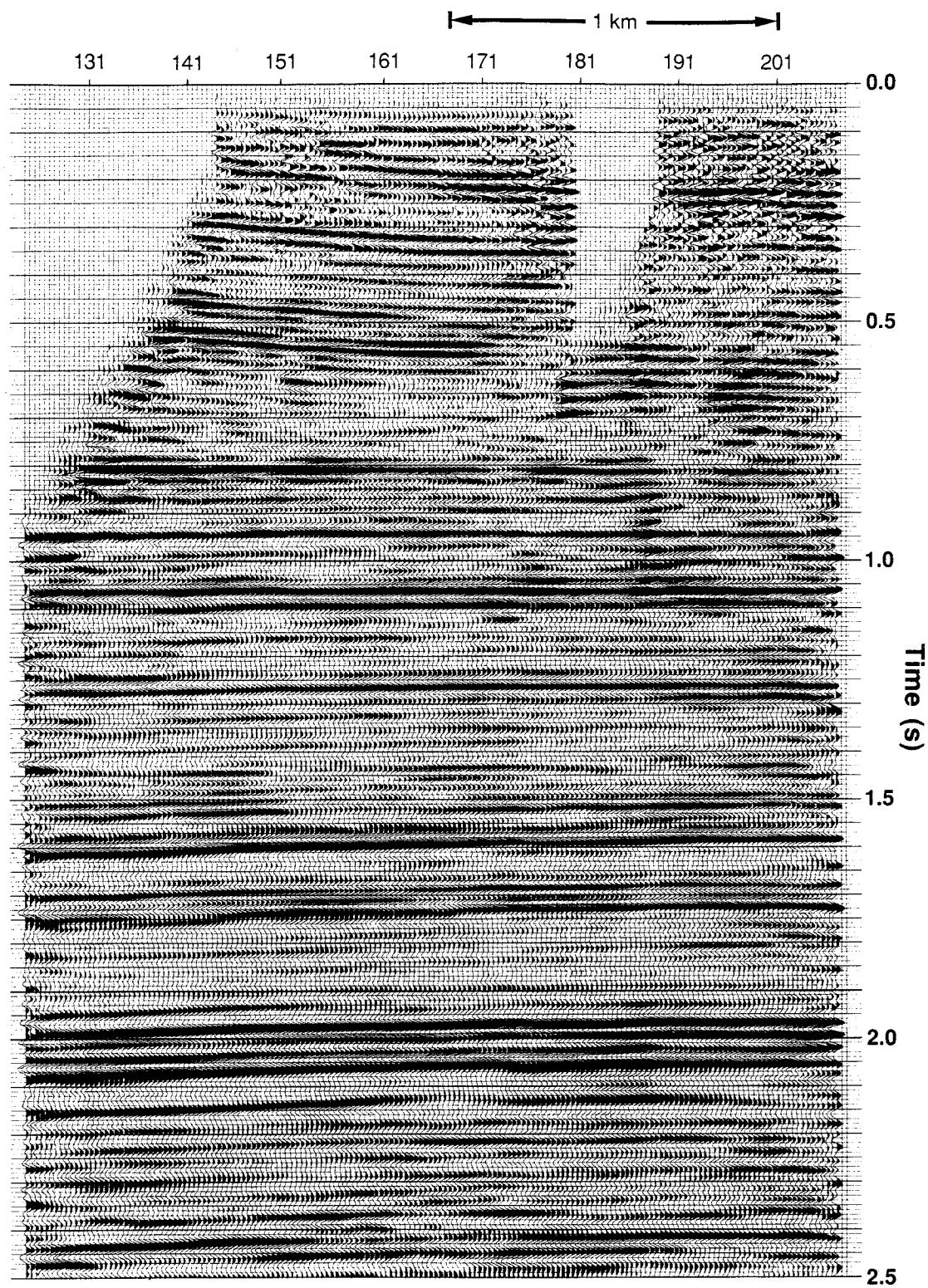


FIG. 7.7. Stack section of conventional vertical-component data with poststack  $f$ - $x$  and  $f$ - $k$  filters applied.

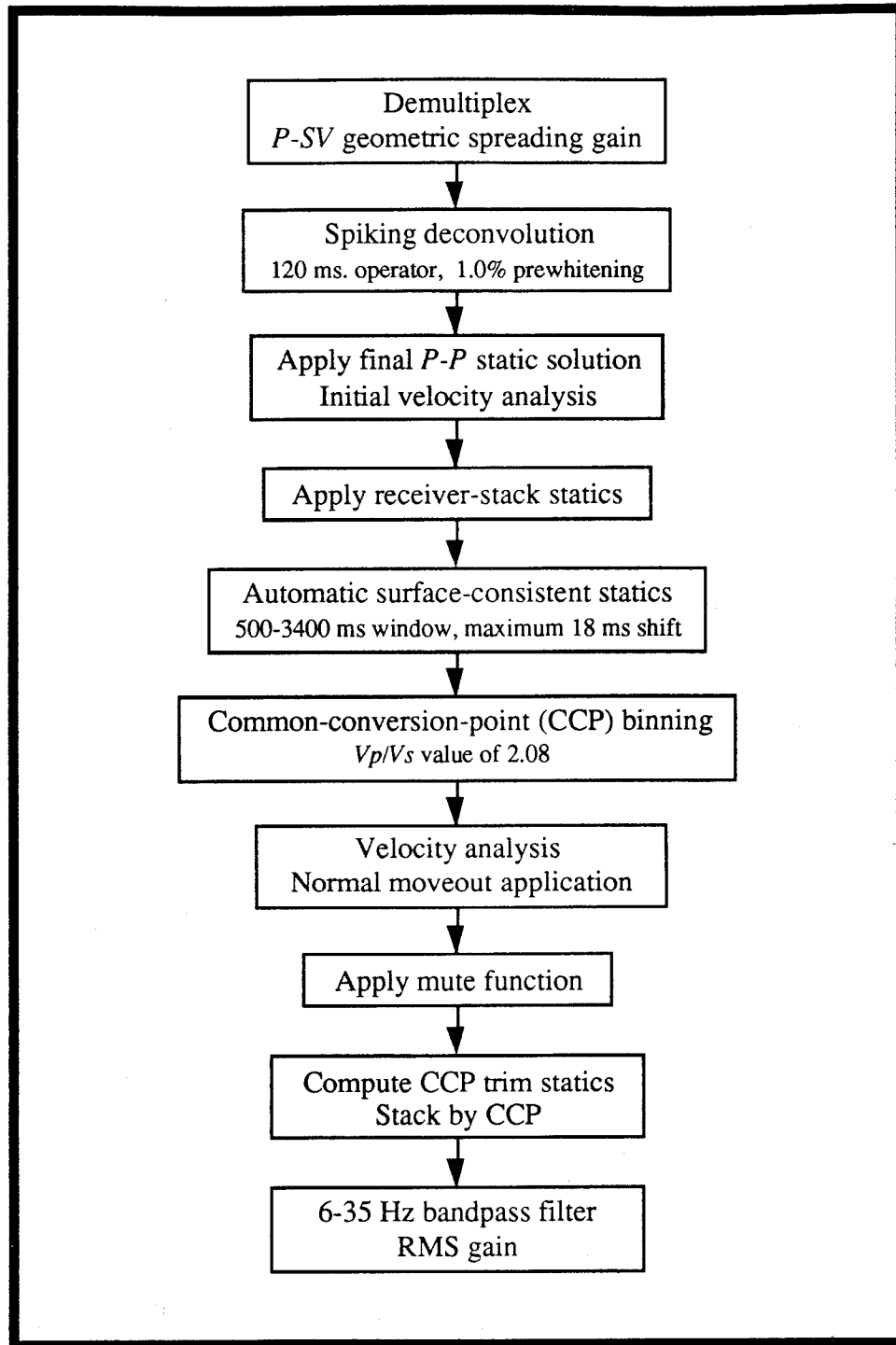
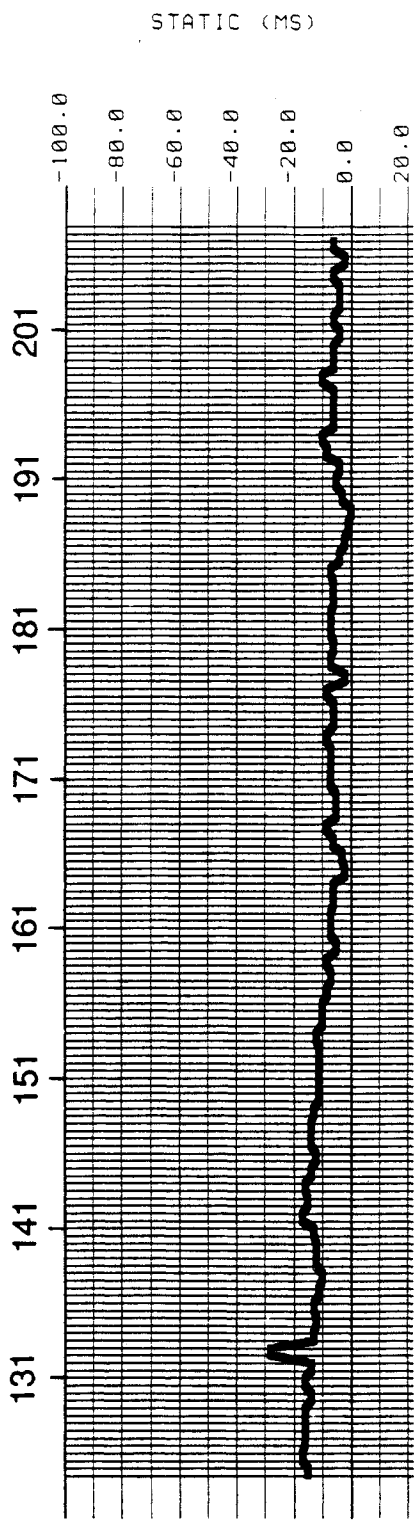
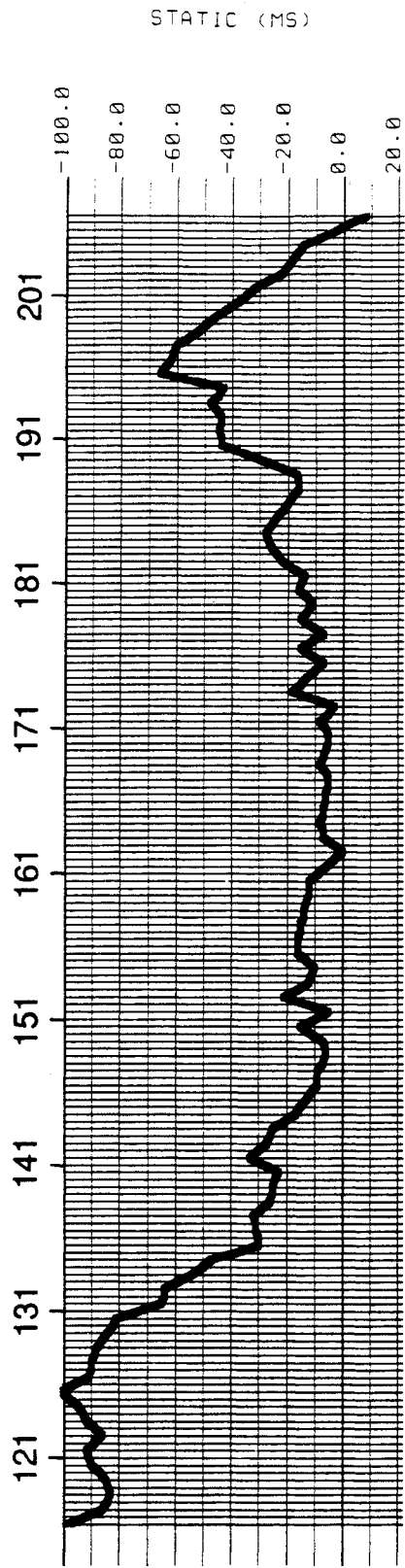


FIG. 7.8. Processing flowchart for the radial-component (P-SV) data.



(a)



(b)

FIG. 7.9. Final receiver static solutions for (a) vertical component (P-P); (b) radial component (P-SV).

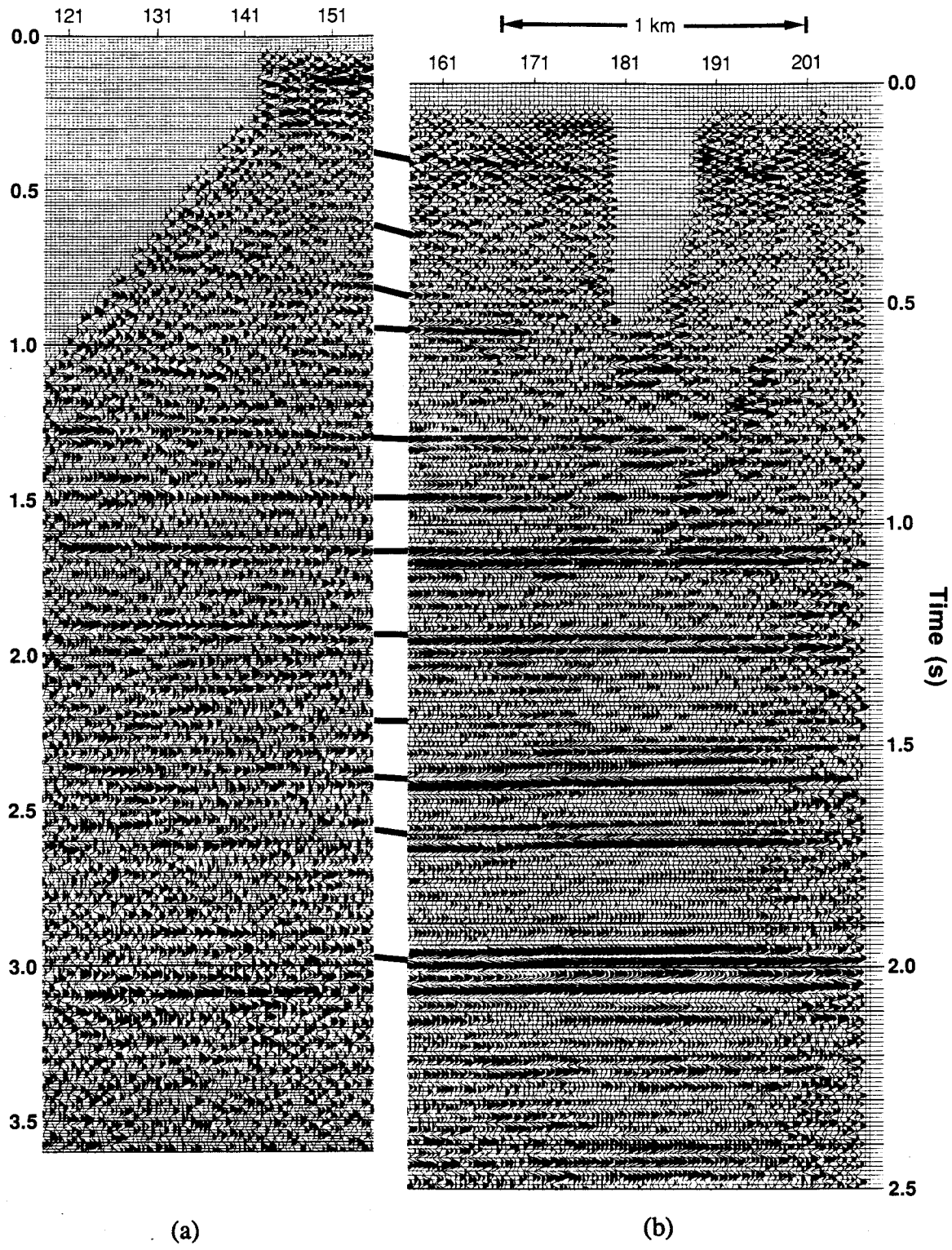


FIG. 7.10. Reflector correlation between stack sections for (a) radial component; (b) single-geophone vertical component.

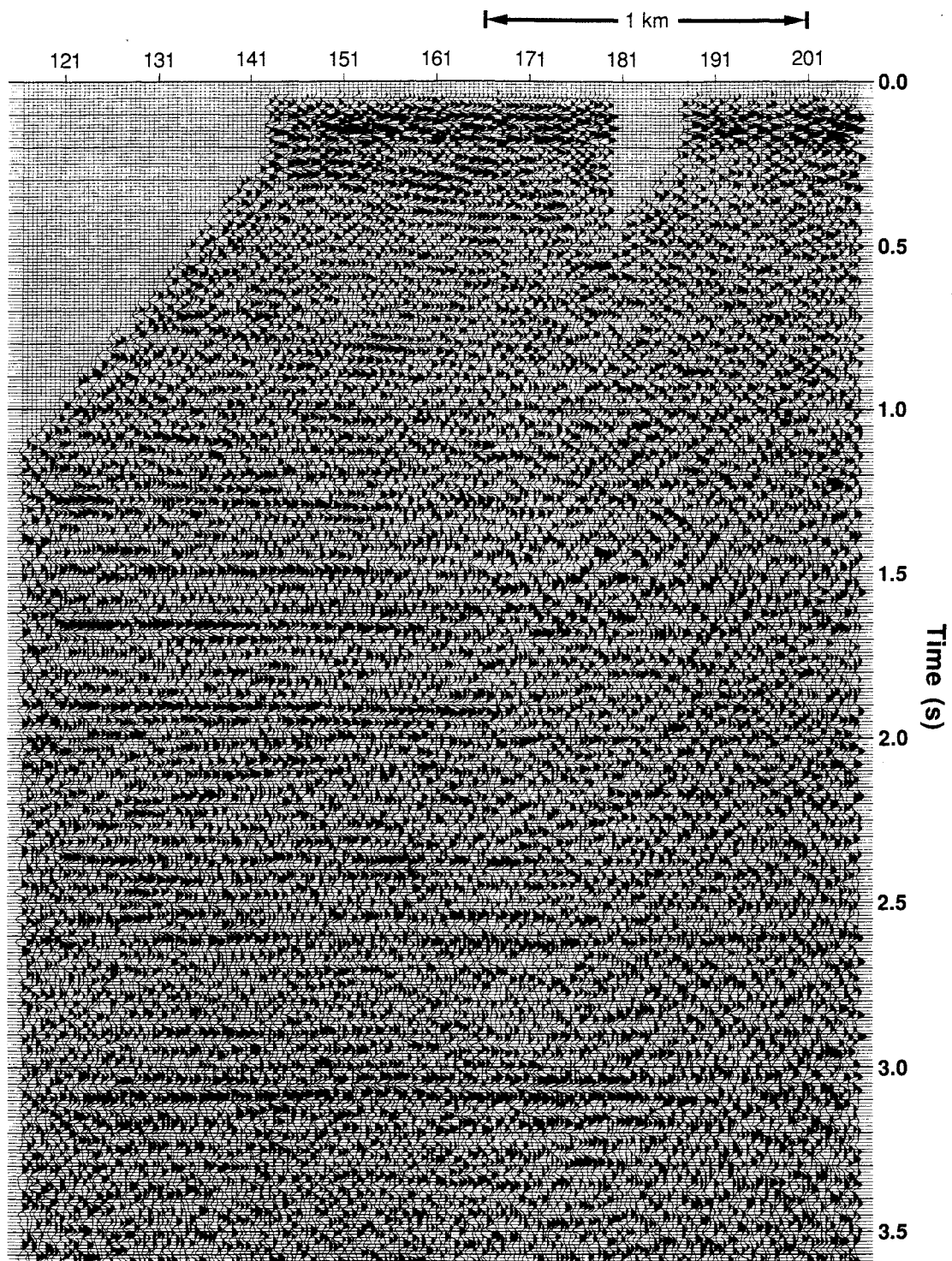


FIG. 7.11. Stack section of radial-component data with asymptotic binning.

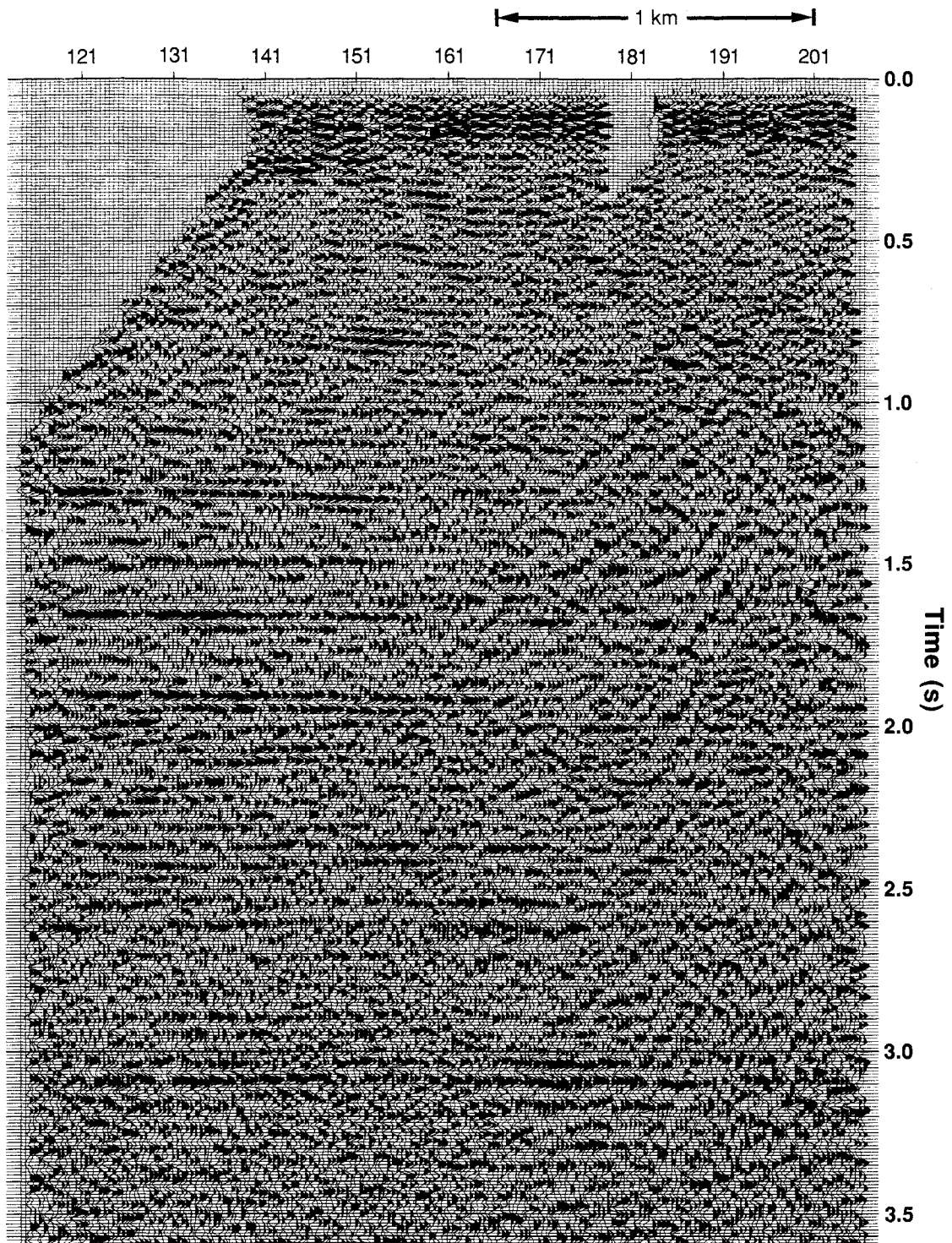


FIG. 7.12. Stack section of radial-component data with depth-variant binning.

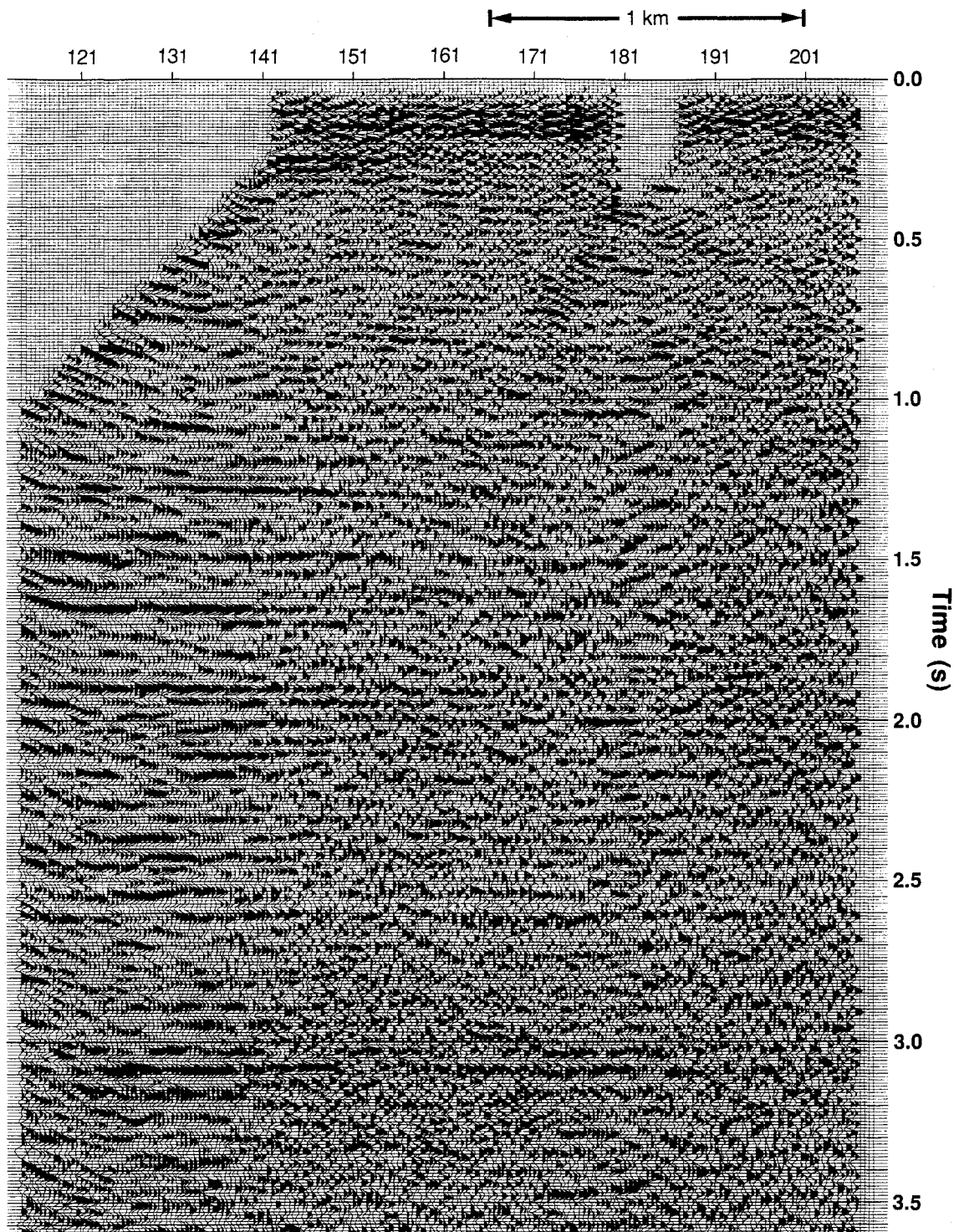


FIG. 7.13. Stack section of radial-component data with  $P$ - $SV$  dip moveout.

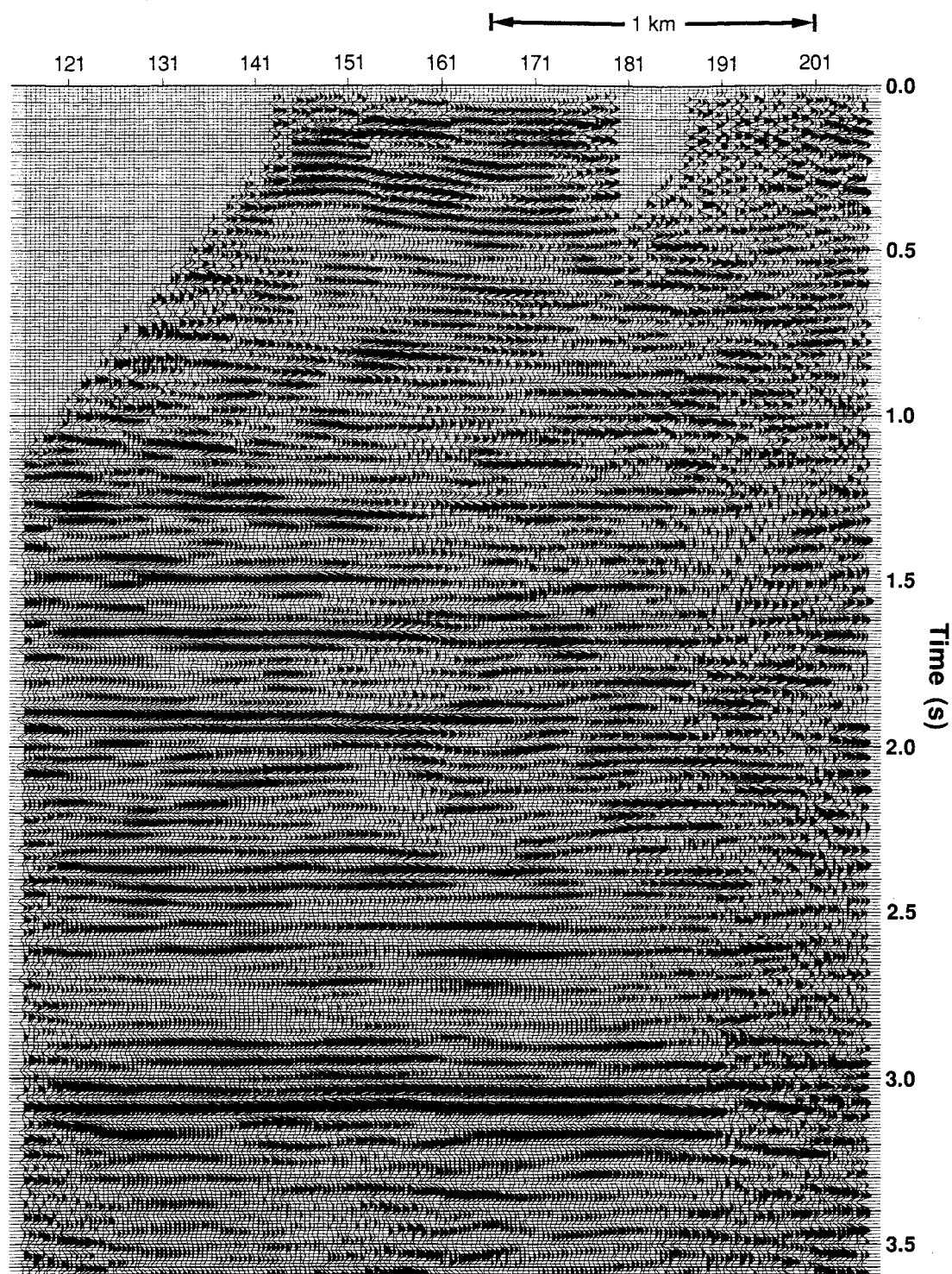


FIG. 7.14. Stack section of radial-component data with asymptotic binning and poststack  $f-x$  and  $f-k$  filters applied.

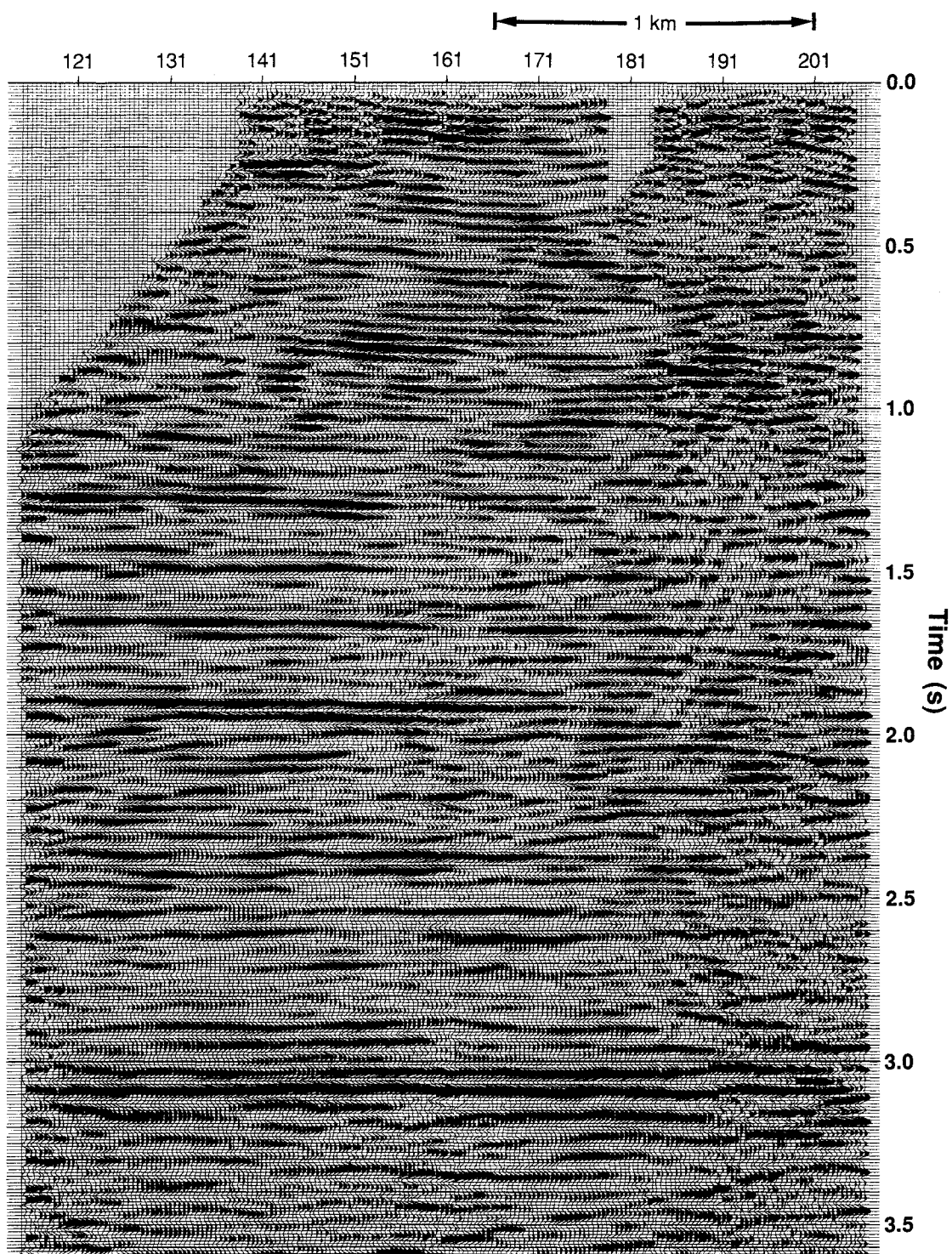


FIG. 7.15. Stack section of radial-component data with depth-variant binning and poststack  $f$ - $x$  and  $f$ - $k$  filters applied.

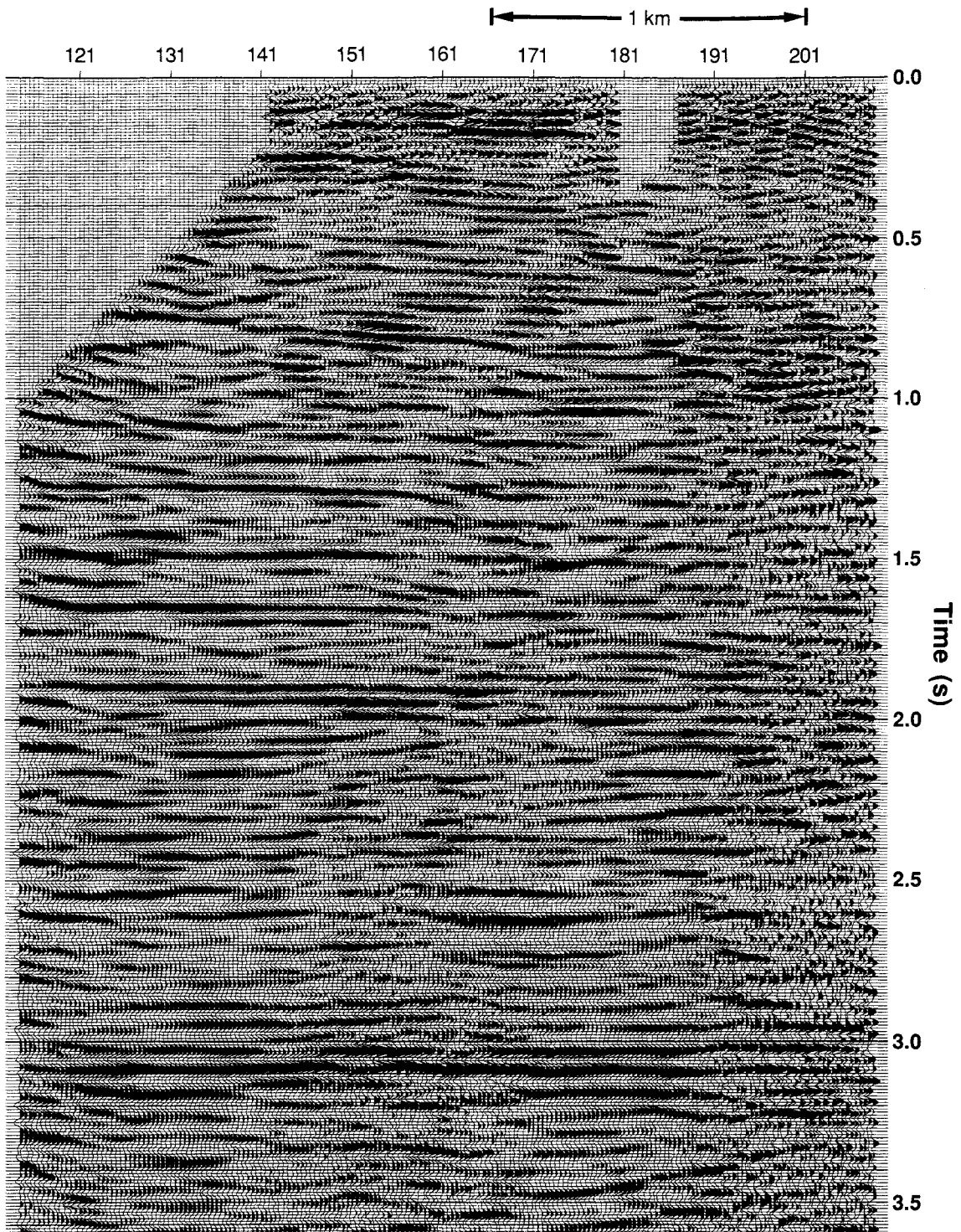


FIG. 7.16. Stack section of radial-component data with  $P$ - $SV$  dip moveout and poststack  $f$ - $x$  and  $f$ - $k$  filters applied.

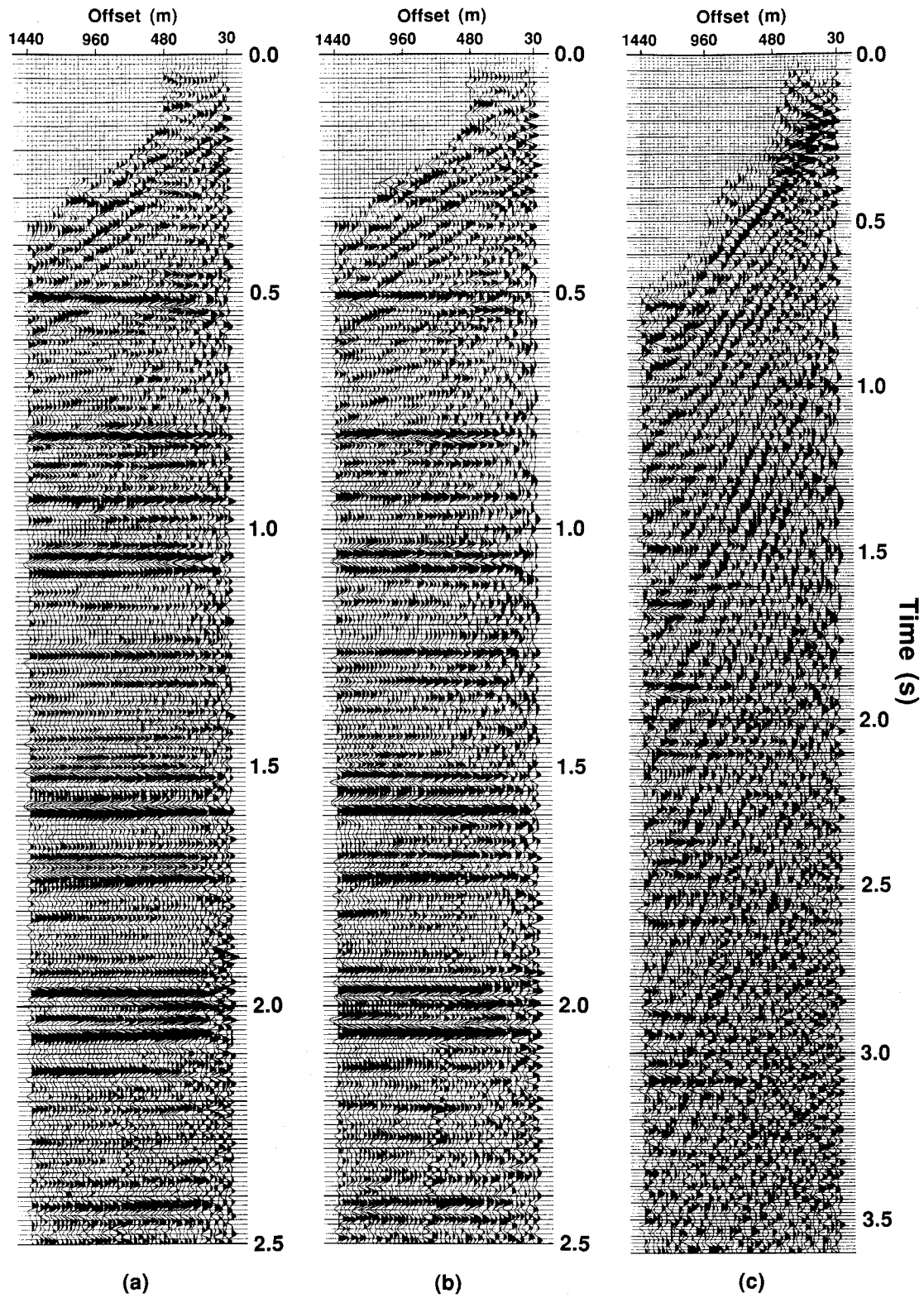


FIG. 7.17. Common-offset stacks from FS90-1: (a) conventional; (b) vertical component; (c) radial component.

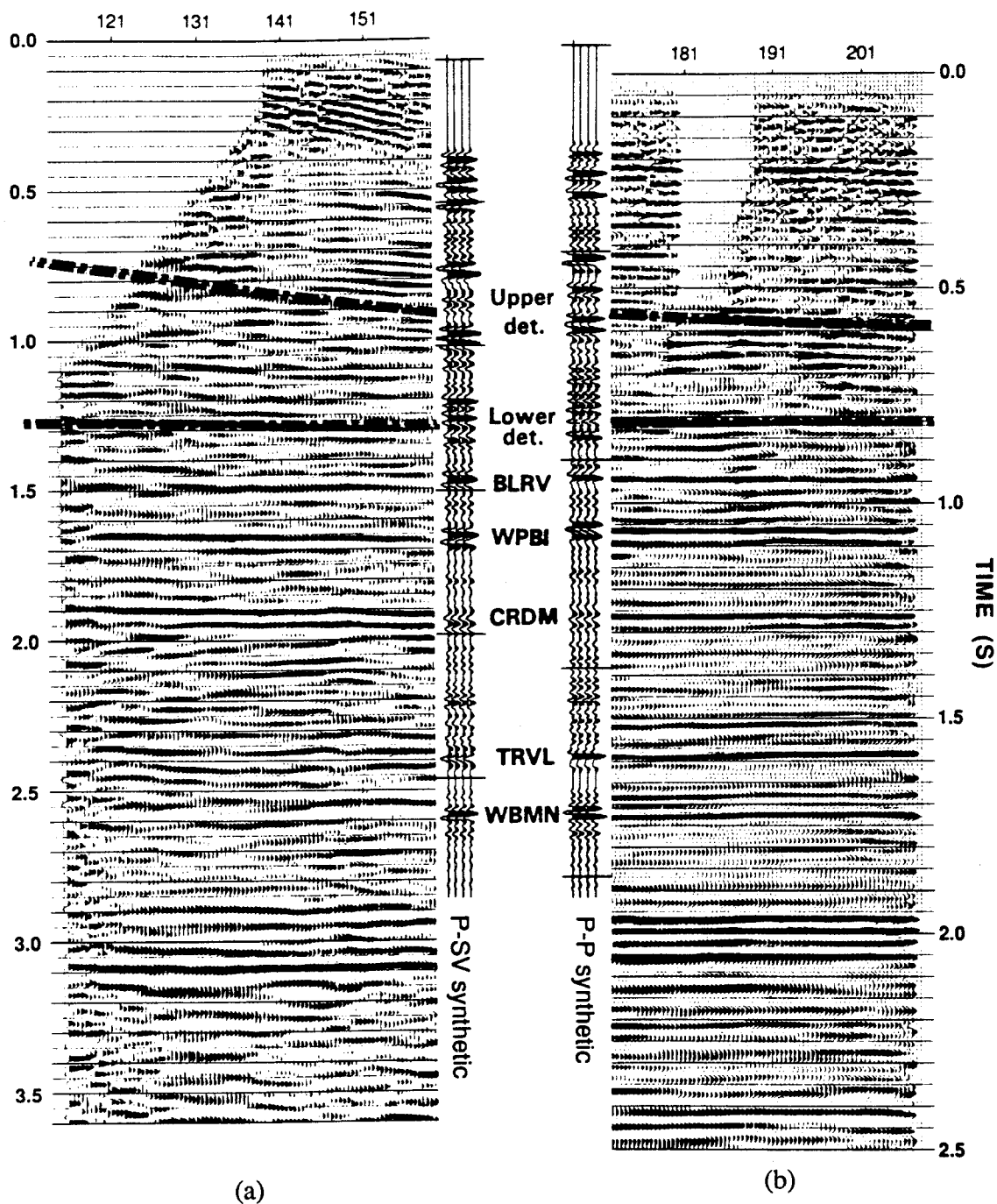


FIG. 7.18. Spliced sections showing correlation between the main events: (a) radial; (b) vertical. Synthetic seismograms are based on  $P$ -wave velocity model at well 6-27-25-4W5 and a  $V_p/V_s$  of 2.08. Abbreviations are: Upper det. = upper detachment zone; Lower det. = lower detachment zone; BLRV = Belly River; WPBI = Wapiabi; CRDM = Cardium; TRVL = Turner Valley; WBMN = Wabamun. (From Lawton and Harrison, 1992).

## 7.4 Discussion

Comparing the stack sections for the vertical-component (Figure 7.4) and the conventional data (Figure 7.6), it is seen that, overall, there is slightly less noise on the conventional section. The continuity of shallow reflections on the conventional section is much better than on the vertical-component section. It is well known that an array of geophones causes more attenuation of shallow events, where differential NMO across the array length is sizable, than does a point receiver. From Figures 7.4 and 7.6, it is seen that for these data, however, single receivers give worse imaging of the shallow data than do the geophone arrays. This is probably due to the presence of high-amplitude ground-roll in this area, which can be seen on the shot records of Figure 7.2. It appears that the ground-roll is attenuated by the geophone array much more than are the shallow events, resulting in improved shallow data. After application of  $f-x$  and  $f-k$  filters, the continuity of shallow reflections in the vertical-component section (Figure 7.5) is improved substantially, but still does not match that of the conventional stack (Figure 7.7).

From the common-offset records (Figure 7.17), the data quality of the radial-component is seen to be poor, with little signal visible at offsets less than about 1 km. Synthetic shot records (Lawton and Harrison, 1992) show that substantial  $P-SV$  amplitudes should occur for most events beyond offsets of approximately 240 m. This suggests that the  $P-SV$  reflections are buried beneath the high-amplitude ground-roll at most offsets.

Although the signal-to-noise ratio is much worse than for the  $P$ -wave sections, numerous reflections can be seen on the  $S$ -wave stacks (Figures 7.14, 7.15, and 7.16). These reflections are greatly enhanced by the  $f-x$  and  $f-k$  filtering process, and, although large amplitude differences occur, they correlate well with events seen on the  $P-P$  stacks. Section quality becomes progressively worse towards the east end of the line where shorter offsets are being stacked.

The continuity of shallow reflections in the asymptotically-binned section (Figure 7.14) is slightly better than that of the depth-variant-binned section (Figure 7.15), but overall quality is much the same. There is generally little improvement on the *P-SV* DMO section (Figure 7.16) relative to Figures 7.14 and 7.15, indicating that DMO has had little effect on *P-SV* stacking. Reflections above about 1.0 s do, however, appear more continuous on the DMO section (Figure 7.16) than on the depth-variant section (Figure 7.15).

## Chapter 8 - Multicomponent processing: Casper Creek South, Wyoming

### 8.1 Introduction

Most multicomponent seismic surveys have been recorded as an aid to interpretation of stratigraphic traps with little structural component. This chapter is concerned with the processing of a data set from an area where significant structure occurs; the Casper Creek South field in Natrona County, Wyoming. This field is composed of a pair of dome-like structures, formed by two doubly-plunging anticlines; major fracturing and dips of as much as  $30^\circ$  are known to occur within these structures. The southern part of the field is a major area of study for the Colorado School of Mines Reservoir Characterization Project. A discussion of the geology of the field can be found in Kramer and Davis (1991).

A multicomponent reflection survey was conducted across the field by Union Oil of California (UNOCAL) in 1988, in which data from a dynamite source were recorded in the vertical, radial, and transverse directions. The orientation of the UNOCAL line relative to the Casper Creek South Field is shown in Figure 8.1. Structural contours of the producing Pennsylvanian Tensleep Sandstone Formation are plotted in the figure, and the line is seen to cross an anticline at an angle of approximately  $35^\circ$  from maximum dip.

The UNOCAL 3-C data set was subjected to an extended converted-wave processing sequence, and the results of this flow, which includes geophone rotation, *P-SV* dip moveout (DMO), and *P-SV* poststack migration, are presented in the following sections. It should be noted that the geophone rotation analysis shown here is not the method outlined in Chapter 3; these data were processed before that method was developed. In this chapter, the energy on the rotated radial-component data is maximized to give an improved signal-to-noise ratio; this maximization does not necessarily provide any information about the orientation of the natural coordinate system (Chapter 3).

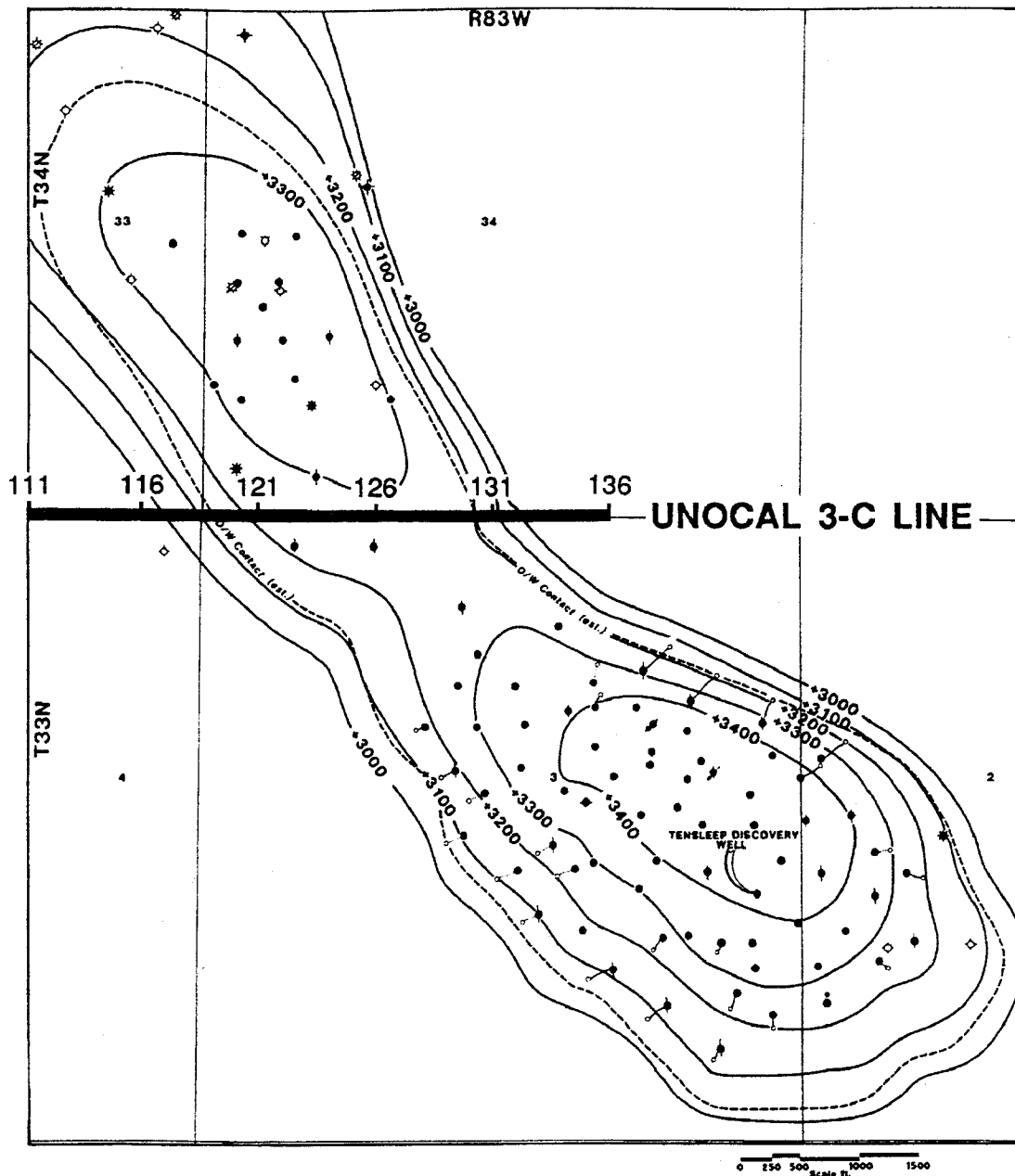


FIG. 8.1. Location map for the Casper Creek South survey. Contours indicate structure on the Tensleep Sandstone Formation in feet ASL (after Ruddiman, 1989).

## 8.2 Data acquisition

The acquisition parameters used in the survey are summarized in Table 8.1. The data were recorded using a 240-channel MDS-10 field system and a single 3-component

Table 8.1. Field acquisition and recording parameters for the Casper Creek South survey.

Energy source	Dynamite
Shot size	4.5 kg
Shot depth	46 m
Geophone array	single geophone
Type of geophones	3-component, 14 Hz
Group interval	15 m (50 ft)
Shot interval	60 m (200 ft)
Instruments	MDS-10
Channels	240
Recording filter	Out-128 Hz
Notch filter	Out
Sample interval	2 ms
Record length	4 s

geophone at each receiver station. The line consisted of a total of 80 receiver stations, from which data were recorded in the vertical, radial, and transverse directions for each sourcepoint. The receiver cable was held constant while the shot position was rolled through the line in an east-west direction. A typical record from shotpoint 131 of the survey is shown in Figure 8.2. The radial and transverse components have been filtered with a 50 Hz highcut to remove high-frequency noise. The data are seen to have a very low signal-to-noise ratio, and reflections are difficult to distinguish on the horizontal components.

### 8.3 Data processing

The vertical-component data were processed using the flow outlined in Figure 8.3. The final stack section shown in Figure 8.4 is seen to have many coherent reflections. At SP 126 the Tensleep Formation is estimated to be at around 470 ms, and basement is at around 640 ms. A structure time difference of about 80 ms occurs between the west end of the line and the crest of the anticline. This stack section was migrated using a finite-difference algorithm (Claerbout and Doherty, 1972), giving the result shown in Figure 8.5.

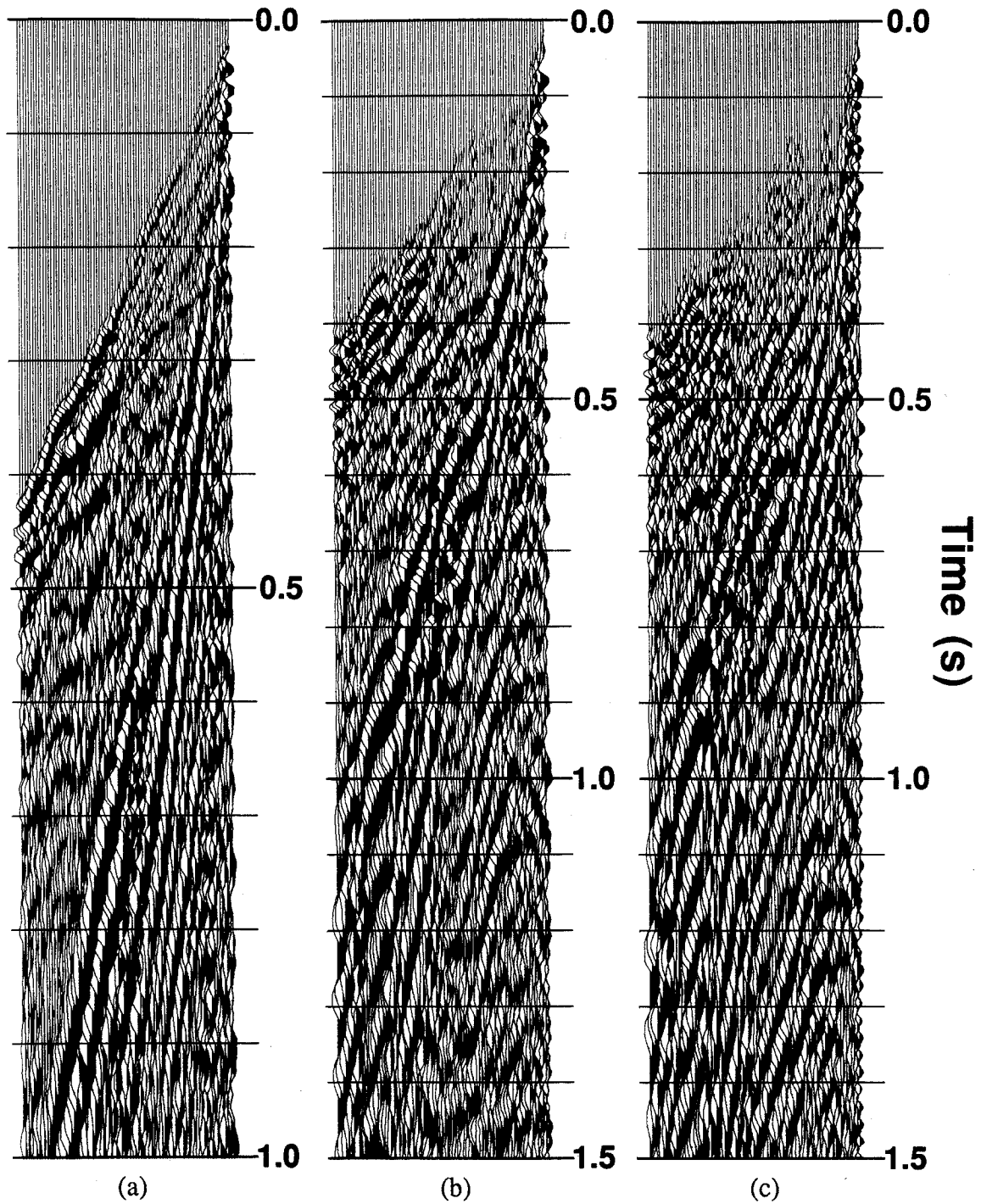


FIG. 8.2. Data from SP 131: (a) vertical component; (b) radial component; (c) transverse component.

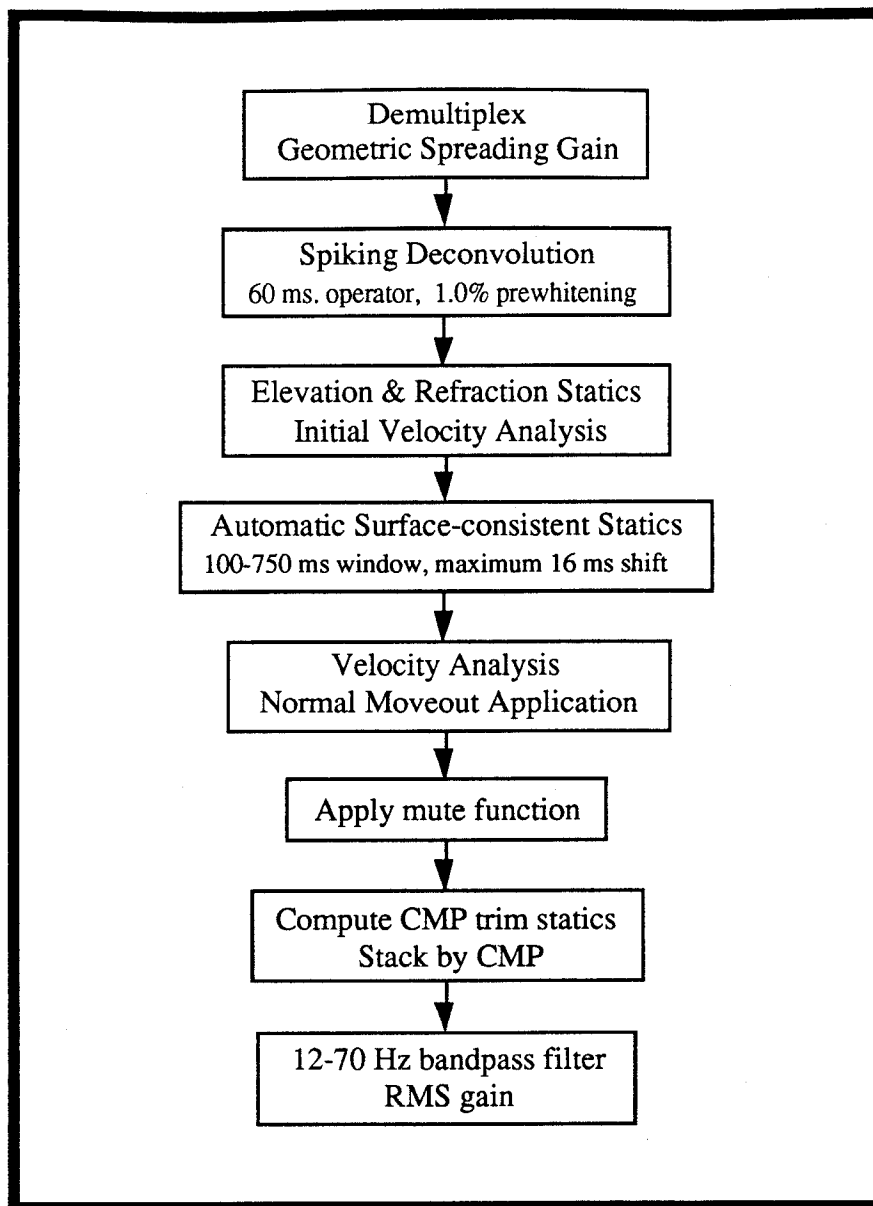


FIG. 8.3. Processing flowchart for the vertical-component ( $P$ - $P$ ) data.

The radial and transverse component data were initially processed using the sequence summarized in Figure 8.6. Obtaining a receiver static solution is complicated by the presence of structure. To illustrate the problem, a common-receiver stack created using the final static and velocity solutions is shown in Figure 8.7. The large difference in structure across the line causes improper stacking of events within the receiver gathers,

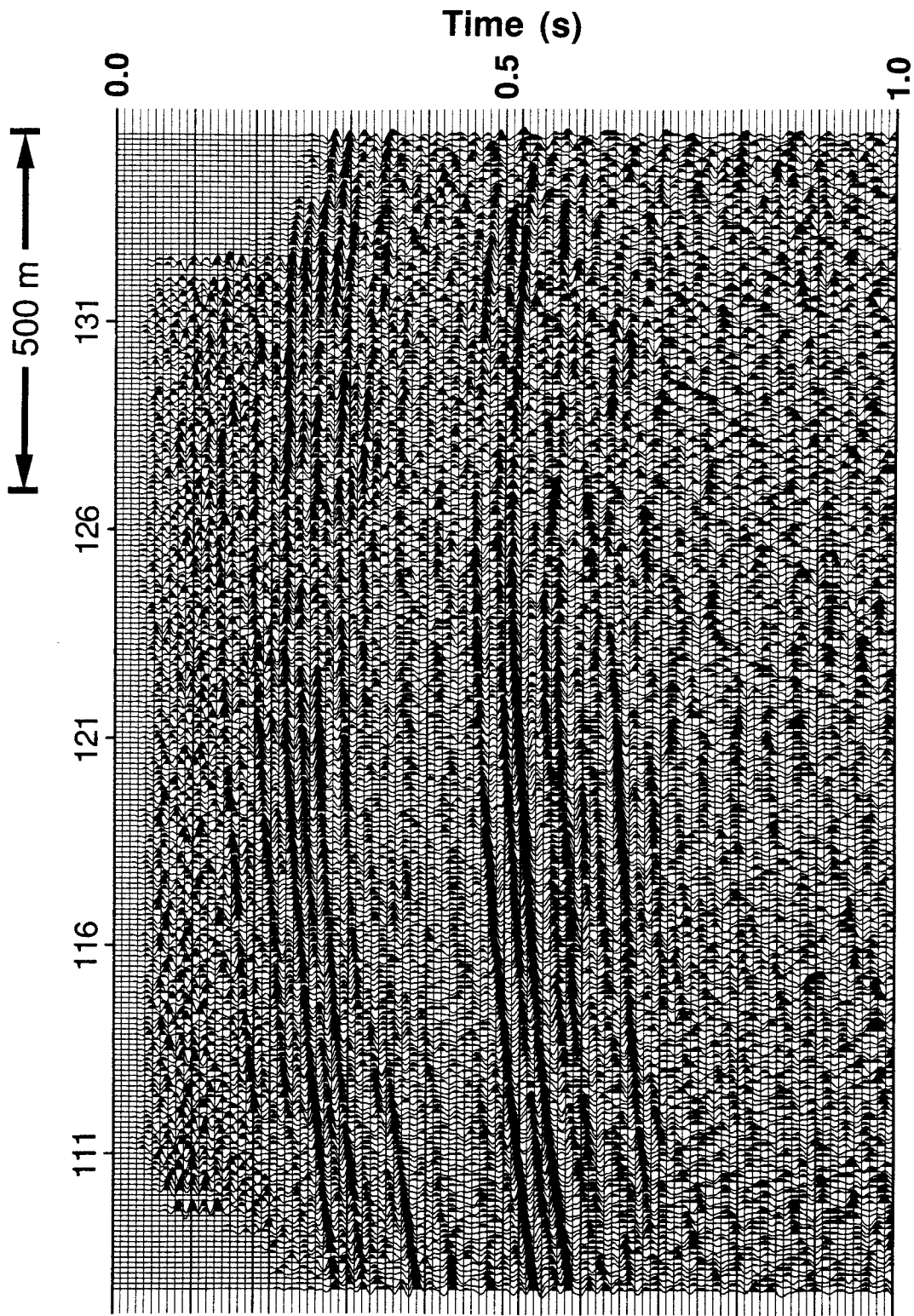


FIG. 8.4. Final stack section for the vertical-component data.

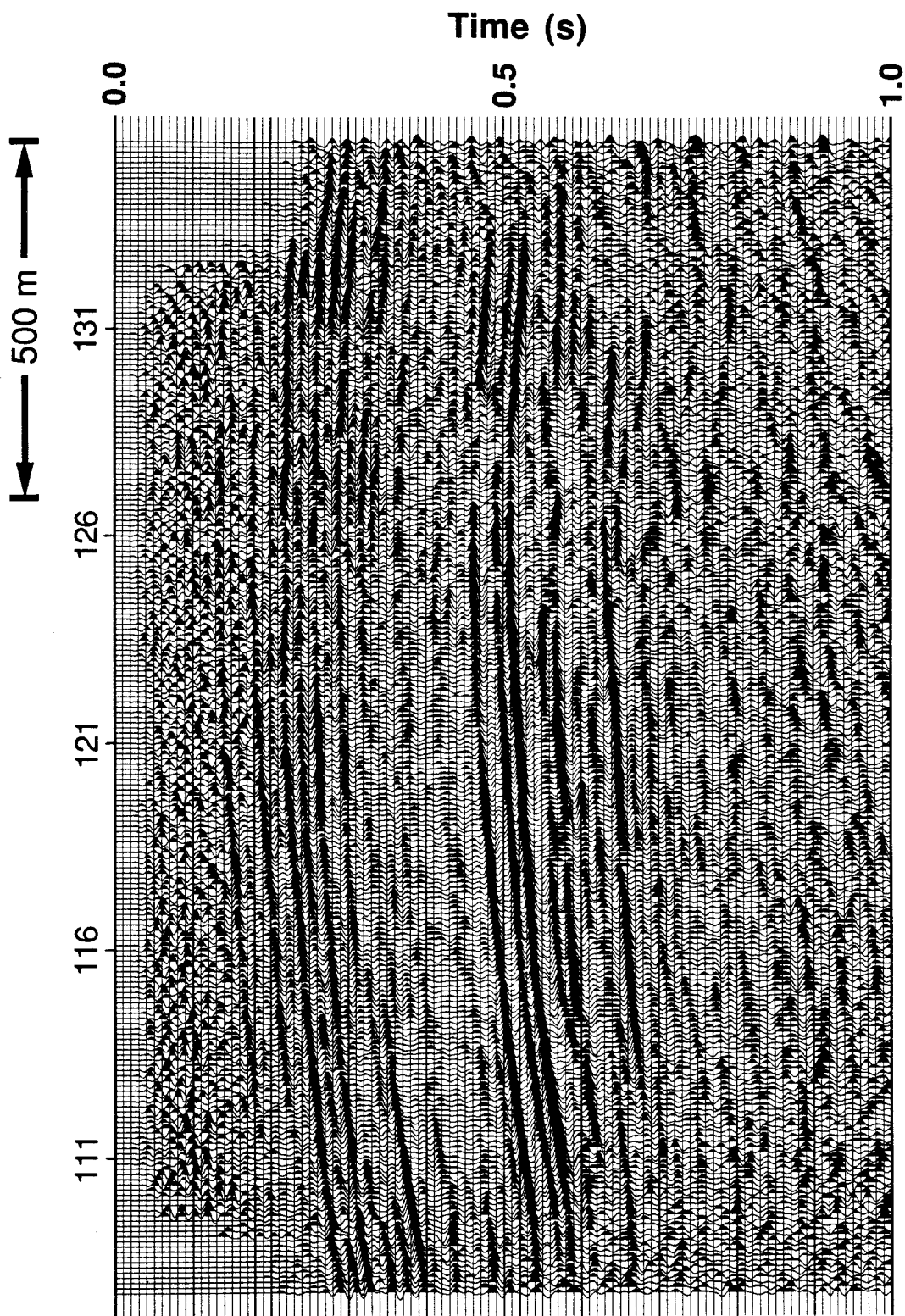


FIG. 8.5. Migrated stack section for the vertical-component data.

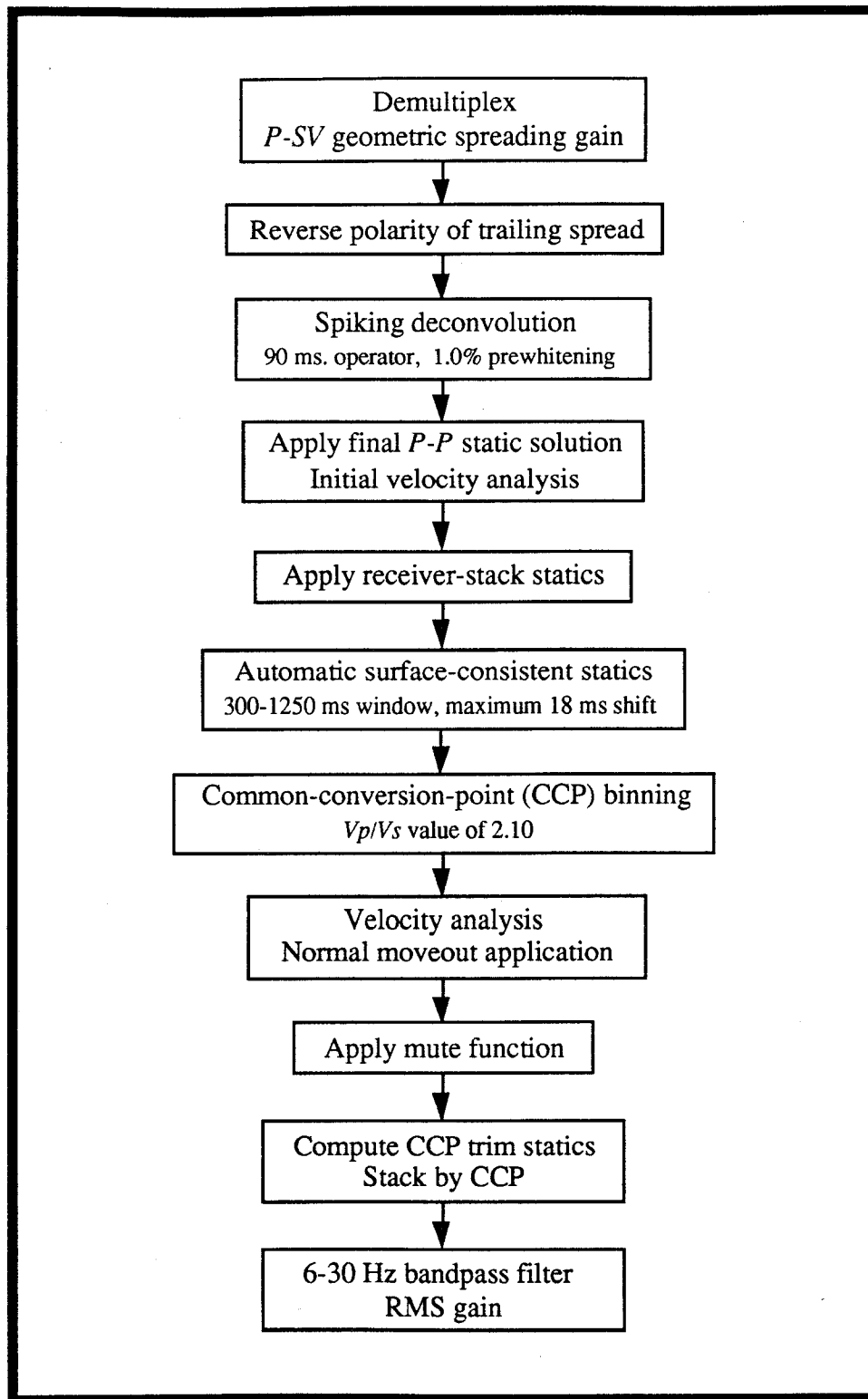


FIG. 8.6. Processing flowchart for the radial and transverse component data sets.

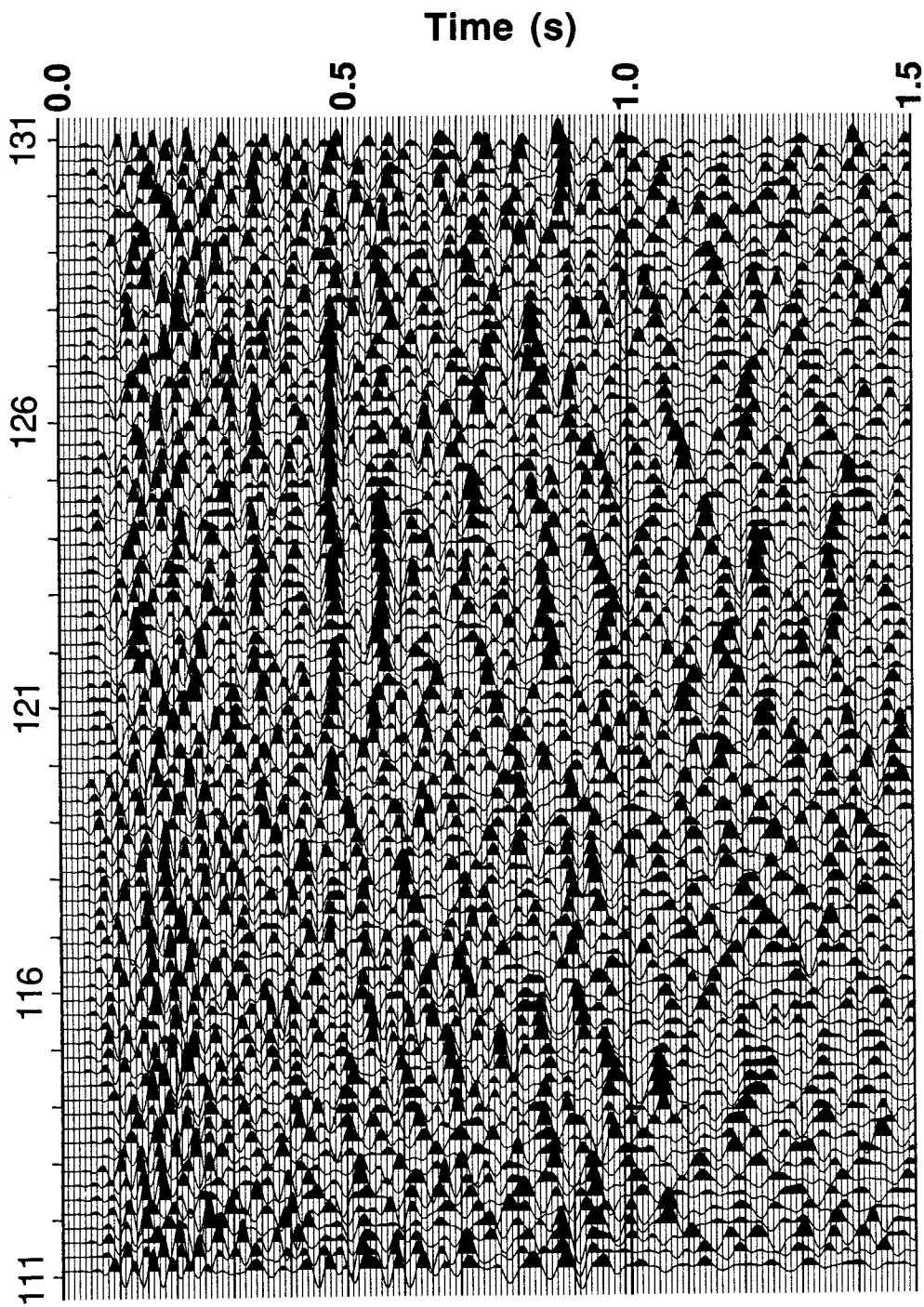


FIG. 8.7. Radial-component common-receiver stack created using the final static and velocity solutions.

giving severe attenuation away from the crest of the anticline. To overcome this problem, differences in CCP structure time were measured from an initial CCP section. Each NMO-corrected trace was then shifted to a common time by removal of the time difference between its CCP time and the time of the reference CCP. This was found to greatly increase the coherency of events on subsequent surface stacks (Figure 8.8). It should be noted that the removal of structure was only done as an aid in determining statics; all other processing was carried out on the uncorrected data. Residual statics were found to be generally within  $\pm 16$  ms, with a maximum value of -36 ms.

An average  $V_p/V_s$  value of 2.10 was determined by event correlation between the vertical and radial sections. The data from the radial and transverse directions were gathered and stacked using this ratio and the asymptotic approximation [equation (2.25)], giving the sections shown in Figures 8.9 and 8.10.

There was found to be significant energy on the transverse-component section, and a geophone rotation test was performed in order to determine the orientation that minimizes the  $P$ - $SV$  energy on the transverse component data. This was done in the hope of improving the quality of the radial-component section at the expense of the transverse section. The test was done by rotating and stacking the two horizontal data components using clockwise angles ranging from  $-60^\circ$  to  $+30^\circ$  in  $15^\circ$  increments. Portions of the resulting stack sections are shown in Figures 8.11 and 8.12. From this test, a rotation angle of  $-22^\circ$  was estimated, and the rotated data were again processed and stacked (Figures 8.13 and 8.14). The resulting radial component section shows better overall signal strength and reflection continuity than does the unrotated radial component section, while the opposite is true for the transverse component.

The rotated radial-component data were restacked using the depth-variant binning method [equations (2.26)] to give the section shown in Figure 8.15. The process gives improved reflection continuity, but deeper events around the time of basement are generally absent.

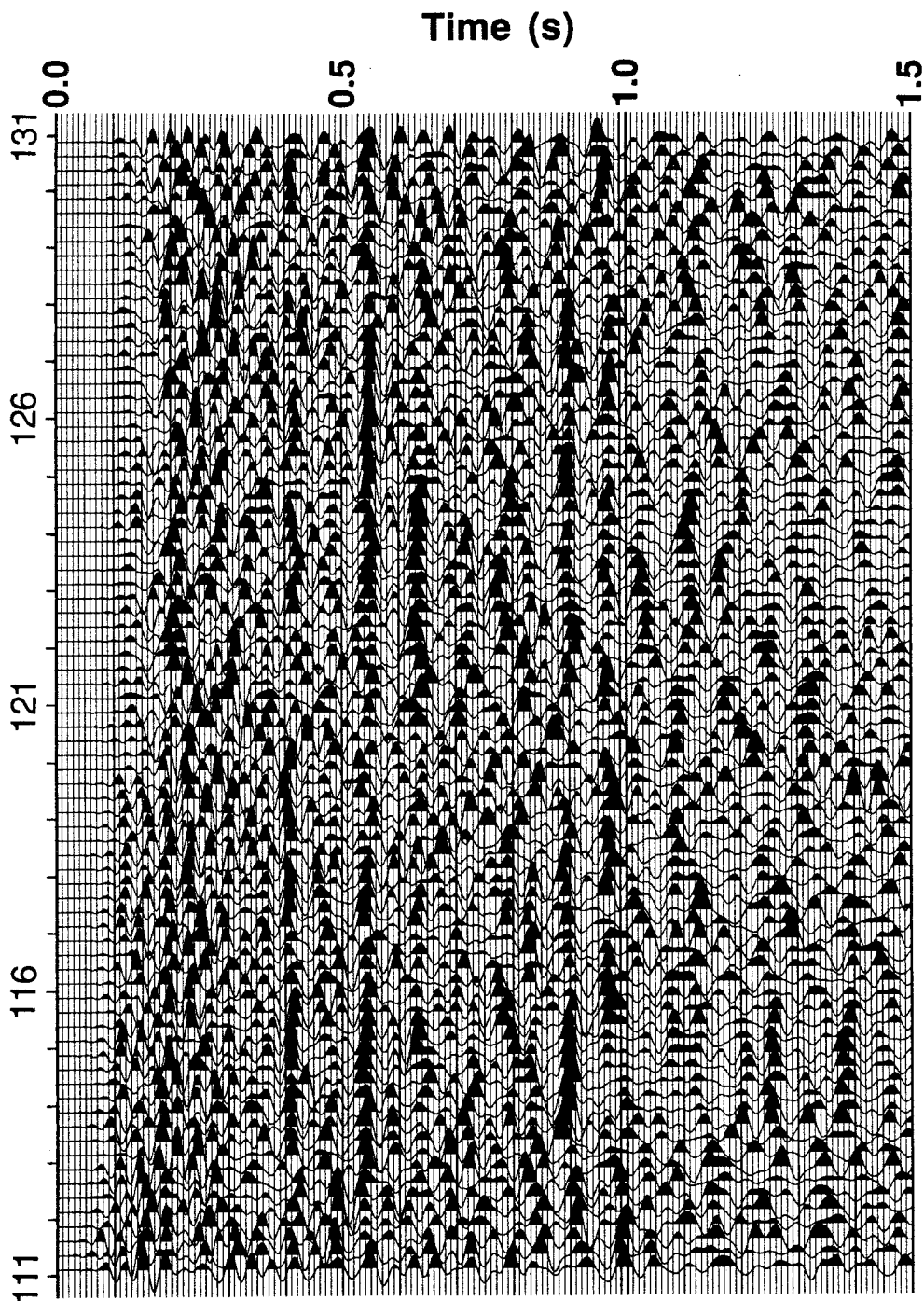


FIG. 8.8. Radial-component common-receiver stack after correction for differences in CCP structure time.

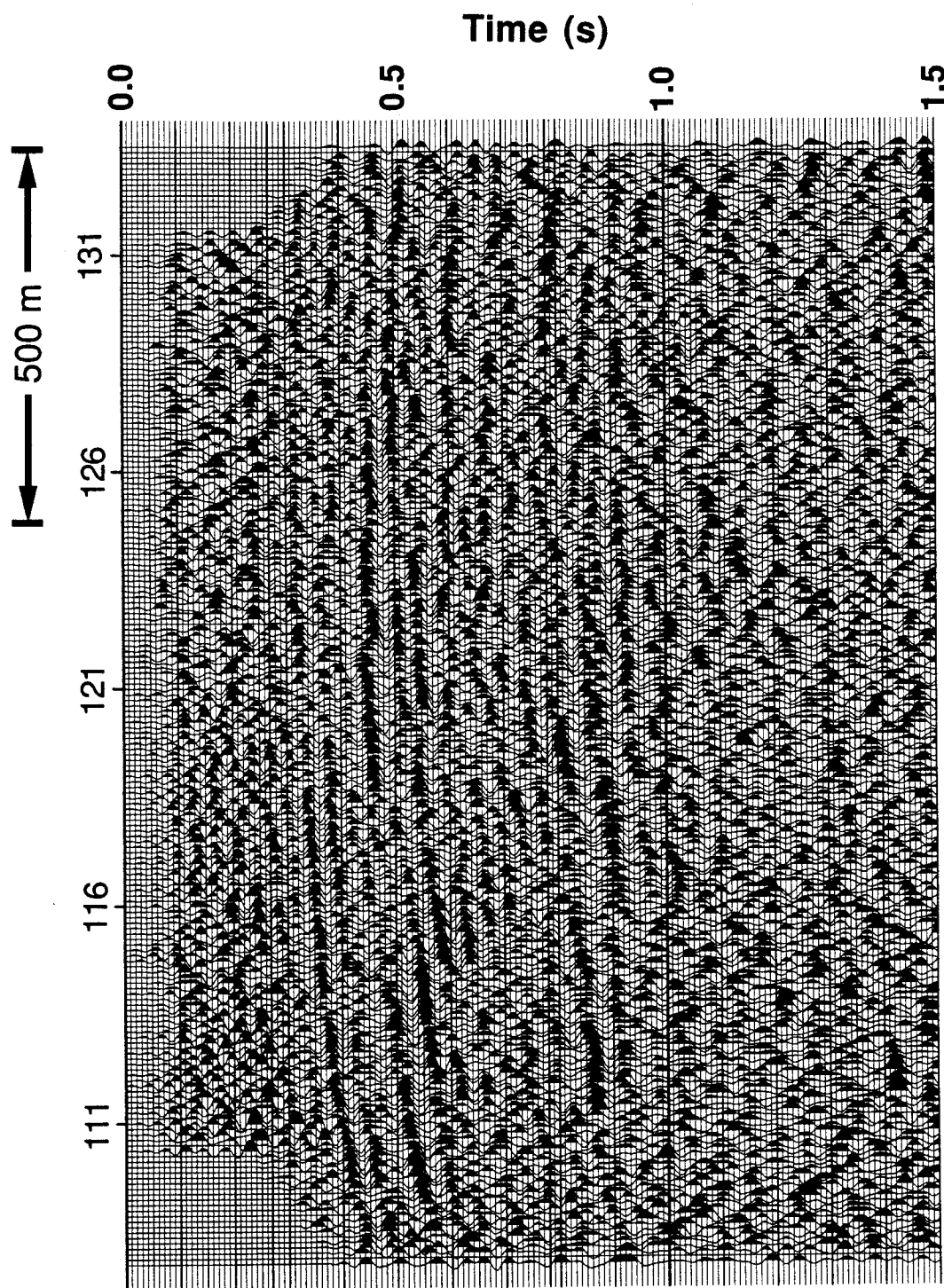


FIG. 8.9. Radial-component data stacked using the asymptotic method.

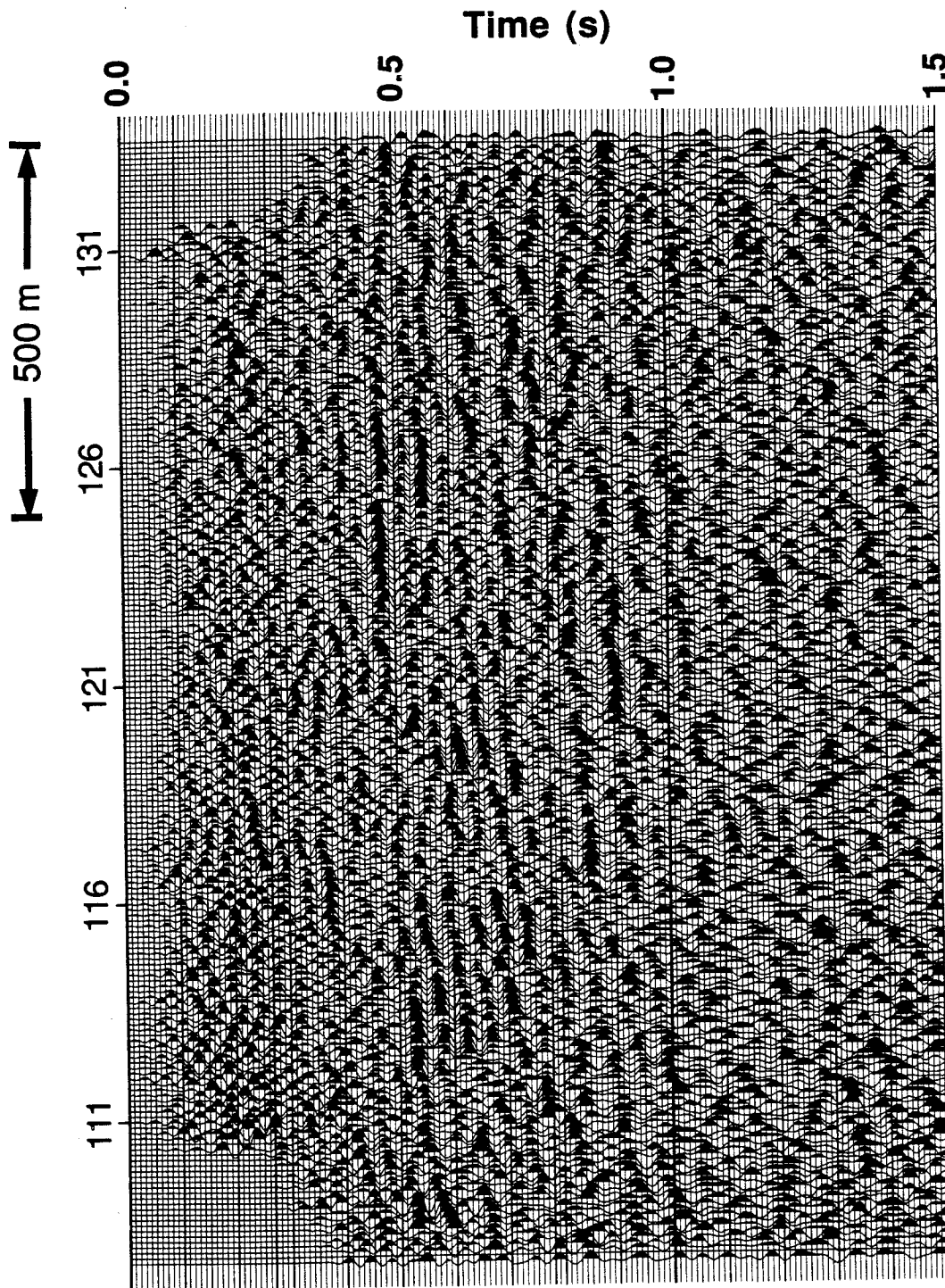


FIG. 8.10. Transverse-component data stacked using the asymptotic method.

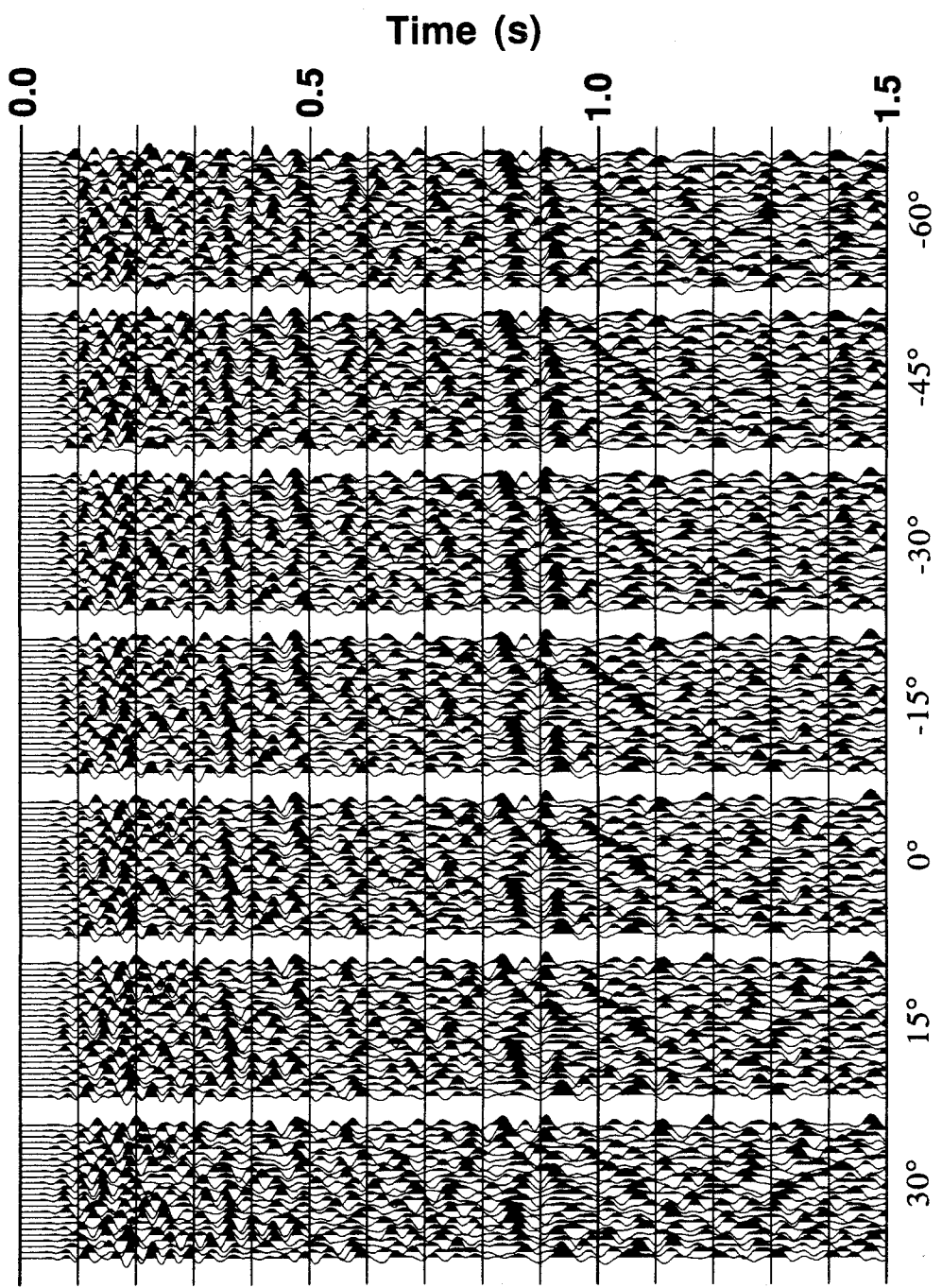


FIG. 8.11. Geophone rotation analysis for radial-component data.

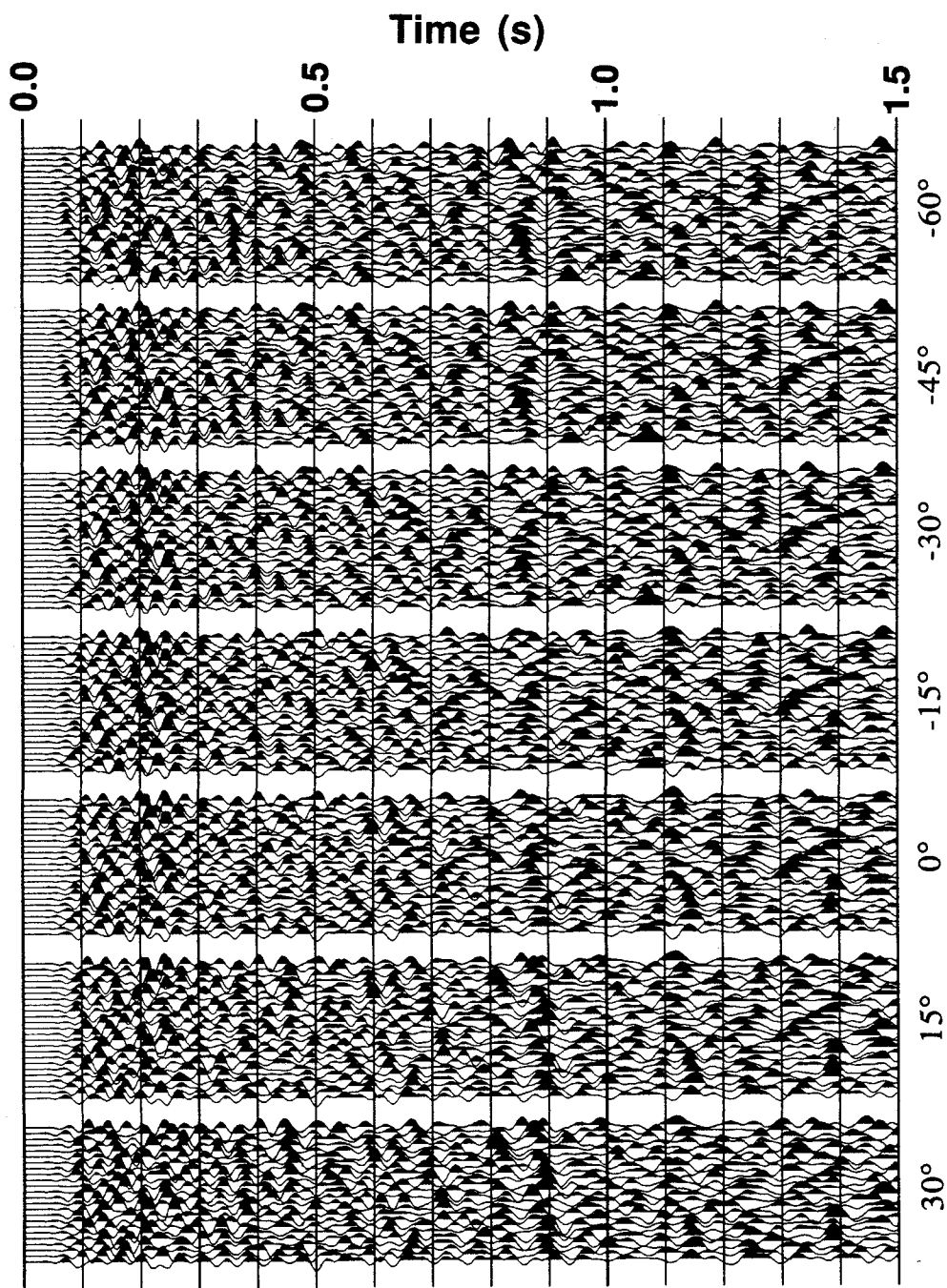


FIG. 8.12. Geophone rotation analysis for transverse-component data.

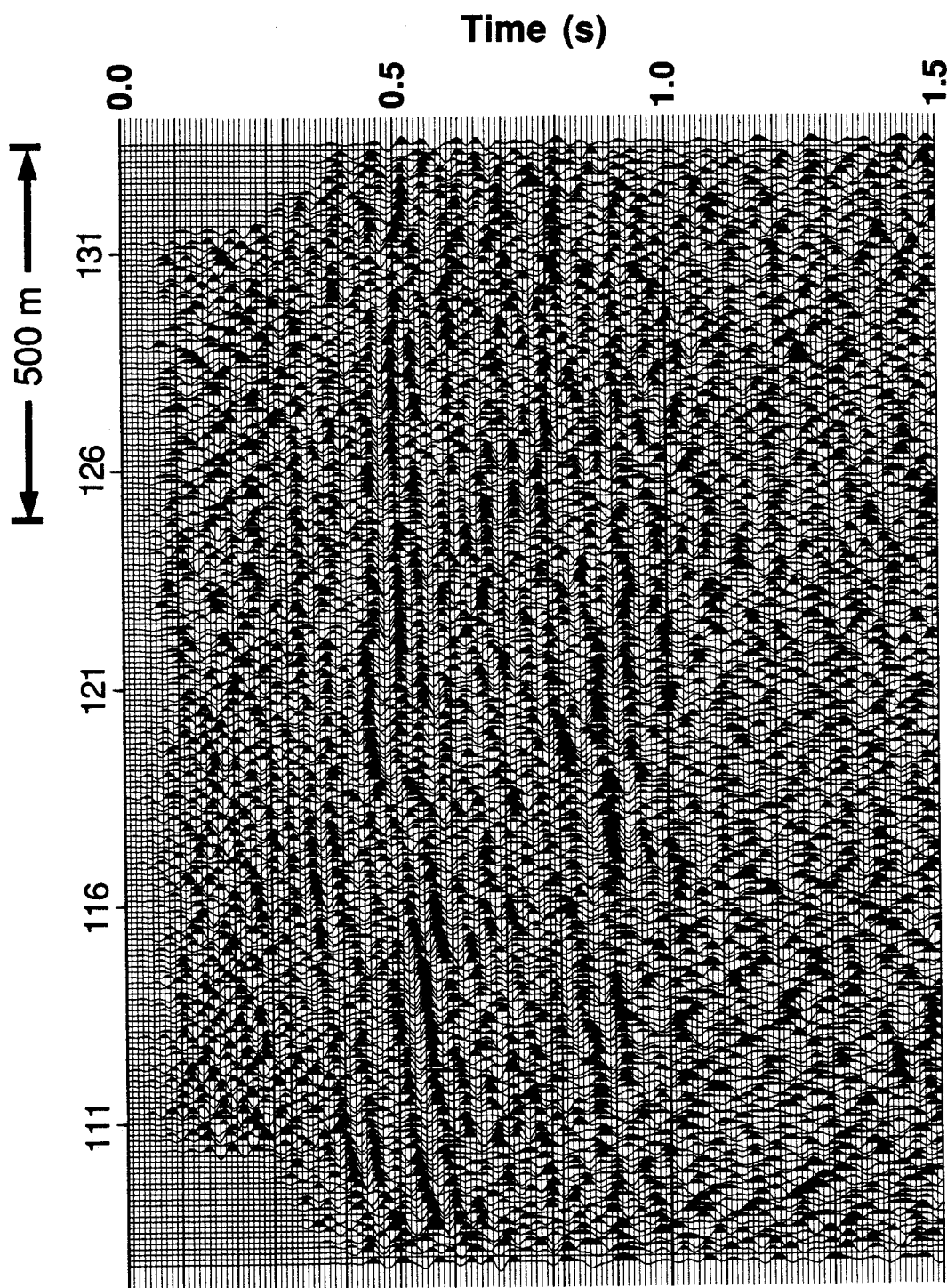


FIG. 8.13. Rotated radial-component data stacked using the asymptotic method.

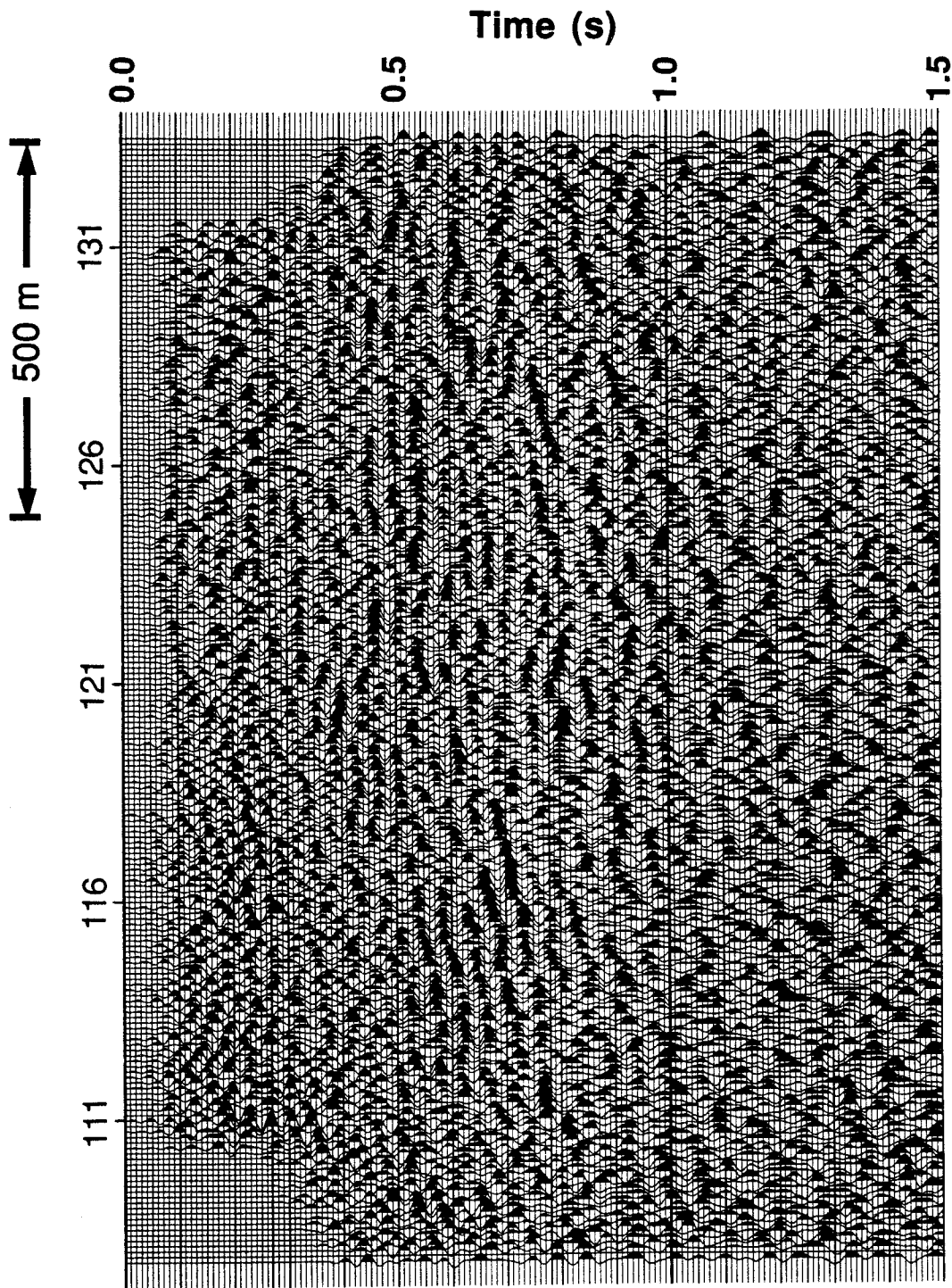


FIG. 8.14. Rotated transverse-component data stacked using the asymptotic method.

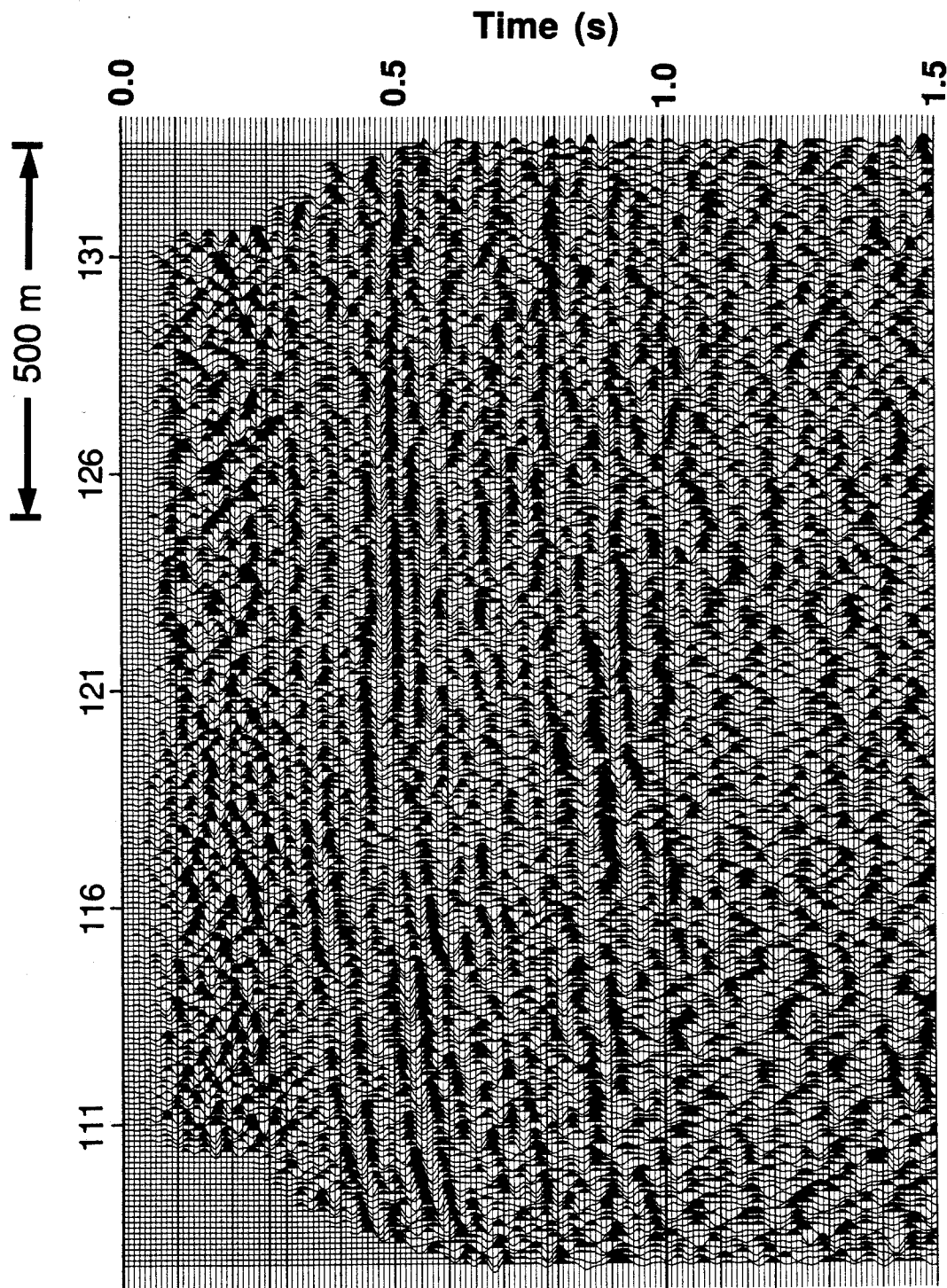


FIG. 8.15. Rotated radial-component data stacked using the depth-variant binning method.

Depth-variant  $P$ - $SV$  DMO (Section 4.8.2) was also applied to the rotated radial-component data set (Figure 8.16). The process gives better overall reflection continuity than does the depth-variant-stacked section in Figure 8.15. Also, the basement reflection has been enhanced, and can be followed across most of the section. Operator noise from the far-offset data is, however, a problem at the ends of the line where fold is insufficient to give proper cancellation. The application of an  $f$ - $k$  filter with a passband of  $\pm 4$  ms/trace and a 6 db reject reduces some of this noise and enhances the continuity of the deeper events (Figure 8.17). Poststack migration using the  $P$ - $SV$  migration velocities [equation (5.24)] was applied to the  $f$ - $k$  -filtered DMO section, producing the result shown in Figure 8.18.

A side-by-side comparison of the vertical-component section and the DMO-corrected radial component is presented in Figure 8.19. Sample NMO-corrected common-offset records for the vertical- and radial-component data are shown in Figure 8.20.

## 8.4 Discussion

The data quality of the radial component is seen from the common-offset stacks of Figure 8.20 to be very poor, with no optimum window for shear reflections. This general absence of good reflection signal, coupled with the presence of substantial amounts of structure, make both static and velocity estimation difficult. As demonstrated in this chapter, the common-receiver stack method of resolving residual statics fails in areas of structure. The method must be modified to compensate for changes in structure time across the section, or some other, more robust, method must be found.

From Figure 8.19, there does appear to be general correspondence between reflections on the vertical and radial sections. The large difference in data bandwidth and quality make the correlation of specific events difficult, especially in the absence of well information. The application of  $P$ - $SV$  dip moveout to the rotated data was able to improve the continuity of deeper reflections over that produced by depth-variant binning. Migration

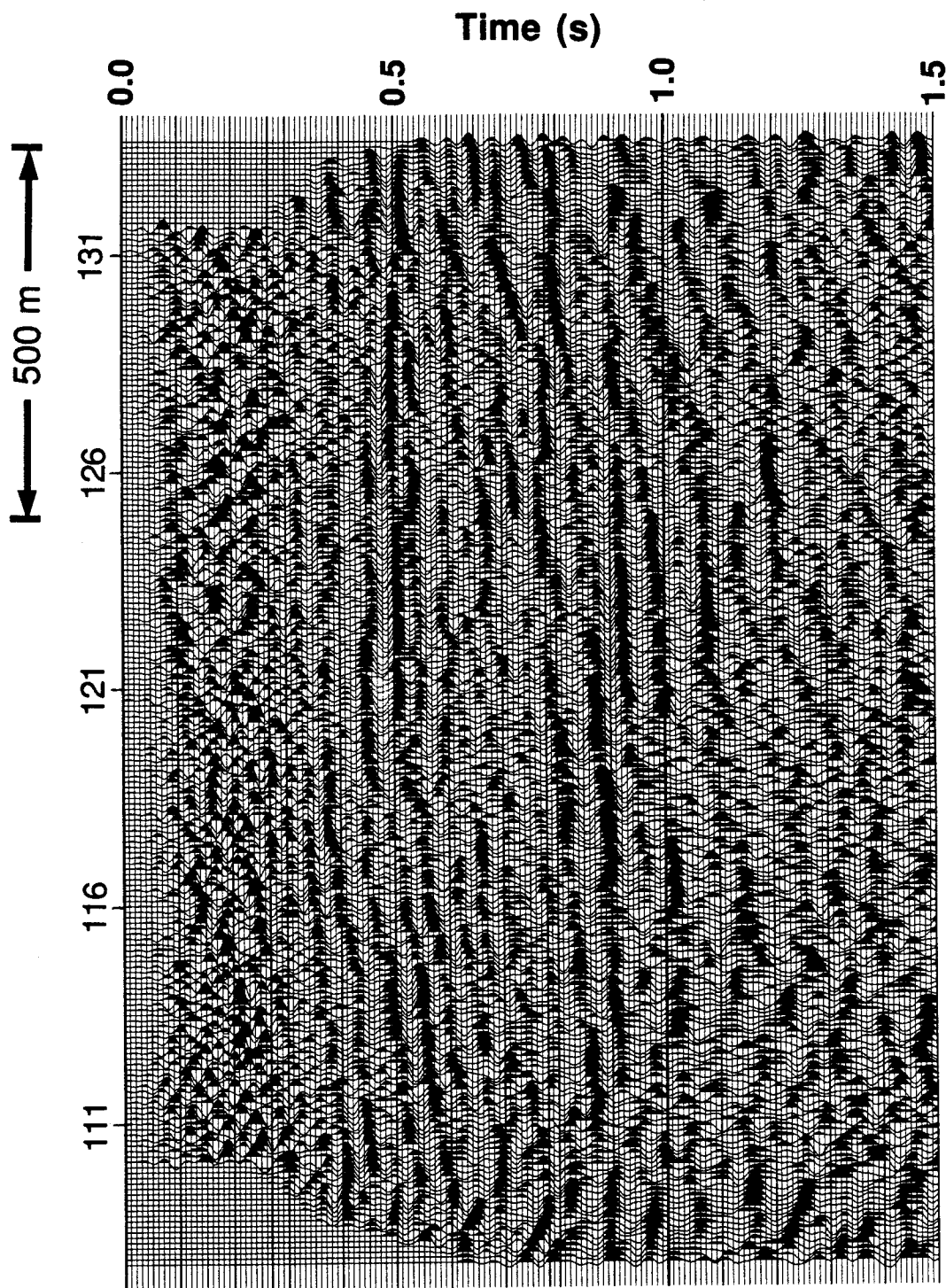


FIG. 8.16. Rotated radial-component data stacked using *P-SV* DMO.

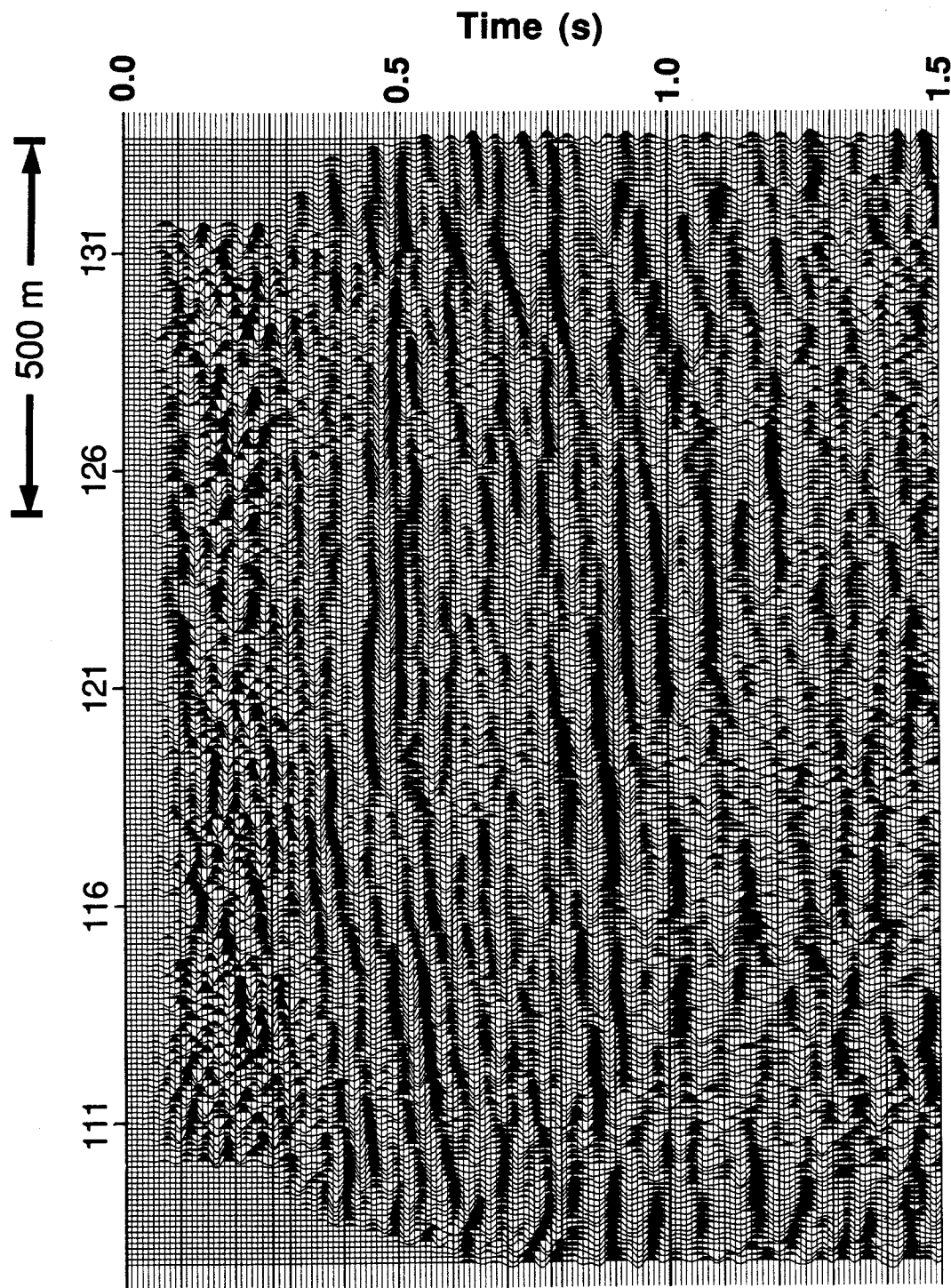


FIG. 8.17.  $f$ - $k$  filter applied to the rotated radial-component data stacked using  $P$ -SV DMO.

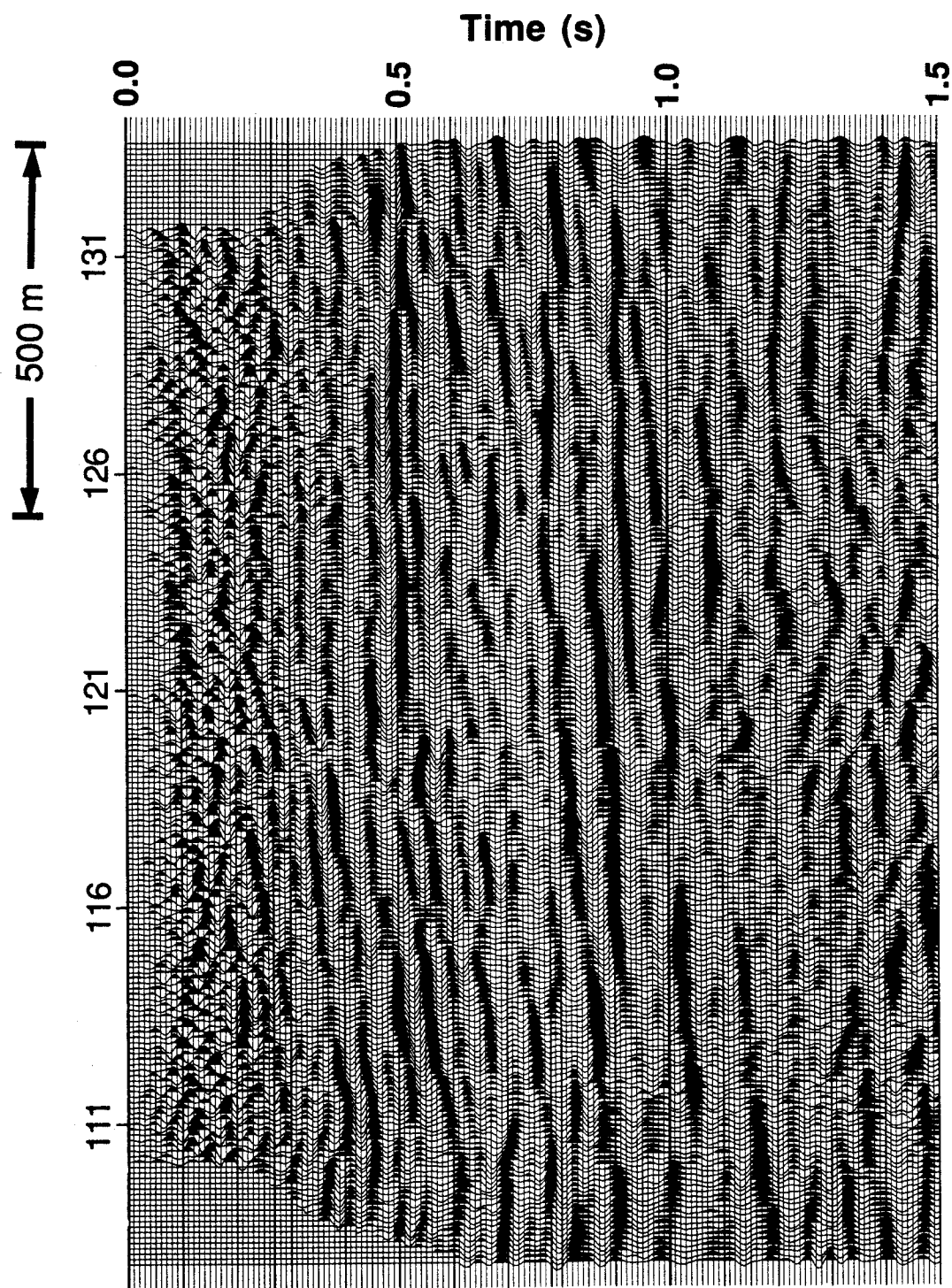


FIG. 8.18. Migration applied to the rotated radial-component data stacked with P-SV  
DMO and  $f-k$  filter.

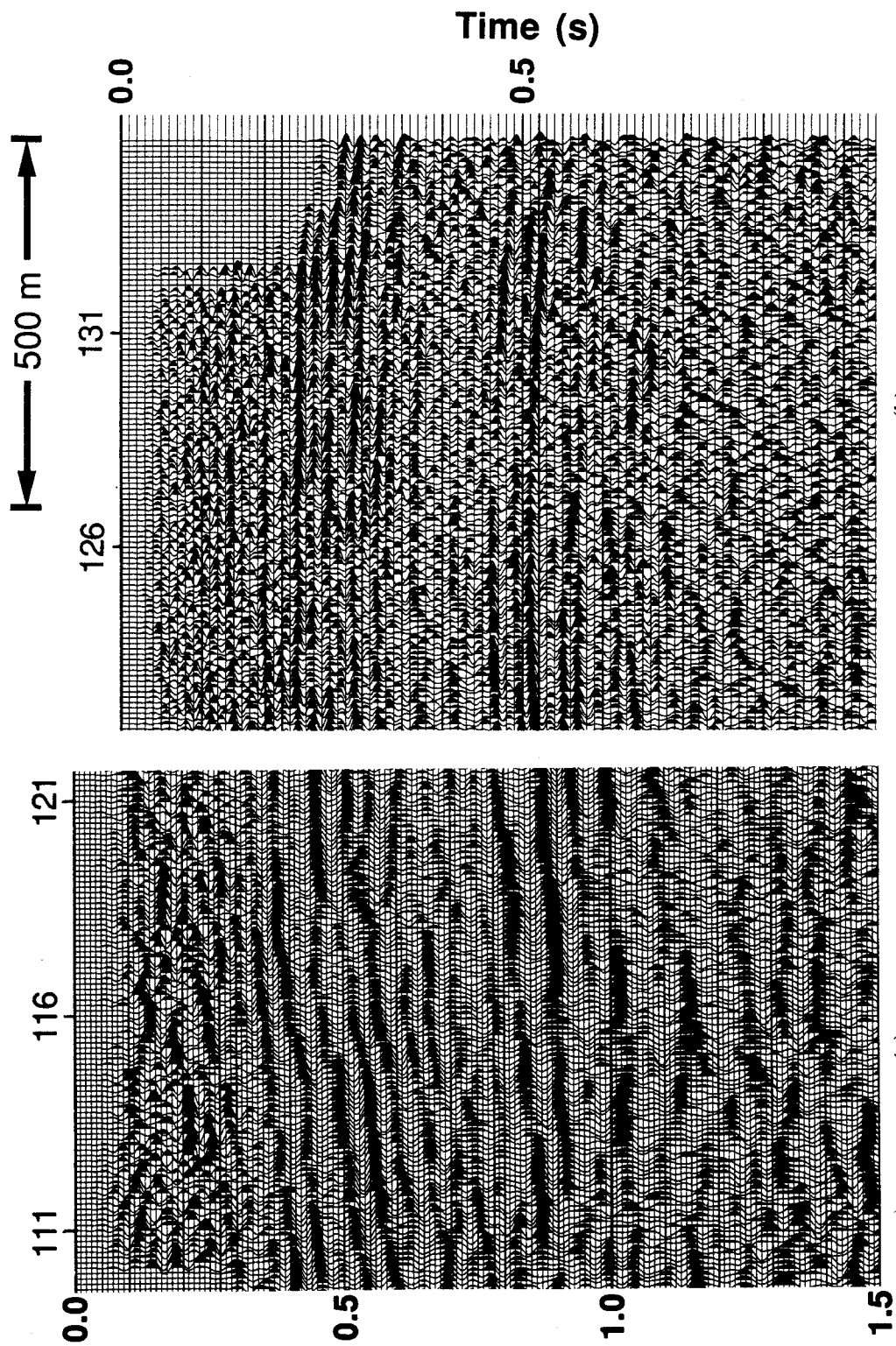


FIG. 8.19. Side-by-side comparison of (a) the  $f-k$  filtered DMO section for the rotated radial-component, and (b) the vertical-component stack section.

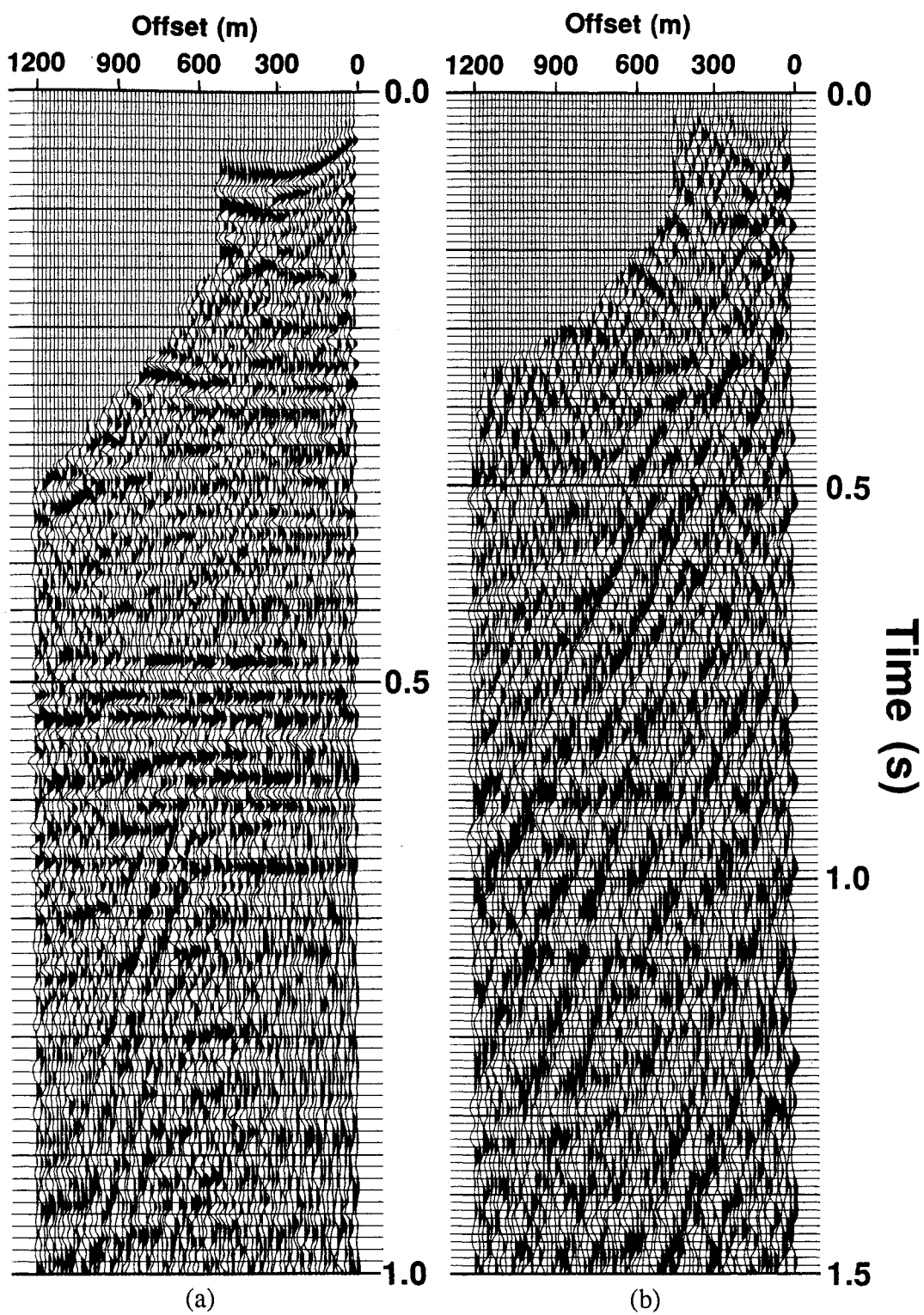


FIG. 8.20. NMO-corrected common-offset stack records: (a) vertical component; (b) radial component.

of the DMO-corrected section gives a result that correlates structurally to the migrated vertical-component stack, but has much lower signal bandwidth and signal-to-noise level.

Although the rotation of the horizontal components did give some overall improvement in the rotated radial-component section, it can be seen in Figures 8.11 and 8.12 that the reflection at about 1100 ms is not maximized by a  $-22^\circ$  rotation. The best rotation angle appears to fall in the range of  $0-15^\circ$ . In support of this, it was found that *P-SV* dip moveout applied to the unrotated data gave a more continuous reflection at 1100 ms than is seen in Figure 8.16. This change in rotation angle with depth might indicate the presence of anisotropy in the 850-1100 ms interval. Through the analysis of multicomponent VSP data from a well south of this line, Kramer and Davis (1991) found that the zone encompassing the Tensleep formation does exhibit velocity anisotropy in the range of 4 to 11%.

This data set could be a good candidate for the rotation analysis method developed in Chapter 3, both to improve data quality by rotation into the natural coordinate system, and to compare the analysis results to those of Kramer and Davis (1991).

## Chapter 9 - Conclusions

### 9.1 Dissertation summary

The main goal of this dissertation has been to summarize and to extend the current state of multicomponent converted-wave processing, as well as to apply the processing algorithms and procedures to a number of field data examples.

The entire processing flow for  $P$ - $SV$  surface data was described in Chapter 2. An equation for geometric spreading compensation was developed, and an algorithm for poststack velocity inversion of converted-wave surface data was presented.

The problem of  $S$ -wave birefringence for the case of a singly-polarized shear source was examined in Chapter 3. An algorithm for the determination of the amount of  $S$ -wave splitting and the orientation of the natural coordinate system was developed. This algorithm is based upon the modeling of the crosscorrelation function between rotated radial and transverse field components. Synthetic examples indicated that it could resolve time delays of about 1 ms or greater for noise-free data with an 8-35 Hz bandwidth; the receiver azimuth relative to the natural coordinate system was accurately determined for time delays of about 2 ms or greater. A study of the method's performance versus signal-to-noise power ratio suggested that a signal-to-noise ratio of about 36 db is needed to obtain both the time-delay and rotation angle from a single receiver data set. For data with a signal-to-noise power ratio of 0 db, an analysis fold of about 60 is required to find the correct time delay and rotation angle. Application of the method to converted-wave data from Carrot Creek, Alberta, produced results that are in agreement with the difference in orientation between the two lines in the survey.

In Chapter 4, an expression for common-conversion-point (CCP) dispersal for  $P$ - $SV$  data was derived, and was found to give greater dispersal for data converted in the down-dip direction than in the up-dip direction. It was shown that the apparent stacking

velocity for the single-layer case is also asymmetric about reflector zero-dip, and that for large positive (down-dip) values the apparent velocity can become imaginary. A dip moveout (DMO) equation for converted-wave data was derived, and was proven to properly account for  $P$ - $SV$  CCP dispersal. A new cubic equation for determining the location to the zero-dip conversion point was also developed. The  $P$ - $SV$  DMO equation was implemented using an integral-summation technique and applied to both synthetic and real data examples. Synthetic data examples in Chapters 4 and 5 showed that  $P$ - $SV$  DMO gives better amplitude preservation of  $P$ - $SV$  diffractions and dipping reflections.

The application of poststack migration to converted-wave stack data was studied in Chapter 5. It was shown that the exploding reflector model does not strictly hold for converted-wave stack data, but is a reasonable approximation if there are no large depth variations in  $V_p/V_s$  value. A  $P$ - $SV$  migration velocity equation was developed, and was found to give velocities that are less than  $P$ - $SV$  stacking velocities by 6-11%. Migration of synthetic  $P$ - $SV$  diffractions demonstrated that stacking velocities produce substantial overmigration, whereas the diffractions are adequately collapsed by the  $P$ - $SV$  migration velocities. Migration of a physical model data set showed that  $P$ - $SV$  data can give a good structural image.

In Chapter 6, the processing techniques developed and discussed in this dissertation were applied to a three-component vibroseis survey from Carrot Creek, Alberta. The radial-component ( $P$ - $SV$ ) stack section was of good quality, with amplitude anomalies that correspond to the known location of oil pools. These anomalies were largely absent on the vertical-component ( $P$ - $P$ ) sections.

The processing results for a two-component data set from Springbank, Alberta, were presented in Chapter 7. The radial-component data were found to be of very poor quality; the stack section, however, had many coherent reflections that correlated well to those of the vertical-component stacked data.

The results of processing a three-component dynamite survey from Casper Creek South, Wyoming, were presented in Chapter 8. Two-component geophone rotation was found to produce some improvement in the rotated radial-component data signal strength. Reflections with substantial dips were imaged on both the  $P$ - $P$  and  $P$ - $SV$  stack sections. The converted-wave section, however, had a higher noise level and much lower bandwidth than the vertical-component ( $P$ - $P$ ) section.

## 9.2 Future work

More work is needed to further evaluate the  $S$ -wave birefringence algorithm developed in Chapter 3. For areas where the orientation of the natural coordinate system changes with depth, the algorithm should be incorporated into a layer-stripping analysis, as has been done for the VSP case with a multiply-polarized source (e.g., Winterstein and Meadows, 1991).

It can be seen from Figure 4.18 that the true DMO response for the multilayered case is much more complex than that predicted by equation (4.49). More work is needed to better determine the range of usefulness of the  $P$ - $SV$  DMO algorithm developed in Chapter 4, and, perhaps, to develop a more rigorous extension of  $P$ - $SV$  DMO for the case of depth-varying velocities.

The largest problem encountered in processing converted-wave data is the difficulty in determining an  $S$ -wave receiver static solution. Although common-receiver stacks can often be used to obtain a solution for the high-frequency static component, they do not give any information about the very-low-frequency static components. This makes the structure of events on converted-wave sections unreliable. More work is needed to determine the usefulness of source-generated shear refractions for resolving both high- and low-frequency  $S$ -wave receiver statics.

Finally, the bandwidth of *P-SV* surface data is typically about one-half that of *P*-wave surface data, giving less vertical resolution. Anything that can be done in processing to extend the bandwidth of converted-wave data would be very useful.

## References

- Aki, K., and Richards, P. G., 1980, *Quantitative Seismology*, **1**: W.H. Freeman and Company.
- Alford, R. M., 1986, Shear data in the presence of azimuthal anisotropy: Dilley, Texas: 56th Ann. Internat. Mtg., Soc. Expl. Geophys., Expanded Abstracts, 476-479.
- Anno, P. D., 1987, Two critical aspects of shear-wave analysis: statics solutions and reflection correlations, *in* Danbom, S. H., and Domenico, S. N., Eds., *Shear-wave Exploration: Soc. Expl. Geophys., Geophysical development series* **1**, 48-61.
- Bale, R., and Jakubowicz, H., 1987, Post-stack prestack migration: 57th Ann. Internat. Mtg., Soc. Expl. Geophys., Expanded Abstracts, 714-717.
- Beasley, C., and Mobley, E., 1988, Amplitude and anti-aliasing treatment in (x,t) domain DMO: 58th Ann. Internat. Mtg., Soc. Expl. Geophys., Expanded Abstracts, 1113-1116.
- Behle, A., and Dohr, G., 1985, Converted waves in seismic exploration, *in* Dohr, G. Ed., *Seismic Shear Waves: Handbook of Geophysical Exploration*, **15b**, 178-220.
- Bell, J. S., and Babcock, E. A., 1986, The stress regime of the Western Canadian Basin and implications for hydrocarbon production: *Bull. Can. Petro. Geol.*, **34**, 364-378.
- Beyer, W. H., Ed., 1984, *CRC standard mathematical tables*, 27th edition: CRC Press Inc.
- Biondi, B., and Ronen, J., 1987, Dip moveout in shot profiles: *Geophysics*, **52**, 1473-1482.
- Bolandi, G., Loinger, E., and Rocca, F., 1982, Offset continuation of seismic sections: *Geophys. Prosp.*, **30**, 813-828.

- Brouwer, J., Douma, J., and Helbig, K., 1985, A new look at migration: First Break, **3**, 9-15.
- Canales, L. L., 1984, Random noise attenuation: 54th Ann. Internat. Mtg., Soc. Expl. Geophys., Expanded Abstracts, 525-527.
- Chung, W. Y., and Corrigan, D., 1985, Gathering mode-converted shear waves: a model study: 55th Ann. Internat. Mtg., Soc. Expl. Geophys., Expanded Abstracts, 602-604.
- Claerbout, J. K., and Doherty, S. M., 1972, Downward continuation of moveout-corrected seismograms: Geophysics, **37**, 741-768.
- Claerbout, J. K., 1976, Fundamentals of geophysical data processing with applications to petroleum prospecting: McGraw-Hill Inc.
- Crampin, S., Chesnokov, E. M., and Hipkin, R. G., 1984, Seismic anisotropy - the state of the art: II: Geophys. J. Roy. Astro. Soc., **76**, 1-16.
- Crampin, S., 1989, Analysis of polarization diagrams: SEG research workshop, Snowbird, Utah, Technical Abstracts, 96.
- Deregowski, S. M., and Rocca, F., 1981, Geometrical optics and wave theory of constant offset sections in layered media: Geophys. Prosp., **29**, 384-406.
- Deregowski, S. M., 1982, Dip-moveout and reflector point dispersal: Geophys. Prosp., **30**, 318-322.
- Deregowski, S. M., 1985, An integral implementation of dip moveout: Presented at the 47th Ann. Mtg., EAEG.
- Dix, C. H., 1955, Seismic velocities from surface measurements: Geophysics, **20**, 68-86.
- Domenico, S. N., 1984, Rock lithology and porosity determination from shear and compressional wave velocity: Geophysics, **49**, 1188-1195.
- Douma, J. and Helbig, K., 1987, What can the polarization of shear waves tell us?: First Break, **5**, 95-104.

- Eaton, D. W. S., Slotboom, R. T., Stewart, R. R., and Lawton, D. C., 1990, Depth-variant converted-wave stacking: 60th Ann. Internat. Mtg., Soc. Expl. Geophys., Expanded Abstracts, 1107-1110.
- Eaton, D. W. S., Stewart, R. R., and Harrison, M. P., 1991, The Fresnel zone for converted P-SV waves: *Geophysics*, **56**, 360-364.
- Edelman, H. A. K., 1985, Shear-wave energy sources, *in* Dohr, G. Ed., *Seismic Shear Waves: Handbook of Geophysical Exploration*, **15b**, 134-177.
- Fix, J. E., Robertson, J. D., and Pritchett, W. C., 1987, Shear-wave reflections in three West Texas basins with high-velocity surface rocks, *in* Danbom, S. H., and Domenico, S. N., Eds., *Shear-wave Exploration: Soc. Expl. Geophys., Geophysical development series 1*, 180-196.
- Fromm, G., Krey, Th., and Wiest, B., 1985, Static and dynamic corrections, *in* Dohr, G. Ed., *Seismic Shear Waves: Handbook of Geophysical Exploration*, **15a**, 191-225.
- Gadzag, J., 1978, Wave equation migration with the phase-shift method: *Geophysics*, **43**, 1342-1351.
- Galbraith, J. M., and Millington, G. F., 1979, Low frequency recovery in the inversion of seismograms: *Can. J. Expl. Geophys.*, **15**, 30-39.
- Garotta, R., 1985, Observation of shear waves and correlation with P events, *in* Dohr, G. Ed., *Seismic Shear Waves: Handbook of Geophysical Exploration*, **15b**, 1-86.
- Garotta, R., 1987, Two-component acquisition as a routine procedure, *in* Danbom, S. H., and Domenico, S. N., Eds., *Shear-wave Exploration: Soc. Expl. Geophys., Geophysical development series 1*, 122-136.
- Garotta, R., and Granger, P. Y., 1988, Acquisition and processing of 3C x 3D data using converted waves: 58th Ann. Internat. Mtg., Soc. Expl. Geophys., Expanded Abstracts, 995-997.
- Gordy, P.L., Frey, F. R., and Norris, D. K., 1977, Geological guide for the CSPG and the 1977 Waterton Glacier Park Field Conference: C.S.P.G., Calgary.

- Gregory, A. R., 1976, Fluid saturation effects on dynamic elastic properties of sedimentary rocks: *Geophysics*, **41**, 895-921.
- Gulunay, N., 1991, High-resolution CVS: generalized covariance measure: 61st Ann. Internat. Mtg., Soc. Expl. Geophys., Expanded Abstracts, 1264-1268.
- Hale, I. D., 1983, Dip moveout by Fourier transform: Ph.D. thesis, Stanford Univ.
- Hale, D., 1984, Dip moveout by Fourier transform: *Geophysics*, **49**, 741-757.
- Hale, D., 1988, Dip moveout processing: Soc. Expl. Geophys. course notes.
- Harrison, M., 1989, Three-component seismic data processing: Carrot Creek, Alberta: CREWES project annual report, **1**, 6-26.
- Iverson, W. P., Fahmy, B. A., and Smithson, S. B., 1989, VpVs from mode-converted P-SV reflections: *Geophysics*, **54**, 843-852.
- Joiner, S. D., 1989, Sedimentology and Ichnology of the Cardium Carrot Creek Field, West Central Alberta, Canada: unpublished thesis, Univ. of Calgary.
- Judson, D. R., Schultz, P. S., and Sherwood, J. W. C., 1978, Equalizing the stacking velocities of dipping events via DEVELISH: presented at the 48th Ann. Internat. Mtg., Soc. Expl. Geophys.
- Justice, M. G., McCormack, M. D., and Lee, S. S., 1987, Anisotropy in the Marrow Formation of southeast New Mexico, *in* Danbom, S.H., and Domenico, S.N., Eds., Shear-wave Exploration: Soc. Expl. Geophys., Geophysical development series **1**, 154-164.
- Kanasewich, E. R., 1981, Time sequence analysis in geophysics: University of Alberta Press.
- Knopoff, L., 1959, Scattering of compression waves by spherical obstacles: *Geophysics*, **24**, 30-39.
- Kramer, D., and Davis, T. L., 1991, Multicomponent vertical seismic profiles for reservoir characterization, South Casper Creek field, Natrona County, Wyoming: 61st Ann. Internat. Mtg., Soc. Expl. Geophys., Expanded Abstracts, 383-385.

- Kreyszig, E., 1972, *Advanced engineering mathematics*: John Wiley & Sons Inc.
- Lawton, D. C., 1991, Nine-component refraction statics survey: *Can. J. Expl. Geophys.*, **26**, 7-16.
- Lawton, D. C., and Harrison, M. P., 1992, A two-component reflection seismic survey, Springbank, Alberta: *Can. J. Expl. Geophys.*, **27**, in press.
- Levin, F. K., 1971, Apparent velocity from dipping interface reflections: *Geophysics*, **36**, 510-516.
- Lewis, C., Davis, T. L., Vuillermoz, C., Gurch, M., Iverson, W., and Schipperijn, A. P., 1989, Three-dimensional multicomponent imaging of reservoir heterogeneity, Silo Field, Wyoming: 59th Ann. Internat. Mtg., Soc. Expl. Geophys., Expanded Abstracts, 763-766.
- Loewenthal, D., Lu, L., Roberson, R., and Sherwood, J. W. C., 1976, The wave equation applied to migration: *Geophys. Prosp.*, **24**, 380-389.
- Martin, M. A., Davis, T. L., and O'Rourke, T. J., 1986, An integrated three-component approach to fracture detection: 56th Ann. Internat. Mtg., Soc. Expl. Geophys., Expanded Abstracts, 235-236.
- McBeth, C., and Crampin, S., 1991, Comparison of signal processing techniques for estimating the effects of anisotropy: *Geoph. Prosp.*, **39**, 357-385.
- McBeth, C., 1990, Inversion of shear-wave polarizations for anisotropy using three-component offset VSPs: 60th Ann. Internat. Mtg., Soc. Expl. Geophys., Expanded Abstracts, 1404-1406.
- Muskat, M., and Meres, M. W., 1940, Reflection and transmission coefficients for plane waves in elastic media: *Geophysics*, **49**, 1637-1648.
- Naville, C., 1986, Detection of anisotropy using shear-wave splitting in VSP surveys: requirements and applications: 56th Ann. Internat. Mtg., Soc. Expl. Geophys., Expanded Abstracts, 391-394.

- Nazar, B., 1991, An interpretive study of multicomponent seismic data from the Carrot Creek area of west-central Alberta: M.Sc. thesis, Univ. of Calgary.
- Neidell, N. S., and Taner, M. T., 1971, Semblance and other coherency measures for multichannel data: *Geophysics*, **36**, 482-497.
- Newman, P., 1973, Divergence effects in a layered earth: *Geophysics*, **38**, 481-488.
- Notfors, C. D., and Godfrey, R. J., 1987, Dip moveout in the frequency-wavenumber domain: *Geophysics*, **52**, 1718-1721.
- Ostrander, W. J., 1984, Plane-wave reflection coefficients for gas sands and nonnormal angles of incidence: *Geophysics*, **49**, 149-155.
- Peron, J., 1990, Estimation of fracture directions from zero-offset VSP by two- and four-component rotation: 60th Ann. Internat. Mtg., Soc. Expl. Geophys., Expanded Abstracts, 1443-1446.
- Pickett, G., 1963, Acoustic character logs and their application in formation evaluation: *J. Petr. Tech.*, **15**, 659-667.
- Pieprzak, A. P., and Bramblett, N. V., 1990, Amplitude preserving DMO summation algorithm for 2-D and marine 3-D: 60th Ann. Internat. Mtg., Soc. Expl. Geophys., Expanded Abstracts, 1358-1361.
- Ruddiman, B., 1989, Casper Creek South, *in* Cardinal, C., Miller, T., Stewart, W., and Trotter, J., Eds., Wyoming oil and gas fields symposium - Bighorn and Wind River basins: Wyoming Geological Association, 88-89.
- Schafer, A., 1989, Determination of shear wave statics using converted, refracted waves from a compressional source: CREWES project annual report, **1**, 39-41.
- Schulte, L., and Edelmann, H. A. K., 1988, Azimuthal anisotropy proven to be a useful approach for multicomponent shear-wave data processing: 58th Ann. Internat. Mtg., Soc. Expl. Geophys., Expanded Abstracts, 1156-1158.
- Sheriff, R. E., 1973, Encyclopedic dictionary of exploration geophysics: Society of Exploration Geophysicists.

- Shuey, R. T., 1985, A simplification of the Zoeppritz equations: *Geophysics*, **50**, 609-614.
- Slack, R. D., Ebrom, D. A., and Tatham, R. H., 1991, Thin layers and shear-wave splitting: 61st Ann. Internat. Mtg., Soc. Expl. Geophys., Expanded Abstracts, 1549-1552.
- Slotboom, R. T., 1990, Converted-wave (P-SV) moveout estimation: 60th Ann. Internat. Mtg., Soc. Expl. Geophys., Expanded Abstracts, 1104-1106.
- Spencer, T. W., and Chi, H. C., 1991, Thin-layer fracture density: *Geophysics*, **56**, 833-843.
- Squires, S. G., Kim, C. D. Y., and Kim, D. Y., 1989, Interpretation of total wave-field data over Lost Hills field, Kern County, California: *Geophysics*, **54**, 1420-1429.
- Stewart, R. R., 1991, Rapid map and inversion of P-SV waves: *Geophysics*, **56**, 859-862.
- Stewart, R. R., and Marchisio, G., 1991, Side-scanning seismic: Analysis and a physical modeling study: presented at the 1991 Ann. Nat. Can. Soc. Expl. Geophys. Mtg., Calgary.
- Stolt, R. H., 1978, Migration by Fourier transform: *Geophysics*, **43**, 23-48.
- Taner, M. T., and Koehler, F., 1969, Velocity spectra - digital computer derivation and applications of velocity functions: *Geophysics*, **34**, 859-884.
- Tatham, R. H., and Stoffa, P. L., 1976,  $V_p/V_s$  - a potential hydrocarbon indicator: *Geophysics*, **41**, 837-849.
- Tatham, R. H., 1985, Shear waves and lithology, *in* Dohr, G. Ed., *Seismic Shear Waves: Handbook of Geophysical Exploration*, **15b**, 87-133.
- Tessmer, G. and Behle, A., 1988, Common reflection point data-stacking technique for converted waves: *Geophys. Prosp.*, **36**, 661-688.

- Thomsen, L., 1988, Reflection seismology over azimuthally anisotropic media: *Geophysics*, **53**, 304-313.
- Ursin, B., 1990, Offset-dependent geometrical spreading in a layered medium: *Geophysics*, **55**, 492-496.
- Wiest, B., and Edelmann, H. A. K., 1984, Static corrections for shear wave sections: *Geophys. Prosp.*, **32**, 1091-1102.
- Wiggins, R. A., Lerner, K. L., and Wisecup, R. D., 1976, Residual statics analysis as a general linear inverse problem: *Geophysics*, **41**, 922-938.
- Winterstein, D. F., 1989, Comparison of three methods for finding polarization direction of the fast shear wave: SEG research workshop, Snowbird, Utah, Technical Abstracts, 118-119.
- Winterstein, D. F., 1990, Velocity anisotropy terminology for geophysicists: *Geophysics*, **55**, 1070-1088.
- Winterstein, D. F., and Meadows, M. A., 1991, Changes in shear-wave polarization azimuth with depth in Cymric and Railroad Gap oil fields: *Geophysics*, **56**, 1349-1364.
- Wren, A. E., 1984, Seismic techniques in Cardium exploration: *Can. J. Expl. Geophys.*, **20**, 55-59.
- Yardley, G., and Crampin, S., 1990, Automatic determination of anisotropic parameters from shear-wave splitting in the Lost Hills VSP: 60th Ann. Internat. Mtg., Soc. Expl. Geophys., Expanded Abstracts, 1424-1426.
- Yilmaz, O., and Claerbout, J. F., 1980, Prestack partial migration: *Geophysics*, **45**, 1753-1779.
- Zoeppritz, K., 1919, *Über reflexion and durchgang seismischer wellen durch un stetig kerlsflaschen*, Berlin: *Über Erdbebenwellen VIIB*, Nachrichten der Koniglichen Gesellschaft der Wissenschaften Zu Gottingen, Math-Phys.